Magnon Bose-Einstein Condensation, Magnetization Processes and Magneto-transport in Nanocrystalline Gadolinium

A thesis submitted in partial fulfillment
of the award of the degree of
Doctor of Philosophy

By
Shinto P. Mathew

School of Physics
University of Hyderabad
Hyderabad - 500 046 India
July 2011

D E C L A R A T I O N

I hereby declare that the matter embodied in this thesis is the result of the investigations carried out by me in the School of Physics, University of Hyderabad, under the supervision of Prof. S. N. Kaul.

Place: Hyderabad — Shinto P. Mathew

Date:

C E R T I F I C A T E

This is to certify that the work contained in this thesis entitled, **"Magnon Bose-Einstein Condensation, Magnetization Processes and Magneto-transport in Nanocrystalline Gadolinium"**, has been carried out by Mr. Shinto P. Mathew under my direct supervision and the same has not been submitted for the award of research degree of any university.

Place: Hyderabad (Thesis Supervisor)

Date:

Dean

School of Physics

To
all my mentors
who have shaped me
to the whole of what I am

Acknowledgements

I am extremely grateful to my supervisor, Prof. S. N. Kaul, for his constant guidance, encouragement, valuable critical comments and for his unabated support throughout my work. His patience and enthusiasm for physics have instilled inspiration in me. My six years of association with him has helped me in a great deal to develop my rudimentary knowledge of Physics. I would also like to acknowledge the kind and encouraging words of Mrs. Manju Kaul.

I express my sincere gratitude to Dr. Srinath; especially for the support and guidance he happily provided while learning interfacing and LabView programming. I thank my lab mate Yugandhar for his assistance and support in carrying out the experiments and for the good time we shared in the lab.

I would also like to thank the Dean, School of Physics, for making available all the necessary facilities for conducting the experiments. My thanks are also due to Prof. R. Birringer and Ms. Anne-Catherine Probst, University of Saarland, Germany, for providing the samples used in this work. I am thankful to the senior scientific officer Mr. C. S. Murthy and the member of technical staff Mr. Suresh of Central Instrumentation Laboratory, for their co-operation and help. I am also thankful to all non-teaching staff, particularly Mr. K. Srinivas, Mr. Abraham and Mr. Machandar for their assistance throughout my Ph.D. I acknowledge the kind help rendered by Mr. Montoo Kumar and Giri Bahadoor in transferring liquid helium and nitrogen.

I thank my senior lab mates Ashutosh, Basheed and Sanjeev for the support and aid they rendered during the initial years in the lab and for their memorable company which eased my otherwise busy times in the lab.

I should also like to thank my lab mates Umasankar, Ravi, Pavan, Sendil and Suresh for their help whenever I sought. I thank Ravikumar for assisting me in programming and interfacing and Devendra, Ramudu, Swaroop, Sathish and Vasu for their help on various occasions.

I thank K. M. Ajith, Abhilash, Joji, Juby, Rohith and Sudheendran for being my friends and for the company and fun-filled moments they gave which soothed me during my off-lab hours with evening strolls and tea. I remember with love the attention and care given by Azhar, Dinesh, Biju, Rajesh and Suraj during my recuperation from an injury and I am also indebted to them for being the support system on which I have often banked. I extend my "thanks" to all my NRS friends, especially Ajith Kumar, Themeem, Rajesh Mash, Siraj, Mujeeb, Shihab, Ashique, Naufel and Pranav for the memorable time spent together and for making my life on the campus colourful and enjoyable. I am also thankful to Neethu, Treasa, Sonia, Bivi, Shefeeqque, Jaleel, Rejeena, Mini and Monisha for their friendship.

I am grateful to CSIR and CFN for their financial support during my research work without which I could not have carried out my work.

And finally, but immensely, I acknowledge with gratitude the support and encouragement given by my parents, sisters and other members of my family and their role as the support system on which I bank.

Contents

Chapter 1

Introduction

Recent research in magnetism is driven by a growing interest in investigating ever decreasing sizes of magnetic entities. This trend started with the early studies in magnetic thin films and later in magnetic multilayers [1]. Studies on low dimensional and fine particle systems are basically concerned with two aspects: (i) size reduction, where the focus is on how the reduced dimensions and confinement affect the macroscopic magnetic properties, and (ii) the proximity effects, where the focus is on how the interactions between magnetic entities can be controlled and understood to produce specific magnetic structures with artificially modified properties. In the former case, the surface properties are important since the number of surface/interface atoms become significant proportions of the whole structure. Subsequently, for a better understanding of the effect of grain boundary/interfacial effect on the magnetic properties, studies were more focussed on nanocrystalline iron [2 - 5], nickel [5 - 13], cobalt [5, 14], terbium [15] and gadolinium [16 - 19] etc.

1.1 Nanocrystalline Elemental Ferromagnets

Gleiter [2] first reported a 40% decrease in saturation magnetization compared to bulk iron for nanocrystalline iron with 6 nm grain size. This behaviour was attributed to the differences in the magnetic microstructure between nanocrystalline and conventional polycrystalline iron. In the case of ultrafine particles (10 - 50 nm) of Ni, Co and Fe, Gong *et al.* [5] observed a rapid decrease in saturation magnetization with decreasing grain size, which they ascribed to antiferromagnetic oxide layer on the ultrafine metal particles. Schaefer *et al.* [6] also noted a decrease in saturation magnetization in consolidated nanocrystalline Ni powder which they explained in terms of structural disorder. Furthermore, Yao *et al.* [7] too found that the saturation magnetization of ultrafine Ni particles decreases drastically with decreasing grain size. Michels *et al.* [18] reported that the spontaneous magnetization of nanocrystalline Gd samples with an average grain size of 33 nm was approximately 75% of the value for polycrystalline Gd. All the above-said materials were prepared by consolidating nanocrystalline particles produced by inert gas condensation technique, which yields material with high internal porosity that can provide large surface areas for oxide formation after exposing the sample to air. In contrast, Aus *et al.* [8] reported that the saturation magnetization of nanocrystalline Ni was not strongly dependent on the grain size and for nanocrystalline Ni with an average grain size of 10 nm, the observed M_S was only 10% less than for the polycrystalline Ni. These results were obtained on bulk nanocrystalline Ni produced by electrodeposition and were explained in terms of negligible porosity and oxide formation in this material. These findings, that the reduction in M_S is only 10%, is in agreement with the results of the cal-

culations that assessed the effect of structural disorder introduced by grain boundaries on the magnetic properties of nanocrystalline metals [20].

Bonetti *et al.* [4] have studied the magnetic properties of nanocrystalline Fe with an average grain size of 12 nm, prepared by mechanical energy transfer technique through ball milling, using ac susceptibility, time-dependent magnetization and the thermoremanent magnetization measurements. A transition from a high-temperature ferromagnetic state to a low-temperature disordered frozen magnetic state, observed at a characteristic temperature, $\sim 70\ K$, in nanocrystalline Fe, was attributed to the competition between the interfacial anisotropy brought about by the structural disorder at the grain boundary and magnetocrystalline anisotropy. Nevertheless, the measured magnetization at 5 K for an applied field of 50 kOe was very close to the saturation magnetization of bulk polycrystalline iron.

There have been a few other studies that concentrated on the spin structure at the grain boundaries of nanocrystalline terbium [15] and gadolinium [16, 18]. Weissmüller *et al.* [15] have studied the grain size and grain boundary effects on various aspects of magnetic properties of nanocrystalline terbium, prepared by inert-gas codensation technique. A significant reduction in magnetization and the remanence is observed at all fields and temperatures as the grain size reduces. Their analysis of the autocorrelation function of the spin misalignment obtained by the small-angle neutron scattering studies revealed that the spin orientation varies considerably over the length scales smaller than the grain size. The correlation length of spin-spin misalignment, l_c, calculated for nanocrystalline terbium with an average grain size of 10(2) nm is $\sim 2\ nm$ at 5 K. The reduction in magnetization and remanence, as Weissmüller *et al.* [15] have concluded, is

not due to a reduction in the atomic magnetic moment but results from the spin disorder within the grain boundaries.

Michels *et al.* [17] have studied the grain size dependence of the ferromagnetic - to - paramagnetic transition temperature, T_C, of nanocrystalline gadolinium, prepared by inert-gas condensation technique, using the differential scanning calorimetry and ac susceptibility measurements. They found that the reduction in T_C, ΔT_C, is inversely proportional to the grain size and $\Delta T_C \sim 20K$ for nanocrystalline Gd with an average grain size of 10 nm compared to the course-grain Gd. They have suggested that the grain size dependent T_C in nanocrystalline Gd may have its root in the interface stress, arising from the fact that the mere presence of the grain boundary region induces an internal hydrostatic pressure, of the order of 1 GPa in 13 nm-sized nanocrystalline Gd.

Kruk *et al.* [16] have used Mössbauer spectroscopy to study the effect of spin structure of the grain boundary region of nanocrystalline gadolinium, prepared by inert-gas condensation technique, on the magnetic properties of nanocrystalline gadolinium. Mössbauer spectroscopy using the ^{155}Gd isotope, a unique local probe to investigate both the grain boundary and crystalline component, allowed them to identify two structurally distinct phases along with its volume fraction in nanocrystalline Gd. It is found that 15% and 25% are the volume fraction of grain boundary in nanocrystalline gadolinium with the average grain sizes of 13 nm and 18 nm, respectively. They found a correlation between the average grain size and induced strong magnetic anisotropy in the nanocrystalline counterpart. At some critical grain size, the Gd magnetic moments change abruptly their direction from an angle of 20° characteristic of the course-grained sample to 73° for the

nanocrystalline samples. The magnetic anisotropy driving this rotation is attributed to the compressive stress that is induced in the crystalline component by the interface stress of the grain boundaries, as suggested by Michels *et al.* [17]. Mössbauer spectroscopy study also enabled them to identify that the Gd magnetic moments in the core area of grain boundaries are randomly oriented with respect to their local crystallographic axes. The smaller value of the isomer shift of Gd in the crystalline component compared to that of the grain boundary component indicated a lower s-electron density in the core region of the grain boundary than in the grain interiors.

Michels *et al.* [18] have used the small-angle neutron scattering technique to probe the nature of both the interior and grain boundary regions of nanocrystalline gadolinium, prepared by inert-gas condensation technique. They found a clover-leaf-shaped anisotropy which suggests the presence of a perturbed magnetization distribution originating from the core regions of the grain boundaries [21]. The correlation length of spin-spin misalignment, l_c, a measure of the average distance over which perturbations in the spin structure decay, calculated from the autocorrelation function, varies on a length scale $(5 - 10\ nm)$ smaller than the grain size. This nanoscale longitudinal magnetization fluctuations are, therefore, attributed to the grain boundary induced spin disorder.

Shand *et al.* [19] have studied the magnetic properties and critical behaviour of nanocrystalline gadolinium, prepared by melt-spun technique. The main observations and their interpretations given by Shand *et al.* [19] are as follows. (i) The irreversibility in magnetization at low temperatures and low fields, is due to the anisotropy. (ii) Failure to saturate magnetization even at fields as high as 70 kOe, is attributed to the random anisotropy

in each grain. (iii) Reduction in saturation magnetization and the ferromagnetic - to - paramagnetic transition temperature, T_C, is brought about by the reduction in the nearest-neighbor coordination number even when a uniform strain is observed in the XRD measurements.

In all these studies on nanocrystalline elemental ferromagnets, focused on the finite size and proximity effect on the bulk magnetic properties, yielded contradictory results which attracted different interpretations in terms of spin misalignment, oxide layers and reduction in coordination number at the grain boundary in nanocrystalline material. These conflicting results are an indication of the fact that the magnetic properties of nanocrystalline metals can be tuned to a large extent by engineering the grain boundary. Moreover, it is found that an extensive study of the spin structure at the grain boundary were carried out only on rare earths such as terbium and gadolinium, that too at a few temperatures such as 4.2 K and 78 K. However, even these studies could not clearly bring out the exact nature and type of spin structure of the grain boundaries in nanocrystalline gadolinium and terbium.

1.2 Nanocrystalline Gadolinium

In order to study the exact nature of the intra-grain and interfacial anisotropies and their effect on various thermodynamic properties, nanocrystalline gadolinium is the correct choice for the following reasons.

- A fairly good knowledge about the spin structure in the grain-boundary region exists.

- The ferromagnetic - to - paramagnetic transition temperature, T_C, of nanocrystalline gadolinium is expected to be much smaller than $T_C = 293\ K$ of the bulk counterpart [22]. Now that the T_C of nanocrystalline gadolinium falls well below the characteristic temperature of nanocrystalline system [23] ($\geqslant 0.2 \times T_{melting} = 316\ K$) above which the grain growth starts, extensive measurements can be carried out over an extended periods of time without the complications arising from the grain growth during measurements.

- Nanocrystalline gadolinium is theoretically predicted [24] to be a potential working material for room temperature magnetic refrigeration applications.

As far as the room temperature magnetic refrigeration is concerned, gadolinium metal is one of the working materials with maximum relative cooling power (at T_C) near room temperature [25]. Efforts to replace Gd metal as a prototype magnetic refrigerant material did not succeed so far. There are Gd-based compounds [26] with higher relative cooling power, but the operating temperature is far below the room temperature. Michels *et al.* [17] have shown that the finite size can be used as a parameter to alter the ferromagnetic - to - paramagnetic transition temperature, T_C and Shir *et al.* [24] have theoretically predicted that the magnetocaloric properties will not change with the nanocrystallization of gadolinium. Therefore, it is should be possible to tune the working temperature with nanocrystallization without affecting the relative cooling power. Nelson *et al.* [27] have tried to study the magnetocaloric properties of nanocrystalline gadolinium prepared by the homogeneous alkalide reduction method. Their study failed to explore the possibility of room temperature magnetic cooling as the nanocrystalline

gadolinium, prepared by the chemical root contained high level of impurities (inherent to the preparation method), and hence turned out to be superparamagnetic.

Critical evaluation of the literature available prior to the present work

There were a lot of studies carried out on nanocrystalline elemental ferromagnets in order to understand the effect of crystallite size on bulk magnetic properties such as magnetization and coercivity. Most of these results were interpreted without having a proper understanding of the grain boundary region and hence no wonder that these results are conflicting. Extensive studies of spin structure in the grain boundary region were carried out only on nanocrystalline gadolinium. These studies, employing Mössbauer spectroscopy [16] and small angle neutron scattering [18] experiments, could give some useful clues about the nature of the spin structure at the grain boundary and that too only at a few selected temperatures. Reduction in the saturation magnetization and the nature of interfacial anisotropy of gadolinium is interpreted in terms of the random spins at the grain boundary. Magnetization process and ferromagnetic resonance studies on nanocrystalline gadolinium, that could furnish additional information about the nature of effective anisotropy, are lacking and so are the investigations of the effect of grain size on the low-lying magnetic excitations, electrical- and magneto-transport. The only attempt [27] to study the magnetocaloric effect in nanocrystalline gadolinium was a failure due to the superparamagnetic nature of the prepared sample. Due to the poor quality of grain boundary, the theoretical prediction [24], that the nanocrystallinity does not affect the magnetocaloric effect, could not be tested.

1.3 Aim and Scope of the Thesis

In the light of the above appraisal of the literature, the main objectives of the thesis are:

- To ascertain how the finite size affects the magnetization processes and magnetic anisotropy prevalent in crystalline gadolinium.
- Use of the ferromagnetic resonance technique to establish the types of anisotropies present in nanocrystalline gadolinium.
- To study the effect of size-reduction on the low-lying magnetic excitations.
- To explore the possibility of using grain size to tune the magnetocaloric effect.
- Does the electrical- and magneto-transport in nanocrystalline gadolinium differ from that in the crystalline counterpart?

References

1. B. Heinrich and J. A. C. Bland, *Ultrathin Magnetic Structures II* (Springer, Berlin, 1994).

2. H. Gleiter, *Progr. Mater. Sci.* **33**, 223 (1989).

3. L. D. Bianco, A. Hernando, E. Bonetti and E. Navarro, *Phys. Rev. B* **56**, 8894 (1997).

4. E. Bonetti, L. D. Bianco, D. Fiorani, D. Rinaldi, R. Caciuffo and A. Hernando, *Phys. Rev. Lett.* **83**, 2829 (1999).

5. W. Gong, H. Li, Z. Zhao and J. Chen, *J. Appl. Phys.* **69**, 5119 (1991).

6. H. E. Schaefer, H. Kisker, H. Kronmüller and R. Wurschum, *Nanostr. Mater.* **1**, 77 (1992).

7. Y. D. Yao, Y. Y. Chen, C. M. Hsu, H. M. Lin, C. Y. Tung, M. F. Tai, D. H. Wang, K. T. Wu and C. T. Suo, *Nanostr. Mater.* **6**, 993 (1995).

8. M. J. Aus, B. Szpunar, A. M. El-Sherik, U. Erb, G. Palumbo and K. T. Aust, *Scripta. Metal. Mater.* **27**, 1639 (1992).

9. L. Daroczi, D. L. Beke, G. Posgay, G. F. Zhou and H. Bakker, *Nanostr. Mater.* **2**, 512 (1993).

10. I. Daroczi, D. L. Beke, G. Posgay and M. Kisvarga, *Nanostr. Mater.* **6**, 981 (1995).

11. I. Bakonyi, E. Toth-Kadar, J. Toth, T. Tarnoczi and A. Cziraki, *Processing and properties of nanocrystalline materials*, edited by C. Suryanarayana, J. Singh F. H. Froes (The Minerals, Metals and Materials Society, 1996).

12. J. Weissmüller, R. D. McMicheal, J. Barker, H. J. Brown, U. Erb and R. D. Shull, *Mater. Res. Soc. Symp. Proc.* **457**, 231 (1997).

13. H. Kisker, T. Gessmann, R. Wurschum, H. Kronmüller and H. E. Schaefer, *Nanostr. Mater.* **6**, 925 (1995).

14. M. J. Aus, C. Cheung, B. Szpunar, U. Erb and J. Szpunar, *J. Mater. Sci. Lett.* **17**, 1949 (1998).

15. J. Weissmüller, A. Michels, D. Michels, A. Wiedenmann, C. E. Krill III, H. M. Sauer and R. Birringer, *Phys. Rev. B* **69**, 054402 (2004).

16. R. Kruk, M. Ghafari, H. Hahn, D. Michels, R. Birringer, C. E. Krill III, R. Kmiec and M. Marszalek, *Phys. Rev. B* **73**, 054420 (2006).

17. D. Michels, C. E. Krill III and R. Birringer, *J. Magn. Magn. Mater.* **250**, 203 (2002).

18. A. Michels, F. Döbrich, M. Elmas, A. Ferdinand, J. Markmann, M. Sharp, H. Eckerlebe, J. Kohlbrecher and R. Birringer, *Europhys. Lett.* **81**, 66003 (2008).

19. P. M. Shand, J. G. Bohnet, J. Goertzen, J. E. Shield, D. Schmitter, G. Shelburne and D. L. Leslie-Pelecky, *Phys. Rev. B* **77**, 184415 (2008).

20. B. Szpunar, U. Erb, G. Palumbo, K. T. Aust and L. J. Lewis, *Phys. Rev. B* **53**, 5547 (1996).

21. R. Skomski, *J. Phys.: Condens. Matter* **15**, R841 (2003).

22. S. N. Kaul and S. Srinath, *Phys. Rev. B* **62** 1114 (2000).

23. T. R. Malow and C. C. Koch, *Synthesis and Processing of Nanocrystalline Powder*, edited by D. L. Bourell (The Minerals, Metals and Materials Society, Warrendale, PA, 1996) p **33**.

24. F. Shir, L. Yanik, L. H. Bennett, E. D. Torre and R. D. Shull, *J. Appl. Phys.* **93**, 8295 (2003).

25. K. A. Gschneidner, Jr. and V. K. Pecharsky, *Annu. Rev. Mater. Sci.* **30** 387 (2000).

26. V. K. Pecharsky and K. A. Gschneidner, Jr., *Phys. Rev. Lett.* **78** 4494 (1997).

27. J. A. Nelson, L. H. Bennett and M. J. Wagner, *J. Am. Chem. Soc.* **124**, 2979 (2002).

Chapter 2

Experimental Techniques

2.1 Sample Preparation

2.1.1 Inert Gas Condensation

A schematic diagram of the inert gas condensation [1, 2] setup is shown in figure 2.1. 99.99% pure gadolinium, used as the starting material, is placed in the tungsten boat. The chamber is flushed with helium gas (99.9996% purity) several times and a 3 *mbar* pressure of ultra high pure helium gas is maintained in the chamber, after pumping down to a vacuum better than 10^{-7} *mbar* using a turbo-molecular pump. Ultra-pure gadolinium metal is evaporated at a temperature ($> 1312^{o}$C) well above the melting point. This temperature is monitored using a thermocouple, which is connected to a temperature controller unit with a power supply to maintain the required temperature to within a few degree Celsius. In the inert-gas-evaporation process, the metal atoms effused from the source rapidly loose their energy by collisions with the gas molecules, i.e., macroscopically the metal vapor is

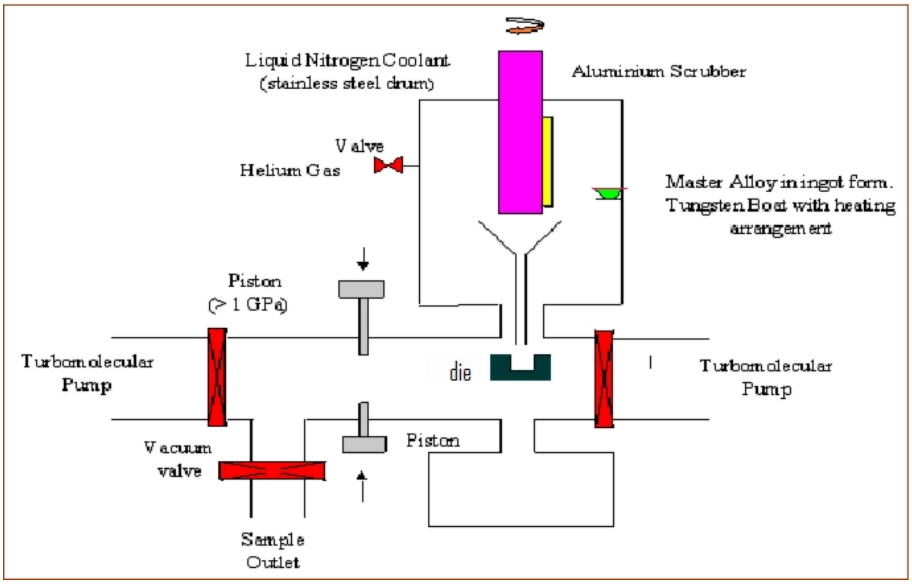

Figure 2.1: Schematic diagram of inert gas condensation setup.

cooled by the gas. The cooling rate, thus, depends on the collision mean free path (10^{-7}m), which is, inturn, depends on the chamber gas pressure. Such an efficient cooling produces locally a high supersaturation of metal vapor, which leads to a homogeneous nucleation. The spontaneously crystalized particles are drifted by the gas convection towards the stainless steel drum, which is maintained at liquid nitrogen temperature (77K) and rotating at a certain velocity. The 'critical diameter', χ_c, for the spontaneously formed single crystal particles, given by the simple equilibrium thermodynamics [1], is given by

$$\chi_c = 4\xi[\rho RT\ ln(p_v/p_0)]^{-1} \tag{2.1}$$

where ρ is the density, R is the gas constant for the metal vapor at absolute temperature T, ξ is a material dependent parameter, and p_v/p_0 represents the supersaturation ratio, i.e., the true vapor pressure, determined by the

source temperature, T_s, divided by the equilibrium vapor pressure at the actual temperature. Due to the rapid cooling of the metal vapor, χ_c is expected to be extremely small. Once the nucleation has taken place, the growth begins and this entire process occurs in a layer just above the hot metal surfaces. In this preparation technique, the large particles are formed at higher evaporation rates or, equivalently, at higher source temperature. The average size and size distribution can be tuned by choosing appropriate source temperature and inert gas pressure.

The condensed ultra-fine particles are then removed from the rotating steel drum by the Aluminium scrubber and collected in the die with the help of a funnel. The dye is then moved to a piston-and-anvil device, where it is subsequently compacted *in situ* up to pressures as high as 5 GPa so as to form discs of diameter 8 mm and thickness 0.6 mm. The density of the resulting disc-shaped sample is approximately 99% of the bulk Gd [3, 4].

From the nanocrystalline Gd samples with an average grain size 12(2) nm or 18(2) nm, synthesized by this technique, discs of 4 mm diameter, strips of dimensions 2 $mm \times 2$ mm and strips of 1 mm width and 6 mm length, for magnetization, specific heat and resistivity measurements, respectively, were spark-cut after completing the XRD, EDAX FESEM and AFM measurements.

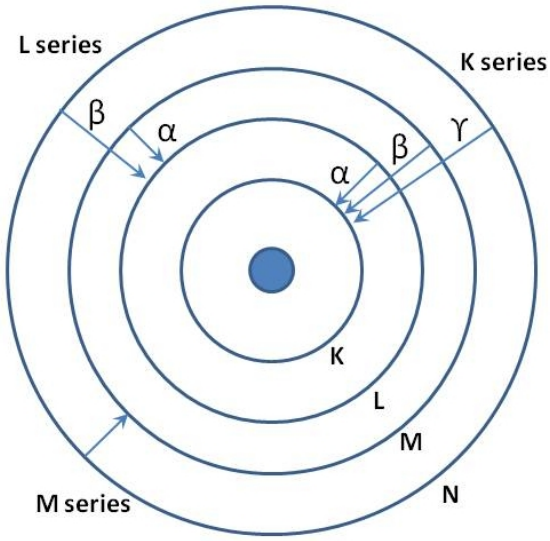

Figure 2.2: Elements in an EDX spectrum are identified based on the energy content of the x-rays emitted by their electrons as they (electrons) make transitions from a higher-energy shell to a lower-energy one.

2.2 Compositional Analysis

2.2.1 Energy Dispersive Absorption of X-rays (EDAX)

Energy Dispersive Absorption of x-rays (EDAX) or Energy Dispersive x-ray analysis (EDX) is a method used to determine the energy spectrum of x-ray radiation emitted by a sample. It is a technique used for identifying the elemental composition of the specimen in an area of interest thereof. The EDAX attachment works as an integrated feature of a scanning electron microscope (SEM), and cannot operate, on its own, without the SEM.

During EDAX analysis, the specimen is bombarded with an electron

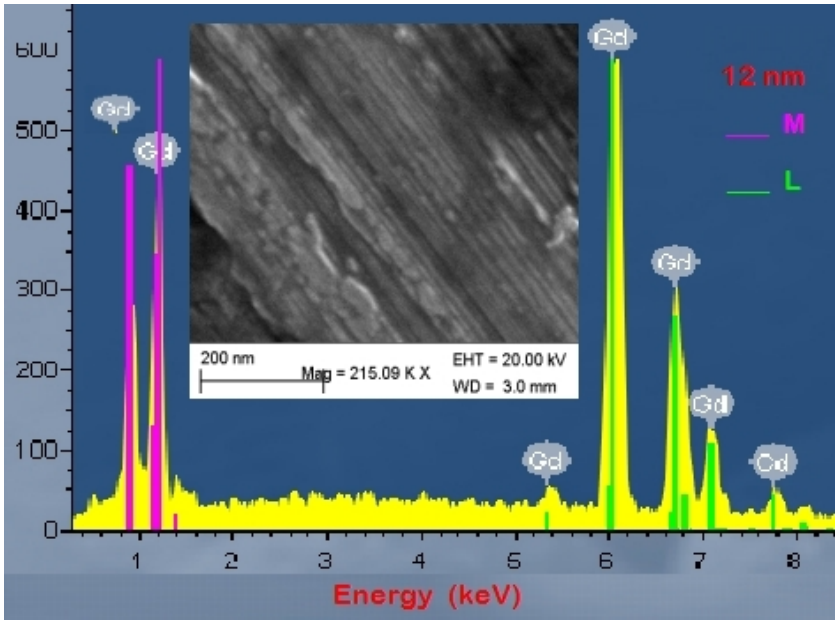

Figure 2.3: EDAX spectrum measured on Gd sample with the average grain size of $d = 12\ nm$. The inset shows the SEM micrograph.

beam inside the scanning electron microscope. The bombarding electrons collide with the electrons of the atoms constituting the specimen, knocking some of them off in the process. A position vacated by an ejected inner shell electron is eventually occupied by a higher-energy electron from an outer shell. To be able to do so, however, the transferring outer electron must give up some of its energy by emitting x-rays of energy equal to the energy difference between the outer and inner shells. The amount of energy released by the transferring electron thus depends on which shell it is transferring from, as well as on which shell it is transferring to. Furthermore, the atom of every element releases x-rays with unique amounts of energy during the transferring process. Thus, by measuring the x-ray energy spectrum emitted by a specimen during electron beam bombardment, the identity of the atoms

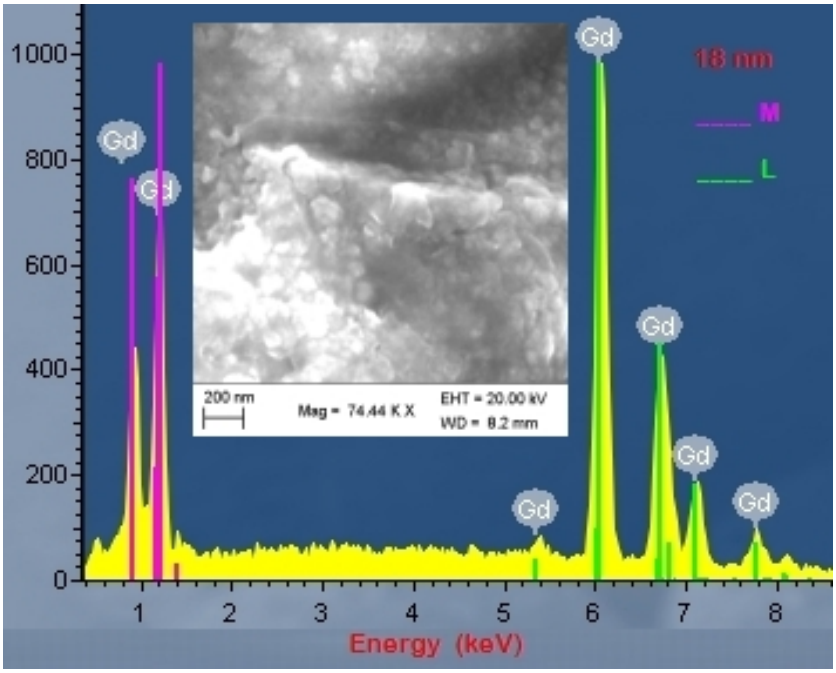

Figure 2.4: EDAX spectrum measured on Gd sample with the average grain size of $d = 18\ nm$. The inset shows the SEM micrograph.

from which the x-rays are emitted can be established. Therefore, the output of an EDAX analysis is an EDAX spectrum. The EDAX spectrum is just a plot of how frequently x-rays of some given energy are received by the detector. An EDAX spectrum normally displays peaks corresponding to the energy levels for which the most x-rays had been received. Each of these peaks is unique to an atom, and therefore, corresponds to a single element. The higher the intensity of a peak in a spectrum, the more the concentration of the element in the specimen.

An EDAX spectrum plot not only identifies the element corresponding to each of its peaks, but the type of x-rays to which it corresponds as well. For example, a peak corresponding to the amount of energy possessed by

x-rays emitted by an electron in the L-shell when it makes a transition to the K-shell is identified as a K_α peak. The peak corresponding to x-rays emitted by M-shell electrons when it falls into the K-shell is identified as a K_β peak, as shown in figure 2.2. The EDAX measurements were carried out using *Carl Zeiss Smarts SEM* Field Emission SEM up to 20 KV bias voltage over a $\sim 30 \times 30$ μm area at a number of regions. The one of the many measured EDAX spectra for the 12 nm and 18 nm samples are shown in figure 2.3 and 2.4.

2.3 Characterization

2.3.1 X-ray Diffraction (XRD)

Experimental Procedure

INEL CPS 120 x-ray diffractometer with Co-K_α radiation (wavelength=1.78956 Å) was used to record the x-ray patterns of nanocrystalline metallic strips in the position sensitive, fixed 2θ mode (Fig.2.5). The requisites for such an experiment are a radiation source, a monochromator to select a narrow band of wavelengths and a filter to suppress unwanted radiation, a diffractometer with a sample holder, and a position sensitive radiation detector with associated electronic equipment.

The principle of operation [5] of this diffractometer is illustrated in Fig.2.6. The sample in the form of a thin strip is supported on a table, which can be rotated about an axis O perpendicular to the plane of drawing. S is the monochromatic line source of x-rays, obtained from the continuous spectrum by choosing specific reflection from the monochromator -

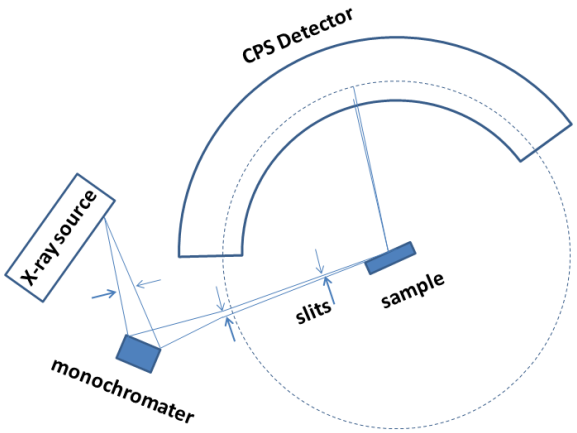

Figure 2.5: A schematic depiction of X-ray diffractometer with curved position sensitive detector.

a single crystal. The monochromator can be rotated about an axis normal to the plane of drawing. S is also normal to the plane of the drawing and therefore parallel to the diffractometer axis O. a and b are the special slits which define and collimate the incident beams. The diffracted x-ray beam is again collimated by the slit F and then enters the counter. The beam from the x-ray monochromator contains not only the strong $K_{\alpha 1}$ but also $K_{\alpha 2}$ line. The intensity of $K_{\alpha 2}$ is relatively weak (50%) compared to $K_{\alpha 1}$ but the angular difference is only $\sim 0.1^o$. By displaying the incident beam on a florescent screen kept at a distance that can resolve $K_{\alpha 1}$ (brighter) and $K_{\alpha 2}$ (lighter), $K_{\alpha 2}$ can be eliminated by carefully adjusting the monochromator angle and the slit width. The beam diffracted by the specimen passes through the receiving slit F before entering the counter and its width is kept

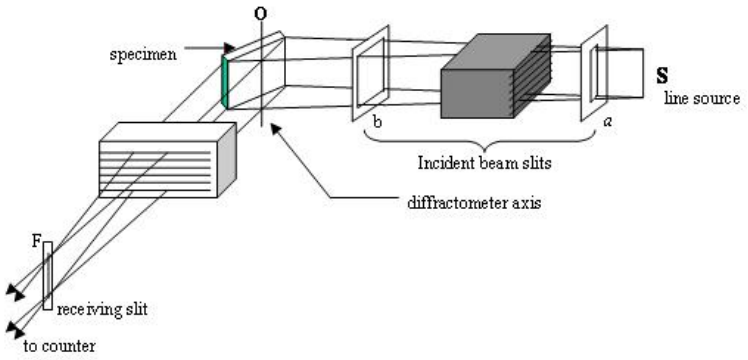

Figure 2.6: Arrangement of soller slits in a diffractometer.

constant in the curved position sensitive (CPS) configuration. The width of the beam admitted to the counter will decide the maximum intensity of any diffraction line being measured.

Curved Position Sensitive Detector

The intensity of the diffracted beam is measured directly by the CPS detector, which converts the incoming x-rays into electric pulses counted by the x-ray detector covering the angle range $5 - 120^o$ and placed concentric with the circle centered on the thin specimens as shown in Fig.2.5.

CPS detector is working based on the principle similar to that used in the gas counter. As shown in the inset to Fig.2.7, CPS detector consists of a curved gas chamber that covers 120^0 of the circle with its center coincide with the sample position. The anode is a firm, curved, knife-edge 'blade'. The cathode is curved and divided in to tiny, equal parts. the different sections of the cathode are connected by a delay line, which permits to determine the position of the photons having penetrated the interior of

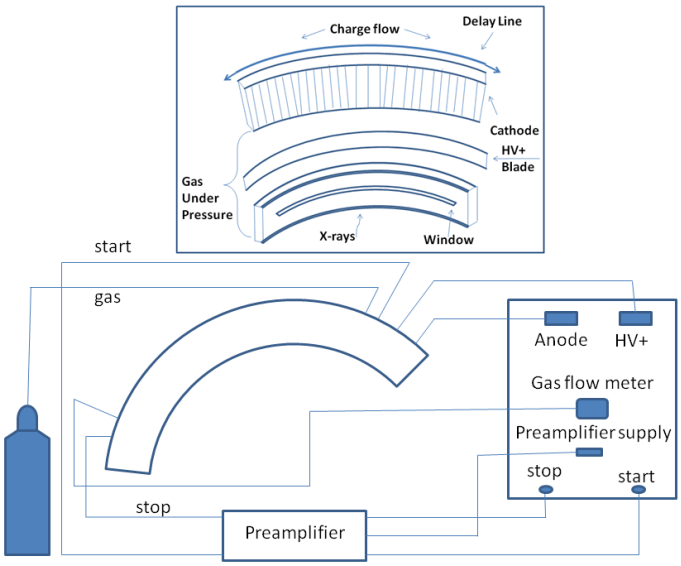

Figure 2.7: Detection system in a diffractometer.

the detector. The detector is filled with gas mixture of Argon (85%) and Ethane (15%) under pressure to increase the quantum efficiency. CPS operates in a 'streamer' mode, which is known for its stability, incomparable signal-to-noise ratio and gain. The detector is placed under an intense electric filed. When a photon interacts with a gas atom, the gas atom gets ionized. This causes the release of electrons, which are accelerated by the electrical field and ionize other atoms. The electrical charges created in this process are then collected by the cathode. The electrical charges are dispersed along both directions of the delay line, and are collected by two pre-amplifiers, which transforms these charges into impulses of current. Because of the focussing of the diffracted rays and the relatively large radius of the diffractometer circle, (about 15 cm), a diffractometer can resolve very closely spaced diffraction lines. Indicative of this is the fact that resolution

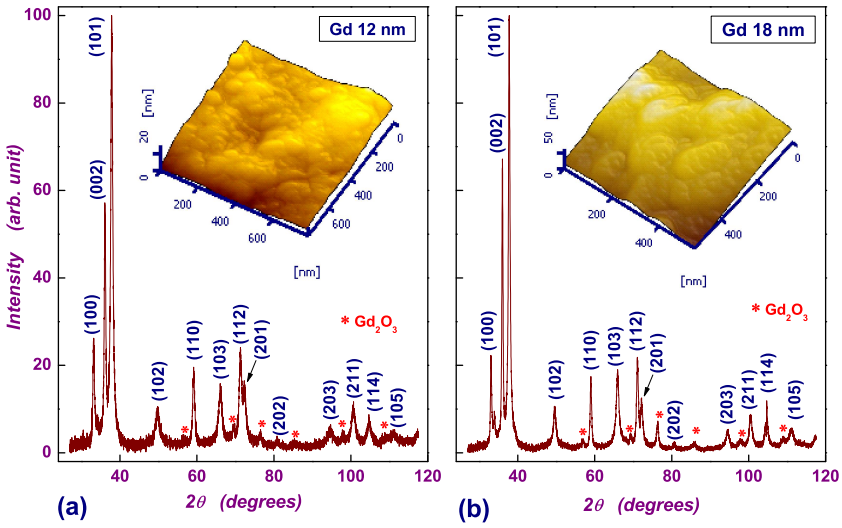

Figure 2.8: Room temperature XRD patterns taken on nanocrystalline Gd samples with average grain size (a) 12 nm and (b) 18 nm. The minor Gd_2O_3 peaks (marked by asterisks) emanate from the oxidized surface layer (see text). The insets display the atomic force micrographs recorded in the dynamic mode.

of the Co K doublet, if K_α is present, can be obtained at 2θ angles as low as about 40^o. Such resolution can only be achieved with a correctly adjusted instrument, and it is necessary to so align the component parts so that the following conditions are satisfied for all diffraction angles:

1. Line source, specimen surface, and receiving-slit axis are all parallel.
2. The specimen surface coincides with the diffractometer axis.
3. The line source and receiving slit both lie on the diffractometer circle.

Figure 2.7 shows the block diagram of the detection system of a diffractometer.

The XRD patterns, corrected for the background counts, are shown in figure 2.8 for the nanocrystalline (nc-) Gd samples with an average grain size of 12 nm and 18 nm. The intensities and positions of the Bragg peaks in the XRD pattern recorded are compared with the one generated using the relevant space groups reported in the literature [6] and indexed. The ratios of the Bragg peak intensities corresponding to the hcp structure of Gd are close to those expected in a powder diffraction pattern. Hence, the observed patterns suggest that the crystallographic directions change randomly from one grain to the other, i.e., the samples are polycrystalline in nature. Employing a detailed lineshape analysis that accounts for the crystal strain and corrects for the instrumental linewidth before making use of the well-known Scherrer formula, the average grain size calculated from the full-width-at-half-maximum of the diffraction peaks at higher angles turns out to be $d = 12(2)$ nm and $d = 18(2)$ nm for the two samples. The lattice parameters determined for the $d = 12$ nm and 18 nm nc-Gd samples are $a = 3.625(5)$ $\mathring{A}$, $c = 5.780(5)$ $\mathring{A}$ and $a = 3.630(5)$ $\mathring{A}$, $c = 5.775(5)$ $\mathring{A}$, respectively. These values are close to those $a = 3.629$ $\mathring{A}$, $c = 5.760$ $\mathring{A}$ reported [6] for bulk Gd.

2.3.2 Scanning Electron Microscopy (SEM)

The primary limitations of SEM, as a general imaging and analytical technique, are the restrictions imposed on the samples by requiring a high vacuum sample environment. Samples have to be clean, dry, and electrically conductive. The Environmental SEM (ESEM) [7] permits one to vary the sample environment through a range of pressures, temperatures and gas compositions. It retains all the features of a conventional SEM, but removes

the high vacuum constraint on the sample environment. Wet, oily, dirty, non-conductive samples may be examined in their natural state without modification or preparation. The ESEM offers a high resolution secondary electron imaging in a gaseous environment of practically any composition, at pressures as high as 50 $Torr$ and temperature as high as 1500^o C.

Description and Working Principle

A SEM consists of an electron column, that creates a beam of electrons; a sample chamber, where the electron beam interacts with the sample; detectors, that monitor a variety of signals from the beam-sample interaction; and a viewing system that constructs images from the signal, as shown in Fig. 2.9.

An electron gun at the top of the column generates the electron beam. In the gun, an electrostatic field directs the electrons, emitted from a very small region on the surface of an electrode, through a small spot called crossover. The gun then accelerates the electrons down the column towards the sample with energies typically ranging from a few hundred to ten thousand volts and generated electron beam has stable and sufficient current and the smallest possible size. The electron emerge from the gun as a divergent beam. A series of magnetic lenses and apertures in the column focuses the beam into a demagnified image of the crossover. Bottom of the column has a set of scan coils which deflects the beam in a scanning pattern over the sample surface. The final lens focuses the beam into the smallest possible spot on the sample surface. Then the beam exits from the column into the sample chamber. The chamber incorporates a stage for manipulating the sample, a door or airlock for interacting and removing the sample. As the beam of

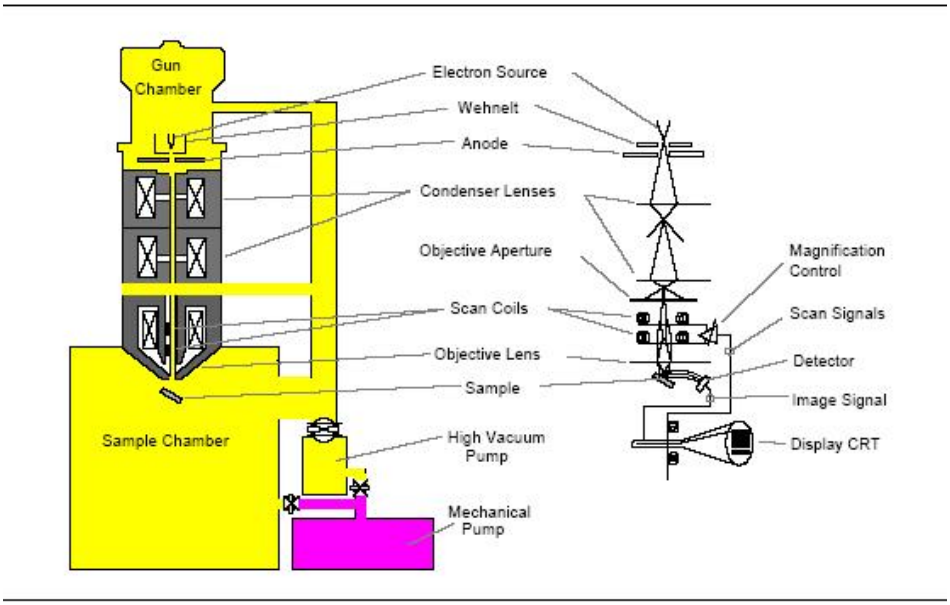

Figure 2.9: A schematic representation of an SEM.

electrons penetrate the sample, they give up energy, which is emitted from the sample in a variety of ways. Each emission mode is potentially in a signal form which creates an image.

Imaging Principle

SEM uses a simple imaging device based on a Cathode Ray Tube (CRT). A CRT consists of a vacuum tube covered at one end (the viewing surface) with light emitting phosphor, and at the other end, an electron gun and a set of deflection coils. The CRT gun forms a beam of electrons and accelerates it towards the phosphor. The deflection scans the beam in a raster pattern over the display surface. The phosphor converts the energy of the incident

electrons into visible light. The intensity of the light depends on the current in the CRT electron beam. By synchronizing the CRT scan with the SEM with the scan modulating the CRT beam current with the imaging signal, the system maps the signal point onto the viewing surface of the CRT, thus creating the image.

The SEM micrographs, recorded on $d = 12\ nm$ and 18 nm nc-Gd samples, are shown as insets in Fig.2.3 and 2.4.

2.3.3 Atomic Force Microscopy (AFM)

The Atomic force microscope (AFM) is a high-resolution version of scanning probe microscope (SPM), where a small probe scans across the sample surface to obtain information about the surface morphology. The information gathered from the interaction of the probe with the surface reveals the physical topography. SPA400 Seiko AFM in the dynamic force mode is used in this work.

Basic Principle

The scanning force microscope was invented by Binning et.al. in 1986 [8]. Scanning force microscope measures the forces acting between a fine tip and a sample. Figure 2.10 schematically shows the basic concept of Atomic force microscopy. The tip attached to the free end of a cantilever is brought very close to a sample surface. Attractive or repulsive forces resulting from the interaction between the tip and the surface cause a positive or negative bending of the cantilever, detected by means of a laser beam which is reflected from the back side of the cantilever.

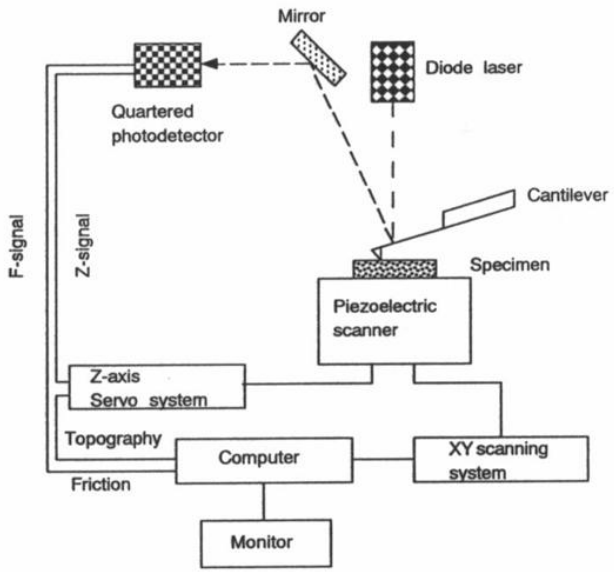

Figure 2.10: Schematic diagram of AFM.

Mode of Operation

Dynamic Force Mode: In dynamic contact mode, the probe cantilever is oscillated at or near its resonance frequency. The oscillating probe tip is then scanned at a height where it barely touches or taps the sample surface. The system monitors the probe position and vibrational amplitude to obtain topographical and other surface property information. Accurate topographical information can be obtained even for very fragile surfaces. Optimum resolutions are about 50 $\mathring{A}$ lateral and $< 1\mathring{A}$ height. Images for phase detection mode, magnetic domains, and local electric fields are also obtained in this mode.

The atomic force micrographs, shown as insets in Fig.2.8, do support the nanocrystalline nature of the samples.

2.4 Physical Property Measurement

2.4.1 Ferromagnetic Resonance (FMR)

FMR Experimental Set-up

To record the FMR spectra for a given sample, a commercial JEOL - FA200 ESR spectrometer, which operates in the X-band of the microwave frequencies, has been used. The block diagram of the spectrometre is given in Fig. 2.11.

Besides the electromagnet, the instrument is equipped with a pair of secondary coils and a sweep generator to give a wide field scan. The coils are usually required to supply an *oscillating* magnetic field of maximum amplitude 5 Oe and frequency of 110 kHz. The arrangement serves two main purposes. First, it provides a modulator or chopper frequency to which the detector amplifier system may be tuned in order to improve the signal-to-noise ratio. Second, use of this arrangement allows the spectrum to be displayed in the derivative mode, which, in turn, facilitates accurate determination of the linewidth and resonance center.

A cavity resonator [9] is placed between the pole pieces of an electromagnet, which produces a steady and uniform magnetic field. This field can be swept by sweep generator at a constant rate and is modulated at 110 kHz. The instrument also consists of the microwave unit, Automatic Frequency Control (AFC) circuit, preamplifier, and gunn oscillator power supply which are all housed in a single unit. A klystron tube, which is tunable over a narrow range with frequency stabilization system is used to generate the microwave radiation which passes as a linearly polarised beam through a

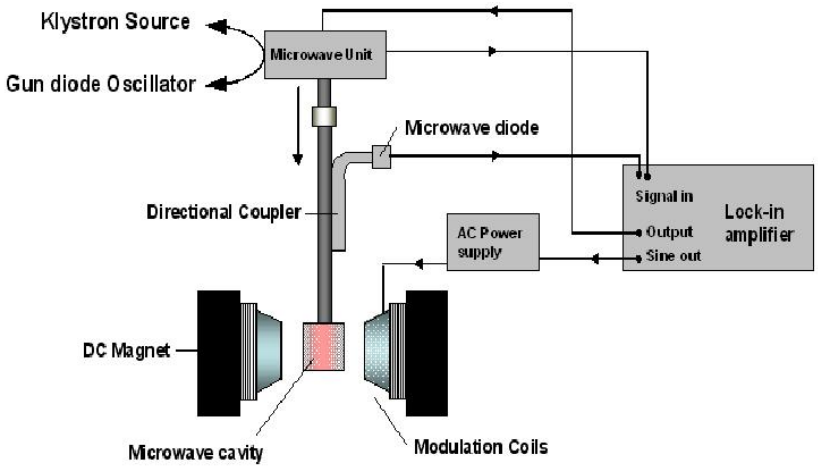

Figure 2.11: Block diagram of the ESR spectrometer.

wave guide. After traversing through a ferrite isolator, which prevents back reflections, the beam is divided at a magnetic tee or hybrid tee. One part of which is fed into a phase shifter and another part into the cavity resonator through a circulator. The sample in a cavity is subjected to the microwave field applied perpendicular to the applied field. At resonance, the sample absorbs energy from microwave field, which results in the change of Q-value of the cavity resonator. This Q-value variation is detected, amplified and recorded when the magnetic field is varied while the microwave frequency is kept constant. An absorption signal having a discernable width is observed. In addition, if an ac magnetic field having the same direction as H and with an amplitude smaller than the absorption signal width is applied to magnetic field H, and when the field is varied, the detected output at each point on the absorption signal will form a sinusoidal wave having the same period as alternating field and an amplitude in proportion to the gradient of the absorption line.

A selective amplifier amplifies this sinusoidal wave and the phase is detected throughout the absorption signal width. The amplifier employs a narrow bandwidth which reduces noise and therefore facilitates the observation and recording of extremely weak absorption signals. Since the crystal noise output is inversely proportional to modulation frequency, the application of a high frequency magnetic field modulation enables high-precision ESR measurements to be carried out. At resonance, the imbalance of the bridge occurs and the reflected microwave energy from the cavity and the reference wave, whose phase is adjusted, are fed into the 4th arm of the direction coupler. The balancing of bridge is achieved by making the reference wave equal in amplitude and opposite in phase, to the reflected wave from the cavity.

Sample Mounting and Procedure for Recording FMR Signals

An appropriate sample mounting technique [10], which ensures high reproducibility in the data by getting rid of specious stress-induced effects, was used for measurements. The sample (a circular disc of diameter 3 mm and thickness 0.7 mm) was mounted on the flat surface and sandwiched with a small flat quartz piece on top and fixed with nonmagnetic tape. The quartz rod was then inserted into the cavity. The cavity is provided with a goniometer arrangement which enables rotation of the sample plane at specific angles with respect to the external field during the angular measurement of resonance field. Ferromagnetic resonance measurements were performed at the operating frequency 9.23 GHz of the spectrometer. The FMR measurements, consisting of recording the field derivative of the microwave power ('P'), dP/dH, that is absorbed during the resonance process

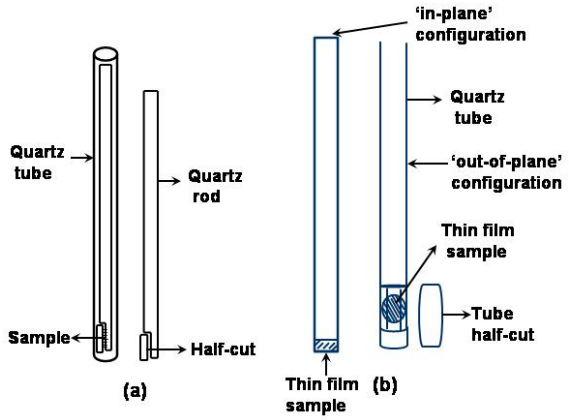

Figure 2.12: Sample mounting with Quartz tube and quartz rod combination (a) for Metallic ribbons (b) for Thin film samples.

as a function of external static magnetic field H, were performed at various temperatures. The 'in-plane' angle-dependent FMR measurements were carried out by varying the angle between the magnetic field and the sample plane at different temperatures using the following sample configurations.

1) 'In-plane' (IP) sample configuration, in which the external field H lies in the sample plane.

2) 'Out-of-plane' (OP) sample configuration, in which external field H lies in a plane perpendicular to the sample plane.

Advantage of Ferromagnetic Resonance

The g factor, damping parameter and anisotropy constants can be accurately determined by using the ferromagnetic resonance technique.

Experimental Accuracy and Sources of Error

Sample mounting plays an important role in the measurement of ferromagnetic resonance. Incorrect sample mounting leads to errors in the FMR data. The magnetic properties of the sample, which are very sensitive to stress, may be affected by certain types of mounting, so much so that they yield distorted lineshapes and irreproducible results. Slight misorientation of the sample from the required sample geometry produces tremendous changes in the values of linewidth and resonance, etc. To minimize or to completely eliminate these errors, the samples should be mounted in a stress-free manner and in the correct orientation for reproducible results. The sample and sample rod should be thoroughly cleaned with ethanol before mounting to eliminate the contamination effects, if any, on the FMR results.

Resolution in the measurements of the external field is an important factor in measuring power absorption derivative spectra accurately since the resolution of the field is 0.01 Oe when the sweep width is high, the upper bound on the error in the measurement of the resonance field is given by above resolution limit and the error in the peak to peak line width measured is twice this value.

2.4.2 Magnetic Property Measurement System SQUID VSM

MPMS SQUID VSM is a SQUID magnetometer based on the 2ω detection technique that makes use of the SQUID and VSM techniques in combination. It can measure DC and AC magnetization (down to $\sim 10^{-9}$ emu) in the temperature range 1.8 K to 400 K with a maximum temperature sweep

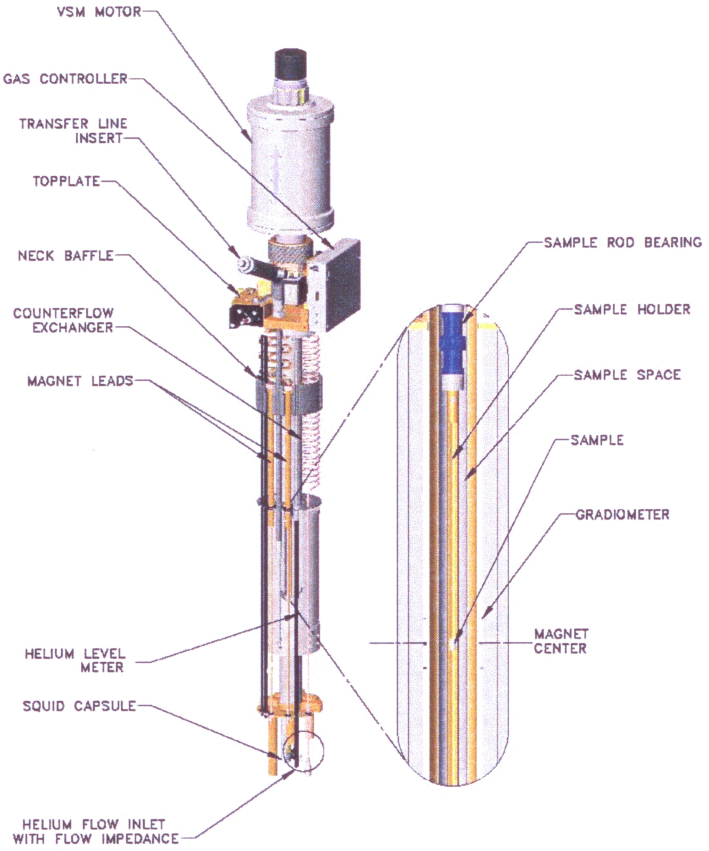

Figure 2.13: VSM head, Sample rod assembly and magnet for MPMS VSM SQUID.

rate of 50 K/min and fields up to ±7T with a maximum field ramp rate of 700 Oe/sec.

Superconducting Quantum Interference Device (SQUID) is an extremely sensitive flux-to-voltage transducer that converts a change in magnetic flux to change in voltage, which is readily detectable with conventional electronics. It is a device which makes use of flux quantization and Josephson tunneling and can operate at temperatures as low as few Kelvin. The sen-

sitivity of a Josephson junction to applied magnetic field increases with the area of the junction, which justifies making the devices large so that the control currents can be reduced to a minimum. The switching speed of the junction, however, decreases as the area increases. In recent devices, the conflicting demands of speed and sensitivity are met by replacing a single junction with two or more junctions connected by a continuous superconducting loop. Such a multi-junction device is called a Josephson interferometer or a Superconducting Quantum Interference Device (SQUID). In the case of two Josephson junctions connected in parallel, as the magnetic flux Φ threading a superconducting loop is changed, the critical current of two junctions oscillates with a period equal to the flux quantum Φ_0. These oscillations arise due to the interference of macroscopic wave functions at two junctions. This phenomenon of superconductiing quantum interference forms the basis of a SQUID.

The superconducting detection coils are configured as a second-order gradiomater, with counterwound outer loops which make the set of coils non-responsive to uniform magnetic fields and linear magnetic field gradients. The detection coils only generate a current in response to local magnetic field disturbances. The current in the detection coils is a function of sample position (see Fig. 2.14) and it is inductively coupled to the instrument's SQUID. The SQUID feedback nulls the current in the detection coils and this nulling current yields the actual SQUID voltage for analysis. The sample is set to vibrate at a frequency, ω, about the center of the detection coils, where the signal peaks as a function of sample position, z. $V(z) = Az^2$ for small vibration amplitude, B and $z(t) = Bsin(\omega t)$, it

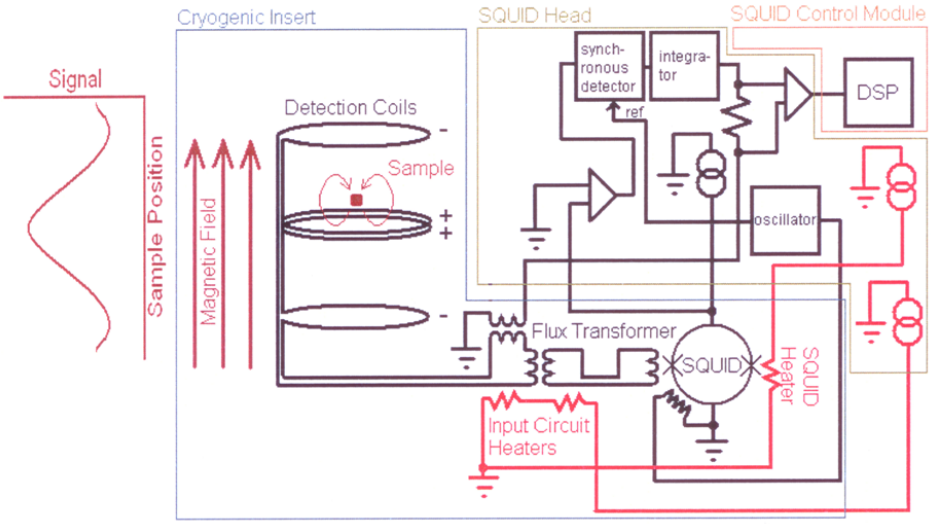

Figure 2.14: SQUID detection system in a simplified diagram.

generates a SQUID signal, V, as a function of time, t

$$V(t) = AB^2 sin^2(\omega t)$$

$$= \frac{AB^2}{2}(1 - cos(2\omega t)) \tag{2.2}$$

where A is a scaling factor related to the magnetic moment of the sample. The lock-in technique is used to isolate and quantify the signal occurring at frequency 2ω, which is caused extensively by the sample. Briefly, this is achieved by multiplying the measured signal with a phase corrected reference signal at 2ω and then extracting the DC component, which is proportional to the 2ω component of the measured signal. This technique quickly and precisely isolates the sample signal from other noise sources, including drifting SQUID signal and mechanical noise sources synchronized to the sample. To locate the sample position in the detection coil, sample signal

for various vertical sample positions are obtained and compared with the response of a point dipole in a uniform magnetic field.

The VSM head or motor, is a long-throw linear motor mounted on springs within its casing for vibration isolation. The VSM head receives a DC signal that controls the sample position and an AC signal that determines the vibration amplitude and frequency from the motor control module. A precision optical encoder in the VSM head reads the position of the motor armature to with in 0.01 mm and fed to the motor control module and used in a feed back loop to obtain precise sample positioning and vibration. The default vibration frequency is 14 Hz and amplitude is 2 mm. This can be varied, within the prescribed limit, to get better accuracy depending on the sample magnetic moment and weight.

2.4.3 Physical Property Measurement System (PPMS)

The Physical Property Measurement System (PPMS) [11] provides a flexible, automated workstation that can perform a variety of experiments requiring precise thermal control. PPMS can be used to perform magnetic, electrical- or magneto-transport, specific heat or thermo-electric power measurements, or can be modified to perform the user-select experiment. The unique open architecture of the PPMS allows to fully configure the basic PPMS platform or to use the PPMS with different measurements options, such as ac susceptibility, DC magnetization, heat capacity, resistivity or ultra-low field.

The PPMS has extremely good temperature control over the entire range of $1.8\ K \leq T \leq 350\ K$. This system possesses a superconducting magnet

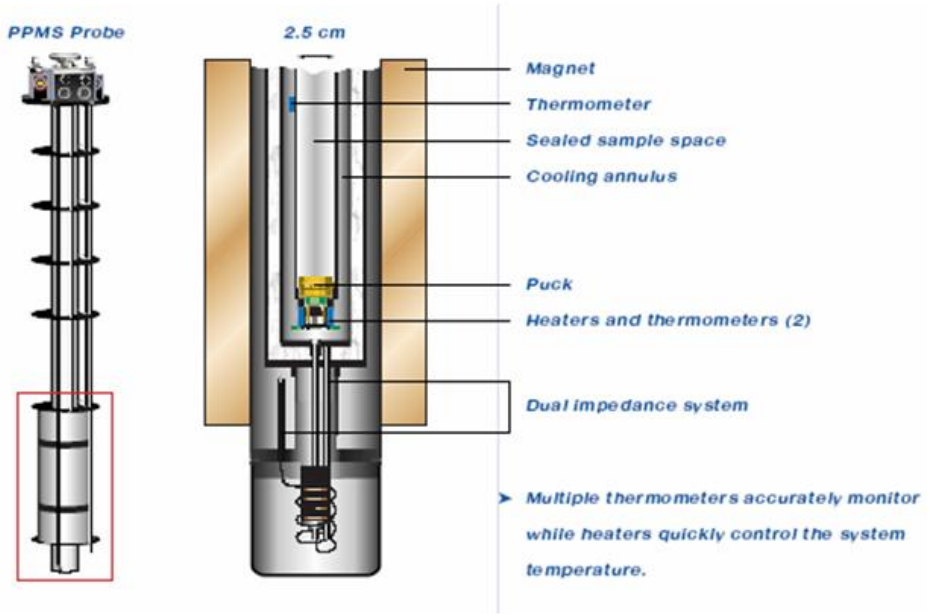

Figure 2.15: Sample rod assemble for PPMS.

which can generate fields up to ±9 Tesla, with a high field-homogeneity (0.01%) within the measuring region. The software also provides options for sweeping the magnetic field in several modes, the most important of which are *linear* and *no-overshoot*. In the linear mode, the field is ramped linearly to the set-point, while in the *no-overshoot* mode, the field is quickly ramped to $\sim$ 70 % of the desired value, then slowly increased to avoid overshooting the set-point. The PPMS platform can apply a constant field during both AC and DC measurements.

AC Measurements System (ACMS) Option

ACMS option is a versatile DC magnetometer and AC susceptometer. The ACMS insert houses the drive and detection coils, thermometer, and electri-

cal connections for the ACMS system. The insert fits directly in the PPMS sample chamber and contains a sample space that lies within the uniform magnetic field region of the host PPMS, so DC field and temperature control can be performed with conventional PPMS methods. The sample is held with the insert's coil-set on the end of a thin rigid sample rod. The sample holder is translated longitudinally by a DC servo-motor located in the ACMS sample transport assembly. The DC servo-motor provides rapid and very smooth longitudinal sample motion. The ACMS sample transport mounts on top of the PPMS probe.

The ACMS contains an AC-drive coil set that provides an alternating excitation field and a detection coil-set that inductively responds to the combined sample moment and excitation field. The copper drive and detection coils are situated within the ACMS inserts, concentric with the superconducting DC magnet of the PPMS (Fig. 2.15). The drive coil is wound longitudinally around the detection coil set. The detection coils are arranged in a first-order gradiometer configuration so as to isolate the sample signal from uniform background sources. This configuration utilizes two sets of counter wound copper coils connected in series and separated by several centimeters. A compensation coil is situated outside the AC drive coil. The drive coil and compensation coil are counterwound and connected in series so that they receive same excitation signal. A net field remains within the measurement region, but outside the measurement region the fields from the two coils tend to cancel. Each detection coil also contains a low-inductance calibration coil. The two single-turn calibration coils are connected in series and are situated at the center of each detection coil.

DC Magnetization

During DC measurements, a constant field is applied to the measurement region and the sample is moved quickly through both sets of coils, inducing a signal in them according to Faraday's Law. This measurement method is commonly called the *extraction* method. The amplitude of the detection signal depends on both the extraction speed and the sample magnetic moment. The DC servo-motor used by the ACMS extracts samples at speeds of approximately 100 cm/sec., thus increasing the signal strength over conventional DC extraction systems and reducing the contribution of time-dependent errors such as drift and 1/f noise. The short scan time also allows the averaging of several scans for each measurement, further reducing the contributions of random error. These advantages result in a greater accuracy and sensitivity compared to systems with slower sample extraction speeds. A Digital Signal Processor (DSP) is used to analyze the signal and determine the sample magnetic moment.

ac Susceptibility

During an ac susceptibility measurement, an alternating magnetic field (up to ± 10 Oe in a frequency range of 10 Hz to 10 kHz) is applied to the measurement region by exciting the drive and compensation coils. The sample undergoes a five-point measurement process that utilizes the calibration coil to increase measurement accuracy. The first three readings are made with sample positioned in the center of the bottom, then in the top and again in the bottom detection coils. The signal from the detection coil array amplified, low-pass filtered, digitized and stored as waveform blocks in the

data buffer. The points are fitted and compared to the driving signal to determine the real and imaginary components of the response. Two more readings are taken with the sample placed at the center of the detection coil array by switching the calibration coil into the detection circuit with opposing polarities. The real and imaginary components of each response waveform are obtained and it is subtracted to obtain the sample signal as ac susceptibility in real and imaginary components.

Centering the Sample

Knowing the sample location with respect to the detection coil assembly is important to determine the proper range of motion for DC magnetization measurements and the correct sample position relative to the detection coils for AC susceptibility measurements. As long as the sample is mounted relative to the detection coils (approximately 10.5 ± 0.8 cm from the end of the long sample rod on the ACMS sample holder), the ACMS determines the position of the sample within the detection coil by obtaining the sample signal as a function of Z and automatically center it by adjusting the sample position relative to servo motor zero. There is about $8 - mm$ window within which the magnetic center of the sample must lie in order to allow automatic centering. If the sample is not properly centered, it is difficult for the ACMS to determine its true magnetic moment.

VSM Option

VSM option for PPMS is a fast and sensitive DC magnetometer consisting of a VSM linear motor transport head (same as that used in the MPMS

VSM SQUID, except for the working amplitude and frequency of oscillation. For details, see section 2.4.4). To locate the sample and for vibrating it, a compact gradiometer pickup coil for detection and the electronics for driving the linear motor transport and detecting the response from the pick up coils are used. With relatively large oscillation amplitude (1-3 mm peak) and a frequency of 40 Hz, the system can resolve magnetization changes less than 10^{-6} emu at a data rate of 1 Hz. When the sample is set to vibrate sinusoidally, the changing magnetic flux induces a time-dependent voltage in the pickup coil,

$$V_{coil} = \frac{d\Phi}{dt} = \left(\frac{d\Phi}{dz}\right)\left(\frac{dz}{dt}\right)$$

$$= 2\pi f C m A \; sin(2\pi f t) \tag{2.3}$$

where Φ is the flux enclosed by the pickup coil, z is the vertical position of the sample with respect to the coil, t is time, C is the coupling constant, m is the DC magnetic moment of the sample, A is the amplitude and f is the frequency of oscillation. The response from the pickup coil is calibrated with a standard sample. After obtaining the signal profile in the pickup coil, the system identifies the sample position with respect to the pickup coil and locates the sample at the center of the coil after the touch-down process. If the measurement is a temperature dependent one, the sample position may change due to the thermal expansion/contraction of the sample rod. Hence the sample position in the pickup coil has to be monitored by touching the sample rod down and relocate it to the actual position, if it has changed.

Heat Capacity Option

Heat Capacity option uses a relaxation technique that combines the best measurement accuracy with robust analysis techniques. During a measurement, a known amount of heat is applied at constant power for a fixed time, and then this heating period is followed by a cooling period of the same duration. The Quantum Design Heat Capacity option measures the heat capacity at constant pressure, i.e.,

$$C_P = \left(\frac{dQ}{dT}\right)_P \tag{2.4}$$

For measuring heat capacity, the Quantum Design Heat Capacity option controls the heat added to and removed from a sample while monitoring the resulting change in temperature. A platform heater and platform thermometer are attached to the bottom side of the sample platform (figure 2.16). Small wires provide the electrical connection to the platform heater and platform thermometer and also provide the thermal connection and structural support for the platform. The sample is mounted to the platform by using a thin layer of grease, which provides the required thermal contact to the platform. The PPMS Cryopump High-Vacuum option creates sufficient vacuum so that the thermal conductance between the sample platform and the thermal bath (puck) is totally dominated by the conductance of the wires. This gives a reproducible heat link to the bath with a corresponding time constant large enough to allow both the platform and sample to achieve sufficient thermal equilibrium during the measurement. After each measurement cycle, which is a heating period followed by a cooling period, the Heat Capacity option fits the entire temperature response of the sample platform to a model that accounts for both the thermal re-

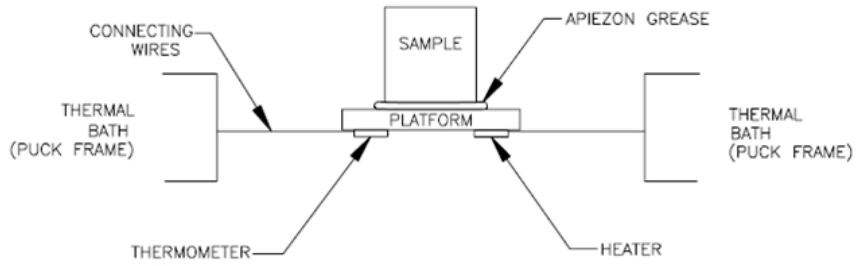

Figure 2.16: Thermal connections to the Sample and Sample Platform in PPMS Heat capacity option.

laxation of the sample platform to the bath temperature and the relaxation between the sample platform and the sample itself [12]. Two separate algorithms fully automate the analysis of the raw data. The most general analysis method invokes the two-tau model [12] which assumes that the thermal contact between the sample and sample platform is poor. The two-tau model simulates the effect of heat flowing between the sample platform and sample, and the effect of heat flowing between the sample platform and puck. The total power deposited on the platform and sample, given by the heat flow scheme, is given by the following equations (two-tau model)

$$C_{platform}\frac{dT_p}{dt} = P(t) - K_w\left(T_p(t) - T_b\right) + K_g\left(T_s(t) - T_p(t)\right) \tag{2.5}$$

$$C_{sample}\frac{dT_p}{dt} = -K_g\left(T_s(t) - T_p(t)\right) \tag{2.6}$$

where $C_{platform}$ is the heat capacity of the sample platform, C_{sample} is the heat capacity of the sample, and K_g is the thermal conductance between the two due to the grease. The respective temperatures of the platform and sample are given by $T_p(t)$ and $T_s(t)$. A second analysis is also performed using a simpler model which assumes that the sample and sample platform

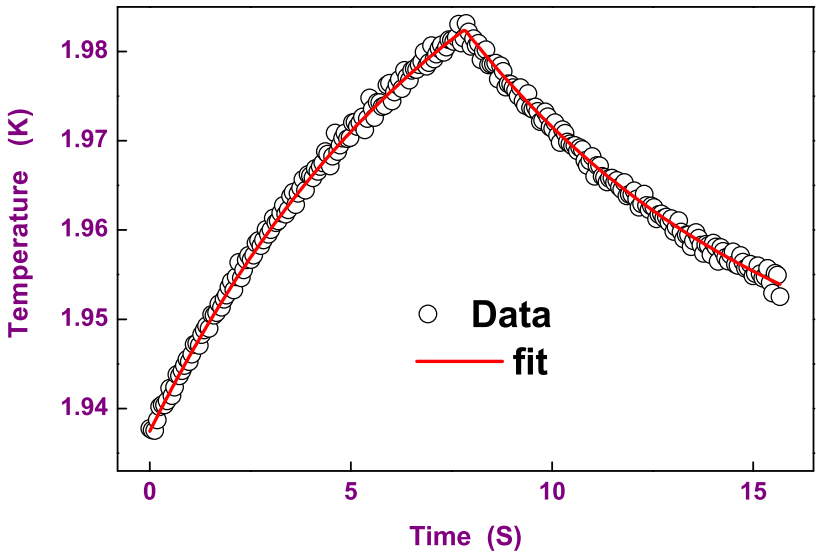

Figure 2.17: The measured temperature versus time data at 1.95K along with the fit.

are in good thermal contact with each other and are at the same temperature during the measurement. In the simple model, the temperature T of the platform as a function of time t obeys the equation

$$C_{total}\frac{dT}{dt} = -K_w\,(T - T_b) + P(t) \tag{2.7}$$

where C_{total} is the total heat capacity of the sample and sample platform; K_w is the thermal conductance of the supporting wires; T_b is the temperature of the thermal bath (puck frame); and P(t) is the power supplied by the heater. The heater power P(t) is equal to P_0 during the heating portion of the measurement and equal to zero during the cooling portion. The solution of this equation is given by exponential functions with a characteristic time

constant τ equal to C_{total}/K. Using a nonlinear least-squares fitting algorithm, the system compares the solution of both the models and determines which model yields the best fit to the measured data. The values of the parameter that give the smallest fit deviation determine the heat capacity (Fig. 2.17)

The Heat Capacity software application calculates the heat capacity of a sample by subtracting the addenda data from the total heat capacity data. The total heat capacity comprises the heat capacity of the sample, the grease, and the sample platform. The two measurements, one with and one without a sample on the sample platform are necessary. For accurate measurement of the sample heat capacity, a small amount of Apiezon N grease is applied to the sample platform just enough to hold the sample and then the heat capacity of the grease and the platform is measured. This constitutes the addenda measurement (data). Grease is used to make a proper thermal contact between the sample and sample platform. Apiezon N Grease has sufficient thermal conductivity and adhesive qualities to attach most samples to the sample platform. Next, the sample is mounted on the sample platform by pressing the sample onto the grease, already applied to the platform and the total heat capacity is measured. Automatic subtraction of the addenda, interpolated at each sample measurement temperature, is performed and the heat capacity of the sample is thus obtained.

Resistivity Option

Resistivity option is a configurable resistance bridge board. It can simultaneously measure resistance/resistivity of 3 samples using four probe method with current reversal option. A resistivity puck with three samples mounted

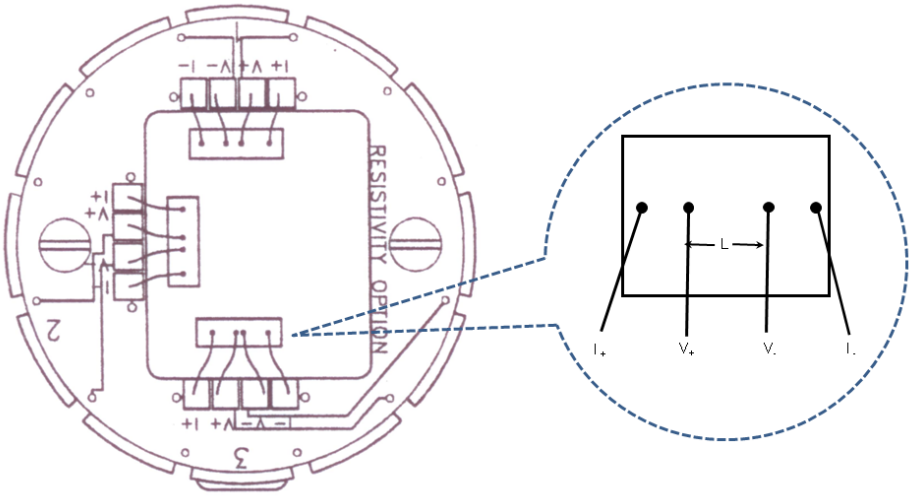

Figure 2.18: The resistivity sample puck with three samples mounted for four-wire resistance measurements.

for four probe measurement is shown in figure 2.18. The user bridge board automatically adjusts the excitation current of its active channels, but the maximum allowable current, power and voltage can be specified. The current, power and voltage limits are $\pm 0.01 - 5mA$, $0.001 - 1mW$ and $1 - 95mV$, respectively. The nominal resolution in the most sensitive range is $3.8nV/5mA = 0.76\mu\Omega$.

2.4.4 Conventional Vibrating Sample Magnetometer

The conventional VSM is known for its sensitivity and precise control of static field (< 0.5 Oe). The basic principle is same as that of the PPMS VSM option (section 2.4.5) but the configuration of the pickup coil is transverse in the conventional VSM. Here, the sample is set to vibrate sinusoidally in a direction perpendicular to the static magnetic field generated by the

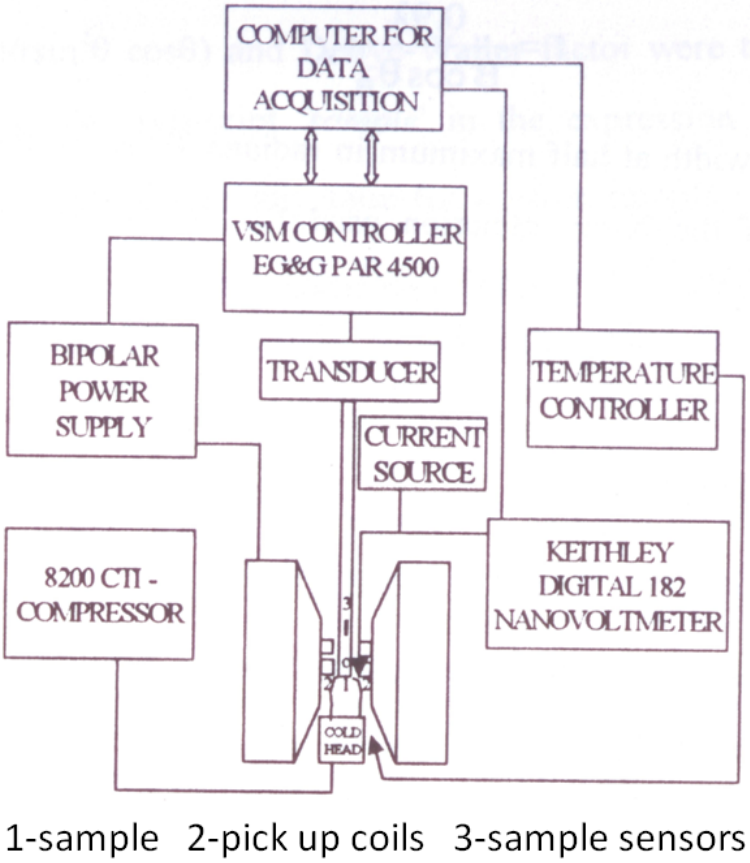

Figure 2.19: Block diagram of Vibrating sample magnetometer.

electromagnet (Fig.2.19). The axis of the pickup coils are also parallel to the static field. The sample signal picked up by the coil assembly is a function of the coordinates (x,y,z) of the sample position with respect to the coils. The optimum sample position is at the center of symmetry of the coil system, where the pickup signal is minimum along x-direction (parallel to field direction) but maximum along y- and z-directions. The task of driving the VSM head at the desired frequency, detecting the sample signal at the same frequency using lock-in method, amplifying and processing the signal

and controlling the electromagnet power supply to generate the required field are carried out by the VSM control unit (EG&G Princeton Applied Research model 4500). A closed cycle refrigerator (CCR) is used to cool the sample down to 12 K and and Lakeshore DRC-93C temperature controller is used to control the system temperature. A platinum PT-100 sensor is used in contact with the sample to measure the sample temperature to an accuracy of $\sim 1\ mK$ with help of a Keithley nano voltmeter and a Lakeshore constant current source. The VSM controller, temperature controller and the nano voltmeter are interfaced to a PC using General Purpose Interfacing Buss (GPIB) and programmed with LabView.

References

1. C. G. Granqvist and R. A. Buhrman, *J. Appl. Phys.* **47**, 2200 (1976).
2. R. Birringer *et al.*, *Phys. Lett. A* **102**, 365 (1984).
3. A. Michels *et al.*, *Euro. Phys. Lett.* **81**, 66003 (2008).
4. D. Michels, C. E. Krill III and R. Birringer, *J. Magn. Magn. Mater.* **250**, 203 (2001).
5. B. D. Cullity, *Elements of X-ray diffraction*, second edi. Addsion-Wesely company, Inc. (1978).
6. *JCPDS Metals and Alloys* Data Book (1999).
7. Environmental Scanning Electron Microscopy, second edi. Philips Electron Optics, Eindhoven, The Netherlands. (1996).
8. G. Binning, C. F. Quate and Ch. Gerber. Atomic force microscope, *Phys. Rev. lett* **56**, 930 (1986).
9. C. P. Poole Jr., Electron Spin Resonance, second edi. John Wiley & Sons, Inc. (1983).
10. S. N. Kaul and T. V. S. M. Mohan Babu , *J. Phys.: Cond. Matter.* **1**, 8509 (1989).
11. Physical Property Measurements System (PPMS), User's Manual, Quantum Design, San Diego, CA, USA, **1084-100A**, (2009).
12. J. S. Hwang, K. J. Lin and C. Tien, *Rev. Sci. Instrum.* **68**, 94 (1997).

Chapter 3

Magnetization Processes

3.1 Introduction

Successful synthesis [1] of pure rare earth elements in the nanocrystalline state in the recent past made it possible to study the effect of interfacial, intragranular and intergranular anisotropies on the magnetic properties of nanocrystalline Gd. The ^{155}Gd Mössbauer investigation [1] has revealed that the Gd magnetic moments at the grain boundaries are randomly oriented with respect to the local crystallographic axes. Intra-particle spin-misalignment fluctuations over nanometer length scale in nanocrystalline (nc) Gd have recently been inferred [2] from the small-angle neutron scattering data taken in external magnetic fields up to 50 kOe. The observation that magnetization cannot be saturated even by applying magnetic fields as intense as 70 kOe in melt-spun [3] Gd is taken to indicate the presence

The following articles are based on the results presented in this Chapter:
1. S. P. Mathew, S. N. Kaul, A. K. Nigam, A. -C. Probst and R. Birringer, *J. Phys.: Conf. Ser.*, **200**, 072047 (2010).
2. S. P. Mathew and S. N. Kaul, *AIP Conf. Proc.*, **1347**, 15 (2011).

of large interfacial magnetic anisotropy [2]. In order to understand the mechanism of magnetization reversal and the role of magnetocrystalline intragrain anisotropy and interfacial magnetic anisotropy, extensive magnetic measurements have been undertaken on nc-Gd.

3.2 Theoretical Considerations

3.2.1 Time-dependent Magnetization: Magnetic Viscosity

The evolution of magnetization following a sudden change (increase or decrease) in applied magnetic field has come to be known as the phenomenon of magnetic viscosity. Néel [4] proposed a simple model for magnetic viscosity in which the magnetization reversal proceeds via thermal activation over a magnetic field-dependent energy barrier, $E_B(H)$, which seperates two local energy minima. For internal and/or external fields (H) below the switching field (H_S), there are two local energy minima whereas for $H > H_S$, only one energy minimum exists. Consequently, for $H < H_S$, magnetization can be in the two magnetization states; one of them corresponds to the metastable state of energy E_1 while the other to the stable state of energy $E_2 < E_1$. If E_m is the energy of the maximum between them, the barrier energy $E_B = E_m - E_1$. The energy barrier could arise from one or more of the sources such as the inter-particle interactions, magnetostatic interactions, intra-grain magnetocrystalline anisotropy and interfacial anisotropy. For a fine particle system, the transition probability for over coming this energy barrier is $P_r = 1 - e^{-t/\tau}$ and hence the growth (decrease) of magnetization with measurement time 't' after the magnetic field of given strength

is suddenly switched on (off) is given by

$$M(t) = M(t_0)\ \left[1 - e^{-t/\tau}\right] \quad or \quad M(t_0)\ e^{-t/\tau} \tag{3.1}$$

where the former and latter expressions refer to the growth and decline, respectively, t_0 is the time at which the field is either turned 'on' or 'off', and τ is the relaxation time, which, in turn, is related to the transition rate Γ for the magnetization to switch from the metastable energy state E_1 to the stable energy state E_2, through the Arrhenius - Néel law [4]

$$\Gamma = \tau^{-1} = \Gamma_0\ e^{-E_B(T,H)/k_BT} \tag{3.2}$$

where Γ_0 is the attempt frequency typically in the range $10^9 - 10^{12}\ Hz$. Thus, the temperature- and field-dependent energy barrier can be expressed as

$$E(T,H) = -k_BT\ ln(\Gamma/\Gamma_0) = k_BT\ ln[t(T,H)/\tau] \tag{3.3}$$

In real systems, a distribution of energy barriers (which can arise from a distribution in inter-particle interactions, anisotropies, domain wall pinning, etc.) leads to a distribution of relaxation times. The probability of finding magnetic moments in a volume element with barrier energy between E_B and $E_B + dE_B$, i.e., $f(E_B)dE_B$, is the sum over all the volume elements having barrier energy in this interval divided by the total volume of the specimen. The averaged magnetization is given by [5, 6]

$$\overline{M}(T,H,t) = \int_0^\infty M(T,H,t) f(E_B) dE_B \tag{3.4}$$

Eq.(7.4) yields the magnetic viscosity, defined as

$$S(T,H,t) = \left[\frac{\partial M(t)}{\partial ln(t)}\right]_{T,H} \quad , \tag{3.5}$$

in the form

$$S(T,H,t) = 2\int_0^\infty (\Gamma t)\ e^{-(\Gamma t)} f(E_B)\ dE_B \tag{3.6}$$

Making use of the fact that the function $(\Gamma t)\ exp(-\Gamma t)$ peaks at

$$E_{B,max} = k_B T\ ln(\Gamma_0 t) \quad , \tag{3.7}$$

the integral in Eq.(7.6) is evaluated by expanding the distribution function $f(E_B)$ in a Taylor Series around $E_{B,max}$ with the result [5, 6]

$$S(T,H,t) = 2\ \sum_{n=0}^{\infty} \frac{1}{n!} \frac{d^n}{dE_B^n} f(E_B)|_{E_B,max} \int_0^\infty (\Gamma t)\ e^{-\Gamma t}\ (E_B - E_{B,max})^n\ dE_B \tag{3.8}$$

If the measurement started at time t_0 such that $\Gamma_0 t_0 \gg 1$, Eq.(7.8) can finally be rewritten in the form [5, 6]

$$S(T,H,t) = 2k_B T\ \sum_{n=0}^{\infty} C_n \frac{(-k_B T)^n}{n!} \frac{d^n}{dE_B^n} f(E_B)|_{E_B,max} \tag{3.9}$$

with

$$C_n = \int_0^\infty (lnx)^n e^{-x}\ dx \tag{3.10}$$

and $x = \Gamma t$. Large value of Γ_0 ensures that the above condition $\Gamma_0 t_0 \gg 1$ holds for all the systems. The time dependence of S in Eq.(7.9) basically arises from the time dependence of $E_{B,max}$, the value of barrier energy at which the energy derivatives of $f(E_B)$ have to be evaluated. If this time dependence is neglected, Eq.(7.4) - (7.6) and (7.10) finally yields the time dependence of magnetization starting from $t = t_0$ as

$$M(T,H,t) = M(T,H,t_0)\ \pm\ S(T,H)\ \ ln(t(T,H)/\tau) \tag{3.11}$$

Street and Woolley [7] were first to recognize that the logarithmic dependence of magnetization on time arises from the distribution in the en-

ergies of the barriers $f(E_B)$ which is a *constant* > 0 (*independent of energy*) over the energy interval $E_{B,min} \leq E_B \leq E_{B,max}$ and zero otherwise. Aharoni [8] contends that the model $f(E) = constant$ can be used only for a wide barrier energy distribution, $f(E)$, in a restricted time region $t_{min} = \tau\ exp(E_{B,min}/k_BT) \ll t \ll t_{max} = \tau\ exp(E_{B,max}/k_BT)$, and for this reason, the model breaks down for large and small time and for a *narrow* distribution $f(E)$. Nevertheless, Eq.(7.11) works quite well in the present context, as in many other systems [9, 10, 11, 12].

As already mentioned earlier, if $E_B(T, H)$ has a distribution, relaxation time will also have a distribution. If the density of relaxation times is $g(\tau)$, the relaxation rate of magnetization is given by [13, 14]

$$\left[\frac{\partial M(t)}{\partial ln(t)}\right]_{T,H} = M(T, H, \tau_m)\ g(\tau_m)\ ; \qquad \tau_m \approx t \tag{3.12}$$

In ac susceptibility measurements, where $\chi(\omega) = \chi'(\omega) + i\chi''(\omega)$, the observation time is equal to $1/\omega$ (ω is the angular frequency of the applied alternating field). If $t = 1/\omega$, the time-dependent magnetization divided by field approximately equals ac susceptibility, i.e., [13, 14]

$$(1/H)M(t) \approx \chi'(\omega) \tag{3.13}$$

For a wide distribution of relaxation times, $\chi''(\omega)$ is related to the density of relaxation times, $g(\tau)$, as [13, 14]

$$\chi''(\omega) = (\pi/2)[M(T, H, \tau_m)/H]\ g(\tau_m)\ ; \qquad \tau_m \approx 1/\omega \tag{3.14}$$

Combining Eqs.(7.5), (7.12) and (7.14) yields the relation

$$\frac{1}{H}S(T, H, t) = \frac{2}{\pi}\ \chi''(\omega) \tag{3.15}$$

3.2.2 Coercivity

The potential energy barrier, responsible for the blocking of magnetization reversal, in terms of magnetic field is given by [15]

$$E(T,H) = E_0(T)\left[1 - (H(T)/H_0(T))\right]^2 \tag{3.16}$$

where $E_0(T)$ is the energy barrier and $H_0(T)$ is the switching field.
Eq. (7.16) can be rewritten as

$$H(T) = H_0(T)\left[1 - (E(T,H)/E_0(T))^{1/2}\right] \tag{3.17}$$

If the temperature-dependent coercivity [16] is attributed to the thermal activation process, combining the Eqs. (7.17) and (7.3), leads to the expression for coercivity,

$$H_C(T) = H_0(T)\ \{1 - [k_B T\ ln(t/\tau)/E_0(T)]^{1/2}\} \tag{3.18}$$

When the shape anisotropy is prominent compared to other anisotropies, the anisotropy energy density can be approximated as,

$$\begin{aligned} K(T) &\approx\ K_{shape}(T) \\ &= (1/2)M_S^2(T)N \end{aligned} \tag{3.19}$$

where N is the demagnetizing factor. In this case, the switching field,

$$\begin{aligned} H_0(T) = 2K(T)/M_S(T) &= NM_S(T) \\ &= H_0\ m(T) \end{aligned} \tag{3.20}$$

and

$$\begin{aligned} E_0(T) = K(T)V &= \frac{1}{2}NVM_S^2(T) \\ &= E_0\ m^2(T) \end{aligned} \tag{3.21}$$

where Eq.(6.19) for $K(T)$ has been substituted in Eqs.(6.20) and (6.21), $m(T) = M_S(T)/M_S(0)$ is the reduced spontaneous magnetization, $H_0 = NM_S(0)$ and $E_0 = \frac{1}{2}NVM_S^2(0)$. The temperature dependence of coercivity is thus given by

$$H_C(T) = H_0 m(T)\{1 - [k_B T\ ln(t/\tau)/E_0 m^2(T)]^{1/2}\} \tag{3.22}$$

3.2.3 Approach-to-saturation

The magnetic properties of ferromagnetic materials are greatly affected by defects in the system. Theoretical analysis of such effects has been very successful in correlating a large number of experimental observations [3, 17, 18, 19, 20]. The magnetization processes at low fields is an extremely complicated theoretical problem.

The earliest theoretical attempt to understand the approach to ferromagnetic saturation, due to Brown [21, 22], holds the inhomogeneous spin states, caused by the internal stresses of dislocations via the magneto-elastic coupling, responsible for the significant deviations from saturation in ferromagnetic crystals containing dislocations. Brown [21, 22] derived the following law of approach-to-saturation at very low temperatures

$$M(H) = M_S \left[1 - \frac{a}{H} - \frac{b}{H^2}\right], \tag{3.23}$$

where M_S is the saturation magnetization. The $1/H$ term is due to dislocation dipoles if the distance between the two dipole dislocations is smaller than the exchange length

$$\kappa_H^{-1} = l_H = \sqrt{\frac{2A}{HM_s}} \tag{3.24}$$

where A is the exchange constant. κ_H^{-1} may be considered as the resolution length of the spontaneous magnetization with respect to internal stress and hence this $1/H$ term possibly would vanish for a perfectly annealed specimen [22]. Subsequently, Néel [23] showed that non-magnetic inclusions also give rise to the $1/H$ law. The coefficient b of the $1/H^2$ term is related to the magnetic anisotropy energy, E_a, as elaborated below [24]

Under the influence of moderately strong magnetic fields, all the domain wall displacements would have been completed and thus the magnetization vector would be almost parallel to the magnetic field. Then the component of magnetization along the magnetic field is

$$\begin{aligned} M &= M_S \, cos\theta \\ &= M_S \left(1 - \frac{\theta^2}{2} + \cdots\right) \end{aligned} \tag{3.25}$$

where θ is the angle between the magnetization and the magnetic field. The torque exerted by the magnetic field $\overrightarrow{M} \times \overrightarrow{H}$ is counterbalanced by the torque caused by the magnetic anisotropy, $-\frac{\partial E_a}{\partial \theta}$, i.e.,

$$MHsin\theta = -\frac{\partial E_a}{\partial \theta} \tag{3.26}$$

Since θ is very small at high fields, or alternatively, $M \cong M_S$, Eq.(6.26) reduces to

$$\theta = \frac{1}{H}\frac{c}{M_S} \tag{3.27}$$

where

$$c = -\left(\frac{\partial E_a}{\partial \theta}\right)_{\theta \sim 0} \tag{3.28}$$

substituting Eq. (6.29) in Eq. (6.25), yields

$$M = M_S \left(1 - \frac{b}{H^2} - \cdot\cdot\right) \tag{3.29}$$

where

$$b = \frac{1}{2}\frac{c^2}{M_S^2} \tag{3.30}$$

The magnetization rotates along the maximum gradient of anisotropy energy

$$c^2 = |\overrightarrow{\nabla} E_a|^2$$

$$= \left(\frac{\partial E_a}{\partial \theta}\right)^2 + \frac{1}{sin^2\theta}\left(\frac{\partial E_a}{\partial \phi}\right)^2 \tag{3.31}$$

Therefore

$$b = \frac{1}{2{M_S}^2}\left[\left(\frac{\partial E_a}{\partial \theta}\right)^2 + \frac{1}{sin^2\theta}\left(\frac{\partial E_a}{\partial \phi}\right)^2\right]$$

$$= \frac{1}{2{M_S}^2}\left[\sum_{i=1}^{3}\left(\frac{\partial E_a}{\partial \alpha_i}\right)^2 - \left(\sum_{i=1}^{3}\left(\frac{\partial E_a}{\partial \alpha_i}\right)\alpha_i\right)^2\right] \tag{3.32}$$

where θ is the angle between H and the easy direction of magnetization, $\hat{n}$, ϕ is the azimuthal angle, α_i are the direction cosines of the magnetization vector, $\overrightarrow{M}$, with respect to $\hat{n}$. For the uniaxial case, E_a is related to the anisotropy constants K_1 and K_2 as

$$E_a = K_1\ sin^2\psi + K_2\ sin^4\psi$$

$$= (K_1 + K_2) - \alpha_3^2\ (K_1 + 2K_2) + \alpha_3^4\ K_2 \tag{3.33}$$

where ψ is the angle between $\overrightarrow{M}$ and $\hat{n}$, and α_3 is the direction cosine of $\overrightarrow{M}$. The coefficient b is thus given by

$$b = \frac{1}{M_S^2}\ \left[\alpha_3^2(1-\alpha_3^2)\right]\left[K_1 + 2K_2(1-\alpha_3^2)\right]^2 \tag{3.34}$$

For a random orientation of grains in a nanocrystalline ferromagnetic sample, averaging of b over all possible directions fetches

$$< b(T) >= \frac{1}{M_S^2(T)}\ [0.2667\ K_1^2(T) + 0.4064\ K_2^2(T) + 0.6095\ K_1(T)\ K_2(T)] \tag{3.35}$$

Random Anisotropy Model

The type of magnetic order in the grain boundary region in the nanocrystalline materials can be modeled with the aid of the models for amorphous magnetism [18, 25], which assume either random space distribution of exchange [26] or random distribution of anisotropy axis [27]. Since the reduction in saturation magnetization in nanocrystalline material [28] is only 10% compared to that of bulk single crystal [29] and the easy axis of magnetization varies randomly from grain to grain, the anisotropy energy is weaker than the exchange energy. The large exchange favours uniform magnetization while the magnetization experiences random local anisotropy field in the grain boundary region and across the grains.

In the macroscopic approach to the description of amorphous magnetism with random anisotropy field $\overrightarrow{n}(x)$ ($\overrightarrow{n}^2(x) = 1$) and $\lambda \ll 1$ (λ is the ratio of anisotropy energy to exchange energy), the easy axes of magnetization are correlated over a length R_a of several atomic spacing a while the directions of local magnetization $\overrightarrow{M}(x)$ are correlated over a length scale R_m. The local magnetization is assumed to rotate smoothly over the volume so that $M^2(x) = const.$ However, $R_a \gg a$ and $R_m \gg R_a$ for the random anisotropy associated with a polycrystallite system. In three-dimensions, the system enters into a spin-glass state when $R_m \sim R_a$. The amorphous magnetic state of the polycrystallite system in presence of external magnetic field, $\overrightarrow{H}$, can be described by the macroscopic energy density [25, 30]

$$\epsilon = \frac{1}{2}\,\alpha \left(\frac{\partial \overrightarrow{M}}{\partial x_i}\right)^2 - \frac{1}{2}\,\beta \left(\overrightarrow{M}.\overrightarrow{n}\right)^2 - \overrightarrow{M}\cdot\overrightarrow{H} \tag{3.36}$$

where the first term in Eq.(5.36) is the exchange energy, second term is

the random anisotropy energy and the third term is the Zeeman energy. The condition $\lambda \ll 1$ corresponds to $\beta a^2/\alpha \ll 1$, $\alpha \propto Ja^2$, where J is the microscopic exchange constant. The characteristic fields associated with random anisotropy and exchange are defined as $H_{ex} \equiv \alpha M_0/R_a^2$, called the exchange field and $H_r \equiv \beta M_0$, called the anisotropy field.

When the random anisotropy field, H_r, is dominating compared to either the exchange field, H_{ex}, or the external field, H, the spins will be pointing in the hemisphere defined by the external magnetic field, H. In the large-field regime ($H \gg H_{ex}$ or $H \gg H_r > H_{ex}$), the noncollinear structure closes even further towards the field: each spin is only slightly tipped from the applied field by the random anisotropy at its site. The tipping angle is then of the order of H_r/H and, hence, the magnetization deviation in the approach to saturation is proportional to $(H_r/H)^2$ and it is given by [30]

$$\frac{\delta M}{M_0} = \frac{1}{15}\left[\frac{H_r}{H + H_{ex}}\right]^2 \tag{3.37}$$

Micromagnetic Model

Contrasted with the crystalline ferromagnets, where the $1/H$ term in the law of approach-to-saturation, Eq.(6.23), arises from lattice imperfections, ΔM_{imp}, additional contribution in the nanocrystalline ferromagnets comes from the intrinsic fluctuations of the material parameters, ΔM_{intr}. As in the case of crystalline ferromagnets at finite temperatures, there is yet another contribution to the total deviation ΔM $(= M_S - M(H))$ of magnetization from its saturation value in nanocrystalline ferromagnets due to the suppression of spin waves by external magnetic field, ΔM_{para}, the so-called *Holstein-Primakoff* spin-wave para-process. Thus, the total deviation ΔM

from saturation is the sum of three terms

$$\delta M = \delta M_{imp} + \delta M_{intr} + \delta M_{para} \tag{3.38}$$

For a ferromagnet with a position-dependent spontaneous magnetization, M(r), in an external magnetic field, H, applied parallel to the x_2-axis, is defined as [18]

$$M(r) = g\mu_B S(r)/\Omega(r) \tag{3.39}$$

where $S(r)$ is the spin quantum number and $\Omega(r)$ is the atomic volume per magnetic atom at position r (x_1, x_2, x_3). For sufficiently large fields, the transverse components M_i ($i = 1, 3$) of $M(r)$

$$\frac{M_{1,3}(r)}{M_S} \to 0 \quad while \quad \frac{M_2(r)}{M_S} \to 1 \tag{3.40}$$

where M_S is the volume average $\langle M(r)\rangle$. The volume average $\langle M_2\rangle$ can be written as [18]

$$\langle M_2\rangle = M_S \left\{1 - \frac{1}{2M_S^2}\left[\langle M_1^2(r)\rangle + \langle M_3^2(r)\rangle\right]\right\} \tag{3.41}$$

where $\langle M_i^2(r)\rangle_{i=1,3}$ is the volume averages of the squares of the transverse components of $M(r)$. The components $M_i(r)$ can be determined from the micromagnetic equations, which are obtained by minimizing the Gibbs free energy, $\wp$, of the ferromagnet [18],

$$\begin{aligned}\wp = \int \Bigg\{ & \frac{1}{2}\sum_{i,m,n} C_{mn}(r)[\nabla_m M_i(r)][\nabla_n M_i(r)] - \frac{1}{2}\sum_i H_{S,i}(r)M_i(r) \\ & + \sum k_{ij}(r)M_i(r)M_j(r) - \sum_i H_i(r)\cdot M_i(r)\Bigg\} d^3r\end{aligned} \tag{3.42}$$

where i refers to the i^{th} components of the field variables M, H_S and H. The position-dependent property tensors are: $C_{mn}(r)$ for the exchange energy and $k_{ij}(r)$ for the local magnetocrystalline energy. The magnetostatic

stray field $\overrightarrow{H}_S = -\overrightarrow{\nabla} U(r)$, where $U(r)$, the magnetostatic potential, obeys Poisson's equation

$$\triangle U(r) = 4\pi \overrightarrow{\nabla} \cdot \overrightarrow{M}(r) \tag{3.43}$$

The micromagnetic equations so obtained may be written as [18]

$$\begin{aligned} &\sum_{m,n=1}^{3} M(r) C_{mn}(r) \nabla_m \nabla_n M_i(r) + \sum_{n=1}^{3} M(r) B_n(r) \nabla_n M_i(r) \\ &- 2(k_{ii}(r) - k_{22}(r)) M_i(r) M(r) - 2 \sum_{j \neq 1} k_{ij}(r) M_j(r) \cdot M(r) \\ &2k_{i2} M^2(r) + H_{S,i}(r) M(r) - H M_i(r) = 0 \end{aligned} \tag{3.44}$$

with $i = 1, 3$, $j \neq 1, 3$ and $B_n(r) = \sum_i \dfrac{\partial C_{in}(r)}{\partial X_i}$, which takes into account the position dependence of the exchange parameter $C_{mn}(r)$. Eq (5.44) describes four types of fluctuations denoted as *intrinsic* and *magnetoelastic* fluctuations. *Intrinsic fluctuations* are due to the *short-range* variations of the material parameters such as i) *magnetostatic fluctuations*, $\delta M(r)$, ii) magnetocrystalline fluctuations, $\delta k_{ij}(r)$ and iii) exchange fluctuations, $\delta C_{mn}(r)$, $\delta B_n(r)$. Magnetoelastic fluctuations are due to modification of $k_{ij}(r)$ by *long-range internal stresses*, σ. Without going into the origin of the fluctuations, $\delta M(r)$, in magnetization, $M(r)$ can be written as

$$M(r) = \langle M(r) \rangle + \delta M(r) \tag{3.45}$$

One source of intrinsic magnetization fluctuations could be the magnetostatic stray fields resulting from volume charges, $\nabla \cdot (\delta M(r))$, that make the orientation of the spontaneous magnetization inhomogeneous. The other source could be the fluctuations of the magnetocrystalline energy, which can be written as

$$k_{i2}(r) = \langle k_{i2}(r) \rangle + \delta k_{i2}(r) \tag{3.46}$$

For a perfectly random orientations of the nanocrystallite axes, the volume average $\langle k_{i2}(r)\rangle$ vanishes. The transverse components, $M_{1,3}$, are linear functions of fluctuations δM and δk. Since the fluctuations are uncorrelated, the volume averages $\langle \delta k \delta M_i\rangle$ vanish and hence the effect of fluctuations δM and δk can be treated separately.

Magnetostatic Fluctuations

Replacing the terms $C_{mn}(r)M(r)$, $B_n(r)M(r)$ and $\langle k_{ij}M^2(r)\rangle$ in the micromagnetic equation (5.44) with their volume averages yields [18]

$$\left(\frac{2A}{M_S}\right)\sum_{m=1}^{3}\nabla_m^2 M_i(r) + \langle M(r)\rangle H_{S,i}(r) - H\cdot M_i(r) = 0 \qquad (3.47)$$

By solving the coupled system of differential equations, Eqs.(3.47) and (5.43), the deviation from saturation, $\triangle M = M_S - \langle M_2(r)\rangle$, for $H >> 4\pi M_S$ is given by [18]

$$\Delta M_{intr} = M_S\ \Omega_0\ \frac{(2A/M_S)^{1/2}}{120\ \pi}\ \kappa_S^4\ \left(\frac{1}{H^{1/2}} - \frac{1}{2}\frac{4\pi M_S}{H^{3/2}} + \cdot\cdot\right) \qquad (3.48)$$

Magnetocrystalline Fluctuations

Neglecting the magnetostatic fluctuations in Eq.(5.44) one obtains [18]

$$\left(\frac{2A}{M_S}\right)\sum_{m=1}^{3}\nabla_m^2 M_i(r) - 2k_{i2}\langle M^2(r)\rangle - H\cdot M_i(r) = 0 \qquad (3.49)$$

Solving the micromagnetic equation, Eq.(3.49), with the fluctuation $\delta k_{i2}(r)$ for a vanishing volume average $\langle k_{i2}\rangle = 0$, the deviation from saturation, ΔM, is obtained as [18]

$$\Delta M_{intr} = \frac{1}{4}\ M_S\ \Omega_0\ \frac{1}{(2\pi)^4}\ \kappa_S^4\ (\langle k_{12}^2\rangle + \langle k_{32}^2\rangle)\ \frac{(2A/M_S)^{1/2}}{H^{1/2}} \qquad (3.50)$$

Disregarding the magnetoelastic fluctuations, at a constant temperature, T, all the material-dependent physical parameters in equations (3.47) and (3.50) remain constant and the magnetization within the framework of the micromagnetic model can be written as

$$M = M_S \left[1 - \frac{a}{H^{1/2}} + \frac{b}{H^{3/2}}\right] + \chi_{hf} H \tag{3.51}$$

The last term in Eq.(3.51) accounts for the increase in magnetization caused by the external magnetic field over and above the spontaneous magnetization at that temperature.

3.3 Results and Discussion

3.3.1 Magnetic Irreversibility

The magnetization measured in the 'zero-field-cooled' ($M_{ZFC}(T)$) and 'field cooled' ($M_{FC}(T)$) modes at various, but fixed, magnetic field (H) values within the temperature range $2\ K \leq T \leq 310\ K$ is shown in Figs.3.1 and 3.2 for the nanocrystalline gadolinium with an average grain size of $d = 12\ nm$ and $18\ nm$, respectively. The irreversibility in magnetization normalized to the measuring field, $M_{irr}/H = [M_{FC}(T) - M_{ZFC}(T)]/H$, deduced from the thermomagnetic curves, is shown in figure 3.4. The temperature below which M_{irr}/H has a finite value marks the temperature, T_B, at which a bifurcation in FC and ZFC thermomagnetic curves occurs. The bifurcation temperature, T_B, shifts to lower temperatures with increasing H so much so that the irreversibility in magnetization is completely suppressed for $H > 3.5\ kOe$ ($2.2\ kOe$) in the $d = 12\ nm$ ($18\ nm$) sample. T_B as a function of field follows the relation $T_B = T_B(H = 0)[1 - (H/H^*)^2]$ with

$T_B(H = 0) = 283.8(9)\ K$ $(287.1(7)\ K)$ and $H^* = 4183(57)\ Oe$ $(2295(7)\ Oe)$ for $d = 12\ nm$ $(18\ nm)$ as shown in figure 3.3. While $T_B(H = 0)$ is very close to the ferromagnetic (FM)-to-paramagnetic (PM) phase transition temperature, T_C, the field required to suppress the irreversibility in magnetization completely, H^*, conforms well with the observation that H^* should lie in the range $3.5\ kOe < H^* < 10\ kOe$ $(2.2\ kOe < H^* < 3.5\ kOe)$ for the $d = 12\ nm$ $(18\ nm)$ sample. Irreversibility in magnetization, of similar kind, is also observed in perovskites [31, 32] (a ferromagnetic system) and it is attributed to the formation of metastable states due to randomly oriented magnetocrystalline anisotropy field in the polycrystallites [32].

The Irreversibility in magnetization at a given temperature $T < T_B \simeq T_C$ arises when a sizable fraction of magnetization is trapped in the low-magnetization metastable state (i.e., $M_{ZFC}(T)$) if system is cooled in 'zero-field' and the filed is applied at the lowest temperature or in the high-magnetization stable state (i.e., $M_{FC}(T)$) if the system is cooled 'in-field' from temperatures well above T_C where the energy barrier does not exist. The measured density of nc-Gd is $\sim$ 99% of bulk [33]. Since the core region of grain boundaries embodies excess volume, resulting in a local density deficit of typically 5% [34], the contribution of grain boundary excess volume to the reduced overall density, for a given crystallite size of 20 nm, is $\sim$ 1%. This density deficit, caused by the atomic site disorder at the grain boundary, leads to competing ferromagnetic and antiferromagnetic interactions between spins and this, in turn, results in a strong interfacial random anisotropy in nc-Gd. Moreover, the intra-grain magnetocrystalline anisotropy, though modified to some extend by the finite size effect, may still have the temperature and field dependence similar to that of single

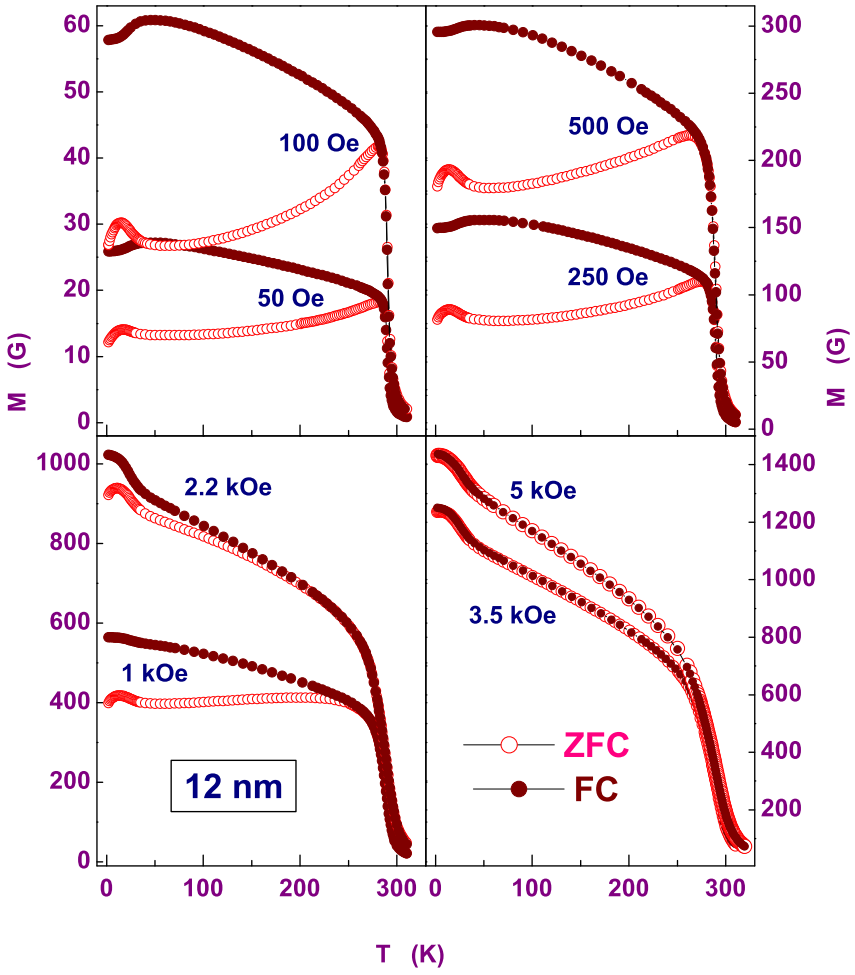

Figure 3.1: The ZFC and FC magnetization as a function of temperature, T, for nc-Gd with the average grain size d = 12 nm.

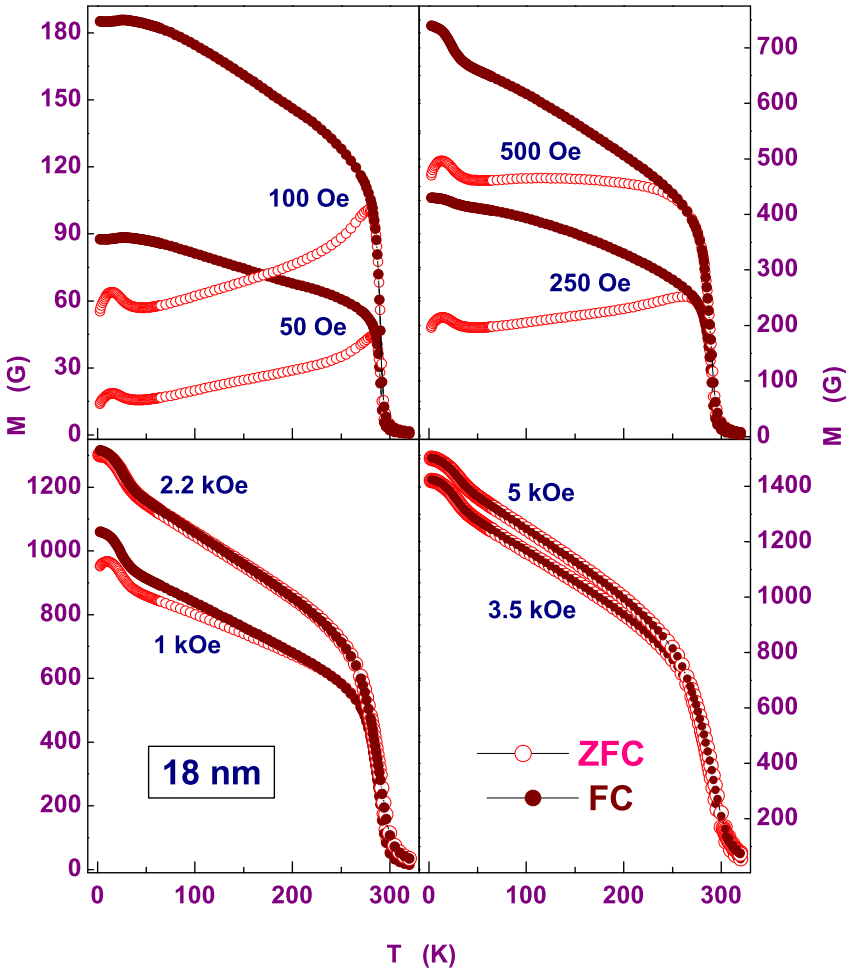

Figure 3.2: The ZFC and FC magnetization as a function of temperature, T, for nc-Gd with the average grain size d = 18 nm.

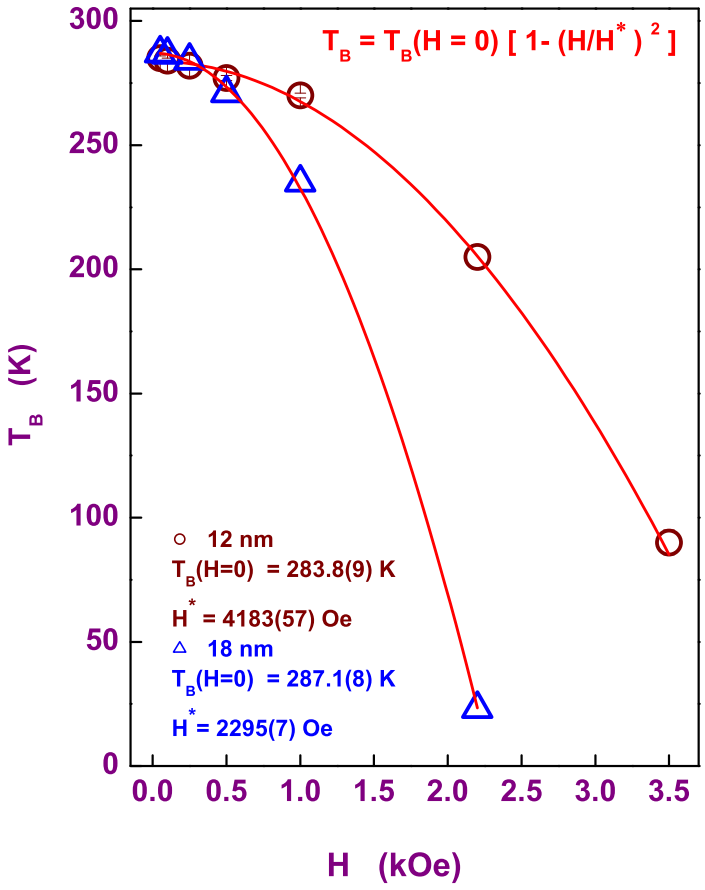

Figure 3.3: The bifurcation temperature, T_B, as a function of magnetic field, for nc-Gd samples with the average grain size d = 12 nm and 18 nm. T_B(H = 0) is very close to the FM - to - PM transition temperature, T_C.

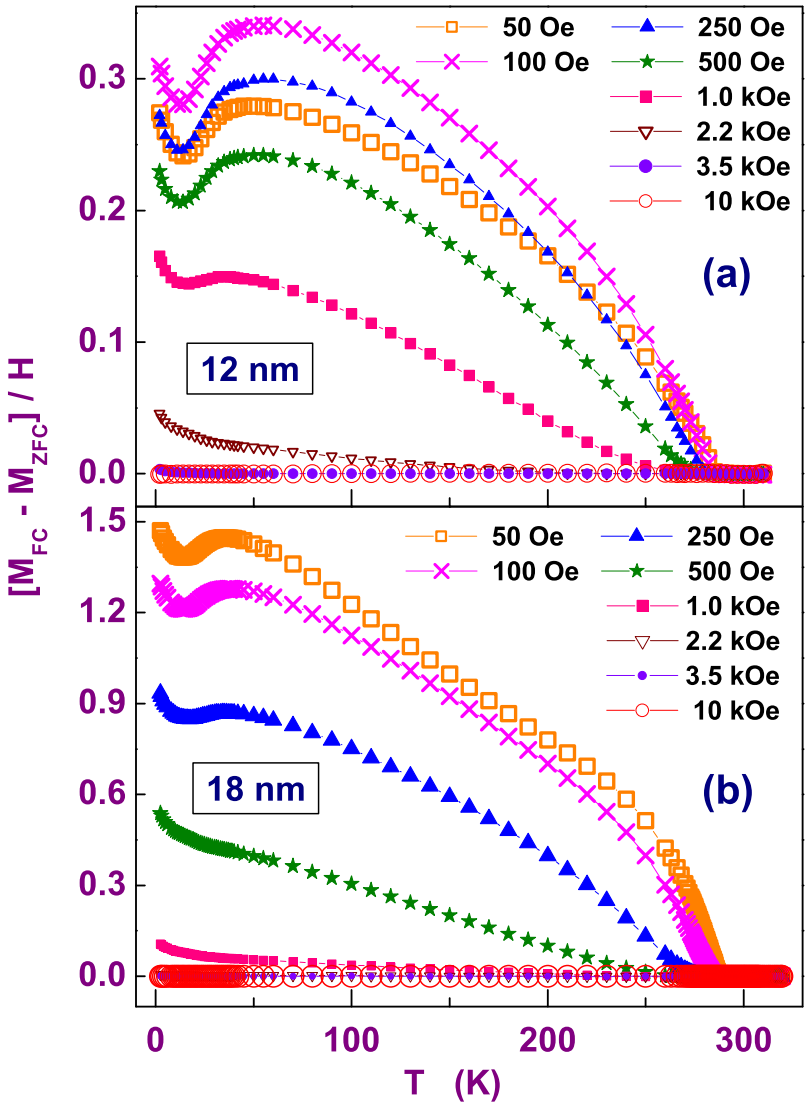

Figure 3.4: The irreversibility in magnetization, normalized to the dc field, for the nanocrystalline Gd sample, (a) d = 12 nm and (b) d = 18 nm.

crystal Gd [35, 36, 37].

In an attempt to qualitatively understand as to how the trapping of the spin system in a metastable or a stable state depends on the thermal/field prehistory of the system and how this process gives rise to a large irreversibility in magnetization, we put forward an intuitive picture of the magnetization state of a single-domain grain in terms of its free energy, E, as a function of the angle between magnetization and the easy direction of magnetization, θ, for a uniaxial system, as given in figure 3.5. When the nanocrystalline ferromagnetic system is cooled in 'zero-field' from a temperature above its ordering temperature, T_C, where the long-range magnetic order sets in, magnetization vector in each grain is frozen along the easy direction of magnetization - either in the M_0 state or M_{180} state, which are equally probable (Fig.3.5(b)). Hence, when the ensemble of grain magnetizations is considered, M_0 and M_{180} states will be equally populated. Since the crystallographic directions of each grain is oriented at random, the magnetization vector in each grain is also oriented at random, giving rise to zero net magnetization as represented by the $H = 0$ case in figure 3.6(a). At finite positive field ($H < H_s$, the switching field), applied parallel to the easy direction of magnetization, the energy, E, versus θ curves get biased such that the stable minimum is at $\theta = 0$ (Fig.3.5(a)). In this condition, the population in the M_0 state, the stable minimum state, will be more than that in the M_{180} state, the metastable minimum state, so that the net magnetization along the field direction is positive. At a finite temperature and field, the spins in the metastable state see an effective energy barrier, ΔE_B, due to the intragranular and interfacial magnetic anisotropies and the external magnetic field. ΔE_B decreases with increasing field but the

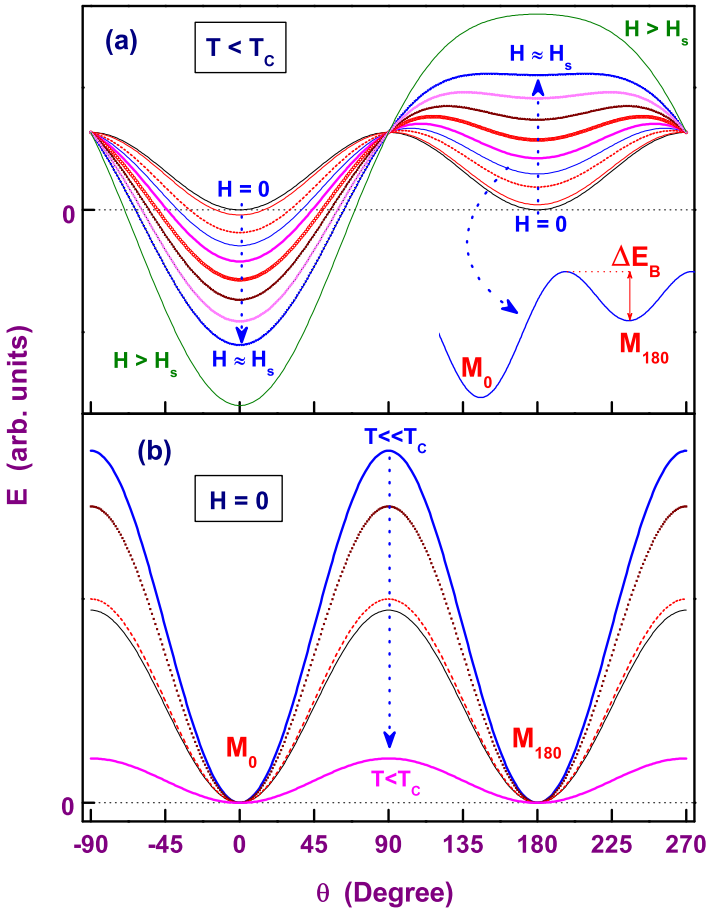

Figure 3.5: A schematic representation of the free energy, E, versus the angle between magnetization and the easy direction of magnetization, θ, for a uniaxial system. M_0 (M_{180}) is the energy state of a single grain when the magnetization is pointing along (opposite to) the easy direction of magnetization $\theta = 0$ ($\theta = 180$). At zero-field, both the M_0 and M_{180} states are equally probable. ΔE_B is the effective energy barrier height seen by the spins in the M_{180} state, which varies with the effective field and temperature. (a) The E versus θ curves at a temperature, $T < T_C$, for various fields starting from $H = 0$ to $H > H_s$ and (b) at various temperatures starting from $T \ll T_C$ to $T < T_C$ in zero field, $H = 0$.

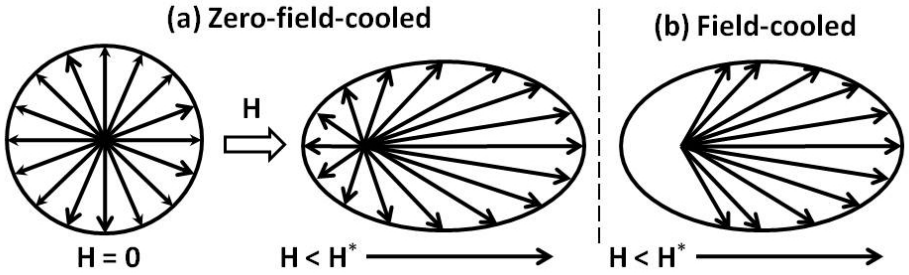

Figure 3.6: A representative picture describing the orientation of magnetization vector in different grains before and after the application of field in the 'zero-field-cooled' state and in the 'field-cooled' state.

temperature dependence of ΔE_B arises from the temperature dependence of the effective anisotropy field. With decreasing ΔE_B, the population of spins in the stable stable increases at the expense of that in the metastable state.

When the magnetic field is applied at the lowest temperature after cooling the system in 'zero-field', the net magnetization along the field direction will be the ensemble average of the magnetizations of the grains, more of them in the stable minimum state, M_0, than in the metastable state, M_{180}. The metastable state corresponds to the low-magnetization state, M_{ZFC}. In this state, the temperature dependence of the component of magnetization along the field direction at fixed fields, $H < H_s$, is governed by three factors, i) the usual decrease in the domain magnetization due to the thermal effect, ii) the population of spins in the metastable state changes depending on how the $\Delta E_B(T)$ compares with thermal energy, k_BT, and iii) the average component of magnetization along the field direction is decided by the relative strength of the temperature-dependent effective

anisotropy field and the external magnetic field. The spin system attains high-magnetization stable state when the system is cooled 'in-field' from a temperature above T_C and the domain formation takes place in presence of external magnetic field, the magnetization in most of the grains corresponds to the stable minimum, M_0, at $\theta = 0$ (Fig.3.5(a)). Therefore, the magnetizations of the grains will be pointing in a hemisphere along the field direction and the population of spins in the metastable state goes on reducing with increasing field (Fig.3.6(b)). Consequently, magnetization enters into the high-magnetization stable state, M_{FC}.

The $M_{ZFC}(T)$ at low fields is a clear depiction of the temperature dependence of the effective anisotropy field. With increasing field, the effective energy barrier height seen by the spins in the metastable state decreases and the thermal energy suffices to activate magnetization across the energy barrier. As a result, the overall magnetization prefers to be in M_{FC} state and this, in turn, reduces the irreversibility in magnetization. When a threshold (switching) field, H_s, is reached, only a single global minimum, corresponding to the high-magnetization stable state, M_{FC}, exists. Thus, the magnetic irreversibility vanishes for $H \geq H_s$. Obviously, H_s depends on temperature; H_s will have its maximum value at $T = 0$ and $H_s = 0$ at $T \geq T_C$ where only the global minimum survives and the critical fluctuations of magnetization ensure that the spontaneous magnetization goes to zero.

3.3.2 Magnetic Viscosity

Time-dependent 'Zero-field-cooled' Magnetization

The time evolution of magnetization at a few representative temperatures, when the magnetic field of strength 100 Oe/500 Oe/1 kOe is suddenly switched on after cooling the system in 'zero-field' to the specific temperature, measured for a time period up to 6 hours is shown in figure 3.7. The first data is collected ~ 7 sec after the magnetic field reached the set value and, subsequently, the data is collected at a time interval of ~ 100 m sec in the measuring time range $7\ sec \leq t \leq 2.2 \times 10^4\ sec$. The field values are chosen to be 100 Oe/500 Oe/1 kOe for the reason that these field values are less than the switching field, $H_s \equiv H^*$ (Fig.3.3). At these fields, the irreversibility in magnetization persists over the temperature range from 2 K to $T \simeq T_C$. The population of the spins in the metastable state, M_{180}, after the system is cooled in 'zero-field' to a specific temperature and at a magnetic field, H (Fig.3.5(a)), reduces as the spins overcome the anisotropy energy barrier, $\Delta E_B(T)$, by the the thermal activation process. If the system is given sufficiently long/infinite time, gradually the spin population of the metastable state, M_{180}, reduces to zero while the population of the M_0 state - the stable, minimum energy state of the system, reaches its equilibrium value $M_{FC}(T)$. The nature of these energy barriers decides the functional form of the growth of M_{ZFC} with time (Eq.(7.11)) at a given temperature $T < T_B$ and the magnetic field $H < H_s$ (Fig.3.3). The linear dependence of magnetization on $ln(t)$ (Fig.(3.7)) suggests that the energy barrier distribution is considerably wide in the measuring time.

The temperature variations of the magnetic viscosity, $S(T, H)$, defined

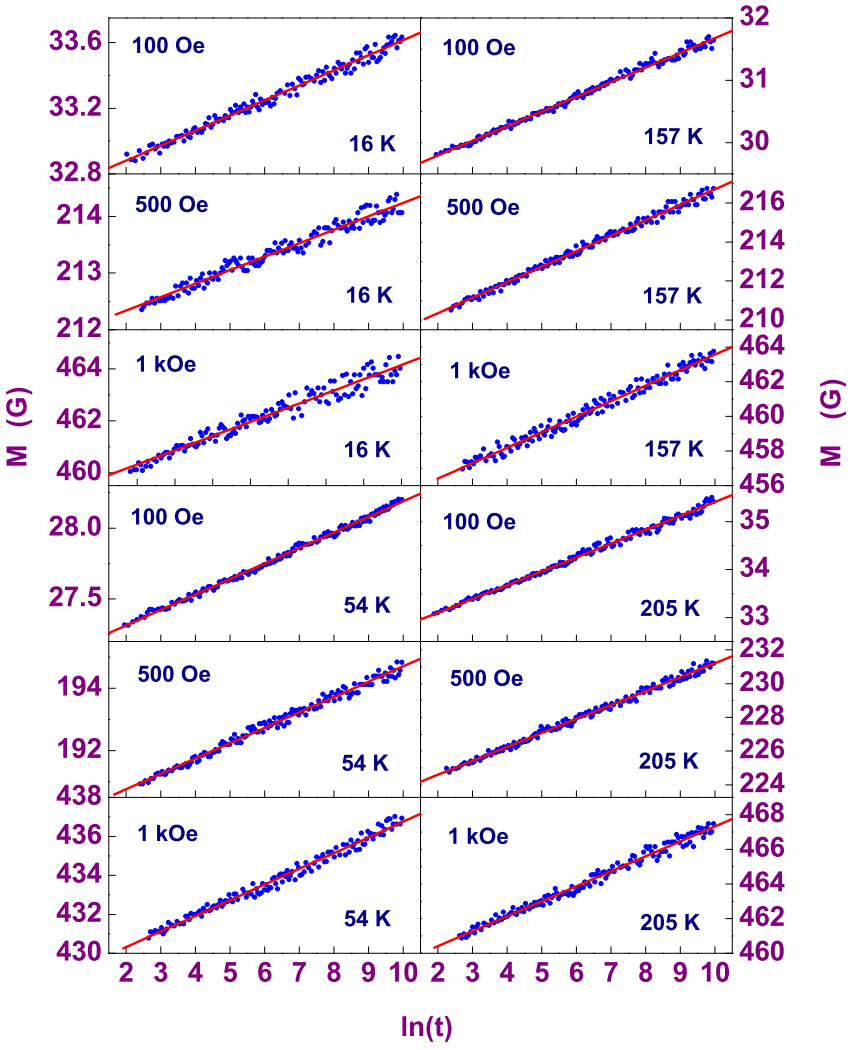

Figure 3.7: The time-dependent magnetization for a dc field strength of 100 Oe, 500 Oe and 1 kOe at a few representative temperatures.

by Eq.(7.5), calculated from the time evolution of the 'zero-field-cooled' magnetization measured at various temperatures $T \lesssim T_C$ and at dc fields of strength of $H_{dc} = 100\ Oe$, 500 Oe and 1 kOe are shown in figure 3.11.

ac Susceptibility

The real ($\chi'_{ext}(T)$) and imaginary ($\chi''_{ext}(T)$) components of susceptibility, shown in figure 3.8, were measured at different but fixed temperatures (stable to within $\pm 1\ mK$) and ac magnetic field of rms amplitude of 1 Oe and frequencies (f) ranging from 11 Hz to 8913 Hz on 12 nm (disc shaped) and 18 nm (strip). For a ferromagnet, the intrinsic magnetic susceptibility, χ_{int}, along the easy direction of magnetization diverges at $T = T_C$. When both shape and magnetocrystalline anisotropies are present, $\chi_{int}(T)$ is related to the measured initial susceptibility, $\chi_{ext}(T)$, as [37]

$$\chi_{int}^{-1}(T) = \chi_{ext}^{-1}(T) - 4\pi N(T) \tag{3.52}$$

where $N(T) = N_d + N_K(T)$, N_d is the demagnetization factor which depends only on the sample shape. As the easy direction of magnetization varies randomly from grain to grain, N_K averages out to zero and hence the peak in $\chi_{ext}(T)$ at $T \simeq T_C$ is demagnetization limited. Due to the temperature dependence of the random inter-grain magnetocrystalline anisotropy as well as that of the intra-grain and interfacial anisotropies, instead of having a demagnetization-limited value throughout the temperature range below T_C [37], $\chi_{ext}(T)$ for nanocrystalline Gd drops gradually as the temperature decreases to reach a flat minimum in the temperature range $100\ K \leq T \leq 200\ K$ before going through a small peak at around 16 K as the temperature is decreased further. $\chi_{ext}(T)$ has similar features for both the $d = 12\ nm$ and

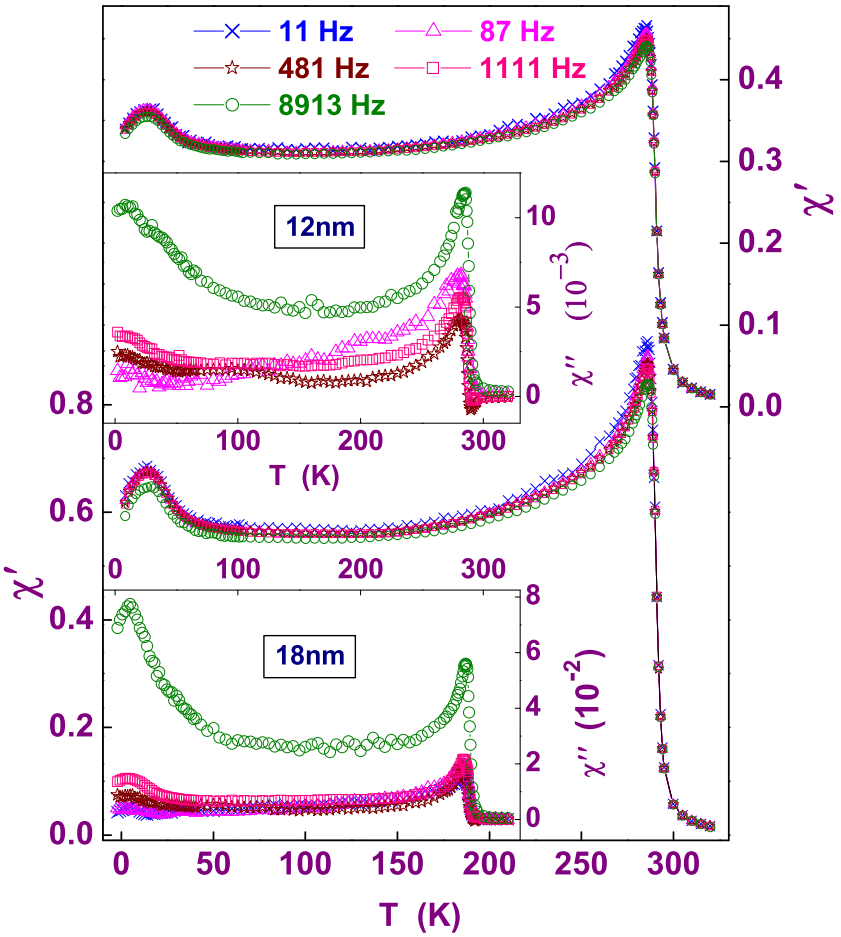

Figure 3.8: The real ($\chi'(T)$) and imaginary ($\chi''(T)$) components of ac susceptibility as functions of temperature measured in an ac driving field of rms amplitude 1 Oe and frequencies ranging from 11 Hz to 8913 Hz.

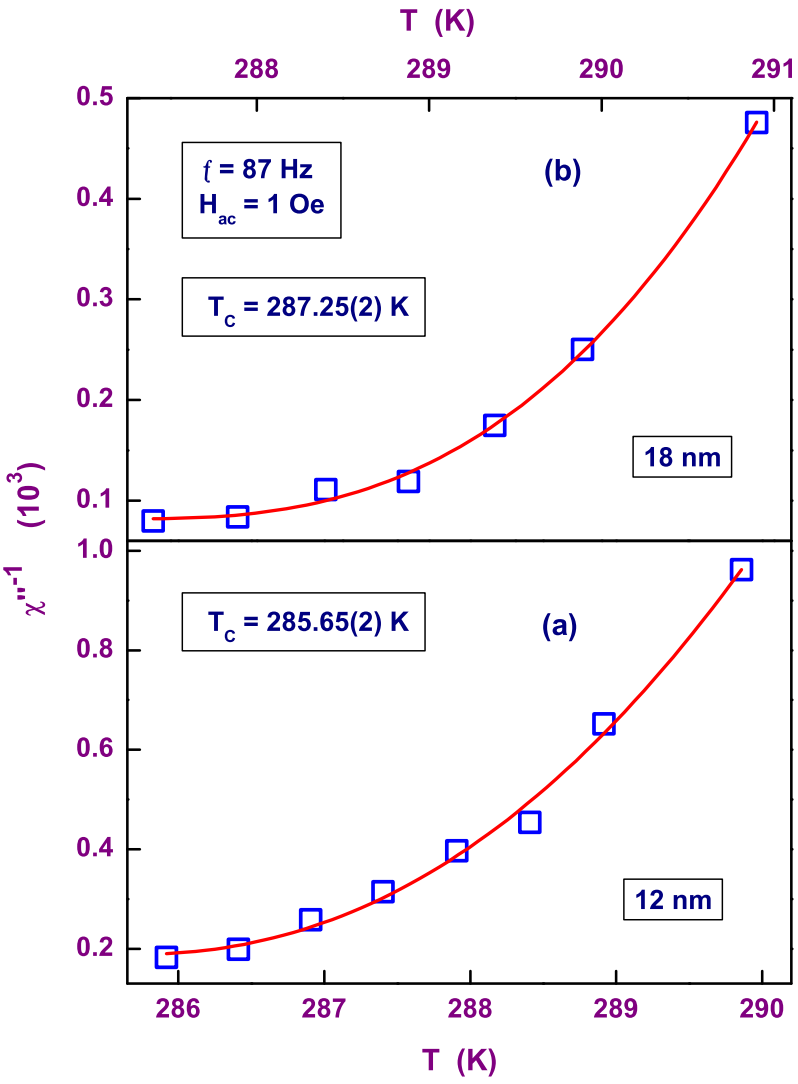

Figure 3.9: Singular behaviour of χ'' for $T \geq T_C$.

18 nm samples. Since the shapes of the $d = 12$ nm and 18 nm samples are different, the demagnetization-limited peak value near T_C ($T_c = 285.63(2)$ K for $d = 12$ nm and 287.22(2) K for $d = 18$ nm) is higher by a factor of 2 for $d = 18$ nm sample compared to that in the 12 nm sample.

At T_C, divergence of χ'' is limited by the shape anisotropy and in the temperature range $T \gtrsim T_C$, χ'' drops abruptly and follows the power law

$$\chi''^{-1} = A_0 + A_1 \left[\frac{T - T_C}{T_C}\right]^{\nu} \quad , \tag{3.53}$$

as shown in figure 3.9. By fitting the power law to the χ'' data with $T_C = 285.65$ K (287.25 K) for the nanocrystalline sample with the average grain size of $d = 12$ nm (18 nm), the parameter values obtained are $A_0 = 188(17)$ (82(5)), $A_1 = 78(55) \times 10^5$ ($46(27) \times 10^6$) and $\nu = 2.18(17)$ (2.67(13)).

The temperature variations of the magnetic viscosity, $S(T, H = 1\ Oe)$, is calculated from the imaginary part of the ac susceptibility, $\chi''(T)$, using the relation between magnetic viscosity, S, and the imaginary part of ac susceptibility (Eq.(7.15)). The magnetic viscosity at an external magnetic field of 1 Oe and fixed temperatures, calculated at various measuring times ($t = 1/f$) starting from 100 μ sec to 100 m sec from $\chi''(T, f)$ measured at various frequencies starting from 11 Hz to 8913 Hz, are shown in figure 3.10 for the nanocrystalline samples with $d = 12$ nm and 18 nm. The time-dependent magnetic viscosity at $H = 1$ Oe shows that it is independent of measuring time above ~ 2 m sec and below which it strongly depends on the measuring time. This observation ascertain that the energy barrier height is independent of time above a measuring time of ~ 2 m sec. In the time-dependent 'zero-field-cooled' magnetization measurement, the first data point was collected at $t \simeq 7$ sec after the magnetic field reached the set

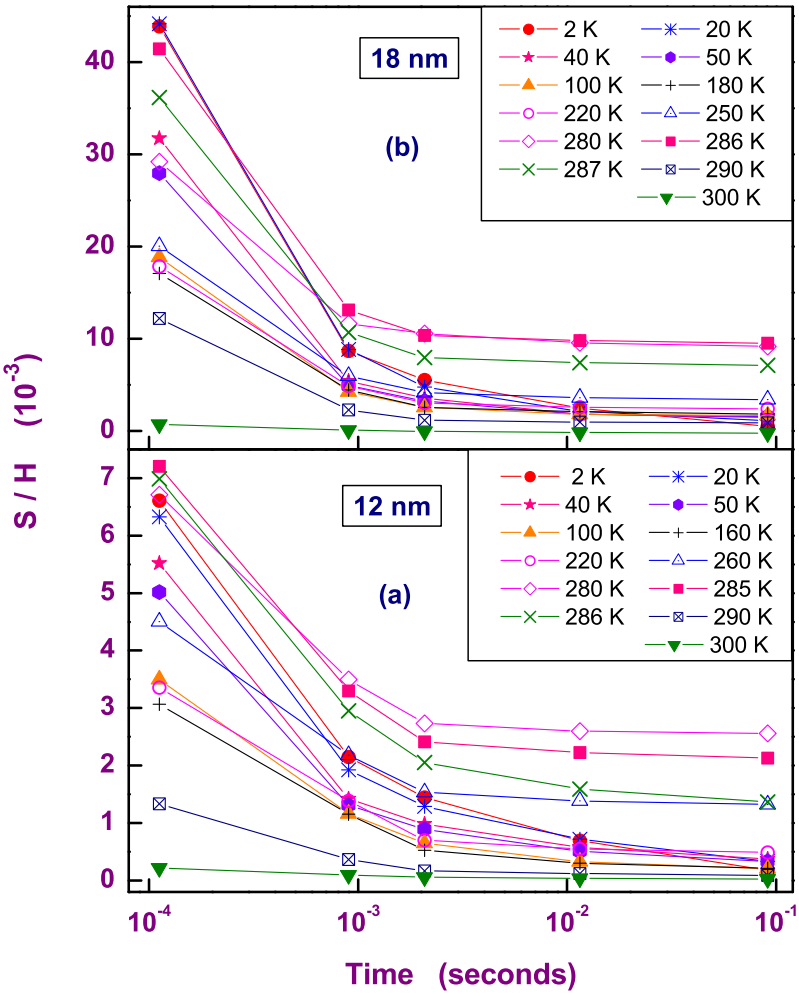

Figure 3.10: Magnetic viscosity as a function of time calculated from the imaginary part of ac susceptibility, χ'', at various fixed temperatures for nanocrystalline Gd with the average grain size of (a) $d = 12\ nm$ and (b) $d = 18\ nm$.

value. At $t \simeq 7\ sec$ ($\gg 2\ m\ sec$), the energy barrier height is independent of time and hence it is not surprising that the magnetization varies linearly with $ln(t)$.

The temperature variations of the magnetic viscosity at different fields, $S(T, H)$, calculated from the time evolution of the 'zero-field-cooled' magnetization, are compared with that obtained from the imaginary part of the ac susceptibility, $\chi''(T)$, in figure 3.11. The main observations are i) the increase in magnetic viscosity, S, with decreasing magnetic field and increasing temperature and ii) the magnetic viscosity, S, peaks at $T \approx T_C$ at $H = 1\ Oe$ and the temperature at which S peaks shifts down with increasing field. As described in the intuitive picture (Fig.(3.5)), in the 'zero-field-cooled' nanocrystalline ferromagnetic system, the population in the metastable state, M_{180}, is decided by the effective energy barrier, ΔE_B, seen by the spins in the metastable state and at temperature, T ($k_B T$). According to Eq.(7.9), magnetic viscosity, S, depends on both the effective energy barrier, ΔE_B, and the thermal energy, $k_B T$. At a fixed temperature, T, when the magnetic field increases, the effective energy barrier decreases (Fig.(3.5)) and, in turn, the population of spins in the metastable state decreases. This gives rise to the reduction in magnetic viscosity, S, with increasing magnetic field (Fig.(3.11)). Similarly, when temperature increases at a fixed field, the energy barrier height changes due to the temperature-dependence of the effective anisotropy field and also the probability for the thermal activation increases (Eq.(7.2)). At the lowest field ($H = 1\ Oe$, Fig.(3.11)), where the effective energy barrier height is maximum with approximately half of the total population of spins in the metastable state, the magnetic viscosity, S, increases with increasing temperature till T_C,

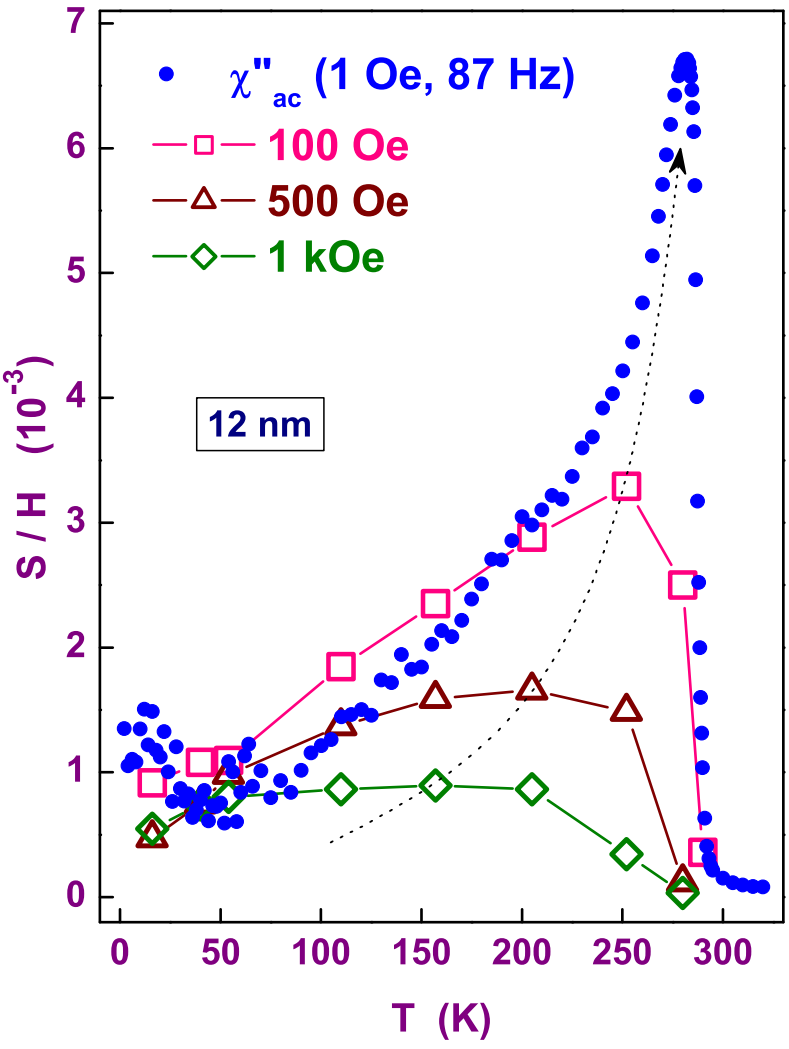

Figure 3.11: Magnetic viscosity, S, as a function of temperature at fields 100 Oe, 500 Oe and 1 kOe is compared with that obtained from $\chi''(T)$, measured at $H_{ac} = 1\ Oe$ and $\nu = 87\ Hz$, using Eq.(7.15).

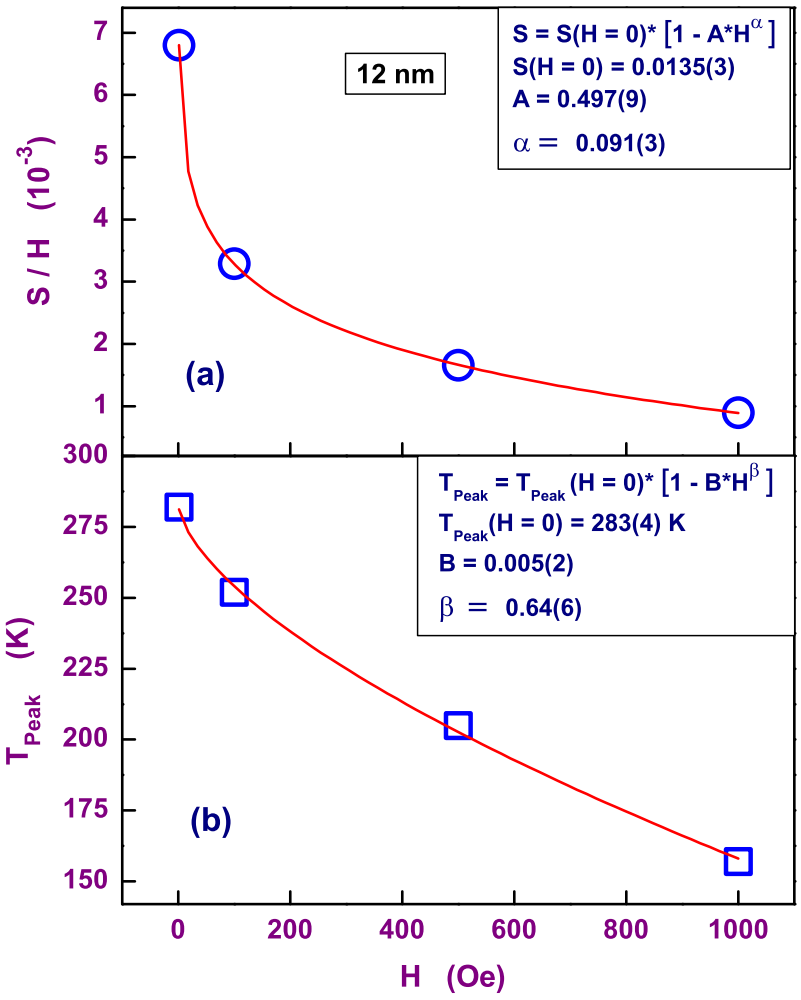

Figure 3.12: (a) The peak value and (b) peak temperature of the normalized magnetic viscosity of nanocrystalline Gd with average grain size of $d = 12\ nm$ as functions of external magnetic field together with the empirical fits to the data.

where the energy barrier collapses and beyond which the magnetic viscosity, S, drops drastically. At higher fields but $H < H_s$, as the population in the metastable state is less, the magnetic viscosity, S, starts decreasing at a temperature much less than T_C and this temperature decreases further with increasing field. The temperature- and field-dependent magnetic viscosity, S(T,H), is an evidence for the presence of a strongly temperature-dependent energy barriers and hence for the magnetocrystalline and interfacial anisotropies prevalent in nc-Gd.

3.3.3 Coercivity and Remanence

The M-H hysteresis loops, measured up to 15 kOe at various temperatures below T_C, are shown in figures 3.13 and 3.14 for the $d = 12$ nm and 18 nm samples, respectively. The insets of the figures 3.13 and 3.14 show enlarged view of hysteresis at low fields. Figure 3.15 shows the coercive field, H_C (open symbols), and the remanent magnetization, M_r (closed symbols in the inset of Fig.(3.15)) as functions of temperature. This figure also displays the best fits, based on the Eq.(6.22), with $m(T) \equiv M_r(T)$ (continuous curves) and $m(T) \equiv M_{irr}(T)$ (dashed curves). Since the spontaneous magnetization could not be determined from the Arrott (M^2 versus H/M) plots as they exhibit finite curvature even at fields as high as 90 kOe, the remanent magnetization is used instead of spontaneous magnetization to fit the expression for coercivity to the data. The use of irreversibility in magnetization in place of the spontaneous magnetization in the expression for coercivity also generates good fits to the data. The finding that the theoretical fits adequately describe the $H_C(T)$ data strongly indicates that shape anisotropy plays a crucial role in the magnetization reversal process.

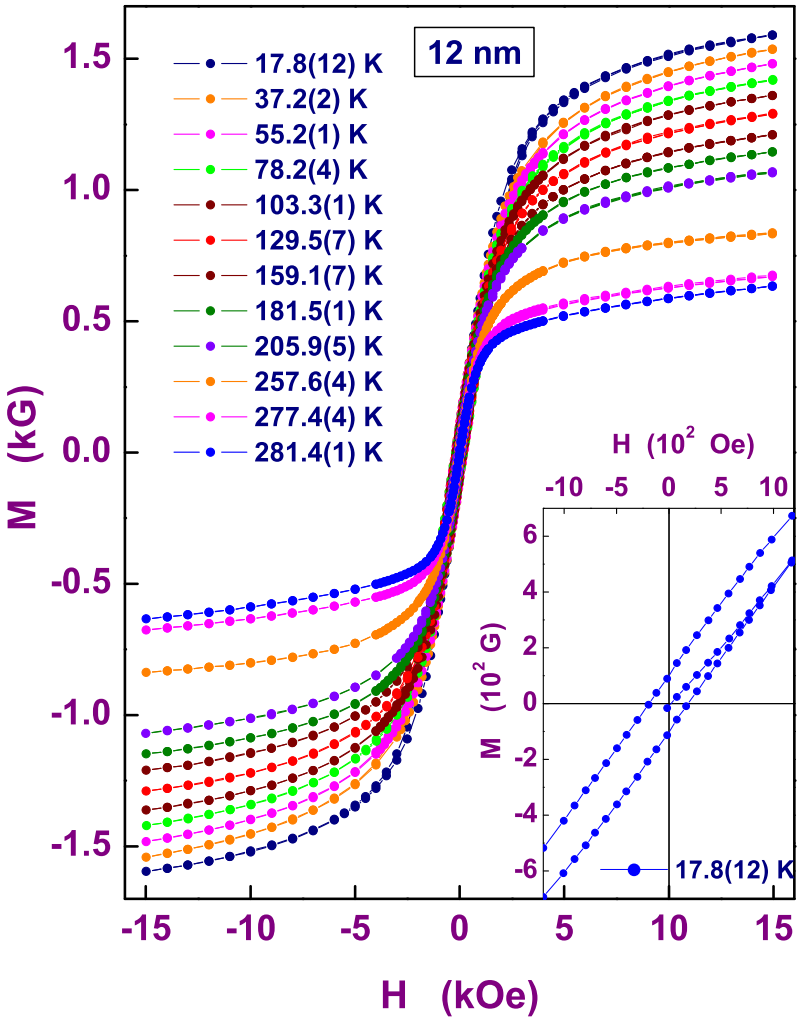

Figure 3.13: The M-H hysteresis loops for the $d = 12\ nm$ sample in the field range $-15\ kOe \leq H \leq 15\ kOe$ at a few representative temperatures. The inset shows the enlarged view of the low-field portions of the hysteresis curve taken at 17.8(12) K.

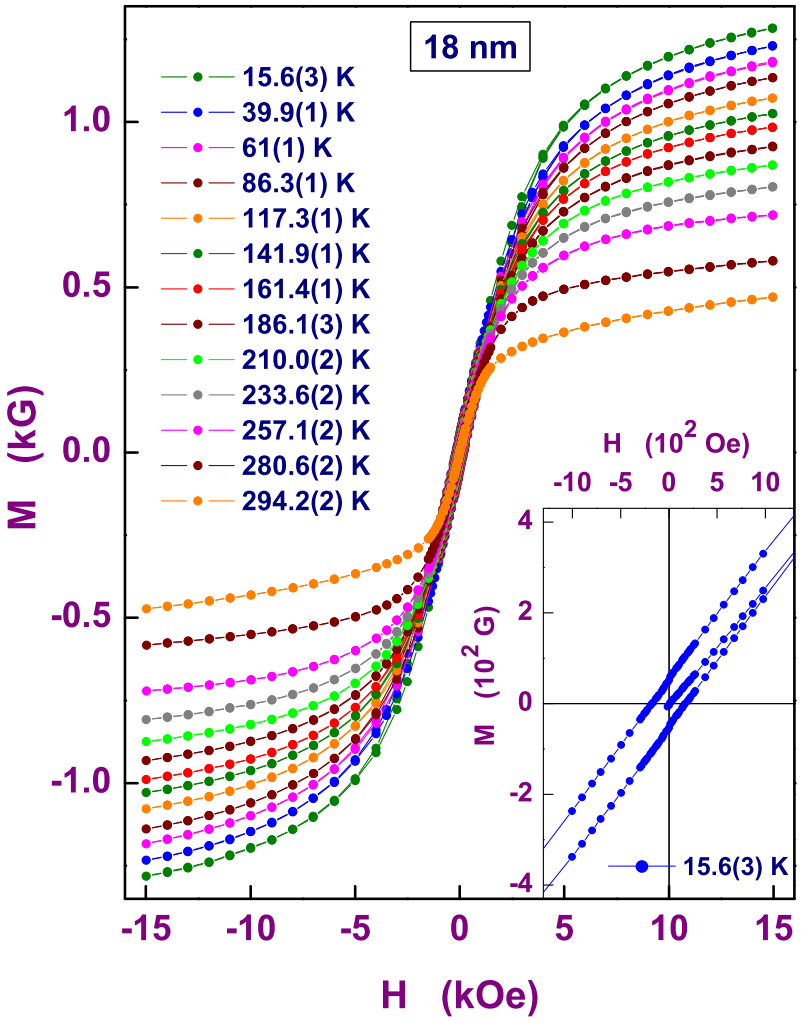

Figure 3.14: The M-H hysteresis loops for the $d = 18\ nm$ sample in the field range $-15\ kOe \leq H \leq 15\ kOe$ at a few representative temperatures. The inset shows the enlarged view of the low-field portions of the hysteresis curve taken at 15.6(3) K.

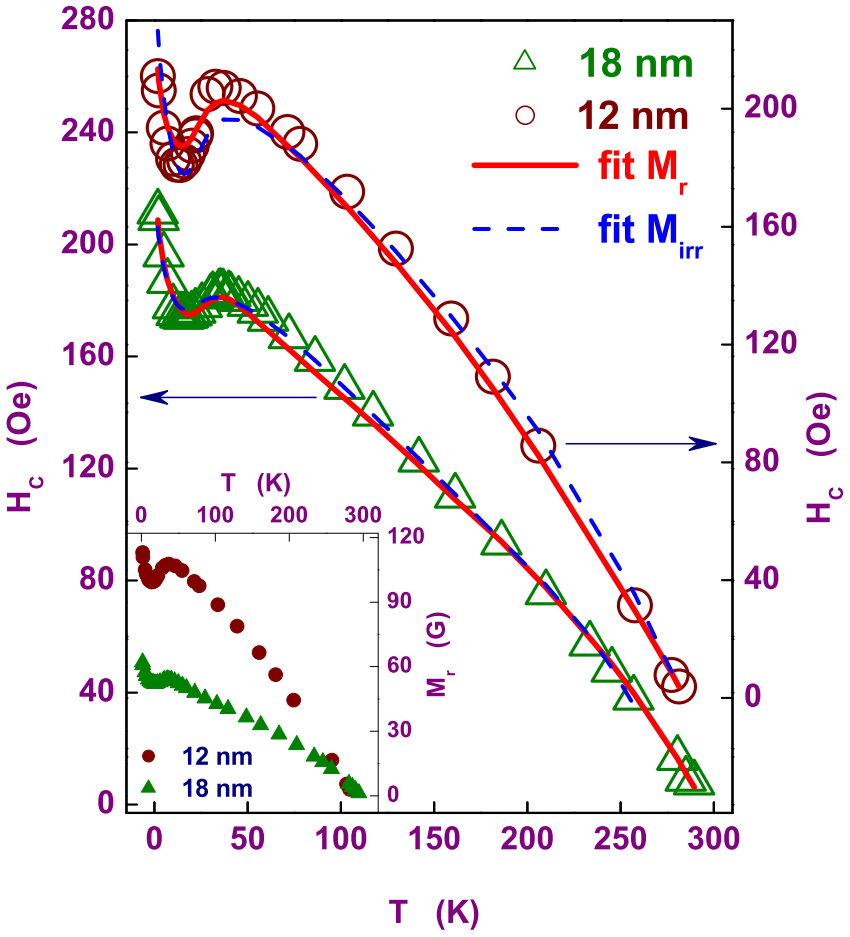

Figure 3.15: The coercive field, H_C as a function of temperature for the d = 12 nm and 18 nm samples along with the fits that set $m(T) = M_r(T)$ (continuous curves) and $m(T) = M_{irr}(T)$ (dashed curves). The inset shows the temperature variation of the remanent magnetization for the d = 12 nm and 18 nm samples.

3.3.4 Approach-to-saturation

Approach-to-saturation (ATS) is another important aspect of the magnetization processes. We observe that, even at fields as high as 120 kOe and temperatures as low as $\cong$ 1.95 K, magnetization does not saturate. In the polycrystalline gadolinium samples with nano-size grains, nc-Gd, crystallographic directions and hence the easy directions of magnetization are oriented at random from grain to grain.

The conventional ATS model (Eq.(6.23)), that takes into account the plastic strain due to defects/grain boundaries (the $1/H$ term) and magnetocrystalline anisotropy (the $1/H^2$ term) together with the high-field susceptibility, fails to describe $M(H)$ at different temperatures in that the temperature variation of the magnetocrystalline anisotropy contribution, b, obtained by fitting Eq.(6.23) to the $M(T, H)$ data, is not in agreement with that calculated (Eq.(5.35)) by assuming a random orientation of the anisotropy field (Fig.3.16).

Next, an attempt is made to ascertain whether or not the random anisotropy (RA) model (Eq.(5.37)) explains the magnetization processes in the high-field regime ($H > H_{ex}$ or $H \gg H_r > H_{ex}$), where the non-collinear spin structure progressively collapses into a collinear one around the field. Eventhough, the intra-grain anisotropy field is oriented at random in nc-Gd and the random anisotropy model is expected to fit the data better, the fits deteriorate (in terms of the reduced χ^2) in the low temperature regime. A possible cause for the deviation could be that this model does not take into account the intrinsic magnetocrystalline and magnetostatic fluctuations prevalent in the nanocrystalline system.

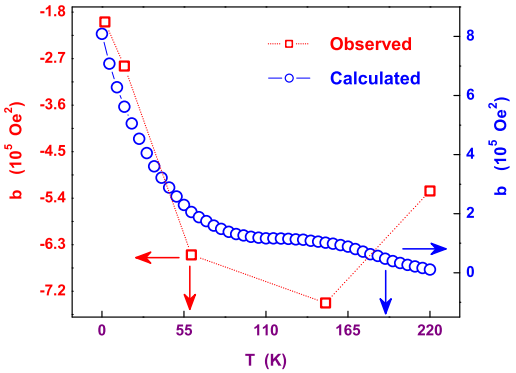

Figure 3.16: .The magnetocrystalline anisotropy contribution, b, to the deviation of the ferromagnetic saturation obtained by fitting Eq.(6.23) to the $M(T,H)$ data along with that calculated (Eq.(5.35)) by assuming random orientation of grains.

By contrast, the micromagnetic model accurately reproduces the observed M(T,H) and compared to that in random anisotropy model, the sum of deviation squares, χ^2, is lower by an order of magnitude (Fig.3.21). In micromagnetic expression, Eq.(3.51), the term $H^{-1/2}$ arises from both magnetostatic and magnetocrystalline fluctuations while the $H^{-3/2}$ term originates from magnetostatic fluctuations alone, as it is evident from Eqs.(3.48) and (3.50), while χ_{hf} is the high-field susceptibility. The temperature variation of the parameters M_S, 'a', 'b' and χ_{hf} is shown in figure 3.20. The temperature variation of the parameter M_S for both $d = 12\ nm$ and $18\ nm$ samples are consistent with the measured high-field magnetization $M(T, H = 120\ kOe)$ for $d = 12\ nm$ [24] and $M(T, H = 90\ kOe)$ for $d = 18\ nm$ [28].

The parameters 'a' and 'b', which are a direct measure of the contribu-

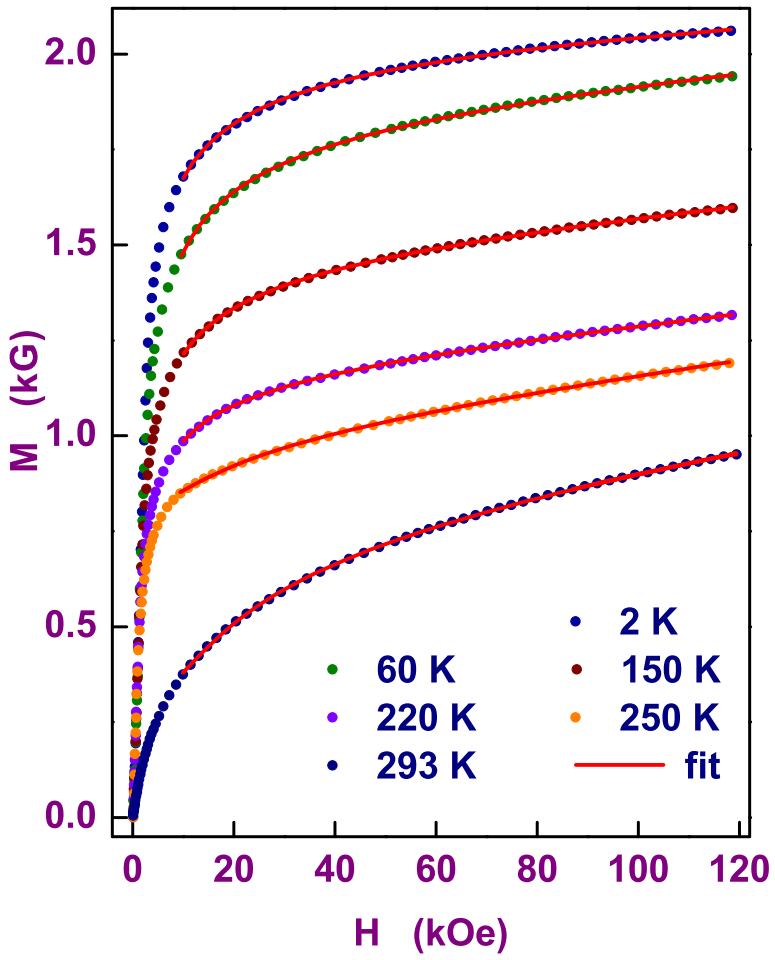

Figure 3.17: The M-H isotherms (symbols) in fields up to 120 kOe for the nanocrystalline Gd with an average grain size of $d = 12$ nm at a few representative temperatures along with the theoretical fits (continuous curves) based on the micromagnetic model, Eq.(3.51).

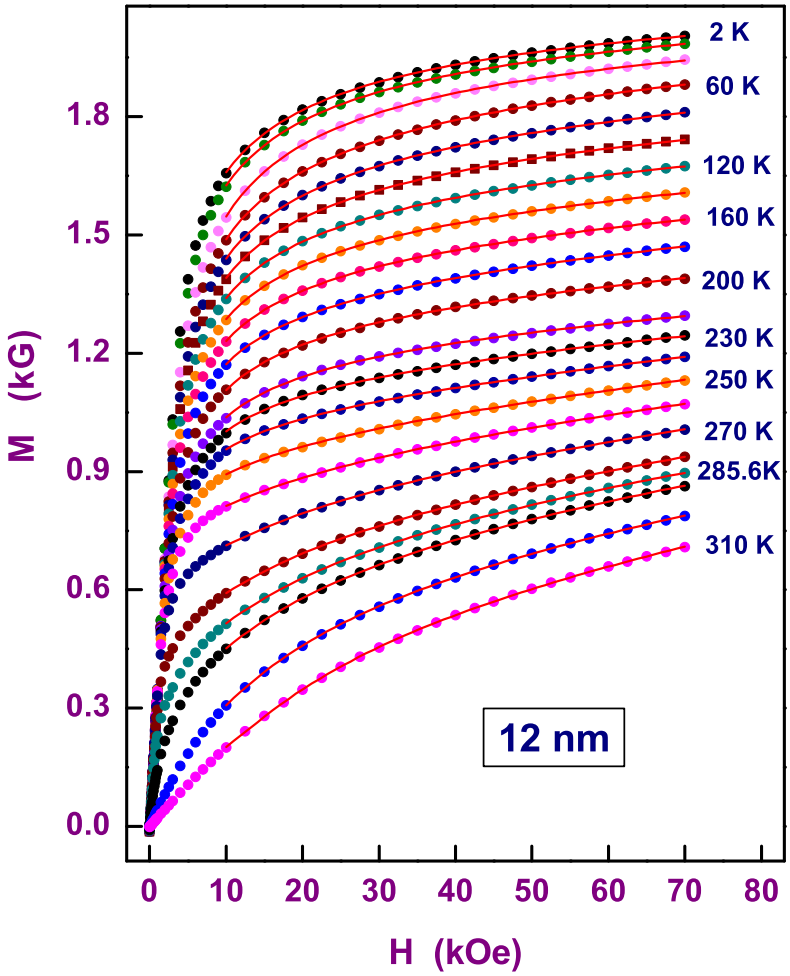

Figure 3.18: The M-H isotherms (symbols) in fields up to 70 kOe for the nanocrystalline Gd with an average grain size of $d = 12$ nm at a few representative temperatures starting from 2 K to 310 K along with the theoretical fits (continuous curves) based on the micromagnetic model, Eq.(3.51).

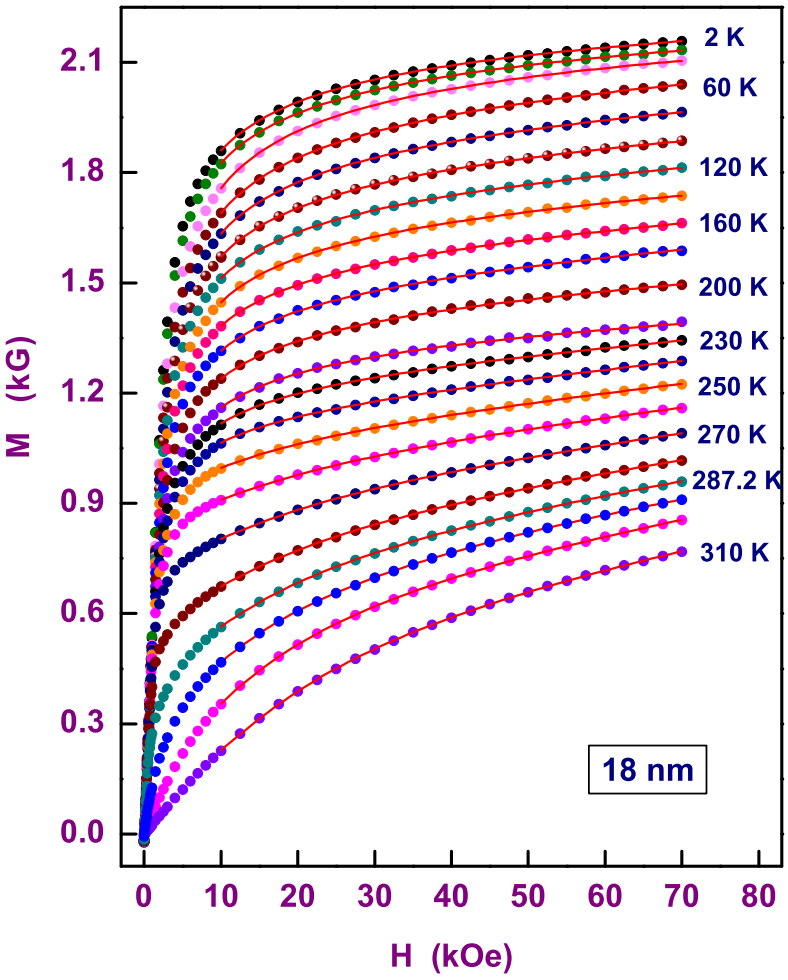

Figure 3.19: The M-H isotherms (symbols) in fields up to 70 kOe for the nanocrystalline Gd with an average grain size of $d = 18$ nm at a few representative temperatures starting from 2 K to 310 K along with the theoretical fits (continuous curves) based on the micromagnetic model, Eq.(3.51).

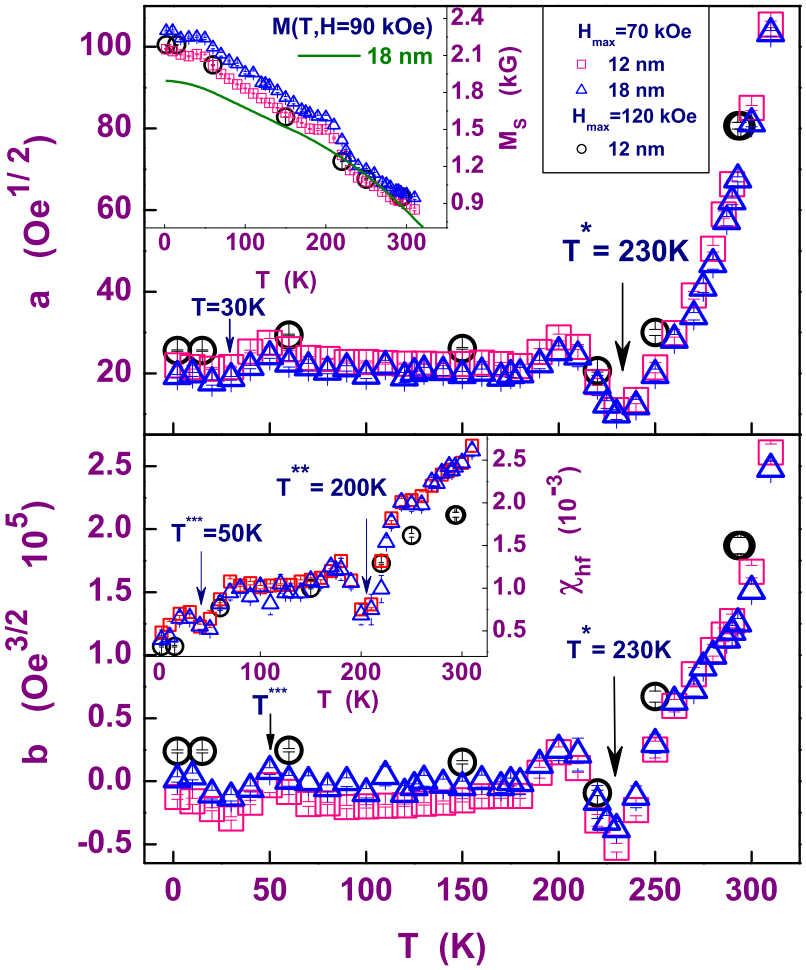

Figure 3.20: The parameters (a) a, (b) b, (inset to a) magnetization, (inset to b) high field susceptibility obtained by fitting the micromagnetic model to the M-H data at various temperatures on nanocrystalline Gd with average grain size 12 nm and 18 nm up to 70 kOe along with that for 12 nm measured up to 120 kOe.

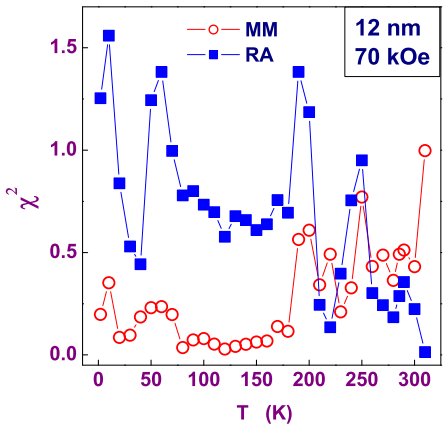

Figure 3.21: The reduced χ^2 for micromagnetic (MM) model is compared with that for random anisotropy (RA) model in the temperature range $2\ K \leq T \leq 310\ K$.

tions of magnetocrystalline and magnetostatic fluctuations, exhibit a dip at $T^* \sim 230\ K$, which suggests that the effective magnetocrystalline anisotropy is going through a minimum around this temperature. The temperature T^* is close to the spin re-orientation temperature $T_{SR} = 230\ K$ observed in the single crystal Gd [37]. At a temperature $T^{**} \simeq 200\ K$, where the parameters 'a' and 'b' as functions of temperature go through a small hump, $\chi_{hf}(T)$ exhibits a dip. Similar characteristic features are present at around $50\ K$, where the magnetocrystalline anisotropy field is expected to be minimum in each grains as is the case in single crystal Gd [35, 36, 37]. As the local magnetocrystalline (more precisely, the intra-grain and the interfacial) anisotropy field has a decisive role to play in the intrinsic fluctuations, it is not surprising that the characteristic temperatures of the effective magnetocrystalline anisotropy field, are reflected in the temperature variations of

the parameters '$a(T)$', '$b(T)$' and $\chi_{hf}(T)$.

3.4 Summary and Conclusion

The magnetization, $M(T, H)$, measured in 'zero-field-cooled' and 'field-cooled' modes, reveals large irreversibility in magnetization below a characteristic field in nanocrystalline Gd. This irreversibility is due to the magnetization of a sizable fraction of the total number of grains are trapped in the metastable state, which is separated from the stable minimum by the energy barrier brought about by the effective magnetocrystalline and interfacial anisotropy fields. The time-dependence of magnetization is due to the thermal activation process, by which the population of spins in the metastable low-magnetization state decreases while that in the stable high-magnetization state increases. The temperature- and field-dependent magnetic viscosity, S, reflects this thermal activation process over the temperature- and field-dependent effective anisotropy energy barrier, which has a distribution because of the variation in the grain sizes. The linear variation of magnetization with $ln(t)$ and the close similarity between $\chi''(T)$ and the viscosity (normalized to H), suggests that the energy barrier distribution, brought about by various anisotropies, is very broad. The temperature-dependent and frequency-independent ac susceptibility also indicates that the orientation of the intra-grain anisotropy field varies randomly from grain to grain in nc-Gd. The temperature-dependent coercivity is in agreement with the fact that the magnetization reversal process is predominantly governed by the shape anisotropy. The considerably slow approach to saturation in nanocrystalline Gd is mainly due to the presence of large magne-

tocrystalline and magnetostatic fluctuations. The temperature variations of the coefficients of the $H^{-1/2}$, $H^{-3/2}$ and the high-field susceptibility terms shows a dip/peak at the characteristic temperatures at which the effective anisotropy field either peaks or vanishes, as in the case of single crystal gadolinium.

References

1. R. Kruk, M. Ghafari, H. Hahn, D. Michels, R. Birringer, C. E. Krill III, R. Kmiec and M. Marszalek, *Phys. Rev. B* **73**, 054420 (2006).

2. A. Michels, F. Dbrich, M. Elmas, A. Ferdinand, J. Markmann, M. Sharp, H. Eckerlebe, J. Kohlbrecher and R. Birringer, *Europhys. Lett.* **81**, 66003 (2008).

3. P. M. Shand, J. G. Bohnet, J. Goertzen, J. E. Shield, D. Schmitter, G. Shelburne and D. L. Leslie-Pelecky, *Phys. Rev. B* **77**, 184415 (2008).

4. L. Néel, *Ann. Geophys* **5**, 99 (1949); W. F. Brown, *Phys. Rev.* **130**, 1677 (1963).

5. D. V. Berkov, *J. Magn. Magn. Mater.* **111**, 327 (1992).

6. R. Schumann and L. Jahn, *J. Magn. Magn. Mater.* **149**, 318 (1995).

7. R. Street and J. C. Wooley, *Proc. Phys. Soc. A* **62**, 562 (1949).

8. A. Aharoni, *J. App. Phys.* **57**, 4702 (1985).

9. M. M. Ibrahim, S. Darwish and M. S. Seehra, *Phys. Rev. B* **51**, 2955 (1995).

10. T. S. Chin, M. F. Wu, S. K. Chen and J. M. Yao, *J. Alloy. Comp.* **222**, 143 (1995).

11. I. Škorvánek, S. Skwirblies and J. Kötzler, *Phys. Rev. B* **64**, 184437 (2001).

12. W. Luo, S. R. Nagel, T. F. Rosenbaum and R. E. Rosensweig, *Phys. Rev. Lett.* **67**, 2721 (1991).

13. L. Lundgren, P. Svedlindh, P. Nordblad and O. Beckman, *Phys. Rev. Lett.* **51**, 911 (1983).

14. L. Lundgren, P. Nordblad, P. Svedlindh and O. Beckman, *J. Appl. Phys.* **57**, 3371 (1985).

15. H. Lin and C. Chinping *Phys. Rev. B* **75**, 184424 (2007).

16. L. He and C. Chen, *Phys. Rev. B* **75**, 184424 (2007).

17. A. T. Aldred, *Phys. Rev. B* **14**, 219 (1976).

18. H. Kronmüller *IEEE. Trans. on magnetics* **MAG-15**, 5 1218 (1979).

19. R. Pauthenet, *J. Appl. Phys.* **53**, 8187 (1982).

20. S. V. Andreev, M. I. Bartashevich, V. I. Pushkarsky, V. N. Maltsev, L. A. Pamyatnukh, E. N. Tarasov, N. V. Kudrevatykh and T. Goto, *J. Alloy. Comp.* **260**, 196 (1997).

21. W. F. Brown, Jr., *Phys. Rev.* **58**, 736 (1940).

22. W. F. Brown, Jr., *Phys. Rev.* **60**, 139 (1941).

23. L. Néel, *J. Phys. Rad.* **9**, 184, 193 (1948).

24. S. P. Mathew, S. N. Kaul, A. K. Nigam, A. -C. Probst and R. Birringer *J. Phys.:Conf. Ser.* **200**, 072047 (2010).

25. E. M. Chudnovsky and R. A. Serota, *Phys. Rev. B* **26**, 2697 (1982).

26. S. F. Edwards and P. W. Anderson, *J. Phys. F* **5**, 965 (1975).

27. R. Harris, M. Plischke and M. J. Zuckermann, *Phys. Rev. Lett.* **31**, 160 (1973).

28. S. P. Mathew, S. N. Kaul, *Appl. Phys. Lett.* **98**, 172505 (2011).

29. H. E. Nigh, S. Legvold and F. H. Spedding, *Phys. Rev.* **132**, 1092 (1963).

30. E. M. Chudnovsky, W. M. Saslow and R. A. Serota, *Phys. Rev. B* **33**, 251 (1986).

31. P. A. Joy, P. S. Anil Kumar and S. K. Date, *J. Phys.: Condens. Matter* **10**, 11049 (1998).

32. A. Senchuk, H. P. Kunkel, R. M. Roshko, C. Viddal, W. Li, G. Williams and X. Z. Zhou, *Eur. Phys. J. B* **37**, 285 (2004).

33. D. Michels, C. E. Krill III and R. Birringer, *J. Magn. Magn. Mater.* **250**, 203 (2002).

34. C. E. Krill III, L. Helfen, D. Michels, H. Natter, A. Fitch, O. Masson and R. Birringer, *Phys. Rev. Lett.* **86**, 842 (2001).

35. C. D. Graham, Jr., *J. Appl. Phys.* **34**, 1341 (1963).

36. J. W. Cable and E. O. Wollan, *Phys. Rev.* **165**, 733 (1968).

37. S. N. Kaul and S. Srinath, *Phys. Rev. B* **62** 1114 (2000).

Chapter 4

Ferromagnetic Resonance (FMR)

4.1 Introduction

Ferromagnetic resonance is the resonant absorption of external microwave radiation in ferromagnetic materials. When a magnetic dipole, due to the spin angular momentum of an electron, is placed in an external magnetic field of uniform strength, H, it precesses around the direction of the magnetic field. The frequency of the precession (the Larmor precession frequency) is related to H by

$$\omega_L = \gamma H \tag{4.1}$$

where $\gamma = g\mu_B/\hbar$ is the magneto-mechanical (gyromagnetic) ratio of the electron. As illustrated in figure. 4.1, resonant absorption of energy can occur when this magnetic dipole is exposed to an external electromagnetic radiation of frequency $\omega = \omega_L$, applied in a plane perpendicular to the

The following article is based on the results presented in this Chapter:
1. S. N. Kaul and S. P. Mathew, *Nanosci. Nanotech. Lett.*, (at press).

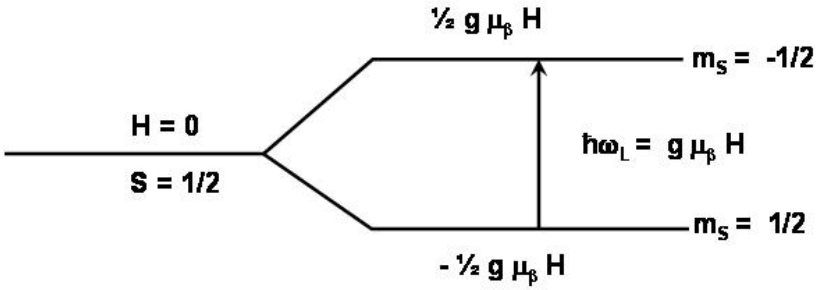

Figure 4.1: Principle of the ESR experiment.

direction of H. The resonance condition ($\omega = \omega_L$) can be written in an alternative form as

$$\hbar\omega = g\mu_B H \tag{4.2}$$

This phenomenon is the well-known electron spin resonance (ESR) which occurs in substances with unpaired electron spins and in which the magnetic moments do not interact with one another. In the case of ferromagnetic substances, the situation is quite different from that of non-interacting spins as in paramagnetics. The phenomenon of ferromagnetic resonance (FMR), first discovered by Griffiths [1], is the resonant microwave absorption in a system of strongly interacting spins. A strong short-range exchange interaction leads to a parallel alignment of spins in the ground state, which, in turn, gives rise to a large resultant magnetization or a large internal field. The spins within a ferromagnetic material thus not only experience the external magnetic field, H, but also the internal (exchange) field due to the remaining spins in the system. Consequently, the resonance condition, Eq.(7.2), needs to be modified in that the external field H has to be replaced by an effective field H_{eff}, which, besides H, takes into account the internal fields as well as the anisotropy fields present in ferromagnetic materials.

4.2 Theoretical Background

Landau and Lifshitz (LL) [2] proposed the first phenomenological equation of motion for magnetization in a ferromagnet in the presence of an external magnetic field H of the form,

$$\frac{d\vec{M}}{dt} = -\gamma\left(\vec{M}\times\vec{H}_{eff}\right) - \frac{\lambda}{M^2}\left(\vec{M}\times\vec{M}\times\vec{H}_{eff}\right) \tag{4.3}$$

The first term on the right-hand-side represents the torque experienced by the magnetization vector, $\vec{M}$, in an effective magnetic field, $H_{eff} = -\partial F/\partial\vec{M}$, where the free-energy functional F[$\vec{M}$] consists of the Zeeman energy, energy contributions from magnetic anisotropies and exchange interaction energy. The second term in Eq.(7.3) is the LL damping torque which governs the relaxation towards equilibrium and the parameter λ characterizes the relaxation rate. As this equation is not entirely correct at low frequencies, Gilbert (G) [3] suggested a modified equation of motion, i.e.,

$$\frac{d\vec{M}}{dt} = -\gamma\left(\vec{M}\times\vec{H}_{eff}\right) + \frac{\lambda}{\gamma M^2}\left(\vec{M}\times\frac{d\vec{M}}{dt}\right) \tag{4.4}$$

In the small damping limit, the Landau-Lifshitz and Gilbert damping forms are equivalent and hence the equation of motion for magnetization, Eq. (7.4), is known as the LLG equation and λ as the LLG damping parameter.

Two approaches have been adopted to determine the resonance frequency or equivalently, resonance field, from Eq.(7.4). In the first approach, coupled differential equations for the time-dependent magnetization components are solved to yield the intensity, FMR lineshape and resonance linewidth. The second approach neglects the dynamical aspects of FMR to arrive at the resonance frequency or field. Both the approaches have cer-

tain advantages and limitations, as brought out clearly below by the model calculations based on them.

4.2.1 Lineshape Calculations

Consider an ellipsoidal isotropic ferromagnetic sample which is subjected to a homogeneous external static magnetic field $\vec{H}$ directed along the z-axis and to a weak alternating magnetic field, $\vec{h}(t) = \vec{h}\ e^{i\omega t}$ ($|\vec{h}(t)| << |\vec{H}|$) acting in the xy plane. As a result of the combined action of these fields, the magnetization comprises a steady and an alternating component, i.e., $\vec{M} = \vec{M}_s + \vec{m}(t)$ with $\vec{m}(t) = \vec{m}\ e^{i\omega t}$ and $|\vec{m}(t)| << |\vec{M}_s|$. Assuming that the steady field is intense enough to saturate the ferromagnetic sample so that $\vec{M}_s$ and $\vec{H}$ point in the same direction, the Gilbert form of equation of motion for magnetization (hereafter referred to as the LLG equation) is given by Eq.(7.4) where $\vec{H}_{eff} = \vec{H} + \vec{h}(t) + \vec{H}_{dem} + \vec{H}_A$, $\vec{H}_{dem} = -D \cdot \vec{M}$ is the demagnetizing field, $\vec{H}_A$ is the magnetic anisotropy field arising from magnetocrystalline anisotropy, which in the present case, is to be taken of uniaxial type; $\vec{H}_K = -\vec{D}_K \cdot \vec{M}$ is the uniaxial anisotropy field with easy axis along $\vec{H}$; $\vec{D}$ and $\vec{D}_k$ are diagonal tensors, $\gamma = g|e|/2mc$ is the gyromagnetic ratio, M is the saturation magnetization and λ is the Gilbert damping parameter. Substitution for $\vec{M}$ and $\vec{H}_{eff}$ in Eq.(7.4) yields [4, 5]

$$\frac{d\vec{m}(t)}{dt} = -\gamma\Bigg[\vec{M}_s \times \vec{h}(t) + \vec{m}(t) \times \vec{H} - \vec{M} \times (\vec{D} \cdot \vec{M}) - \vec{M} \times (\vec{D}_k \cdot \vec{M}) + \frac{\lambda}{\gamma M^2}\left([\vec{M}_s + \vec{m}(t)] \times \frac{d}{dt}[\vec{M}_s + \vec{m}(t)]\right)\Bigg] \tag{4.5}$$

where use has been made of the relation $d\vec{M}_s/dt = 0 = -\gamma(\vec{M}_s \times \vec{H})$ and the term $-\gamma[\vec{m}(t) \times \vec{h}(t)]$ has been dropped because of its small magnitude.

Using the above-mentioned exponential form for $\vec{m}(t)$ and neglecting the second order terms, the Cartesian components of Eq.(7.5) can finally be written in the form [4, 5]

$$(i\omega/\gamma)m_x + [H + (D_y + D_{ky} - D_z - D_{kz})M_s + i\Gamma]\, m_y = M_s h_y \tag{4.6}$$

$$-[H + (D_x + D_{kx} - D_z - D_{kz})M_s + i\Gamma]\, m_x + (i\omega/\gamma)m_y = -M_s h_x \tag{4.7}$$

and

$$m_z = 0 \tag{4.8}$$

where the FMR LLG linewidth $\Gamma = \lambda\omega/\gamma^2 M_s$. Elimination of m_y from Eqs.(7.6) and (7.7) gives

$$m_x = \chi_{xx} h_x + \chi_{xy} h_y \tag{4.9}$$

with

$$\chi_{xx} = \big[H + (D_y + D_{ky} - D_z - D_{kz})M_s + i\Gamma\big] M_s \eta^{-1} \tag{4.10}$$

$$\chi_{xy} = (i\omega/\gamma) M_s \eta^{-1} \tag{4.11}$$

and

$$\begin{aligned}\eta = &[H + (D_x + D_{kx} - D_z - D_{kz})M_s]\,[H + (D_y + D_{ky} - D_z - D_{kz})M_s] \\ &- \Gamma^2 - (\omega/\gamma)^2 + i\Gamma\,[2H + (D_x + D_y + D_{kx} + D_{ky} - 2D_z - 2D_{kz})M_s]\end{aligned} \tag{4.12}$$

Elimination of m_x instead of m_y from Eqs.(7.6) and (7.7) would have resulted in

$$m_y = \chi_{yx} h_x + \chi_{yy} h_y \tag{4.13}$$

where $\chi_{xx} = \chi_{yy} = \chi$ is the dynamic susceptibility and $\chi_{xy} = -\chi_{yx} = iG$, $\vec{G}$ is the gyration vector. Recalling that both the dynamic susceptibility and

dynamic permeability μ are complex, i.e., $\chi = \chi' - i\chi''$ and $\mu = \mu' - i\mu''$, and using the relation $\mu = 1 + 4\pi\chi$, the real and imaginary parts of the (complex) dynamic permeability are given by [4, 5]

$$\mu' = \frac{\begin{array}{c}\alpha\{[H + (D_y + D_{ky} - D_z - D_{kz})M_x][B + (D_x + D_{kx} - D_z - D_{kz})] - \Gamma^2 \\ -(\omega/\gamma)^2\} + \beta\Gamma[(B + H) + (D_x + D_y + D_{kx} + D_{ky} - 2D_z - 2D_{kz})M_s]\end{array}}{(\alpha^2 + \beta^2)} \tag{4.14}$$

$$\mu'' = \frac{\begin{array}{c}\{-\alpha\Gamma[(B + H_k) - (H + H_k)] + \beta[(B + H_k) - (H + H_k)] \\ \times [H + (D_y + D_{ky} - D_z - D_{kz})M_s]\}\end{array}}{(\alpha^2 + \beta^2)} \tag{4.15}$$

with

$$\alpha = [H + (D_x + D_{kx} - D_z - D_{kz})M_s][H + (D_y + D_{ky} - D_z - D_{kz})M_s] - \Gamma^2 - (\omega/\gamma)^2 \tag{4.16}$$

$$\beta = \Gamma[2H + (D_x + D_y + D_{kx} + D_{ky} - 2D_z - 2D_{kz})M_s] \tag{4.17}$$

and

$$B = H + 4\pi M_s \tag{4.18}$$

For a flat circular disc (the sample shape used in the present experiments), with H applied along the symmetry axis (z axis) so far as the uniaxial anisotropy is concerned and lying in the sample plane (parallel geometry or configuration), $D_x = D_z = 0$, $D_y = 4\pi$ (x-axis is taken to coincide with the polar axis), $D_{kx}M_s = D_{ky}M_s = H_k$ and $D_{kz} = 0$. Substituting these values of components of $\vec{D}$ and $\vec{D}_k$, Eqs.(7.14)-(7.17) are simplified to yield [4, 5]

$$\mu' = \frac{\begin{array}{c}[(H + H_k)(B + H_k) - \Gamma^2 - (\omega/\gamma)^2][(B + H_k)^2 - \Gamma^2 - (\omega/\gamma)^2] \\ +2\Gamma^2(B + H_k)(B + H + 2H_k)\end{array}}{[(H + H_k)(B + H_k) - \Gamma^2 - (\omega/\gamma)^2]^2 + \Gamma^2(B + H + 2H_k)^2} \tag{4.19}$$

and

$$\mu'' = \frac{\begin{array}{c}-2\Gamma(B+H_k)[(H+H_k)(B+H_k)-\Gamma^2-(\omega/\gamma)^2] \\ +\Gamma(B+H+2H_k)[(B+H_k)^2-\Gamma^2-(\omega/\gamma)^2]\end{array}}{[(H+H_k)(B+H_k)-\Gamma^2-(\omega/\gamma)^2]^2+\Gamma^2(B+H+2H_k)^2} \tag{4.20}$$

The power absorbed by the sample, which is proportional to the surface impedance, in the parallel geometry, is given by

$$P_{\|} \propto [(\mu'^2+\mu''^2)^{1/2}+\mu'']^{1/2} \tag{4.21}$$

The theoretical variation of the Power absorption derivative, $dP_{\|}/dH$, can, therefore, be computed by combining equations (6.19)-(6.21) and taking the field derivative of the resulting expression. From Eqs.(7.6) and (7.7), the resonance frequency $\omega = \omega_{res}$ is calculated by the condition that m_x and m_y have non-trivial solutions only when $h_x = h_y = 0$. In other words, this implies that

$$\begin{vmatrix} i\omega_{res}/\gamma & \left\{-[H_{res}+(D_y+D_{ky} \right. \\ & \left. -D_z-D_{kz})M_s+i\Gamma]\right\} \\ \left\{-[H_{res}+(D_x+D_{kx} \right. & \\ \left. -D_z-D_{kz})M_s+i\Gamma]\right\} & i\omega_{res}/\gamma \end{vmatrix} = 0 \tag{4.22}$$

where H_{res} is the (steady) resonance field corresponding to ω_{res}. After a few simplifying steps, the following relation is arrived at [4, 5]

$$[(\omega/\gamma)^2+\Gamma^2] = [H_{res}+(D_y+D_{ky}-D_z-D_{kz})M_s][H_{res}+(D_x+D_{kx}-D_z-D_{kz})M_s] \tag{4.23}$$

The subscript for ω_{res} is dropped because in experiments the microwave-field frequency, ω, is kept constant while the steady field, H, is swept through the resonance.

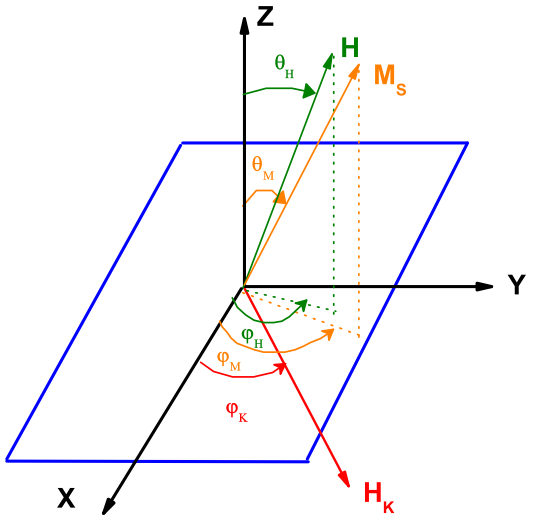

Figure 4.2: Coordinate system showing various angles used in the computation of angular variation of resonance field for the 'in-plane' (IP) and 'out-of-plane' (OP) cases.

4.2.2 Angular Variation: Resonance Field

With the choice of the coordinate system as shown in figure 4.2, different contributions to the free-energy density, F, for a film with cubic magnetocrystalline anisotropy and an in-plane uniaxial anisotropy are given as follows. The direction cosines of magnetization vector, $\vec{M}$, with reference to x, y, z axes are $\alpha_1 = \sin\theta_M \cos\phi_M$; $\alpha_2 = \sin\theta_M \sin\phi_M$ and $\alpha_3 = \cos\theta_M$ so that the contribution of cubic magnetocrystalline anisotropy (MCA) to F is

$$\begin{aligned} F_{K_C} &= K_1(\alpha_1^2\alpha_2^2 + \alpha_2^2\alpha_3^2 + \alpha_3^2\alpha_1^2) + K_2\alpha_1^2\alpha_2^2\alpha_3^2 \\ &= \sin^2\theta_M[K_1\cos^2\theta_M + (K_1 + K_2\cos^2\theta_M)\sin^2\theta_M \sin^2\phi_M \cos^2\phi_M] \end{aligned}$$

The easy axis for the uniaxial anisotropy lies along a direction ($\vec{H}_K$) which makes an angle ϕ_K with x-axis (Fig. 4.2) with the result that the contribution to F due to uniaxial anisotropy is given by $F_{K_u} = K_u \sin^2\theta'$; where θ' is the angle between M and H_k. Recognizing that $\theta' = \cos^{-1}[\sin\theta_M \cos(\phi_M - \phi_K)]$,

$$F_{K_u} = K_u(1 - \cos^2\theta') = K_u[1 - \sin^2\theta_M \cos^2(\phi_M - \phi_K)]$$

Including the Zeeman, F_Z, and shape anisotropy, F_S, contributions, the total free-energy density becomes

$$\begin{aligned} F &= F_Z + F_S + F_{K_c} + F_{K_u} \\ &= -MH(\sin\theta_M \sin\theta_H \cos(\phi_M - \phi_H) + \cos\theta_M \cos\theta_H) + 2\pi M^2 \cos^2\theta_M \\ &\quad + K_1 \sin^2\theta_M(\cos^2\theta_M + \sin^2\theta_M \sin^2\phi_M \cos^2\phi_M) \\ &\quad + K_2 \cos^2\theta_M \sin^4\theta_M \sin^2\phi_M \cos^2\phi_M + K_u[1 - \sin^2\theta_M \cos^2(\phi_M - \phi_K)] \end{aligned} \tag{4.24}$$

The equilibrium conditions for magnetization are $\partial F/\partial\theta_M = 0$ and $\partial F/\partial\phi_M = 0$ and the resonance condition is [6]

$$\left(\frac{\omega}{\gamma}\right)^2 = \frac{1}{M^2 \sin^2\theta_M}\left[\left(\frac{\partial^2 F}{\partial\theta_M^2} \cdot \frac{\partial^2 F}{\partial\phi_M^2}\right)^2 - \left(\frac{\partial^2 F}{\partial\theta_M \partial\phi_M}\right)\right] \tag{4.25}$$

The first equilibrium condition for magnetization, $\partial\mathrm{F}/\partial\theta_M = 0$, yields the result

$$\begin{aligned} H_r(\sin\theta_M \cos\theta_H - \cos\theta_M \sin\theta_H \cos(\phi_M - \phi_H)) &= 2\pi M \sin 2\theta_M \\ &- \frac{K_1}{2M}[\sin 4\theta_M + 4\sin^2\theta_M \sin 2\theta_M \sin^2\phi_M \cos^2\phi_M] \\ &+ \frac{K_2}{4M}[\frac{1}{2}\sin 2\theta_M(\cos 4\theta_M - 4\cos 2\theta_M + 3) \\ &- (3\sin\theta_M - \sin 3\theta_M)(3\cos\theta_M + \cos 3\theta_M)]\sin^2\phi_M \cos^2\phi_M \\ &+ \frac{H_K}{2}\sin 2\theta_M \cos^2(\phi_M - \phi_K) \end{aligned} \tag{4.26}$$

the second equilibrium condition for magnetization, $\partial F/\partial\phi_M = 0$, gives,

$$H_r \sin\theta_H \sin(\phi_H - \phi_M) = \frac{1}{2M}\sin^3\theta_M \sin 4\phi_M (K_1 + K_2\cos^2\theta_M) + \frac{H_K}{2}\sin\theta_M \sin 2(\phi_M - \phi_K) \tag{4.27}$$

where $H_K = 2K/M$, $H_{K_1} = 2K_1/M$ and $H_{K_2} = 2K_2/M$.

'In-plane' case

In the 'in-plane' case, both M_s and H are confined to the sample plane (xy-plane), i.e., $\theta_M = \theta_H = \frac{\pi}{2}$, and the angles ϕ_M, ϕ_H and ϕ_K are measured with respect to the x-axis in the sample plane, i.e., $\phi_M = \phi$, $\phi_H = \psi$ and $\phi_K = \xi$. The resonance and equilibrium conditions in this case are obtained from Eqs.(6.25) and (6.29) as

Resonance condition

$$\left(\frac{\omega}{\gamma}\right)^2 = \left[H_r^{\parallel}\cos(\psi-\phi) + (4\pi M + H_{K_u}\cos^2(\phi-\xi)) + \frac{H_{K_1}}{4}(3+\cos 4\phi) + \frac{H_{K_2}}{8}(1-\cos 4\phi)\right] \times \left[H_r^{\parallel}\cos(\psi-\phi) + H_{K_u}\cos 2(\phi-\xi) + H_{K_1}\cos 4\phi\right] \tag{4.28}$$

Equilibrium condition for magnetization

$$H_r^{\parallel} = \left[H_{K_1}(2\cos^2\phi - 1) + H_{K_u}\right]\left[\frac{\sin\psi}{\sin\phi} - \frac{\cos\psi}{\cos\phi}\right]^{-1} \tag{4.29}$$

'Out-of-plane' case

In the 'out-of-plane' case, H, M and H_K are confined to the xz-plane so that $\phi_H = \phi_M = \phi_K = 0$ and the angles θ_H and θ_M are measured with respect to the z-axis (normal to the sample plane). The resonance and equilibrium conditions in this case are derived from Eqs. (6.25) and (6.26).

Resonance condition

$$\left(\frac{\omega}{\gamma}\right)^2 = \Bigg\{\Bigg[H_r^{\perp}\cos(\alpha-\theta) - (4\pi M + H_{K_u})\cos 2\theta + H_{K_1}\cos 4\theta$$
$$\times\Bigg[H_r^{\perp}\cos(\alpha-\theta) - 4\pi M\cos^2\theta + H_{K_u}\sin^2\theta$$
$$+ H_{K_1}(\sin^2\theta + \cos^2\theta\cos 2\theta) + H_{K_2}\sin^2\theta\cos^2\theta\Bigg] \tag{4.30}$$

where $\theta_H = \alpha$ and $\theta_M = \theta$.

Equilibrium condition for magnetization

$$H_r^{\perp} = [4\pi M + H_{K_u} - H_{K_1}\cos 2\theta]\left[\frac{\cos\alpha}{\cos\theta} - \frac{\sin\alpha}{\sin\theta}\right]^{-1} \tag{4.31}$$

4.2.3 Linewidth

The 'peak-to-peak' ferromagnetic resonance linewidth, ΔH_{pp}, is a measure of the rate at which magnetization relaxes back to equilibrium once the static magnetic field is switched off. The measured FMR linewidth, ΔH_{pp}, is caused by two mechanisms: the intrinsic damping of magnetization, and the magnetic inhomogeneity of the ferromagnetic sample, and is given by

$$\Delta H_{pp} = \Delta H_{inhom} + 1.16\frac{\lambda}{\gamma^2 M(T,H)}\,\omega \tag{4.32}$$

ΔH_{inhom} describes the frequency-independent (inhomogeneous) FMR line-broadening that originates either from two-magnon or multi-magnon scattering from spatially localized magnetic inhomogeneities [7] such as (a) the variation in the crystallographic directions from one nanocrystal to the other, (b) randomly distributed defects, which is a predominant effect in nanocrystalline materials, (c) the distribution in the internal fields, etc. or

from a distribution in the demagnetizing fields [8] or from the exchange-conductivity mechanism [9, 10, 11, 12]. $\Delta \mathrm{H}_{inhom}$ is particularly large when the uniform mode resonance (k = 0) couples to the spin waves with k $\neq$ 0 [13]. Magnetic inhomogeneity is reflected in FMR spectra as a distribution of local resonance fields.

The frequency-dependent intrinsic damping, described by the second term on the right-hand side of the Eq.(7.4) (Gilbert damping term, ΔH_{LLG}), reflects the viscous damping of the magnetization motion (and low-energy spin waves) excited in the FMR process. ΔH_{LLG}, resulting from the LLG relaxation mechanism [4, 5, 9, 14, 15], is a measure of microscopic mechanism by means of which the absorbed microwave energy is dissipated from the spin system to the lattice resulting in the generation of phonons. λ depends on temperature [16], the wavevector $\overrightarrow{K}$, and may exhibit anisotropy [15, 17].

Angular Dependence

The LLG contribution to $\Delta \mathrm{H}_{pp}$ depends on the polar, θ, and azimuthal, ϕ, angles of magnetization [18], and can be calculated from the expression

$$\Delta H_{hom}(\theta,\phi) = \frac{2}{\sqrt{3}} \frac{1}{|\frac{\partial \omega}{\partial H_{res}}|} \frac{\lambda}{M^2} \left(\frac{\partial^2 F}{\partial \theta^2} + \frac{1}{sin^2\theta} \frac{\partial^2 F}{\partial \phi^2} \right) \qquad (4.33)$$

$\Delta \mathrm{H}_{hom}$ goes through a minimum at the principal magnetic directions and it has a maximum where the magnetization direction varies strongly. The magnetization precessing around easy axis is more viscously damped, since it has to move into an unfavorable hard direction. For the magnetic field along the hard axis, $\overrightarrow{M}$ precesses towards the easy direction and is less damped. The viscous damping mechanism has its microscopic origin in the

spin-orbit interaction, which couples the spin to the lattice. The analysis of the angular dependence of ΔH_{pp} is complicated by the fact that an unambiguous separation of the various contributions to ΔH_{pp} is not possible. For this reason, we have not made any attempt to quantify the angular variations of ΔH_{pp} observed in the IP and OP sample configurations.

Exchange Conductivity Contribution

In ferromagnetic materials, apart from the damping term, there is also a contribution to the line-broadening due to the exchange-conductivity mechanism. It is well-known that in highly conducting metallic specimens, microwave field penetrates only a thin surface layer of the sample of thickness $50nm$ and as a result, the dynamic magnetization (exchange-coupled set of spins) becomes inhomogeneous. The spatial variations in magnetization exert a torque on $\vec{M}$ which is expressed as $(2A\gamma/M^2)(\vec{M} \times \nabla^2 \vec{M})$, where A is a phenomenological exchange stiffness parameter. Thus, this exchange-conductivity term should be included in the equation of motion of the magnetization, Eq.(7.4), and then the resulting equation solved in conjunction with the Maxwell's equations to obtain a correct solution for the observed lineshape. The exchange term leads to a shift in the resonance field and also contributes to the broadening of the resonance line. This term would become unimportant if the conductivity is low or if the exchange stiffness is small. The conductivities of nanocrystalline metals are typically one order of magnitude lower than those of single crystals and the average grain size ($\sim 12 - 18\ nm$ in the present case) is much smaller compared to the skin depth. Moreover, the exchange-conductivity effect is seen only at low fields. Thus a total neglect of the exchange-conductivity term in the equation of

motion for magnetization is fully justified in the case of nanocrysatlline metals provided $\overrightarrow{M}$ and $\overrightarrow{H}_{int}$ are replaced by their average values, i.e., $\langle\overrightarrow{M}\rangle$ and $\langle\overrightarrow{H}_{int}\rangle$.

4.3 Microwave Power Absorption Derivative (PAD) Curves and FMR Lineshape Analysis

Microwave power absorption derivative, dP/dH, versus static magnetic field, H, (PAD) curves were recorded on nc-Gd at a fixed microwave field frequency of 9.23 GHz in the parallel ($\|$) sample configuration (in which the static magnetic field is applied in the sample plane) over the temperature ranges 113 $K \leq T \leq$ 223 K and 298 $K \leq T \leq$ 323 K at 2K steps, 223 $K \leq T \leq$ 278 K at 1 K intervals, 275 $K \leq T \leq$ 295 K at 0.5 K intervals (Fig. 4.3), and in the critical region (285.5 ± 1 K) at 0.1 K intervals (Fig. 4.7). The (dP/dH)-H (PAD) curves, at a few selected temperatures in the temperature range 113 $K \leq T \leq$ 323 K, were also recorded as a function of the angle ψ between the static magnetic field vector, $\overrightarrow{H}$, and the easy direction of magnetization within the sample plane in the 'in-plane' (IP) sample configuration, and as a function of the angle α that $\overrightarrow{H}$ makes with the normal to the sample plane in the 'out-of-plane' (OP) sample configuration. From the elaborate FMR lineshape analysis (whose details are given elsewhere [4, 5, 19]), the physical quantities deduced from the dP/dH vs. H curves are the resonance field, H_{res} (defined as the field where the $dP/dH = 0$ line cuts the dP/dH versus H curve or alternatively as the field where dP/dH possesses half the peak-to-peak value if the dP/dH vs. H

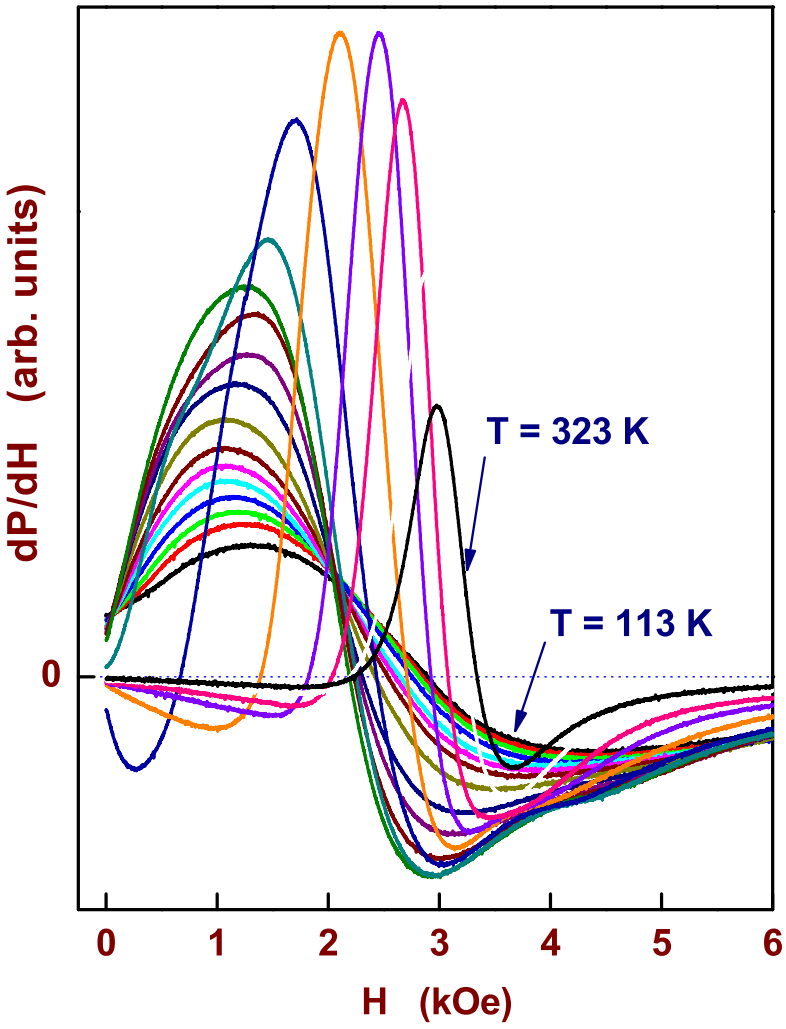

Figure 4.3: The temperature evolution of the microwave power absorption derivative curves in the range 113 $K \leq T \leq 323$ K for the sample n-Gd using the $\|^h$ sample geometry. PAD curves at all temperatures are not displayed for better clarity.

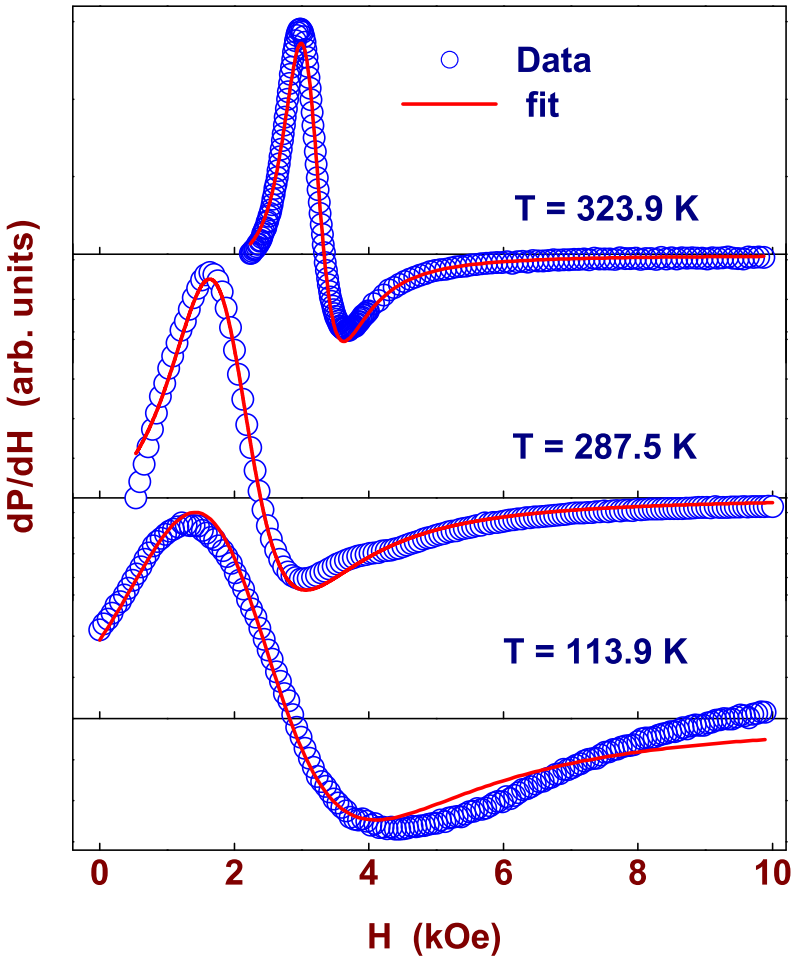

Figure 4.4: Field dependence of the microwave power absorption derivative curves at a few representative temperatures (open symbols) along with the optimum lineshape fits to the data (continuous curve) based on Eqs.(6.19)-(6.21).

curves are symmetrical about the baseline), and the peak-to-peak linewidth, ΔH_{pp} (defined as the field difference between the extrema of the dP/dH versus H curve). It has been observed that the peak-to-peak linewidth, ΔH_{pp}, forms an appreciable fraction of the resonance field, H_{res}, for the nanocrystalline material under study, and hence, the observed value of H_{res} can differ significantly form the actual ("true") resonance center. For this reason, a complete lineshape calculation for each resonance line has been carried out separately. Such a calculation consists of fitting the theoretical expression, Eq.(6.21), with the aid of Eqs.(6.19) and (6.20), by making use of a non-linear least-squares fit computer program which treats the saturation magnetization, M(T), the 'peak-to-peak' linewidth, $\Delta H_{PP} = 1.45\Gamma$, and the 'in-plane' uniaxial anisotropy field, H_K, as free fitting parameters while keeping the Landé splitting factor, g, fixed at the spin-only value 2.00 [20]. Figure 4.4 serves to demonstrate the quality of FMR lineshape fits (continuous curves) to the data (open circles) taken at the end temperatures of the temperature range covered in the present FMR experiments and at $T \approx T_C$, yielded by the lineshape analysis method.

4.3.1 Resonance Field: Temperature Dependence

Figure 4.5 displays the temperature variations of the observed resonance field, $H_{res}(T)$. In a conventional ferromagnet, H_{res} increases slowly with temperature for $T < T_C$ but the rate of increase picks up sharply for $T \geq T_C$. Contrary to this behavior, H_{res} decreases with temperature till the temperature $T^* \cong 280\ K$, near $T_C = 285.5(1)\ K$, is reached. $H_{res}(T)$, however, show a normal behavior only when T exceeds T^*, where $H_{res}(T)$ goes through a steep minimum.

4.3.2 FMR Linewidth: Temperature Dependence

Figure 4.5 displays the temperature variations of the 'peak-to- peak' FMR linewidth, $\Delta H_{PP}(T)$, obtained from the lineshape analysis. In a conventional ferromagnet, ΔH_{PP} is typically of the order of few hundreds of Oe at low temperatures and goes through a sharp cusp at $T \cong T_C$. Contrasted with this behavior, $\Delta H_{PP}(T)$ is abnormally large ($\cong 3.3\ kOe$) at temperatures in the range $113\ K \leq T \leq 185\ K$ and decreases with temperature in approach to $T^* \cong 280\ K$. $\Delta H_{PP}(T)$, however, shows a normal behavior only when T exceeds T^*, where $\Delta H_{PP}(T)$ "peaks".

4.3.3 'In-plane' Uniaxial Anisotropy Field: Temperature Dependence

Inset of Figure 4.5 displays the temperature variation of the 'in-plane' anisotropy field, $H_K(T)$, obtained from the lineshape analysis. $H_K(T)$ exhibits a broad peak at the spin-reorientation temperature [21], (where K_{u_1} changes sign and K_{u_2} is vanishingly small; K_{u_1} and K_{u_2} are the temperature-dependent uniaxial magnetocrystalline anisotropy constants) and falls rapidly in magnitude as the $T_C = 285.5(1)\ K$ is approached. This behavior of H_K is in sharp contrast with that ($H_K = 0$ at $T = T_{SR}$ and peak at $T = T_C$) observed [21] in single crystal Gd when the magnetic field is applied in a direction other than the c-axis (the easy direction of magnetization).

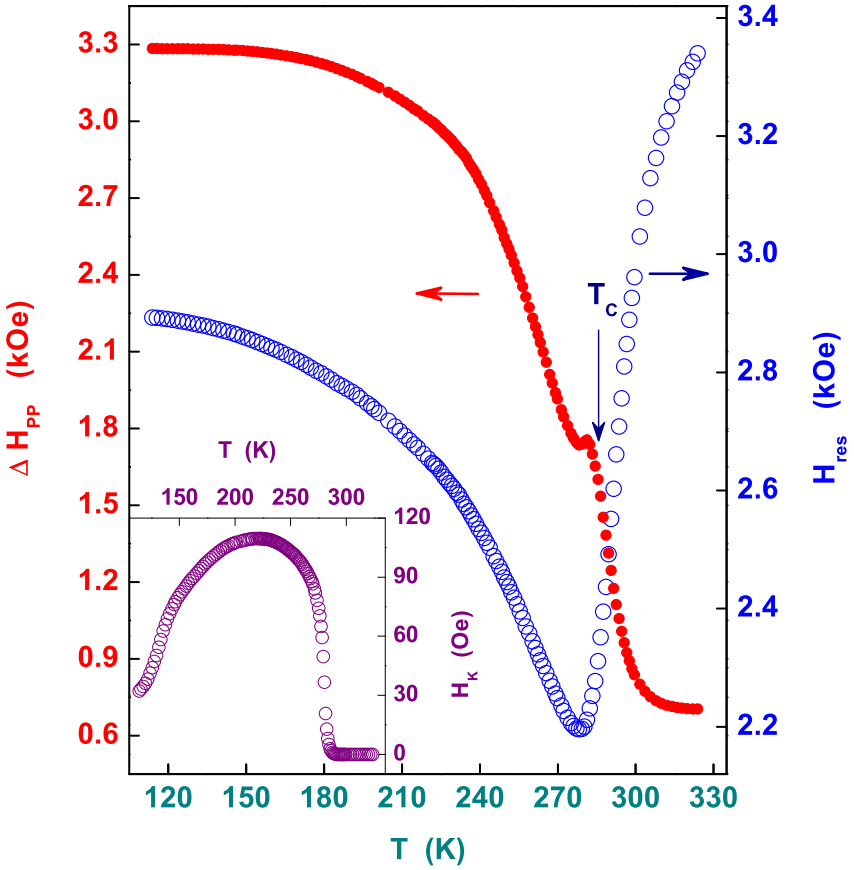

Figure 4.5: The 'peak-to-peak' FMR linewidth, ΔH_{PP}, and the 'in-plane' anisotropy field, H_K (inset), obtained from the lineshape analysis of PAD curves, and the observed resonance field, H_{res}, as a function of temperature.

4.3.4 Magnetization: Temperature Dependence

Figure 4.6 compares the functional dependence of magnetization on temperature, M(T) (open circles), yielded by the lineshape analysis, with that of the bulk magnetization measured [22] at $H = 500\ Oe$ in the 'Zero-Field-Cooled' (ZFC) and 'Field-Cooled' (FC) modes (continuous curves) on the same sample. The inset of Fig.4.6 depicts the temperature variation of the FC magnetization measured [22] at $H = 2.2\ kOe$. The temperature dependence of the saturation magnetization, deduced from the FMR data, is anomalous in that $M(T)$ exhibits a broad minimum at $\cong 142\ K$ followed by a peak at $280.2\ K$ as opposed to a progressive decline in magnetization with increasing temperature followed by a steep fall for $T > T_C$ in a conventional ferromagnet (similar to the functional form of $M(T)$ shown in the inset of Fig.4.6). Another striking aspect of $M(T)$ is that the magnetization has a much lower magnitude at all temperatures compared to that expected for a normal ferromagnet in which M at fixed T gets saturated at fields comparable in strength to H_{res} at that temperature. To elucidate this point further, H_{res}, the ordering field H conjugate to M, has an average value of $2.5\ kOe$ within the range $113\ K \leq T \leq T_C$. A field of this intensity should be able to generate magnetization values at different temperatures similar to, if not higher than, those directly measured [22] on the same sample at $H = 2.2\ kOe$ (inset of Fig.4.6). On the contrary, $M(T)$ is substantially reduced (by a factor ranging from 4.5 at $113\ K$ to 1.5 at $T_C = 285.5\ K$) in magnitude compared to $M(T, H = 2.2\ kOe)$. Instead $M(T)$ has essentially the same functional dependence and magnitude as the ZFC magnetization measured [22] at a much lower field of strength $H = 500\ Oe$. By comparison, the FC magnetization measured at the same field value $H = 500\ Oe$ is

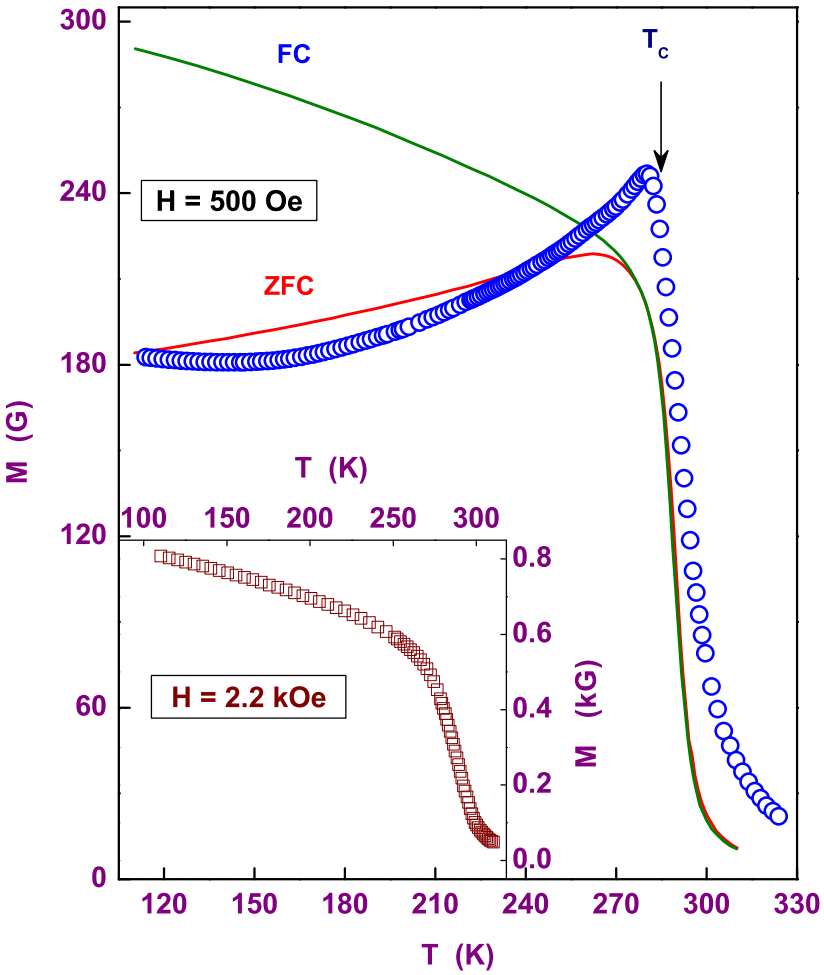

Figure 4.6: Comparison between the saturation magnetization, M(T) (open circles), obtained from lineshape analysis of PAD curves, and the bulk magnetization measured at $H = 500Oe$ in the 'zero-field-cooled' (ZFC) and 'field-cooled' (FC) modes (continuous curves). The inset shows the FC magnetization measured at $H = 2.2kOe$ as a function of temperature.

much higher (Fig.4.6) particularly at $T << T_C$.

The above anomalous features of $\Delta H_{PP}(T)$, $H_K(T)$ and $M(T)$ can be understood as follows. To start with, let us recall that implicit in the line-shape calculations are the conditions: (a) the applied static fields are strong enough to overcome the shape and magnetocrystalline anisotropy fields so that the magnetization is saturated and the entire sample is a single domain, and (b) the magnetization vector, M, lies along the direction of the static field, H, and its magnitude does not change when the static field is swept through resonance. None of these conditions is satisfied in the present case because the crystallographic axes vary randomly from one nano-grain to the other and so also the intra-grain easy direction of magnetization. Consequently, we are dealing with a multi-domain sample in which the domain magnetizations are oriented at random and extremely intense fields are needed to overcome the random intra-grain anisotropy and the interfacial random anisotropy fields. The unusual temperature dependence of H_K thus reflects a strong interplay between these two types of anisotropies with the interfacial random anisotropy proving more decisive in deciding the functional form of $H_K(T)$. In a multi-domain sample (when the fields of the order of resonance field do not suffice to produce saturation), the observed resonance is a convolution of the closely-spaced resonances due to the different nano-grain domains (each intra-grain domain gives rise to a resonance) and hence is invariably much broader than a single-domain resonance. As the sample temperature is raised, the anisotropies progressively weaken and the applied static field, H, is more effective in orienting the domain magnetizations with the result that the observed resonance becomes sharper and sharper, as is evident from Fig.4.5. The dominance of the interfacial

random anisotropy over the random intra-grain anisotropy for temperatures below T_C and the temperature-dependent competition with H explains the strongly suppressed values of $M(T)$ as well. Moreover, in the present FMR experiments, the sweeping rate of H is rapid compared to the spin-spin and spin-lattice relaxation times but slow enough to maintain the steady state (or more precisely, the adiabatic rapid passage) condition temporarily so that the angle that M makes with H is preserved through resonance (even though the magnitude of M is not). It is, therefore, not surprising that the functional form of $M(T)$ resembles that of the ZFC magnetization (Fig.4.6), which is the magnetization developed in the metastable state.

4.3.5 Critical Behaviour

FMR Linewidth

The temperature variation of the 'peak-to-peak' FMR linewidth, $\Delta \mathrm{H}_{pp}(T)$, in the critical region goes through a sharp cusp, which is embedded in the large inhomogeneous and LLG contributions, at the Curie temperature, T_C (Fig. 4.5). This cusp is a manifestation of the critical fluctuations of the order parameter (spontaneous magnetization) that actually drive the FM-PM phase transition. A cusp in $\Delta \mathrm{H}_{pp}(\mathrm{T})$ at $\mathrm{T} = \mathrm{T}_C$ is a feature common to ferromagnets in the bulk [9, 23] and ultrathin [14, 24, 15] forms. Frequency-dependent FMR studies on a large number of ferromagnetic systems in the crystalline or amorphous states [9, 7, 25, 26] have revealed that ΔH_{pp} consists of a frequency-independent part, ΔH_1, and Landau-Lifshitz-Gilbert (LLG) part, $\Delta H_{LLG} = 1.16\ (\lambda\omega/\gamma^2 M)$, which has a linear dependence on the microwave frequency $\omega = 2\ \pi\ \nu$. An empirical relation between ΔH_{pp}

and M^{-1} of the form

$$\Delta H_{pp}(T) = \Delta H(0) + [A/M(H,T)] \tag{4.34}$$

holds in a narrow temperature range in the critical region. The terms $\Delta H(0)$ and $[A/M(H,T)]$ in Eq.(5.34) can be identified with ΔH_{inhom} and ΔH_{LLG}, respectively, in Eq (5.32). The LLG contribution to the linewidth, ΔH_{LLG}, increases with decreasing magnetization. However, the $\Delta H(0)$ decreases with temperature as the above said contribution vanishes with decreasing magnetization, gives rise to a peak at the FM-to-PM transition temperature, T_C.

Scaling of Magnetization

The critical behaviour of magnetization is characterized by magnetization obeying the scaling equation of state (SES) of the form [27]

$$M/|\epsilon|^{\beta} = f_{\pm}(H/|\epsilon|^{\beta+\gamma}) = f_{\pm}(h) \tag{4.35}$$

where $f_{+}(h)$ and $f_{-}(h)$ are the scaling functions for temperatures above and below T_C, respectively. With the choice $T_C = 285.5(1)\ K$, $\beta = 0.5$ and $\gamma = 1.0$, the above scaling equation of state forms a correct description of the $M(T, H_{res})$ data in the critical region as is demonstrated by the double logarithmic plot shown in figure 4.8. Thus, the scaling equation of state analysis of the magnetization data in the critical region yields the ferromagnetic-to-paramagnetic transition temperature, T_C, as 285.5(1) K and the critical exponents β and γ for the spontaneous magnetization and initial susceptibility as the mean-field values $\beta = 0.5$ and $\gamma = 1.0$ (Fig. 4.8). The corresponding values for T_C, β and γ reported in the literature

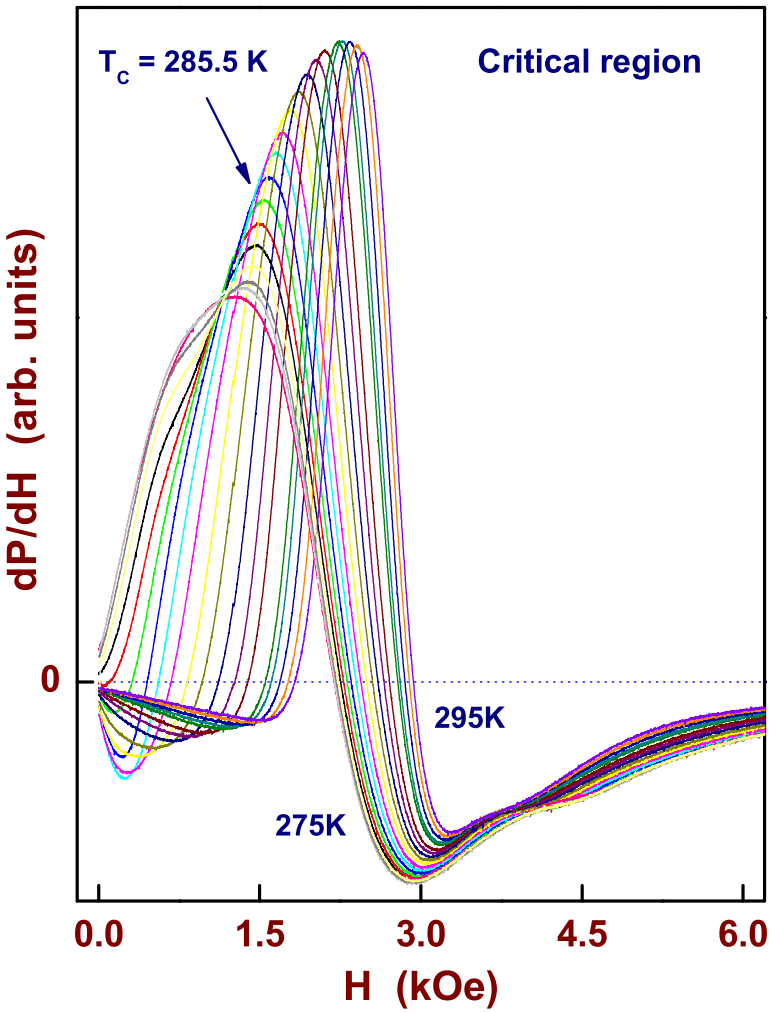

Figure 4.7: The temperature evolution of the microwave power absorption derivative curves in the critical region for the sample n-Gd using the $\|^h$ sample geometry.

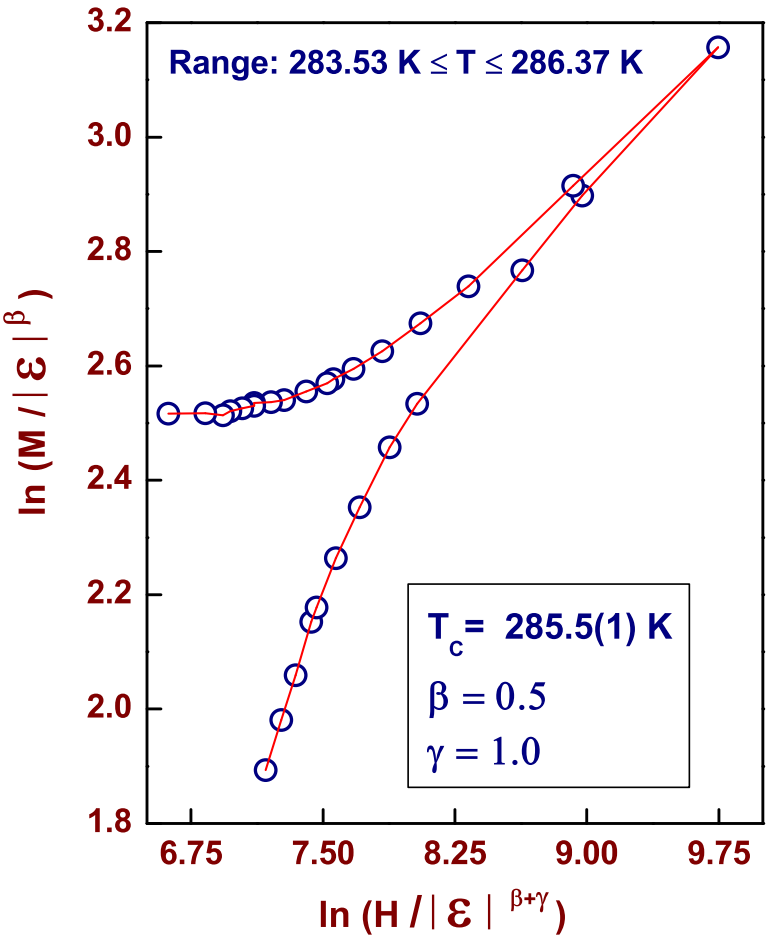

Figure 4.8: Scaling of reduced magnetization, $M/|\epsilon|^{\beta}$, with reduced field, $H/|\epsilon|^{(\beta+\gamma)}$, the $M(T, H_{res})$ data collapse for $T < T_C$ and $T > T_C$ on to two universal curves for the specified choice of β, γ and T_C. Here $\varepsilon|T - T_C|/T_C$.

[28, 29] for single crystal Gd are $T_C = 292.77(1)\ K$, $\beta = 0.5002(6)$ and $\gamma = 1.0008(5)$. This comparison shows that the critical behavior of magnetization is not affected by nanocrystallization.

4.4 Angular Dependence of FMR Spectra: 'In-plane' and 'Out-of-plane' Sample Configurations

4.4.1 Angular Variation of the Resonance Field

The PAD curves were recorded at various fixed temperatures from 134 K to 294 K as a function of the angle ψ between the static magnetic field, $\overrightarrow{H}$, and the easy-direction within the sample plane in the 'in-plane' (IP) configuration, and as a function of the angle α that $\overrightarrow{H}$ makes with the normal to the sample plane in the 'out-of-plane' (OP) configuration. The angular variations of the PAD curves with the angles ψ and α in the IP and OP samples configurations displayed in the figures 4.9 and 4.10, are characteristic of the nanocrystalline systems. The functional dependences of the resonance field, H_{res}, and the 'peak-to-peak' linewidth, ΔH_{pp}, on the angles ψ and α for the two sample geometries, deduced from the observed dP/dH versus H curves (Figs. 4.9 and 4.10), are depicted in figures 4.11, 4.12 for H_{res} and 4.13(a and b) for ΔH_{pp}. Figures 4.11 and 4.12 present the following features. In the IP case, H_{res} as a function of the angle ψ goes through two maxima at $\psi \simeq 45^o$ and 135^o and three minima at $\psi = 0^o$, 90^o and 180^o; H_{res} has the same value (within the uncertainty limits) at $\psi = 0^o$ and 180^o but has a higher value at $\psi = 90^o$ than at $\psi = 0^o$ or 180^o. Such

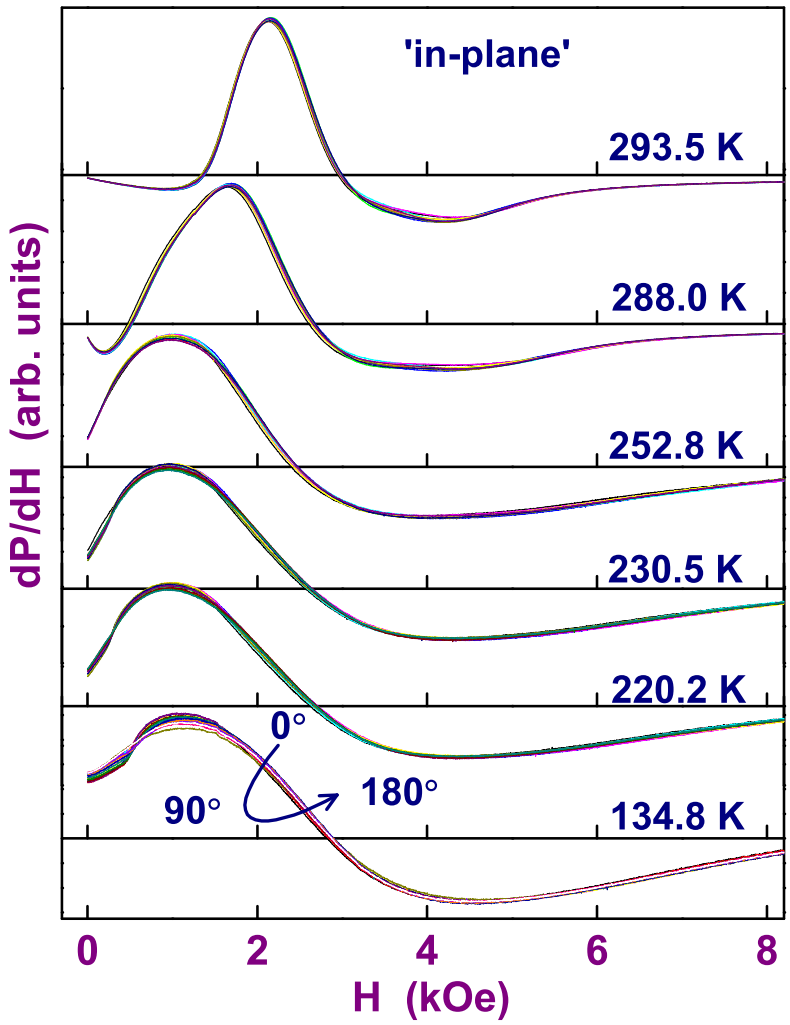

Figure 4.9: The 'in-plane' angular variation of the PAD curves taken at the specified temperatures.

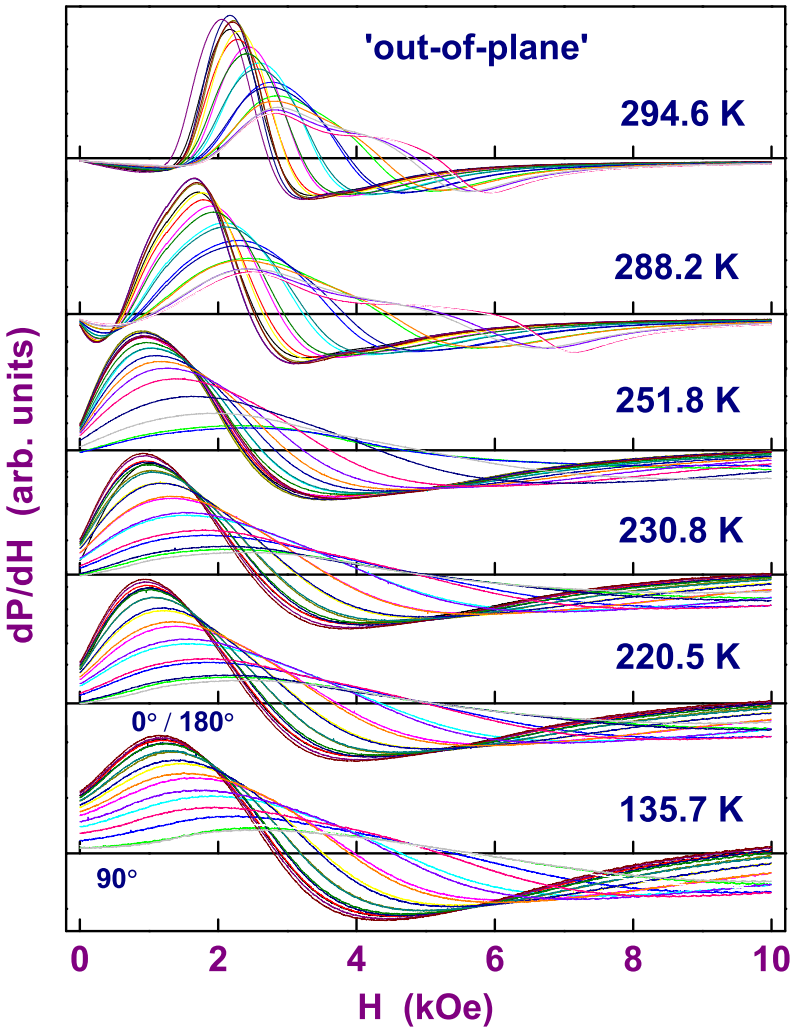

Figure 4.10: The 'out-of-plane' angular variation of the PAD curves at specified temperatures.

a functional form of $H_{res}(\psi)$ is symptomatic of the simultaneous presence of cubic (two maxima at $\psi \simeq 45^o$ and 135^o with three equal minima at $\psi = 0^o$, 90^o and 180^o and uniaxial (a peak at $\psi = 90^o$ with two equal minima at $\psi = 0^o$ and 180^o) magnetic anisotropies. By contrast, in the OP case, H_{res} has nearly the same values for the angles $\alpha = -90^o$ and $+90^o$ and H_{res} reaches values higher than the upper limit of $H = 11\ kOe$ in the present FMR setup as $\alpha = 0^o$ is approached either from below or from above. This angular dependence of H_{res} on α is also consistent with the simultaneous presence of cubic, uniaxial and shape magnetic anisotropies. In figures. 4.11 and 4.12, the continuous curves through the data points (symbols) denote the variations in H_{res} with the angle ψ or α yielded by the resonance and equilibrium magnetization conditions in the IP or OP case, i.e., equations (5.28) and (5.29) or (5.30) and (5.31), when the self-consistent procedure, illustrated below, is adopted. For a given direction of $\overrightarrow{H}$ represented by a certain value of the angle ψ (α) in the IP (OP) case, the corresponding *equilibrium value* of the magnetization angle ψ (θ) and the values of H_{k_1} and H_{k_u} for each sample are self-consistently calculated from equations (5.28) and (5.29) (equations (5.30) and (5.31)) using the experimentally observed value of $H_{res}(\psi)$ ($H_{res}(\alpha)$) in a non-linear least-squares fit computer program. To elucidate this procedure further, we treat the IP case as an illustrative example (as the same procedure is adopted to arrive at $\theta(\alpha)$ in the OP case). For a given field angle ψ, the magnetization angle ϕ is calculated from Eq. (5.29) using the H_{res} observed at that angle ψ, magnetization M given by the lineshape analysis and rough values for the anisotropy constants K_1 and K_u so as to arrive at the initial values of $H_{k_1} = 2k_1/M$ and $H_{k_u} = 2k_u/M$. H_{res} at this value of ψ, calculated from Eq.(5.28) by setting $\xi = 0$ and employing ϕ computed

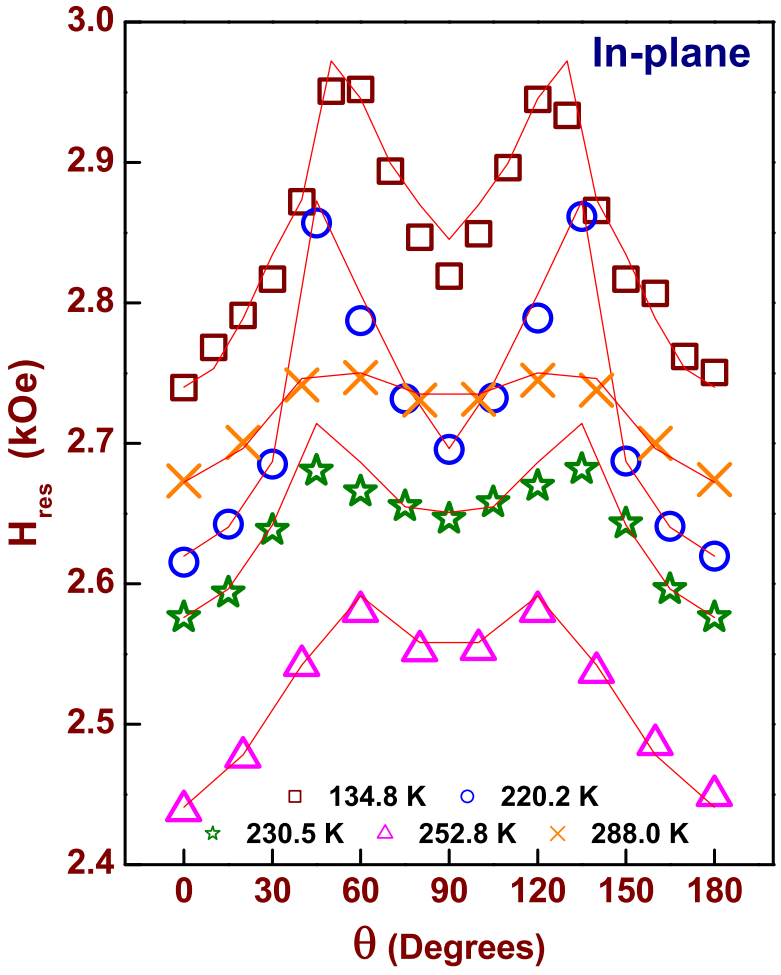

Figure 4.11: The 'in-plane' H_{res} as a function of field angle θ, at various temperatures.

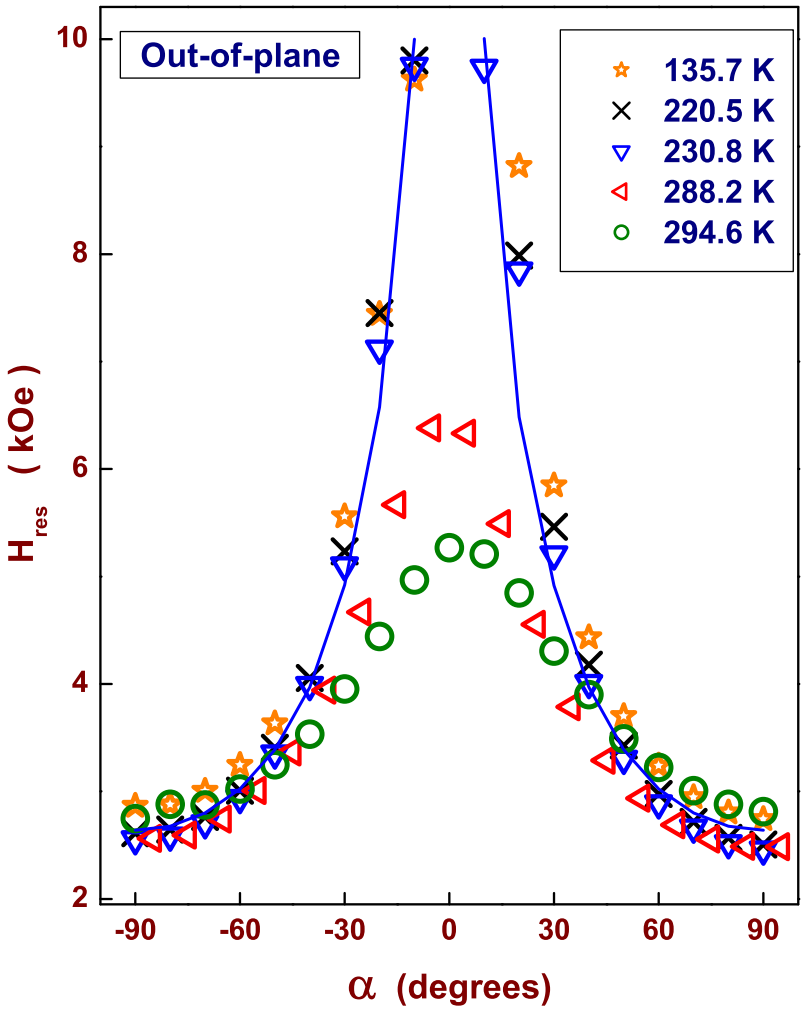

Figure 4.12: The 'out-of-plane' H_{res} as a function of field angle α, at various temperatures.

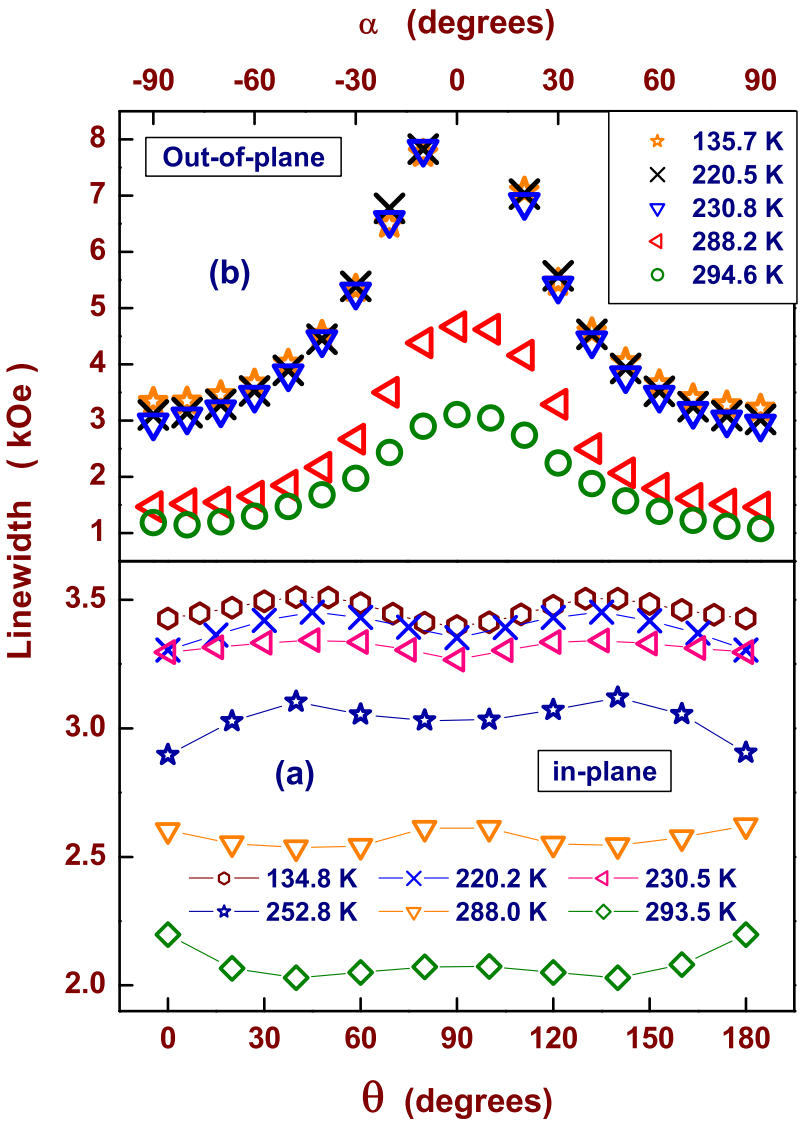

Figure 4.13: The (a) 'in-plane' and (b) 'out-of-plane' linewidth as a function of field angle θ, at various temperatures.

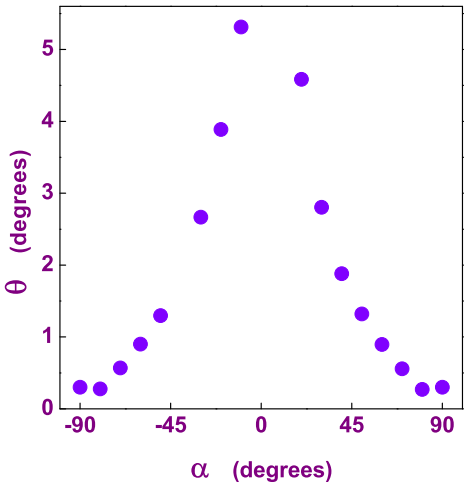

Figure 4.14: The variation of the equilibrium value of magnetization angle θ with field angle α.

from Eq. (5.29), and the same values of M, H_{k_1} and H_{k_u} as those used in Eq. (5.29), is compared with the observed value of H_{res} in a theory by treating K_1 and K_u as free-fitting parameters. The above procedure is repeated with the new values of K_1 and K_u till the values of K_1, K_u and ϕ computed from Eq. (5.29), when used in Eq.(5.28), yield the value of H_{res} at a given ψ that conforms well with the corresponding observed value of H_{res}.

The equilibrium values of the magnetization angle θ, so obtained, are plotted against α in figure 4.14. It is also observed that $\phi \simeq \psi$ till $\psi = 90^o$ and beyond $\phi \simeq 180^o - \psi$ till 180^o. In view of Eq. (5.29), the observation that $\phi \simeq \psi$ basically reflects the fact that both the effective H_{K_1} and H_{K_u} are negligibly small compared to H_{res}. Alternatively, this result implies that for any direction of the external static magnetic field in the sample plane,

H_{res} greatly exceeds both the demagnetizing field (which is extremely small in the IP configuration), H_{K_1} and H_{K_u}, and hence the direction of $\overrightarrow{M_s}$ nearly coincides with $\overrightarrow{H}_{res}$. On the other hand, in the OP case, the increase in θ is only marginal (from 0^o to about 5^o) as the angle α increases (decreases) from -90^o to -45^o (90^o to 45^o) but picks up abruptly for values of α in the range -45^o to 0^o or 45^o to 0^o. This observation can be understood as follows. For angles α ranging between -90^o and -45^o or between 90^o and 45^o, the magnetization vector $\overrightarrow{M_s}$ is unable to keep pace with the alterations in the direction of the static magnetic field because the angle between $\overrightarrow{M_s}$ and $\overrightarrow{H}_{res}$ as well as $|\overrightarrow{H}_{res}|$ are small and hence the torque experienced by $\overrightarrow{M_s}$ due to $\overrightarrow{H}_{res}$ is not strong enough to counter the tendency of both shape, cubic and uniaxial anistoropies to configure $\overrightarrow{M_s}$ to the sample plane. Consequently, θ possesses small values in this range of α. By contrast, when α lies between $\pm 20^o$ and 0^o, both the magnitude of H_{res} and angle between $\overrightarrow{M_s}$ and $\overrightarrow{H}_{res}$, are large with the result that the torque exerted by $\overrightarrow{H}_{res}$ on $\overrightarrow{M_s}$ is now able to work against the dictates of the shape and uniaxial anisotropies (cubic anisotropy favours the movement of $\overrightarrow{M_s}$ towards $\alpha = 0$ direction) and causes θ to increase steeply in this angle range.

4.5 Summary and Conclusion

Extensive ferromagnetic resonance (FMR) measurements have been performed at temperatures in the range $113\ K \leq T \leq 323\ K$ on the nanocrystalline Gd sample with average grain size 12(2) nm in the parallel configuration. An elaborate lineshape analysis of the PAD curves taken at different temperatures in the parallel sample configuration on nanocrystalline Gd

clearly brings out the role of the random intra-grain anisotropy and the interfacial random anisotropy in giving rise to several anomalous features in the temperature variations of resonance field, H_{res}, linewidth, ΔH_{pp}, anisotropy field, H_K and magnetization, M that include: a dip (peak) in $H_{res}(T)$ ($M(T)$) at a temperature very close to, but below, the Curie point, T_C, unusually broad linewidths at low and intermediate temperatures and a steep decline in $\Delta H_{pp}(T)$ as $T \to T_C$, a broad maximum in $H_K(T)$ at the spin reorientation temperature, and strongly suppressed $M(T)$ particularly at $T \ll T_C$ which resembles the functional dependence of 'zero-field-cooled' magnetization observed at a field that is an order of magnitude smaller than $H_{res}(T)$. The Scaling equation of state analysis of the magnetization data obtained by the lineshape analysis in the critical region yields $T_C = 285.5(1)\ K$ and mean-field critical exponents. The angle-dependent FMR measurements taken in the 'in-plane' (IP) and 'out-of-plane' (OP) sample configurations have been recorded at a number of fixed temperatures from $T = 113\ K$ to $T = 323\ K$ and the lineshape analysis reveal that besides the shape anisotropy, the cubic and uniaxial magnetic anisotropies are simultaneously present and they mimic the random intra-grain anisotropy and the interfacial random anisotropy.

References

1. J. H. E. Griffiths, *Nature* **158**, 670 (1946).
2. L. Landau and E. Lifshitz, *Phys. Z. Sowjetunion* **8**, 153 (1935).
3. T.L. Gilbert, *Phys. Rev.* **100**, 1243 (1955).
4. S. N. Kaul and V. Siruguri, *J. Phys. F* **17**, L255 (1987).
5. S. N. Kaul and V. Siruguri, *J. Phys.: Condens. Matter* **4**, 505 (1992).
6. J. Smit and H.G. Beljers, *Philips Res. Rep.* **10**, 113 (1955); H. Suhl, Phys. Rev. **97**, 555 (1955).
7. M. L. Spano and S. M. Bhagat, J. Magn. Magn. Mater., **24**, 143 (1981).
8. S. M. Bhagat, S. Harldson and O. Beckman *J. Phys. Chem. Solids* **38**, 593 (1977).
9. D. S. Rodbell, *Phys. Rev. Lett.* **13**, 471 (1964).
10. D. S. Rodbell, *Physica* **1**, 279 (1965).
11. S. M. Bhagat and H. O. Stevens, *J. Appl. Phys.* **39**, 1067 (1968).
12. S. Haradlson and L. Petterson, *J. Phys. Chem. Solids* **42**, 681 (1981).
13. S. V. Vonsovskii *Ferromagnetic resonance*, (Pergamon Press, London 1966).
14. Y. Li and K. Baberschke, *J. Magn. Magn. Mater.* **93**, 345 (1991); Y. Li, M. Farle and K. Baberschke, Phys. Rev. B **41**, 9596 (1990).

15. W. Platow, A. N. Anisimov, G. L. Dunifer, M. Farle and K. Baberschke *Phys. Rev. B* **58**, 5611 (1998).

16. Z. Frait, D. Fraitova, *Spin-wave resonance in metals Spin Waves and Magnetic Excitations*, **2**, ed. A. S. Borovik-Romanov and S. K. Schiha (Amsterdam: Elsevier).

17. F. Schreiber, J. Pflaum, Z. Frait, Th. Mühge and J. Pelzl, *Solid. State. Commum.* **93**, 965 (1995).

18. H. Suhl, *Phys. Rev.* **97**, 55 (1955).

19. V Siruguri and S N Kaul, *J. Phys.: Condens. Matter* **8**, 4567 (1996).

20. T. W. Moore and D. S. Rodbell, *J. Appl. Phys.* **35**, 906 (1964)

21. S. N. Kaul and S. Srinath, Phys. Rev. B, **62**, 1114 (2000)

22. S. P. Mathew *et al.*, *J. Phys.:Conf. Ser.* **200**, 072047 (2010)

23. F. Sporel and E. Biller, *Solid State Commun.* **17**, 833 (1975).

24. Y. Li and K. Baberschke, *Phys. Rev. Lett.* **68**, 1208 (1992).

25. B. Heinrich *et al.*, *J. App. Phys.* **55**, 1814 (1984).

26. S. M. Bhagat, D. J. Webb and M. A. Manheimer, *J. Magn. Magn. Mater.* **53**, 209 (1985).

27. S. N. Kaul, *J. Magn. Magn. Mater.* **53**, 5 (1985)

28. S. Srinath, H. Kronmuller and S. N. Kaul, *Phys. Rev. B* **59**, 1145 (1999)

29. S. Srinath and S. N. Kaul, *Phys. Rev. B* **60**, 12133 (1999)

Chapter 5

Bose-Einstein Condensation

5.1 Introduction

Historically, a thermodynamic phase transition in an ideal Bose gas at ultra-low temperatures, in which a sizable fraction of the total number of atoms or molecules with an integer spin (bosons) *spontaneously condense* into a single lowest-energy quantum state, came to be termed as the phenomenon of Bose-Einstein condensation (BEC). BEC thus represents a rare quantum phenomenon in which BE condensates exhibit spontaneous quantum coherence over macroscopic length and time scales. Though BEC is modified a great deal by interactions in Bose liquids, the superfluid transition in liquid ^4He remained, by far, the most celebrated manifestation of BEC till nearly two decades ago when BEC was observed in ultra-cold dilute gases of alkali atoms at nano-Kelvin temperatures [1]. Theoretical predic-

The following articles are based on the results presented in this Chapter:
1. S. N. Kaul and S. P. Mathew, *Phys. Rev. Lett.*, **106**, 247204 (2011).
2. S. P. Mathew and S. N. Kaul, *J. Phys.: Conden. Matter*, **23**, 266003 (2011).
3. S. N. Kaul and S. P. Mathew, *AIP Conf. Proc.*, **1347**, 41 (2011).

tions [2, 3, 4] that bosonic elementary excitations in solids, quantum liquids and giant molecules can also undergo the BEC transition have served as a strong motivation to search for new systems where BEC could be observed. Subsequently, BEC of quasiparticles at cryogenic temperatures has been reported in a wide variety of systems such as excitons in bulk Ge [5], biexcitons in CuCl [6] and $GaAs/Ga_{0.94}In_{0.06}As$ quantum wells [7], phonons in Bi [8] and magnetic field-induced BEC of magnons in spin-dimer compounds $BaCuSi_2O_6$ [9], $Ba_3Cr_2O_8$ [10, 11], $Sr_3Cr_2O_8$ [12], $KCuCl_3$ [13, 14, 15], $TlCuCl_3$ [16, 17, 18, 19, 20], NH_4CuCl_3 [21, 22] and $Pb_2V_3O_9$ [23], quasi two-dimensional spin-1/2 antiferromagnet Cs_2CuCl_4 [24] and the spin-gap compound $NiCl_2 - 4SC(NH_2)_2$ [25]. Considerable attention given to magnons, compared to other quasiparticle excitations, recognizes their unique properties that make them potential candidates for BEC. These attributes are: (i) at temperatures far below the magnetic ordering temperature, T_C, magnons behave as weakly interacting bosons, (ii) magnons have a much longer lifetime compared to the magnon-magnon scattering time, τ_{m-m} (which is of the order of 10^{-8}s) and magnon-phonon scattering time, which is orders of magnitude smaller than τ_{m-m}, and (iii) magnon density can be tuned by varying external magnetic field or temperature or both and can reach values as high as $10^{19}cm^{-3}$. Recently, by sustaining a high density ($10^{18} - 10^{19}cm^{-3}$) of quasiequilibrium magnons in epitaxial yttrium iron garnet films of thickness $5 - 20\mu m$ through continuous microwave parametric pumping, magnons have been shown to undergo BEC even at room temperature [26].

However, the above works on BEC of magnons are not entirely free of criticism [27, 28, 29], as elucidated below. In spin-gap quantum antiferro-

magnets [9] - [23], the phase transition from non-magnetic (singlet) state to a magnetically ordered (triplet) state driven by an external magnetic field and the consequent appearance of field-induced magnetization has been interpreted in terms of the condensation of magnetic excitations. Bugrij and Loktev [28] and Demokritov et al [29] argue that the BEC as such does not occur in these systems because (i) a rearrangement of the ground state of the system by the application of field generates virtual magnons as opposed to the real ones needed for BEC, and (ii) in quantum antiferromagnets, ingeneral, and in the compounds $ACuCl_3(A = K, Tl, NH_4)$, in purticular, the U(1) rotational symmetry around the applied magnetic field is broken by magnetocrystalline anisotropy [30] rather than by field-induced magnetic order, as required for the BEC of gapless Goldstone magnon modes or triplons. Since spontaneous coherence is essential to the phenomenon of BEC, Snoke [27] contends that, to prove that the BEC state actually exists, it is necessary to demonstrate that there is coherence and that this coherence is spontaneous. Barring the recent demonstration of coherence of magnon condensates in experiments involving incoherent pumping of magnons [31], earlier experiments using coherent magnon pumping demonstrate, at best, a pile-up of magnon population near the ground state but provide no direct test of coherence [27] as the apparent spontaneous coherence could be induced by the coherent pumping. Notwithstanding such issues, BEC of quasiparticles continues to be a intensely-pursued research area in condensed matter physics since it has led to a deeper understanding of the exotic ground states in strongly-correlated electron systems.

In this thesis, we present the observation of BEC of magnons in nanocrystalline gadolinium (nc-Gd) at temperatures $\leq 20K$ based on a detailed

study of magnetization and specific heat. This work marks the first attempt to self-consistently determine the BEC transition temperature, T_c, at different magnetic fields, and the chemical potential and the average occupation number for the ground state as functions of temperature and magnetic field (H). Increase in the average grain size from d = 12 nm to d = 18 nm enhances the transition temperature $T_c(H = 0)$ from 16.5 K to 20.5 K but drastically reduces the spontaneous quantum phase coherence length of the BE condensate wavefunction. The results provide a strong evidence for the BEC of magnons in nc-Gd.

5.2 Theoretical Considerations

With a view to put the magnetization and specific heat results in a proper theoretical perspective, the experimental signatures for BEC, predicted by the theory, are briefly introduced in this section.

5.2.1 Bose-Einstein Condensation in Ideal Bose Gas

For an ideal Bose gas of N non-interacting identical particles with mass m, the Hamiltonian is [32]

$$H = \sum_{i=1}^{N} \frac{P_i^2}{2m} \tag{5.1}$$

where $P_i^2 = \mathbf{P_i} \cdot \mathbf{P_i}$, and $\mathbf{P_i}$ is the momentum operator of the i^{th} particle. Energy eigenvalues of an ideal system is a sum of single-particle energies, called *levels*, given by

$$\epsilon_k = \frac{P^2}{2m} \tag{5.2}$$

where $P \equiv |\mathbf{P}|$ and $\mathbf{P}$ is the momentum eigenvalue of the single particle:

$$\mathbf{P} = \frac{2\pi\hbar}{L}\mathbf{n} = \hbar\,\mathbf{k} \tag{5.3}$$

in which $\mathbf{n}$ is a vector whose components are 0 or $\pm$ integers and L is the cube root of the volume of the system: $L \equiv V^{1/3}$. A state of an ideal system can be specified by specifying a set of occupation numbers $\{n_k\}$ so defined that there are n_k particles having the wave vector k. Obviously the total energy E and the total number of particles N of the state are given given by

$$E = \sum_k \epsilon_k n_k \tag{5.4}$$

and

$$N = \sum_k n_k \tag{5.5}$$

The grant partition function for the Bose gas is

$$\begin{aligned} \Im(z, V, T) &= \sum_{N=0}^{\infty} \sum_{\substack{\{n_k\} \\ \sum n_k = N}} z^N e^{-\beta \sum \epsilon_k n_k} \\ &= \sum_{N=0}^{\infty} \sum_{\substack{\{n_k\} \\ \sum n_k = N}} \prod_k (z e^{-\beta \epsilon_k})^{n_k} \end{aligned} \tag{5.6}$$

where fugacity, z, and temperature, $\beta \equiv (k_B T)^{-1}$, are the Lagrange multipliers to be determined from the condition Eqs.(7.4) and (7.5). The double

summation in Eq.(7.6) is equivalent to summing each n_k independently.

$$\begin{aligned}\Im(z,V,T) &= \sum_{n_0}\sum_{n_1}\cdots[(ze^{-\beta\epsilon_0})^{n_0}(ze^{-\beta\epsilon_1})^{n_1}\cdots] \\ &= \left[\sum_{n_0}(ze^{-\beta\epsilon_0})^{n_0}\right]\left[\sum_{n_1}(ze^{-\beta\epsilon_1})^{n_1}\right]\cdots \\ &= \prod_k\left[\sum_n(ze^{-\beta\epsilon_k})^n\right] = \prod_k\frac{1}{1-ze^{-\beta\epsilon_k}} \qquad (5.7)\end{aligned}$$

The equation of state is

$$\frac{PV}{k_BT} = log\ \Im(z,V,T) = -\sum_k log(1-ze^{-\beta\epsilon_k}) \qquad (5.8)$$

from which z is to be eliminated with the help of the equation

$$N = z\frac{\partial}{\partial z}log\ \Im(z,V,T) = \sum_k\frac{ze^{-\beta\epsilon_k}}{1-ze^{-\beta\epsilon_k}} \qquad (5.9)$$

The average occupation numbers $\langle n_k\rangle$ is given by

$$\begin{aligned}\langle n_k\rangle &= \frac{1}{\Im}\sum_{N=0}^{\infty} z^N \sum_{\substack{\{n_k\}\\ \sum n_k=N}} n_k e^{-\beta\sum\epsilon_k n_k} \\ &= -\frac{1}{\beta}\frac{\partial}{\partial\epsilon_k}log\Im = \frac{ze^{-\beta\epsilon_k}}{1-ze^{-\beta\epsilon_k}} \qquad (5.10)\end{aligned}$$

Eqs.(7.8) and (7.9) diverge as $z\to 1$, because the single term corresponding to $k=0$ diverges and thus the term $k=0$ may be as important as the entire sum. Splitting off the terms in Eqs.(7.8) and (7.9) corresponding to $k=0$ and replacing the rest of the sums by integrals lead to

$$\frac{P}{k_BT} = -\frac{1}{2\pi^2}\int_0^\infty dk\ k^2 log(1-ze^{-\beta\epsilon_k}) - \frac{1}{V}log(1-z) \qquad (5.11)$$

$$\frac{1}{\nu} = \frac{1}{2\pi^2}\int_0^\infty dk\ k^2\frac{1}{z^{-1}e^{\beta\epsilon_k}-1} + \frac{1}{V}\frac{z}{1-z} \qquad (5.12)$$

where $\nu = V/N$. Eqs.(7.11) and (7.12) can be rewritten in the form

$$\frac{P}{k_B T} = \frac{1}{\lambda^3}\, g_{5/2}(z) - \frac{1}{V}\, log(1-z) \tag{5.13}$$

$$\frac{1}{\nu} = \frac{1}{\lambda^3}\, g_{3/2}(z) + \frac{1}{V}\, \frac{z}{1-z} \tag{5.14}$$

where $\lambda = \sqrt{2\pi\hbar^2/mk_BT}$ is the thermal de Broglie wavelength, z is the fugacity and

$$g_{5/2}(z) = -\frac{4}{\sqrt{\pi}} \int_0^\infty dx\; x^2\; log(1 - ze^{-x^2}) = \sum_{l=1}^{\infty} \frac{z^l}{l^{5/2}} \tag{5.15}$$

$$g_{3/2}(z) = z\frac{\partial}{\partial z} g_{5/2}(z) = \sum_{l=1}^{\infty} \frac{z^l}{l^{3/2}} \tag{5.16}$$

This class of functions, $g_n(z)$, is the Bose-Einstein functions. Eq.(7.10) implies that the average occupation number $\langle n_0 \rangle$ for the single-particle level with $k = 0$ is

$$\langle n_0 \rangle = \frac{z}{1-z} \tag{5.17}$$

If a finite fraction of all the particles in the system occupy the single level with $k = 0$, $\langle n_0 \rangle / V$ significantly contributes to Eq.(7.14). The critical temperature, T_c, at which the thermal de Broglie wavelength becomes comparable to the average interparticle separation, is

$$\begin{aligned} T_c &= (2\pi\hbar^2/m^* k_B)/[\nu g_{3/2}(1)]^{2/3} \\ &= (2\pi\hbar^2/m^* k_B)[\zeta(3/2)]^{-2/3}(n^{2/3}) \end{aligned} \tag{5.18}$$

Standard statistical mechanics treatment then yields the following expressions [32] for the entropy per unit volume, s, and specific heat per unit volume, c_v, for the ideal Bose gas.

$$s = \frac{5\; k_B}{2} \left(\frac{mk_BT}{2\;\pi\hbar^2} \right)^{3/2} g_{5/2}(1), \qquad T < T_c \tag{5.19}$$

$$s = \frac{5\ k_B}{2}\left(\frac{mk_BT}{2\ \pi\hbar^2}\right)^{3/2} g_{5/2}(z) - Nk_B\ log\ z, \qquad T > T_c \qquad (5.20)$$

and

$$c_v = \frac{15\ k_B}{4}\left(\frac{mk_BT}{2\ \pi\hbar^2}\right)^{3/2} g_{5/2}(1), \qquad T < T_c \qquad (5.21)$$

$$c_v = \frac{15\ k_B}{4}\left(\frac{mk_BT}{2\ \pi\hbar^2}\right)^{3/2} g_{5/2}(z) - \frac{9}{4}\ Nk_B\ \frac{g_{3/2}(z)}{g_{1/2}(z)}, \qquad T > T_c \qquad (5.22)$$

According to the expressions (6.19) - (6.22), the experimental signature of BEC is that both entropy and specific heat should vanish as $T^{3/2}$ in the limit $T \to 0$ (i.e., as the condensate fraction with $s = 0$ increases drastically near absolute zero) and exhibit a sharp kink at $T = T_c$.

5.2.2 Bose-Einstein Condensation of Magnons

Assuming quadratic magnon dispersion at long wavelengths and measuring the wavevector (momentum) **k** from the minimum of the magnon dispersion, the low-energy effective Hamiltonian for the ($S^z = 1$) magnons in the presence of magnetic field, H, is given by

$$H = \sum_k (\hbar\omega_k + \Delta - \mu)\, a_k^\dagger a_k + \frac{1}{2}\sum_{k,k',q} v(\mathbf{q})\ a_{k+q}^\dagger a_{k'-q}^\dagger a_k a_{k'} \qquad (5.23)$$

where $\varepsilon_k = \hbar\omega_k = D(T)k^2 \equiv \hbar^2\ k^2/2m^*$ so that the effective mass $m^* \equiv \hbar^2/2\ D(T)$, $D(T)$ is the spin-wave stiffness and $\Delta = \Delta_0 + g\mu_B H$ is the gap introduced in the spin-wave spectrum by the dipole-dipole interactions and/or magnetocrystalline anisotropy, (Δ_0), and by the external magnetic field, ($g\mu_B H$). The second term in Eq.(6.23) represents the two-magnon interaction and gives rise to the 'remormalization' of D with temperature in accordance with the relation [33]

$$D(T) = D(0)\ [1 - D_2T^2 - D_{5/2}T^{5/2}] \qquad (5.24)$$

where $D(0)$ is the spin-wave stiffness at $T = 0K$ and the $T^{5/2}$ (T^2) term arises from the *direct* (*indirect*) magnon-magnon interactions (mediated by the conduction-electron spins). At low temperatures, the indirect magnon-magnon interactions dominate and hence the $T^{5/2}$ term in Eq.(6.24) is dropped in subsequent calculations. The momentum distribution of magnons in the normal (uncondensed) phase is

$$\langle n_k \rangle \equiv \langle a_k^\dagger a_k \rangle = \frac{1}{e^{\beta(\hbar\omega_k + \Delta - \mu)} - 1} \tag{5.25}$$

The magnon density of states [34]

$$D_{sw}(\omega_k) = \frac{1}{4\pi^2} \left(\frac{\hbar}{D(T)} \right)^{3/2} \omega_k^{1/2} \tag{5.26}$$

The magnon density $n = N/V$ has to be determined self-consistently by

$$n = \sum_k \langle n_k \rangle = \int_0^\infty \langle n_k \rangle D_{sw}(\omega_k)\, d\omega_k = \lambda^{-3} \sum_{l=1}^{\infty} \frac{(z_{eff})^l}{l^{3/2}} \tag{5.27}$$

with the thermal de Broglie wavelength $\lambda \equiv \sqrt{4\pi D(T)/k_B T} = \sqrt{2\pi\hbar^2/m^* k_B T}$,

$$z_{eff} = z\ e^{-\beta\Delta} \tag{5.28}$$

and the fugacity $z = e^{\beta\mu}$ given by the equation of state for non-interacting Bose gas (Eq.7.14), which can be casted into the form

$$\frac{1}{V} \times \frac{z}{1-z} = n \left[1 - \frac{g_{3/2}(z)}{g_{3/2}(1)} \times \left(\frac{T}{T_c} \right)^{3/2} \right] \tag{5.29}$$

or

$$\frac{< n_0(T) >}{N} = \left[1 - \frac{g_{3/2}(z)}{g_{3/2}(1)} \times \left(\frac{T}{T_c} \right)^{3/2} \right] \tag{5.30}$$

where V is the volume over which the condensate wavefunction retains its phase coherence, $n \equiv N/V$ is the magnon number density, $g_{3/2}(z) \equiv \sum_{l=1}^{\infty} z^l/l^{3/2}$ is the Bose-Einstein function.

Magnetization

For a ferromagnet, the decline in magnetization, M(T,H), due to the thermally-excited spin waves at temperature, T, and external magnetic field, H, is given by

$$M(T,H) = M(0,H) - g\mu_B \; n \tag{5.31}$$

with magnon density n given by Eq.(6.29), i.e., by

$$M(T,H) = M(0,H) - g\mu_B \int_0^\infty \frac{D_{SW}(\varepsilon_k) \; d\varepsilon_k}{e^{\beta(\varepsilon_k + \triangle - \mu)} - 1} \tag{5.32}$$

$$M(T,H) = M(0,H) - g\mu_B \left[\frac{k_B T}{4\pi D(T)}\right]^{3/2} \; \sum_{l=1}^{\infty} \frac{(z_{eff})^l}{l^{3/2}} \tag{5.33}$$

If $\mu = 0$, Eq.(5.32) yields the conventional spin-wave relation for magnetization

$$M(T,H) = M(0,H) - g\mu_B \; Z\left(\frac{3}{2}, t_H\right) \left[\frac{k_B T}{4\pi D(T)}\right]^{3/2} \tag{5.34}$$

where the Bose-Einstein integral function

$$Z(\frac{3}{2}, t_H) = \sum\nolimits_{n=1}^{\infty} n^{-\frac{3}{2}} exp(-nt_H) \tag{5.35}$$

with $\mathrm{t}_H = \mathrm{T}_g/\mathrm{T} = \Delta/\mathrm{k}_B\mathrm{T}$. Since the magnons (Bosons) are essentially non-interacting at low temperatures, they can condense into the ground state in increasing numbers as the temperature falls below the Bose-Einstein condensation temperature, T_c, where $\mu \to 0$.

Specific Heat

Internal energy per unit volume of an ensemble of Bosons is given by

$$U = \int_0^\infty \hbar\omega_k \; \langle n_k \rangle \; D_{sw}(\omega_k) \; d\omega_k \tag{5.36}$$

where $\langle n_k \rangle$ is the average number of magnons excited in the wave vector mode k

$$\begin{aligned} U &= \frac{1}{4\pi^2\ [D(T)]^{3/2}} \int_0^\infty \frac{\hbar\omega_k^{3/2}\ d\hbar\omega_k}{e^{\beta(\hbar\omega_k + \triangle - \mu)} - 1} \\ &= \frac{3}{2} \frac{(k_B T)^{5/2}}{[4\pi\ D(T)]^{3/2}} \sum_{l=1}^{\infty} \frac{e^{-l\beta(\Delta-\mu)}}{l^{5/2}} \\ &= \frac{3}{2} \frac{(k_B T)^{5/2}}{[4\pi\ D(T)]^{3/2}} \sum_{l=1}^{\infty} \frac{(z_{eff})^l}{l^{5/2}} \end{aligned} \tag{5.37}$$

Magnon specific heat per unit volume

$$c_{mag} = \left(\frac{dU}{dT}\right)_V = \frac{3}{16\pi^{3/2}} \frac{d}{dT} \left(\frac{(k_B T)^{5/2}}{D(T)^{3/2}} \sum_{l=1}^{\infty} \frac{(z_{eff})^l}{l^{5/2}} \right) \tag{5.38}$$

or

$$c_{mag} = \frac{3k_B}{2} \left(\frac{k_B T}{4\pi D(T)}\right)^{3/2} \left\{ \left[\frac{5}{2} + \frac{3D_2 T^2}{1 - D_2 T^2}\right] \sum_{l=1}^{\infty} \frac{(z_{eff})^l}{l^{5/2}} - ln z_{eff} \sum_{l=1}^{\infty} \frac{(z_{eff})^l}{l^{3/2}} \right\} \tag{5.39}$$

Magnetic Entropy

The magnetic-field induced change in the magnetic part of entropy density, Δs_{mag}, can be calculated from the measured 'zero-field', $C_H(H = 0)$, and 'in-field', $C_H(H)$, specific heat using the relation

$$\Delta S_{mag} = S(H) - S(H = 0) = \int_0^T \frac{C_H(H) - C_H(H = 0)}{T} dT \tag{5.40}$$

ΔS_{mag} can also be determined from magnetization, $M_H(T)$, using the Maxwell thermodynamic relation

$$(\partial S_{mag}/\partial H)_T = (\partial M/\partial T)_H \tag{5.41}$$

The temperature variations of the field-induced change in magnetic entropy can be calculated as

$$(\Delta S_{mag})_T = [S_{mag}(H) - S_{mag}(H=0)]_T = \int_0^H (\partial M/\partial T)_H (dH)_T \quad (5.42)$$

5.3 Results and Discussion

5.3.1 Magnetization

Thermomagnetic curves, M(T), taken in the 'field-cooled' mode over the temperature range $1.8K \leq T \leq 320K$ at fixed magnetic fields, H, ranging between 50 Oe and 90 kOe are shown in figure 5.1. A detailed analysis [35] of these curves based on the conventional spin wave relation, Eq.(5.34), attempted, revealed that an upturn in M(T) at low temperatures ($T < T^*(H)$) for $H \geq 1kOe$ marks an anomalous softening of magnon modes in that the spin-wave stiffness suddenly drops to nearly one third of its bulk value [36] as the temperature falls below T^*. In order to ascertain if this softening of magnon modes is a consequence of the Bose-Einstein condensation (BEC) of magnons, the following self-consistent procedure is employed. In the first step, using certain initial values of volume, V and the BEC transition temperature, T_c, Eq.(5.30) is solved in conjunction with Eq.(6.29), to yield fugacity as a function of temperature, $z(T)$, in a given temperature range, $T_{min} = 1.8K \leq T \leq T_{max}$. These values of $z(T)$ are then inserted into Eq.(5.30) and M(T) for a fixed field strength is calculated using the value of intrinsic spin-wave energy gap $\Delta_0 = 0.155(3)meV$, previously reported [36] for single-crystal Gd, and some starting values of $D(0)$ and D_2 in the expression for $D(T)$, Eq.(6.24). M(T), so calculated, $M(T)_{cal}$, is compared

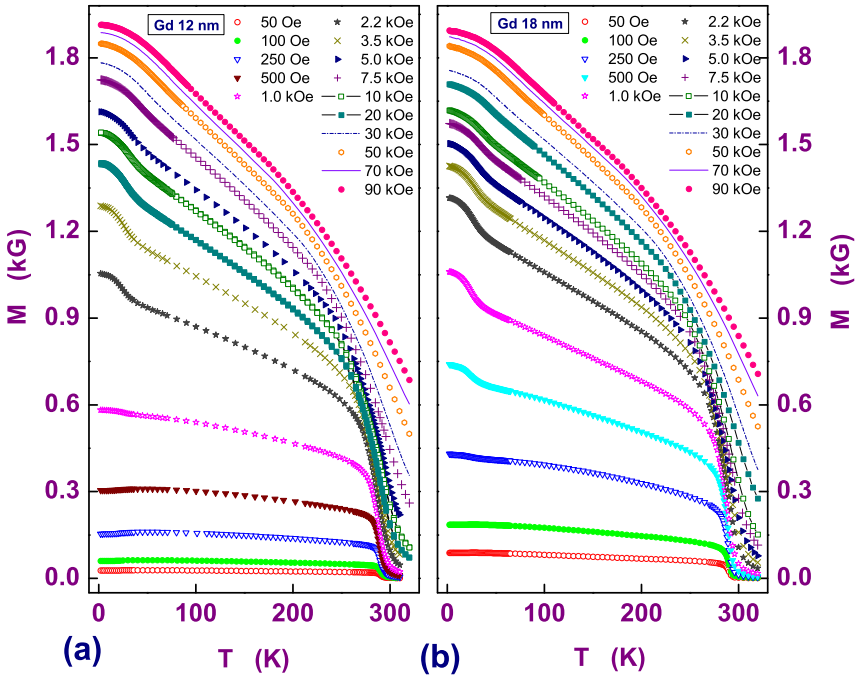

Figure 5.1: Magnetization of nanocrystalline gadolinium with average grain size (a) 12 nm and (b) 18 nm as a function of temperature at fixed fields ranging from 50 Oe to 90 kOe.

with the observed M(T), $M(T)_{obs}$, over the chosen temperature range and this iterative process is repeated for a different set of values for V, T_c (and hence $z(T)$), $D(0)$ and D_2 till the agreement between $M(T)_{cal}$ and $M(T)_{obs}$ in that temperature range is optimized. The same self-consistent procedure is followed in each of the temperature ranges. In the 'range-of-fit' (ROF) analysis, the temperature range of the BEC fit is progressively widened by keeping T_{min} fixed at 1.8 K and increasing T_{max} and the variations of the parameters V, T_c, $D(0)$ and D_2 with T_{max} are monitored. The highest temperature, T^{up}, up to which Eq.(5.33) accurately describes $M(T)_{obs}$ at a given H is arrived at when the values of all the free parameters remain essentially unaltered (within the uncertainty limits) as the T_{max} is raised towards T^{up} but change drastically when T_{max} exceeds T^{up}. The optimum BEC fits, based on Eq.(5.33), so obtained, are shown as continuous curves through the data points (symbols) in figure 5.2. The insets in this figure serve to demonstrate that the conventional spin-wave theory, Eq.(5.34), corresponding to the $\mu = 0$ case, can, at best, describe $M(T)_{obs}$ in an extremely narrow range at low temperatures ($T \to 0$) as compared to the BEC fits, which accurately reproduce the observed temperature variation of magnetization over a much wider temperature range which widens further with increasing H. Note that the $M(T)$ data taken at $H < 2.2kOe$ ($H < 1.0kOe$) for d = 12 nm (d = 18 nm) are neither amenable to the spin-wave analysis nor to an analysis based on the BEC picture because the temperature dependence of magnetization, particularly at low temperatures and low fields, is complicated by the temperature-dependent magnetocrystalline and shape anisotropies.

The ROF analysis yields the variations of the parameters V, T_c, $D(0)$

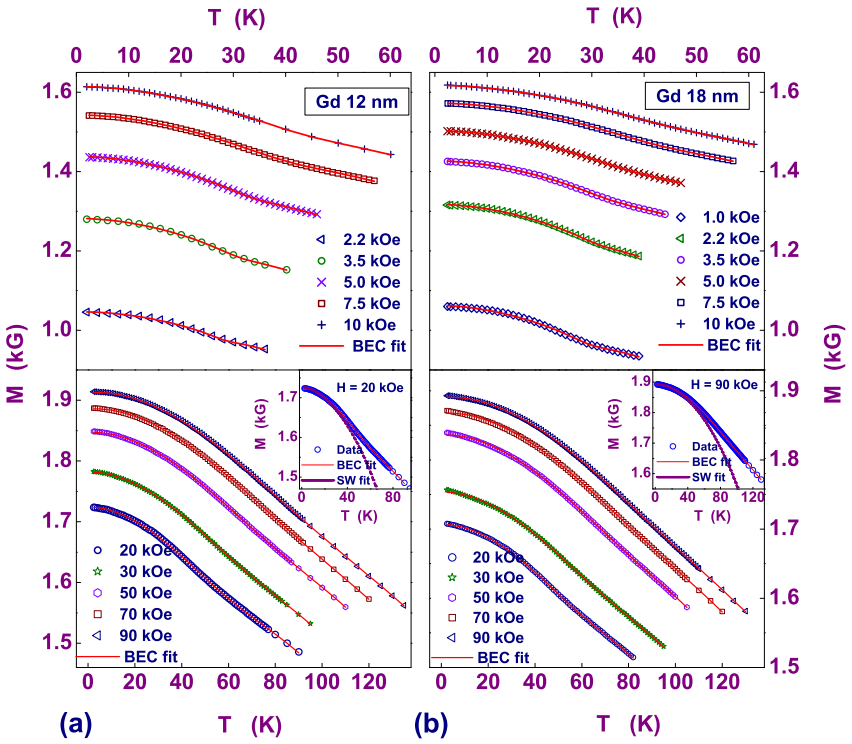

Figure 5.2: The observed (symbols) decline in magnetization with temperature in nanocrystalline gadolinium with average grain size (a) 12 nm and (b) 18 nm at fixed fields in the range (a) 2.2 kOe - 90 kOe and (b) 1.0 kOe - 90 kOe along with the corresponding BEC fits (continuous curves through the M(T) data) based on equations (5.33), (6.29) and (5.30). The insets of Fig.5.2(a) and Fig.5.2(b) highlight a typical comparison between the BEC fits (continuous curves) and the conventional spin-wave fits (dotted curves), based on Eq.(5.34), to the M(T) data taken at 20 kOe and 90 kOe for d = 12 nm and 18 nm, respectively.

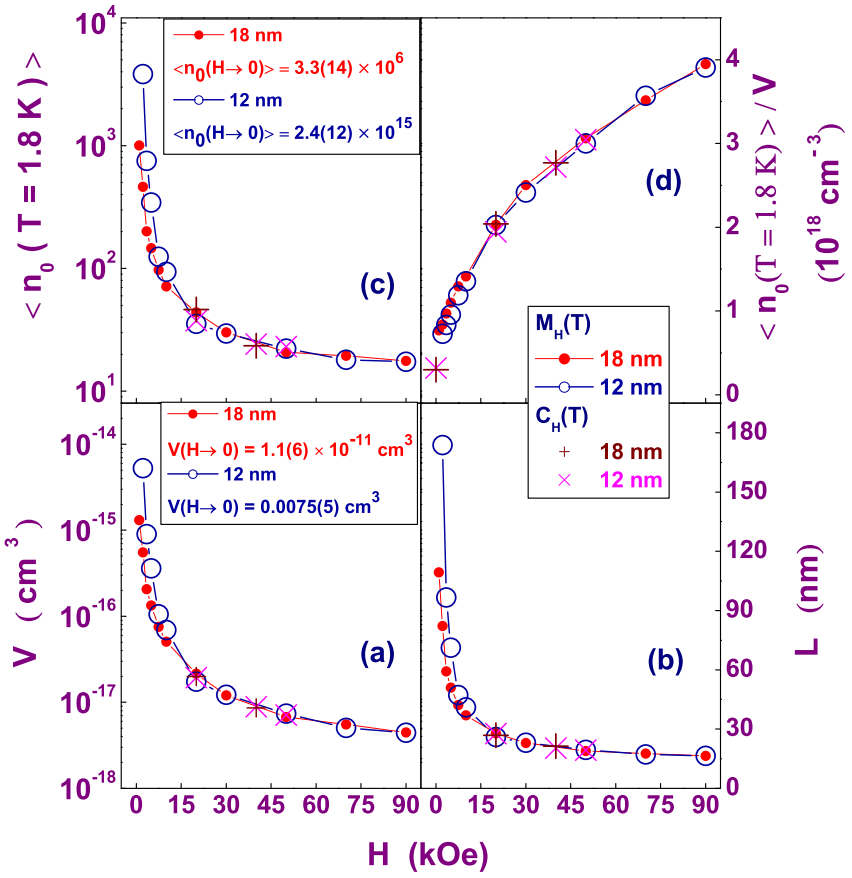

Figure 5.3: The variations with magnetic field of the average occupation number for the ground state, $< n_0 >$, the volume V (length $L = V^{1/3}$) over which the condensate wavefunction retains its phase coherence and the occupation number density, $< n_0 > /V$.

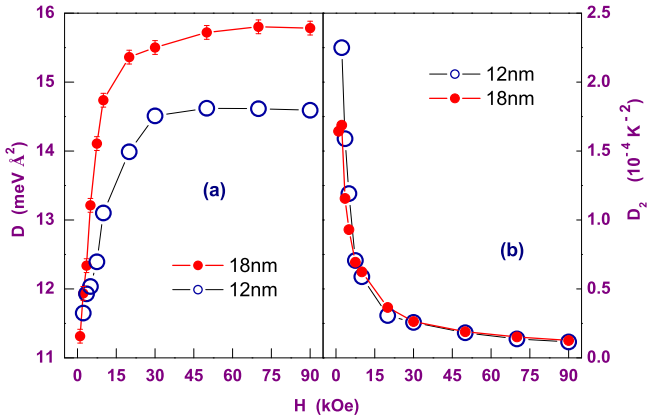

Figure 5.4: (a) The variations of the spin-wave stiffness at $0K$, $D(0)$ and (b) the coefficient, D_2, of the T^2 term in Eq.(6.24) with magnetic field.

and D_2 with H displayed in the figures 5.3 - 5.5. The main observations are as follows. The volume V (length $L = V^{1/3}$) over which the condensate wavefunction retains its phase coherence shrinks by nearly three orders (an order) of magnitude (Fig.5.3) from its value at low fields and approaches the volume of a single grain (average grain size) as fields in excess of 30 kOe are applied; the initial drop being more in the case d = 12nm. The effect of magnetic field is to (i) create a gap in the spin-wave spectrum, in addition to the intrinsic gap Δ_0, (ii) stiffen the spin system so as to make the thermal excitation of spin waves more difficult (sharp increase in spin-wave stiffness, $D(0)$, at low fields, Fig.5.4), (iii) progressively destroy phase coherence (steep drop in V, Fig.5.3), and (iv) increase T_c in accordance with the relation $T_c(H) = T_c(H = 0) + aH^{1/\phi}$, with the exponent $\phi = 3/2$ (Fig.5.5) that is characteristic [17, 37, 38] of BEC, up to $H = 20kOe$ ($30kOe$) for d = 12 nm (18 nm).

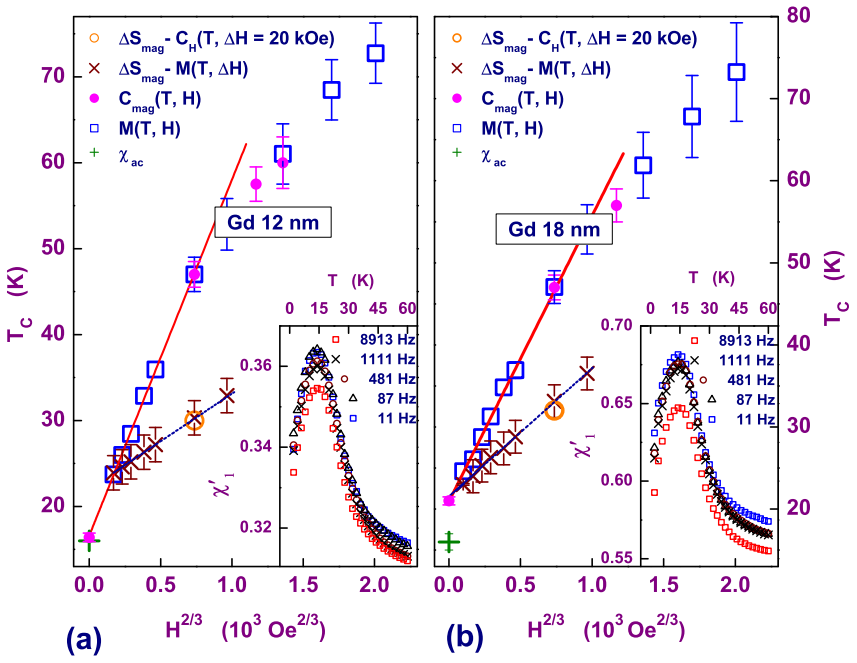

Figure 5.5: The BEC transition temperature, T_c, obtained from $M(T)$ (open squares), $\chi_{ac}(T)$ (plus sign) and $C_{mag}(T)$ (solid circles) as well as the characteristic temperature, $T_p^\star$, identified with the peak in $\Delta S_{mag}(T)$, deduced from $M(T)$ (crosses) and $C_H(T, \Delta H)$ (open circles), plotted against $H^{2/3}$ for (a) d = 12 nm and (b) d = 18 nm. The insets display the frequency-independent peak in ac susceptibility at $\simeq 15K$.

The insets of Fig.5.5 highlight a *broad peak* in the in-phase component of ac susceptibility, measured at an ac driving field of $h = 1Oe$, at $T_{peak} \cong 15K$ (single crystal Gd does not exhibit any such peak at low temperatures), with no discernible shift in T_{peak} over three decades (10 Hz - 10 kHz) of driving-field frequency. We attribute this peak to the magnon BEC phase transition at $H = 0$ so that T_{peak} equals $T_c(H = 0)$ and is represented by the plus sign in the phase diagram (Fig.5.5). Absence of a frequency-dependent peak-shift strongly indicates that the magnon lifetime is much larger than the magnon-magnon or magnon-phonon scattering time and hence the magnons are in a quasi-equilibrium state.

The variation of fugacity with temperature, $z(T)$, that optimizes agreement between $M(T)_{cal}$ and $M(T)_{obs}$ at different but fixed fields permits an accurate determination of the average occupation number for the ground state $\langle n_0 \rangle = z/(1-z)$ and the chemical potential, $\mu = k_B T \ \ln z$, as functions of temperature and field. $\langle n_0 \rangle$ as a function of magnetic field, H, at T = 1.8 K or as a function of temperature at constant H, and the chemical potential in units of $k_B T$, $\mu/k_B T = \ln z$, at different temperatures (fields) but fixed H (temperature), so obtained, are displayed in figures 5.3, 5.6 - 5.9 (inset of Fig.5.9). In order to gain further insight into the nature of the BEC transition at $H = 0$, an empirical fit to the $V(H)$ and $\langle n_0(T = 1.8K, H) \rangle$ data, shown in Fig.5.3, is attempted based on the relation $x(H) = x(H \to 0)H^{-\alpha} + x(H = 90kOe)$ (x stands for either V or $\langle n_0(T = 1.8K) \rangle$) in the field range $\leq 20kOe$ ($\leq 30kOe$), where $T_c(H)$ obeys the BEC relation $T_c(H) = T_c(H = 0) + aH^{2/3}$ (straight lines in Fig.5.5) for d = 12 nm (18 nm). This exercise yields the best least-squares fits (continuous curves) to the data (symbols) over the field range

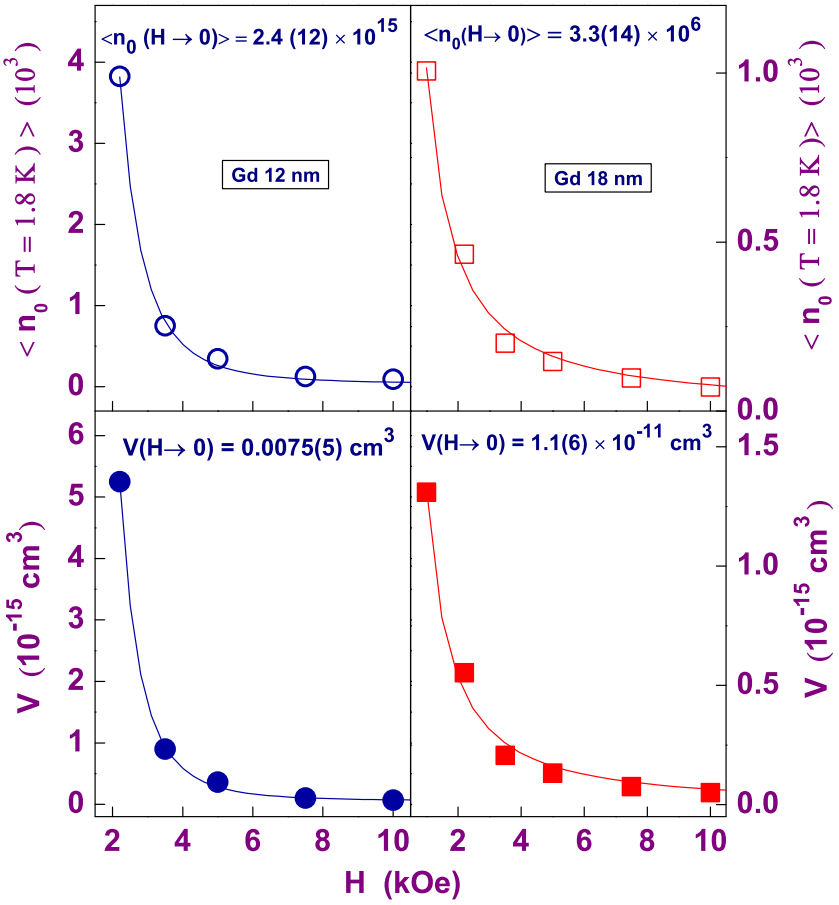

Figure 5.6: The observed (symbols) variations with magnetic field of the average occupation number for the ground state, $< n_0(T = 1.8K) >$ and the volume V over which the condensate wavefunction retains its phase coherence for $H \leq 30kOe$ and the corresponding empirical fits (continuous curves), for details, see text.

$2.2kOe \leq H \leq 20kOe$ ($1.0kOe \leq H \leq 30kOe$) corresponding to the parameter values $\langle n_0(T = 1.8K, H \to 0)\rangle = 2.4(12) \times 10^{15}$ ($= 3.3(14) \times 10^6$), $V(H \to 0) = 0.0075(5)\ cm^3 \cong$ sample volume ($= 1.1(6) \times 10^{-11}\ cm^3$) and $\alpha = 3.58(14)$ ($\alpha = 1.17(6)$) for d = 12 nm (18 nm). Figure 5.6 illustrates the quality of such fits at relatively low fields ($H \leq 10kOe$) where the variation of x with H is very rapid. This result indicates that, in the limit $H \to 0$, a large fraction of the magnons (magnon density as high as $\langle n_0(T = 1.8K, H \to 0)\rangle / V(H \to 0) \approx 3 \times 10^{17} cm^{-3}$) excited at $T = 1.8K$ spontaneously condense into the ground state in both the samples d = 12 nm and 18 nm but the condensate wavefunction retains its phase coherence over the entire sample volume only in the case of d = 12 nm. Incidently, the value of intrinsic spin-wave energy gap [36] $\Delta_0 = 0.155(3) meV$ corresponds to a temperature of $T_0 = 1.80(5)K$ so that the long-wavelength magnons with a density $\sim 10^{18} - 10^{19}\ cm^{-3}$ can be easily excited at $T \geq 1.8K$. However, regardless of the values of $\langle n_0(T = 1.8K, H)\rangle$ and $V(H)$ at a given H (including those obtained from the magnon part of the specific heat, $C_{mag}(T, H)$, at $H = 0$ or $H \neq 0$ and denoted by crosses and plus signs) for the samples with d = 12 nm and 18 nm, the ratio $\langle n_0(T = 1.8K, H)\rangle / V(H)$ is the same (within the uncertainty limits) for both the samples and increases with H, as is evident from Fig.5.3(d). In accordance with the BEC predictions, Eqs.(6.18) and (5.30), $T_c(H) \propto [\langle n_0(T = 1.8K, H)\rangle / V(H)]^{2/3}$ (Fig.5.7) while at constant H, the ratio $\langle n_0(T, H)\rangle / \langle n_0(T = 1.8K, H)\rangle$ scales with $[T/T_c(H)]^{3/2}$ (Fig.5.8).

In the true thermodynamic limit (i.e., as $V \to \infty$), the spontaneous quantum phase coherence of the BE condensate wavefunction extends over *infinite distances* at temperatures $T \leq T_c$ with the result that the fugacity

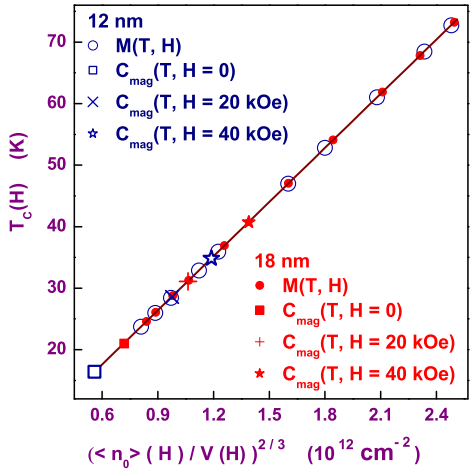

Figure 5.7: Scaling of $T_c(H)$ with $[< n_0(T = 1.8K, H) > /V(H)]^{2/3}$.

$z(T) = 1$ for $0 \leq T \leq T_c$ and falls off rapidly above T_c or equivalently, the chemical potential $\mu(T) = 0$ for $0 \leq T \leq T_c$ and falls to larger negative values at $T > T_c$. Thus, according to Eq.(5.30), the condensate fraction $\langle n_0(T) \rangle / N$ should drop with temperature as $(T/T_c)^{3/2}$ from unity at $T = 0$ to zero at $T = T_c$ and remain zero for $T \geq T_c$. This behaviour, with slight modifications brought about by the system size-limited coherence length (elaborated in the specific heat subsection) is indeed observed only when $H = 0$ (continuous lines in figures 5.8 and 5.9). As the effective coherence volume V shrinks with increasing H, the sharp kink in $z(T)$ or $\mu(T)$ at $T = T_c$ gets smeared out progressively and z (μ) assumes lower and lower values compared to unity (zero) even at $T = 0$ (as is evident from figure 5.9) with the result that the smearing of the transition at T_c occurs and the ratio $\langle n_0(T, H) \rangle / \langle n_0(T = 1.8K, H) \rangle$ acquires higher and higher values even

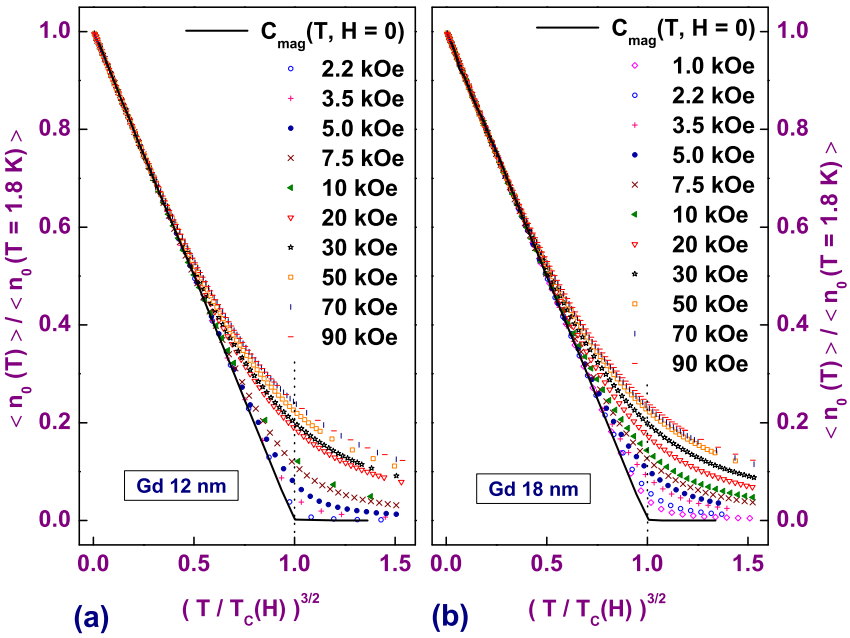

Figure 5.8: Scaling of the normalized average occupation magnon number for the ground state with $(T/T_c)^{3/2}$ at different fields for (a) d = 12 nm and (b) d = 18 nm.

at temperatures in the vicinity of T_c (Fig.5.8). Furthermore, the insets of Fig.5.9 highlight the typical variation of μ/k_BT with H for $H \geq 2.2kOe$ $(H \geq 1.0kOe)$ at temperatures $T \leq T_c$, which is adequately described by the expression $\mu(H) = \mu_0 + \mu' \, exp(-H/H_c)$ with the values for the parameters μ_0, μ' and H_c at $T = 1.8K$ specified in the insets. From these values, it is clear that at temperatures well below T_c, $\mu = 0$ only in the limit $H \to 0$, as has already been concluded above.

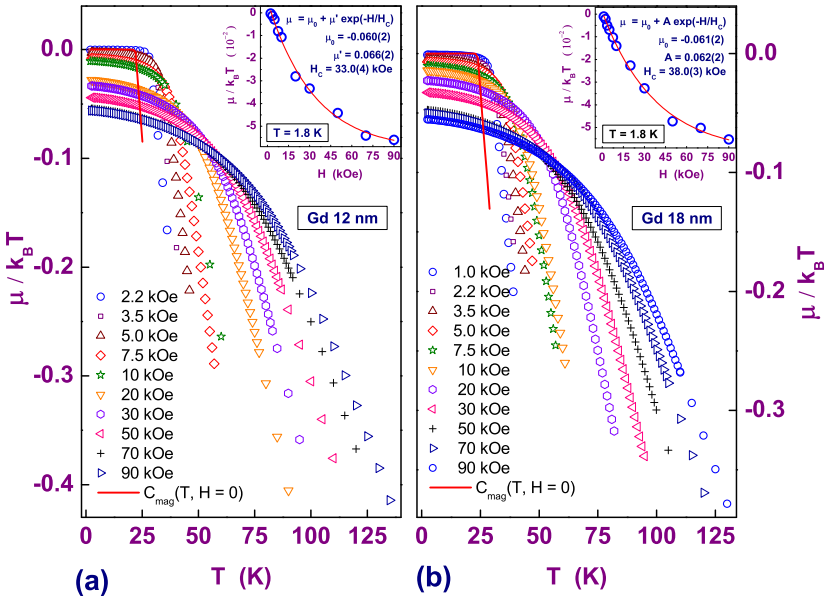

Figure 5.9: The temperature variations of the normalized chemical potential, μ/k_BT, at various fixed field values for (a) d = 12 nm and (b) d = 18 nm. Insets show the typical variation of the chemical potential with magnetic field at a representative temperature, $T = 1.8K$, well below T_c. The chemical potential approaches zero as $T \to 0$ and drops exponentially with H.

5.3.2 Specific Heat

Next, we proceed to cross-check whether BEC of magnons forms a proper description of the magnon part, C_{mag}, of the specific heat, C_p, as well. Recalling that

$$C_H(T) = C_{el}(T) + C_{ph}(T) + C_{mag}(T) \tag{5.43}$$

with the electronic (el), phonon (ph) and magnon (mag) contributions given by

$$C_{el}(T) = \gamma\ T \tag{5.44}$$

$$C_{ph}(T) = 9\ N\ k_B\ \left(\frac{T}{\Theta_D}\right)^3\ \int_0^{\Theta_D/T}\ dx\ \frac{x^4\ e^x}{(e^x-1)^2} \tag{5.45}$$

and Eq.(5.39), respectively, least-squares fits to the $C_H(T)$ data are attempted based on the equations (6.29), (5.30), (5.39), (5.43) - (5.45) by treating γ, Θ_D, V and T_c as free fitting parameters while keeping $D(0)$ and D_2 fixed at the values (Fig.5.4) obtained earlier from $M(T)$ (so as to limit the number of free parameters to a bare minimum). We follow the same self-consistent procedure as that for $M(T)$ to arrive at the temperature variation of the fugacity $z(T)$ and the optimum theoretical fits (continuous curves in figure 5.10) to the observed $C_H(T)$ (open symbols in Fig.5.10). In order to get a feel for the relative magnitudes of the lattice, electronic and magnon contributions to the specific heat, the temperature variations of $C_{ph}(T)$, $C_{el}(T)$ and $C_{mag}(T)$ at $H = 40kOe$ (representative of those at other fields as well), deduced from the above fits, are also displayed in Fig.5.10. The temperature range over which the BEC picture adequately describes $C_{mag}(T)$, and hence $C_H(T)$, widens with H, e.g., from $1.8K \leq T \leq 25K$ or $29K$ at 'zero-field' (i.e., in the rest-field $\simeq 2\ Oe$ of the superconducting magnet) to $1.8K \leq T \leq 90K$ at $H = 50kOe$. The main

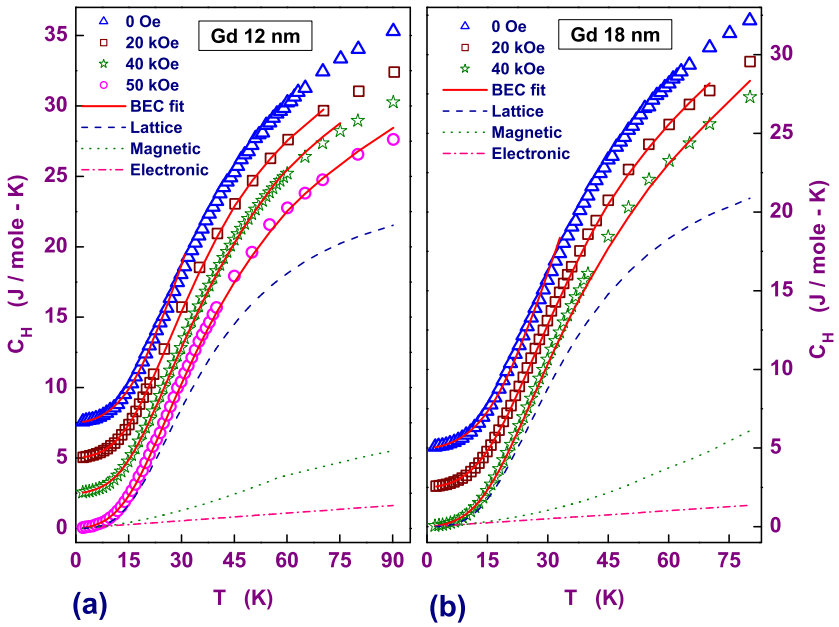

Figure 5.10: The (total) specific heat, C_H, as a function of temperature in zero field (open triangles), at $H = 20kOe$ (open squares), $H = 40kOe$ (open stars) and $H = 50kOe$ (open circles) for (a) d = 12 nm and (b) d = 18 nm. Note that for the sake of clarity, a constant shift of 2.5 $J/mole - K$ in the ordinate scale is given to the successive $C_H(T)$ data. The continuous curves are the optimum fits obtained by adding the electronic, lattice and (BEC) magnon contributions to the specific heat. As an illustration, the temperature variations of the individual electronic, lattice and magnon contributions to the $C_H(T)$ data, taken at $H = 40kOe$, are displayed.

observations, based on the above analysis of the $C_H(T)$ data in terms of the BEC picture, are as follows. (I) At finite magnetic fields (H = 20 kOe, 40 kOe and 50 kOe for d = 12 nm, and H = 20 kOe and 40 kOe for d = 18 nm) common to the magnetization, $M(T,H)$, and specific heat, $C_H(T)$, measurements, the values of $T_c(H)$, the phase coherence volume, $V(H)$, and fugacity $z(T,H)$ or chemical potential $\mu(T,H)$ determined from both the sets of data over the same/similar temperature ranges, match exactly (figures 5.3, 5.5, 5.7 - 5.9). Moreover, the values of $T_c(H=0)$ obtained by extrapolating the $T_c(H)$ data, deduced from $M(T,H)$, to $H=0$, using the characteristic BEC relation $T_c(H) = T_c(H=0) + a\ H^{2/3}$, are in perfect agreement with those ($T_c = 16.5(5)K$ and $20.5(5)K$ for d = 12 nm and d = 18 nm, respectively) directly determined from $C_{mag}(T, H=0)$. Similarly, the extrapolated 'zero-field' values of $\langle n_0(T=1.8K)\rangle$ and V obtained from the $M(T,H)$ data, i.e., $\langle n_0(T=1.8K, H\rightarrow 0)\rangle$ and $V(H\rightarrow 0)$ in figures 5.3 and 5.6, conform well with the corresponding values extracted from $C_{mag}(T, H=0)$. (II) The BEC fits, shown in Fig.5.10, also yield the parameters relevant to the phonon (lattice) and electronic contributions to specific heat. Debye temperature is *field-independent* but depends on the temperature range, i.e., $\Theta_D = 172(2)K$ $(160(2)K)$ in the range $1.8K \leq T \leq 25K$ $(1.8K \leq T \leq 90K)$ whereas the electronic specific heat coefficient has the *field- and temperature-independent* values $\gamma = 18.1(1)\ mJ/mole - K^2$ for d = 12 nm and $\gamma = 17.0(1)\ mJ/mole - K^2$ for d = 18 nm. The presently determined values for γ and Θ_D, when compared with those, $\gamma = 4.48(7)\ mJ/mole - K^2$ and $\Theta_D = 169(1)K$, previously reported [39] for single crystal Gd, indicate that the electron-electron and/or electron-phonon mass enhancement is quite significant in the nanocrystalline state.

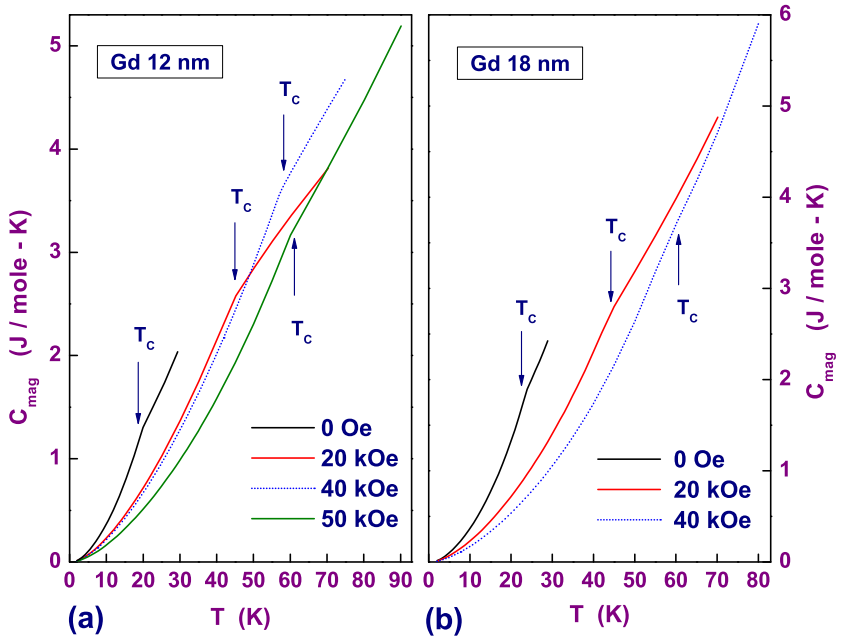

Figure 5.11: The temperature variation of the BEC magnon contribution C_{mag} and the expected slope change at T_c.

As expected for a well-defined BEC phase transition, concomitant with the near-zero chemical potential (i.e., $\mu/k_BT \simeq 0$ or equivalently, $z(T) \simeq 1$) for $T \leq T_c$ and a sharp kink in $\mu(T)/k_BT$ at $T = T_c(H = 0)$ (denoted by solid lines in Fig.5.9), the condensate fraction $\langle n_0(T, H = 0)\rangle/\langle n_0(T = 1.8K, H = 0)\rangle$ decreases linearly with the reduced temperature $[T/T_c(H = 0)]^{3/2}$ (solid lines in Fig.5.8) so as to drop to zero at $T = T_c(H = 0)$, in accordance with Eq.(5.30), and remains zero for $T \geq T_c(H = 0)$ where μ/k_BT exhibits an abrupt linear fall to large negative values with increasing temperature. Alternatively, closer the value of the chemical potential (fugacity) to zero (unity), closer the phase coherence length to infinity. With increasing magnetic field, the chemical potential assumes larger negative values even at temperatures well below $T_c(H = 0)$ and the sharp kink in $\mu(T)/k_BT$ at $T = T_c(H = 0)$, and so also the BEC phase transition, gets smeared out (Fig.5.9) as the phase coherence length shrinks and the BEC condensate fraction drops. Consistent with the above inferences, the BEC magnon contribution to the specific heat as a function of temperature, $C_{mag}(T)$, exhibits a sharp slope change at $T = T_c(H = 0)$, and as H increases, this kink in $C_{mag}(T)$ at $T_c(H)$ progressively loses its sharpness and T_c shifts to higher temperatures, as is evident from figure 5.11.

5.3.3 Magnetic Entropy

Lest the agreement with the BEC theory is misconstrued as an artifact of the self-consistent procedure, the magnetic field-induced change in the magnetic entropy, ΔS_{mag}, was determined from the $M(T)$ data taken at various fixed values of H by using the Maxwell thermodynamic relation $(\partial S_{mag}/\partial H)_T = (\partial M/\partial T)_H$, i.e., $-(\Delta S_{mag})_T = [S_{mag}(H) - S_{mag}(H =$

$0)]_T = \int_0^H (\partial M/\partial T)_H (dH)_T$. Figure 5.12 shows ΔS_{mag}, so obtained at fixed field strengths, plotted against $[T/T_c(H=0)]^{3/2}$, with $T_c(H=0) = 16.5(5)K$ $(20.5(5)K)$ for d = 12 nm (18 nm) obtained from the specific heat data. Fig.5.12 also compares the change in the entropy $-\triangle S_{mag} = S(H = 20kOe) - S(H = 0)$, calculated at different temperatures from Eq.(5.42) using the specific heat, $C_H(T)$, data recorded at $H = 0$ and $H = 20kOe$, with that determined from the $M(T)$ data at $H = 20kOe$. The two sets of data are in good overall agreement. Such a close agreement is observed at higher fields as well. $\Delta S_{mag}(T)$ exhibits a peak (which broadens with increasing field so much so that it becomes completely ill-defined for $H > 20kOe$) at the temperature $T = T_p^\star(\Delta H = H-(H=0))$ and decreases with temperature as $T^{3/2}$ in the limit $T \to 0$ so as to approach zero particularly at low fields. Thus, the field-induced change in magnetic entropy, like the magnetic entropy itself, follows the characteristic BEC behavour (i.e., the $T^{3/2}$ variation at temperatures well below T_c and a slope change at T_c) with the distinction that $T_p^\star(\Delta H)$ does not coincide with $T_c(H)$ except at the lowest field. Since the magnon condensate fraction (with zero entropy) reduces with increasing field (due to the destruction of phase coherence by H), the value of $\Delta S_{mag}(T)$ at $T = 0$ increases with H. Another striking feature is that, even though $T_p^\star(\Delta H)$ lies consistently below $T_c(H)$ for fields $H > 2.2kOe$ and the deviation between the two sets of data grows with H, the variation of $T_p^\star$ with ΔH (represented by crosses in Fig.5.5), like $T_c(H)$, is consistent with the functional form $T_c(H) = T_c(H=0) + aH^{1/\phi}$, with the exponent $\phi = 3/2$, *characteristic* of BEC. Thus, $T_p^\star$ is the characteristic BEC temperature for the *field-induced change* in magnon entropy much the same way as T_c is for *absolute* magnon entropy at a given field ($H = 0$ or $H \neq 0$).

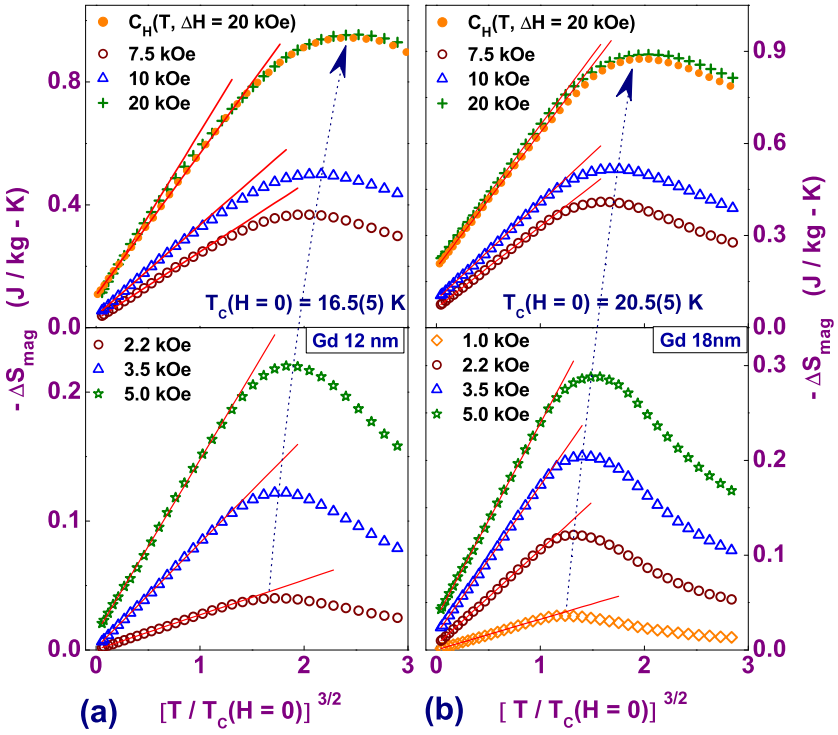

Figure 5.12: Magnetic entropy, $-\Delta S_{mag}$, at various fields obtained from $M(T)$ (open symbols), plotted against $(T/T_c(H=0))^{3/2}$ for (a) d = 12 nm and (b) d = 18 nm. The continuous straight lines through the data serve to highlight the $T^{3/2}$ variation of entropy for temperatures well below T_c. The peak temperature, $T_p{}^{\star}$, shifts to higher temperatures with increasing field. The $-\Delta s_{mag}$, calculated from the change in specific heat, $C_H(T, \Delta H)$, caused by a change in the external magnetic field of $\Delta H = 20kOe$ conforms well with the $-\Delta s_{mag}$ calculated from $M(T, \Delta H = 20kOe)$.

5.3.4 Comparison with Known BEC Systems

Next, nc-Gd is compared with the systems that are known to undergo BEC of magnons. In spin-gap/spin-dimer compounds (yttrium iron garnet films), the applied magnetic field (microwave parametric pumping) tunes the system to the quantum critical point (critical quasi-equilibrium magnon density) so as to *induce* BEC. By contrast, as is the case for an ideal BEC, the temperature drives the BEC transition in nc-Gd. The applied field needed to induce BEC in quantum antiferromagnets is often quite large and hence for a direct comparison with the theory, the bulk properties cannot be measured in the BEC regime with the same ease as in nc-Gd, where a true BEC phase transition occurs in zero-field (Fig.5.8 and 5.9). This makes nc-Gd a unique system in which the BEC picture can be put to a stringent test. Moreover, as in nc-Gd, the deviations from the conventional spin-wave behavior of magnetization at low temperatures, observed previously in elongated Fe nanoparticles [40], ferrite nanoparticles [41] and Co/Pt nanopillars [42], could well be the manifestation of the BEC of magnons. Thus, nanocrystalline/nanostructured magnets may form an entirely new class of magnon BEC systems.

5.4 Summary and Conclusion

High-precision magnetization, $M(T, H)$, and specific heat, $C(T, H)$, measurements have been performed on nanocrystalline gadolinium samples of average grain size d = 12 nm and 18 nm over wide ranges of temperature (T) and magnetic fields (H). Recognizing the limitation of the conventional spin-wave (SW) theory to correctly describe the $M(T, H)$ and $C(T, H)$ data

and that due to magnon-magnon interactions, the magnon number is not conserved, the assembly of magnons is treated as the grand canonical ensemble and the Hamiltonian, Eq.(6.23), accordingly includes the temperature- and magnetic field-dependent chemical potential. From the expressions for the magnon contributions to $M(T,H)$ and $C(T,H)$, so derived, the Bose-Einstein Condensation (BEC) transition temperature, $T_c(H)$, the volume, $V(H)$, (length, $L(H) = V(H)^{1/3}$) over which the condensate wavefunction retains its *spontaneous* phase coherence, the chemical potential, $\mu(T,H)$, and the average occupation number for the ground state, $\langle n_0(T,H)\rangle$, are accurately determined using a self-consistent approach. Increase in the average grain size from d = 12 nm to d = 18 nm enhances the transition temperature $T_c(H=0)$ from 16.5 K to 20.5 K but drastically reduces the spontaneous phase coherence length of the BE condensate wavefunction. The variation of T_c with magnetic field has the characteristic BEC form $T_c(H) = T_c(H=0) + a\,H^{2/3}$. In conformity with the predictions of the BEC theory, (i) the condensate fraction $\langle n_0(T,H)\rangle/\langle n_0(T=1.8K,H)\rangle$ decreases linearly with the reduced temperature $[T/T_c(H)]^{3/2}$ at constant fields for $T < T_c(H)$, (ii) in the limit $H \rightarrow 0$, $\mu(T,H) \cong 0$ (the condensate fraction scales with $[T/T_c(H=0)]^{3/2}$ so as to drop to zero at $T_c(H=0)$) for $T \leq T_c$ and abruptly falls to large negative values (remains zero) as the temperature exceeds T_c, and (iii) the magnetic field-induced change in magnon entropy, deduced from both $M(T,H)$ and $C(T,H)$, follows the $T^{3/2}$ power law at low temperatures $T \ll T_p^{\star}$ and goes through a peak at $T_p^{\star}$. Both $T_c(H)$ and $T_p^{\star}(\Delta H = H - (H=0))$ follow the BEC $H^{2/3}$ law but T_c is the BEC temperature for the *absolute* magnon entropy at a given field ($H = 0$ or $H \neq 0$) while $T_p^{\star}$ is the BEC temperature for the *field-induced change* in magnon entropy.

Based on the above-mentioned observations, we arrive at the following intuitive picture of Bose-Einstein Condensation (BEC) of magnons in nanocrystalline (n-) gadolinium. In the absence of the external magnetic field, the interplay between the intra-grain and interfacial (grain boundary) anisotropies [43] in n-Gd results in a non-collinear spin state with reduced spin-wave stiffness (softening of spin wave modes) and spontaneous phase coherence of magnon BE condensate wavefunction as the temperature falls below the BEC transition temperature T_c, which is well-defined only when $H = 0$. Increasing the average grain size alters the interfacial anisotropy, in particular, and thereby the interplay. Modified interplay, in turn, causes a reduction in the non-collinearity, increases the spin-wave stiffness D, suppresses the spontaneous phase coherence and hence the condensate fraction. Considering that the mass m^* of a Boson (magnon) in Eq.(6.18) is related to $D \equiv D(T = 0, H = 0)$ as $m^* = \hbar^2/2D$, m^* decreases as D increases and consequently, it follows from Eq.(6.18) that T_c increases with average grain size provided the occupation number density $\langle n_0(T = 1.8K)\rangle/V$ remains unaltered, as is presently the case (Fig.5.3). Magnetic field tends to make the spin structure more collinear, destroy phase coherence and reduce the average occupation number for the ground state $\langle n_0(T = 1.8K)\rangle$ (Fig.5.3) such that $\langle n_0(T = 1.8K)\rangle/V$ increases with H and so does T_c in accordance with Eq.(6.18).

References

1. M. H. Anderson, J. R. Ensher, S. R. Mathews, C. E. Wieman and E. A. Cornell, *Science* **269**, 198 (1995).

2. H. Fröhlich, *Phys. Lett. A* **26**, 402 (1968).

3. S. A. Moskalenko and D. W. Snoke, *Bose-Einstein Condensation of Excitons and Biexcitons* (Cambridge University Press, Cambridge, 2000).

4. L. P. Pitaevskii and S. V. Iordanskii, *Sov. Phys. Usp.* **23**, 317 (1980).

5. V. B. Timofeev, V. D. Kulakovskii and I. V. Kukushkin, *Physica (Amsterdam)* **117 & 118B**, 327 (1983).

6. N. Peyghambarian, L. L. Chase and A. Mysyrowicz, *Phys. Rev. B* **27**, 2325 (1983).

7. P. G. Savvidis, J. J. Baumberg, R. M. Stevenson, M. S. Skolnick, D. M. Whittaker and J. S. Roberts, *Phys. Rev. Lett.* **84**, 1547 (2000).

8. O. V. Misochko, M. Hase, K. Ishioka and M. Kitajima, *Phys. Lett. A* **321**, 381 (2004).

9. M. Jaime, V. F. Correa, N. Harrison, C. D. Batista, N. Kawashima, Y. Kazuma, G. A. Jorge, R. Stern, I. Heinmaa, S. A. Zvyagin, Y. Sasago and K. Uchinokura, *Phys. Rev. Lett.* **93**, 087203 (2004).

10. M. Kofu, H. Ueda, H. Nojiri, Y. Oshima, T. Zenmoto, K. C. Rule, S. Gerischer, B. Lake, C. D. Batista, Y. Ueda and S. -H. Lee *Phys. Rev. Lett.* **102**, 177204 (2009).

11. A. A. Aczel, Y. Kohama, M. Jaime, K. Ninios, H. B. Chan, L. Balicas, H. A. Dabkowska and G. M. Luke *Phys. Rev. B* **79**, 100409 (2009).

12. A. A. Aczel, Y. Kohama, C. Marcenat, F. Weickert, M. Jaime, O. E. Ayala-Valenzuela, R. D. McDonald, S. D. Salesnic H. A. Dabkowska and G. M. Luke *Phys. Rev. Lett.* **103**, 207203 (2009).

13. A. Oosawa, T. Takamasu, K. Tatani, H. Abe, N. Tsujii, O. Suzuki, H. Tanaka, G. Kido and K. Kindo, *Phys. Rev. B.* **66**, 104405 (2002).

14. N. Cavadini, Ch. Rüegg, A. Furrer, H. -U. Güdel, K. Krämer, H. Mutka and P. Vorderwisch, *Phys. Rev. B.* **65**, 132415 (2002).

15. T. Kato, K. Takatsu, H. Tanaka, W. Shiramura, M. Mori, K. Nakajima and K. Kakurai, *J. Phys. Soc. Jpn.* **67**, 752 (1998).

16. C. Rüegg, N. Cavadini, A. Furrer, H. -U. Güdel, K. Krämer, H. Mutka, A. Wildes, K. Habicht and P. Vorderwisch, *Nature* **423**, 62 (2003).

17. T. Nikuni, M. Oshikawa, A. Oosawa and H. Tanaka, *Phys. Rev. Lett.* 84, 5868 (2000).

18. H. Tanaka, A. Oosawa, T. Kato, H. Uekusa, Y. Ohashi, K. Kakurai and A. Hoser, *J. Phys. Soc. Jpn.* **70**, 939 (2001).

19. A. Oosawa, M. Ishii and H. Tanaka, *J. Phys.: Condens. Matter* **11**, 265 (1999).

20. F. Yamada, T. Ono, H. Tanaka, G. Misguich, M. Oshikawa and T. Sakakibara, *J. Phys. Soc. Jpn.* **77**, 013701 (2008).

21. W. Shiramura, K. Takatsu, B. Kurniawan, H. Tanaka, H. Uekusa, Y. Ohashi, K. Takizawa, H. Mitamura and T. Goto, *J. Phys. Soc. Jpn.* **67**, 1548 (1998).

22. B. Wolf, S. Zherlitsyn, S. Schmidt, H. Schwenk, B. Lüthi, H. Kageyama, Y. Ueda and H. Tanaka, *J. Mag. Mag. Mater.* **226-230**, 1973 (2001).

23. B. S. Conner, H. D. Zhou, Y. J. Jo, L. Balicas, C. R. Wiebe, J. P. Carlo, Y. J. Uemura, A. A. Aczel, T. J. Williams and G. M. Luke, *Phys. Rev. B* **81**, 132401 (2010).

24. T. Radu, H. Wilhelm, V. Yushankhai, D. Kovrizhin, R. Coldea, Z. Tylczynski, T. Lühmann and F. Steglich, *Phys. Rev. Lett.* **95**, 127202 (2005).

25. L. Yin, J. S. Xia, V. S. Zapf, N. S. Sullivan and A. Paduan-Filho, *Phys. Rev. Lett.* **101**, 187205 (2008).

26. S. O. Demokritov, V. E. Demidov, O. Dzyapko, G. A. Melkov, A. A. Serga, B. Hillebrands and A. N. Slavin, *Nature* **443**, 80 (2006).

27. D. Snoke, *Nature* **443**, 403 (2006).

28. A. I. Bugrij and V. M. Loktev, *Low Temp. Phys.* **33**, 37 (2007).

29. S. O. Demokritov, V. E. Demidov, O. Dzyapko, G. A. Melkov and A. N. Slavin, *New J. Phys.* **10**, 045029 (2008).

30. V. N. Glaskov, A. I. Smirnov, H. Tanaka and A. Oosawa, *Phys. Rev. B* **69**, 184410 (2004).

31. A. V. Chumak et. al., *Phys. Rev. Lett.* **102**, 187205 (2009).

32. Kersen Haung, *Statistical mechanics* (John Wiley, New York, 1963) p **262**

33. T. Izuyama and R. Kubo, *J. Appl. Phys.* **35**, 1074 (1964).

34. S. N. Kaul, Handbook of Magnetism and Advanced Magnetic Materials *Fundamentals and Theory* vol **1**, ed Kronmüller H and Parkin S (John Wiley, New York, 2007) p 305

35. S. P. Mathew, S. N. Kaul, A. K. Nigam, A. -C. Probst and R. Birringer, *J. Phys. :Conf. Ser.* **200**, 072047 (2010).

36. J. W. Cable, R. M. Nicklow and N. Wakabayashi, *Phys. Rev. B* **32** 3 1710 (1985).

37. O. Nohadani, S. Wessel, B. Normand and S. Hass, *Phys. Rev. B* **69**, 220402 (2004).

38. T. Giamarchi and A. M. Tsvelik, *Phys. Rev. B* **59**, 17 11398 (1999).

39. R. W. Hill, S. J. Collocott, K. A. Gschneidner and F. A. Schmidt, *J. Phys. F: Met. Phys.* **17**, 1867 (1987).

40. P. Crespo, J. M. González, A. Hernando and F. J. Yndurain, *Phys. Rev. B* **69**, 012403 (2004).

41. K. Mandal, S. Mitra and P. A. Kumar, *Europhys. Lett.* **75**, 618 (2006).

42. L. H. Bennett and E. Della Torre, *Physica B* **403**, 324 (2008).

43. S. N. Kaul and S. P. Mathew, *Nanosci. Nanotech. Lett.* at press (2011).

Chapter 6

Magnetocaloric Effect (MCE)

6.1 Introduction

The magnetocaloric effect (MCE) is the *adiabatic* temperature change (ΔT_{ad}), either heating or cooling, in magnetic materials due to the application of magnetic field. *Isothermal* entropy change (ΔS) is also a parameter to describe the MCE. Initially, MCE, known as *adiabatic demagnetization*, was used to achieve temperature less than 1 K using paramagnetic salts. As expected, the maximum field-induced change in magnetic entropy occurs around the ferromagnetic-to-paramagnetic transition temperature, T_C. Realizing this fact, the application of MCE for magnetic cooling in a wide temperature range including room temperature, and even higher, was investigated in the pioneer experimental work by *Brown* in 1976 [1]. He suggested the use of ferromagnetic rare-earths or rare-earth based compounds with a Curie temperature in or around room temperature for magnetic re-

The following article is based on the results presented in this Chapter:
1. S. P. Mathew and S. N. Kaul, *Appl. Phys. Lett.*, **98**, 172505 (2011).

frigeration (MR). Among such systems, gadolinium turned out to be the most suitable working material for magnetic refrigeration in a temperature range around room temperature because Gd has a T_C of 293 K concomitant with a maximum *adiabatic* temperature change of ~ 14 K for $\Delta H = 70$ kOe [1]. In the recent years, MCE has attracted considerable attention because of its potential application in the energy-efficient and environment-friendly refrigeration technology over a vast temperature regime including room temperature [2, 3]. MCE is also used as a complimentary tool to understand the thermodynamics in magnetic materials.

The magnetic cooling efficiency of a magnetocaloric material is evaluated by the relative cooling power (RCP), which is defined as the product of the maximum (max) *isothermal* entropy change, $\triangle S_{mag}(T,H)$, or *adiabatic* temperature change, $\triangle T_{ad}(T,H)$, during the magnetization process, and the corresponding full-width-at-half-maximum (δT_{FWHM}), i.e.,

$$RCP(S) = \Delta S_{mag}(T,H)^{max} \times \delta T_{FWHM} \tag{6.1}$$

$$RCP(T) = \Delta T_{ad}(T,H)^{max} \times \delta T_{FWHM} \tag{6.2}$$

Figure 6.1 shows how $\triangle {S_{mag}}^{max}$ (or $\triangle {T_{ad}}^{max}$) and δT_{FWHM} are evaluated from a typical $-\Delta S_{mag}(T)$ data. In view of Eqs.(1) and (2), for a material to qualify for MR at room temperature, three main requirements have to be met. The material should possess: (i) a large $\triangle S_{mag}(T,H)$ and $\triangle T_{ad}(T,H)$, (ii) a peak in $\triangle S_{mag}(T,H)$ and $\triangle T_{ad}(T,H)$ (which usually occurs at the ferromagnetic (FM) to paramagnetic (PM) transition temperature, T_C) at or near room temperature, and (iii) sufficiently large δT_{FWHM} of the $\triangle S_{mag}(T,H)$ and $\triangle T_{ad}(T,H)$ peak. MCE has been investigated in a very large number and a wide variety of systems [2, 3, 4, 5, 6] with a

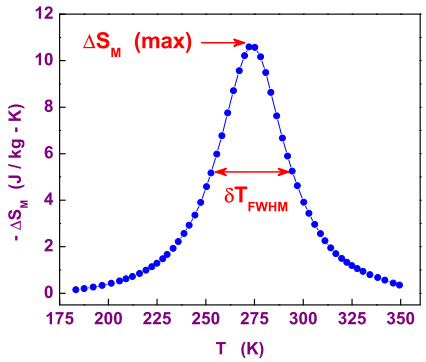

Figure 6.1: The evaluation of relative cooling power based on the temperature dependence of magnetic entropy change.

view to find a material with sufficiently large RCP near room temperature over a reasonably wide temperature range. Much higher *adiabatic* temperature change has been reported [7] in Gd based alloy, $Gd_5(Si_2Ge_2)$, with $\Delta T_{ad} \sim 15\ K$ for $\Delta H = 50\ kOe$, but at $T_C = 276\ K$ and over a very narrow temperature range and hence a much less RCP. This rules out $Gd_5(Si_2Ge_2)$ from being used as a working material for room temperature magnetic refrigeration. Efforts to replace Gd metal or Gd-based alloys/compounds as a prototype magnetic refrigerant material did not succeed so far. In most cases, a relatively small δT_{FWHM} is the main culprit.

In this thesis, a simple strategy to overcome this bottleneck has been proposed. In FM systems of *infinite* size, the critical fluctuations of spontaneous magnetization (order parameter) have maximum amplitude and are correlated over infinite distance (i.e., the spin-spin correlation length, ξ, diverges) at $T_C(\infty)$. In an *isothermal* magnetization process, the maximum

change in magnetic entropy occurs at T_C as the spin fluctuations with the greatest amplitude at T_C get suppressed by magnetic field. Finite size of a system (e.g., a grain of nanometer size) limits the divergence of ξ and thereby causes a size-dependent shift in T_C to lower temperatures (better known as the finite-size scaling). In a nanocrystalline (nc-) sample, distribution of nanocrystallite sizes thus gives rise to a distribution of $T_C's$. Since critical fluctuations have a much larger amplitude at T_C in bulk FM systems than in their nanocrystalline counterparts, the *isothermal* change in magnetic entropy at T_C caused by an applied magnetic field of given strength is greater in the former case. However, the reduction in the maximum $\triangle S_{mag}$ or $\triangle T_{ad}$ is offset to a large extent by an appreciable increase in δT_{FWHM} due to the distribution of $T_C's$ in nanocrystalline systems. The results of detailed magnetization and specific heat measurements performed on the nc-Gd samples with average grain sizes of $d = 12nm$ and $18nm$ demonstrate that this strategy indeed works.

6.2 Theoretical Considerations

The Gibbs free energy, G, as a function of entropy, S, and external magnetic field, H, is given by

$$G = U - TS - MH \tag{6.3}$$

with the total differential in the case of an isobaric process

$$dG = -S\ dT - M\ dH \tag{6.4}$$

For the Gibbs free energy, G, the internal parameters (generalized thermodynamic quantities) S, and M, conjugated to the external variables T, and

H, can be determined by the following equations of state

$$S(T,H) = -\left(\frac{\partial G}{\partial T}\right)_H \tag{6.5}$$

$$M(T,H) = -\left(\frac{\partial G}{\partial H}\right)_T \tag{6.6}$$

6.2.1 Isothermal Entropy Change

The Maxwell equation can be obtained from Eqs.(7.5) and (7.6) as

$$\left(\frac{\partial S(T,H)}{\partial H}\right)_T = \left(\frac{\partial M(T,H)}{\partial T}\right)_H \tag{6.7}$$

Integrating Eq.(7.7) gives the *isothermal* entropy change, ΔS, for a magnetic field change, ΔH, from 0 to H as

$$\Delta S(T,H) = \int_0^H \left(\frac{\partial M(T,H)}{\partial T}\right)_H dH \tag{6.8}$$

The heat capacity C at constant H is defined as

$$C_H = \left(\frac{\delta Q}{dT}\right)_H \tag{6.9}$$

where δQ is the quantity of heat that changes the system temperature by dT. Using second law of thermodynamics

$$dS = \frac{\delta Q}{T} \quad ; \tag{6.10}$$

the heat capacity can be represented as

$$C_H = T\left(\frac{\partial S}{\partial T}\right)_H \tag{6.11}$$

From Eq.(7.11), the *isothermal* entropy change, ΔS, corresponding to a magnetic field change, ΔH, from 0 to H, can be obtained as

$$\Delta S(T,H) = \int_0^T \frac{C(T,H) - C(T,H=0)}{T}\, dT \tag{6.12}$$

6.2.2 Adiabatic Temperature Change

The total differential of the total entropy of the magnetic system expressed as a function of T and H can be written as

$$dS = \left(\frac{\partial S}{\partial T}\right)_H dT + \left(\frac{\partial S}{\partial H}\right)_T dH \tag{6.13}$$

Using Eqs.(7.7), (7.11) and (7.13), following equation can be obtained for an *adiabatic* process ($dS = 0$)

$$\frac{C_H}{T} dT + \left(\frac{\partial M}{\partial T}\right)_H dH = 0 \tag{6.14}$$

In an *adiabatic* process, an infinitesimal change in temperature due to the change of magnetic field, from Eq.(7.14), is

$$dT = -\frac{T}{C_H}\left(\frac{\partial M}{\partial T}\right)_H dH \tag{6.15}$$

From Eq.(7.15) yields the *adiabatic* temperature change, ΔT_{ad}, correspondinf to a magnetic field change, ΔH, from 0 to H, as

$$\Delta T_{ad}(T,H) = -\int_0^H \left(\frac{T}{C(T,H)}\right)_H \left(\frac{\partial M(T,H)}{\partial T}\right)_H dH \tag{6.16}$$

In general, both T and $C(T,H)$ cannot be moved out of the integral in Eq.(7.16), as $C(T,H)$ strongly depends on both T and H, and is always changing with the change in magnetic field. Eq.(7.16) can be rewritten using *integration by parts* as [8, 9]

$$\begin{aligned}
&\int_0^H \left(\frac{T}{C(T,H)}\right)_H \left(\frac{\partial M(T,H)}{\partial T}\right)_H dH \\
&= \left[\frac{T}{C(T,H)} \int_0^H \left(\frac{\partial M(T,H)}{\partial T}\right)_H dH\right]_0^H \\
&- \int_0^H \left[\frac{d}{dH}\left(\frac{T}{C(T,H)}\right)\left\{\int_0^H \left(\frac{\partial M(T,H)}{\partial T}\right)_H dH\right\}\right] dH
\end{aligned} \tag{6.17}$$

In the phase transition region, the value of $T/C(T,H)$ varies much slower compared to $\partial M(T,H)/\partial T$ with field, the second integral in Eq.(7.17) become negligible and ΔT_{ad} can be calculated as

$$\Delta T_{ad}(T,H) = -\left(\frac{T}{C(T,H)}\right)\Delta S(T,H) \tag{6.18}$$

It is clear from Eq.(6.18) that the value of $|\Delta T_{ad}|$ is large when $(\partial M(T,H)/\partial T)_H$ is large and $C(T,H)$ is small at the same initial temperature.

6.3 Measurement Techniques of MCE

The *adiabatic* temperature change, ΔT_{ad} and *isothermal* entropy change, ΔS, which describe the MCE for given materials, can be measured directly or calculated indirectly from the measured magnetization and/or heat capacity. Only ΔT_{ad} can be measured directly. The magnetization measurement can yield only ΔS whereas the 'in-field' heat capacity measurement can give simultaneously both ΔT_{ad} and ΔS. It is also possible to calculate ΔT_{ad} from magnetization provided the heat capacity at zero-field is available.

6.3.1 Direct Method

In the direct method, under *adiabatic* conditions, the change in sample temperature caused by the application of magnetic field is directly measured. During such measurement, rapid change of magnetic field is required to realize the *adiabatic* condition. This can be achieved by subjecting a stationary sample to a pulse field [2] or by rapidly moving the sample in and out of a uniform magnetic field region. The accuracy of the direct measurement

technique is limited to $5-10\%$ due to the errors in thermometry, errors in field setting and the degree of the thermal isolation of the sample.

6.3.2 Indirect Method

Magnetization

The *isothermal* change in magnetic entropy can be calculated from the temperature-dependent magnetization measured at various fixed magnetic fields using Eq.(7.8). The slope of the temperature-dependent magnetization measured at a fixed field, H_n, is determined for a temperature change, $dT = T_{i+1} - T_i$, at an average temperature, $T_{av} = (T_{i+1} + T_i)/2$ as

$$\left(\frac{\partial M(T_{av})}{\partial T}\right)_{H_n} = \left(\frac{M(T_{i+1}) - M(T_i)}{T_{i+1} - T_i}\right)_{H_n} \tag{6.19}$$

ΔS at a fixed temperature, T_{av}, for a change of magnetic field from H_i to H_f is then obtained by numerically integrating $(\partial M(T_{av})/\partial T)_{H_n}$ from H_i to H_f as

$$\begin{aligned}\Delta S = \frac{1}{2}\left\{\left(\frac{\partial M(T_{av})}{\partial T}\right)_{H_i}\delta H_i + \left(\frac{\partial M(T_{av})}{\partial T}\right)_{H_f}\delta H_f\right\} \\ + \sum_{n=2}^{f-1}\left(\frac{\partial M(T_{av})}{\partial T}\right)_{H_n}\delta H_n\end{aligned} \tag{6.20}$$

where δH_n is the field interval between the successive M(T) measurements. To calculate ΔT_{ad} from magnetization data (Eq.(6.18)), ΔS and the specific heat at fixed field, $C(T, H)$, are required. $C(T, H)$ can be obtained from zero-field specific heat using Eq.(7.11) as

$$C(T, H) = C(T, H = 0) + T\left(\frac{\partial \Delta S(T, H)}{\partial T}\right) \tag{6.21}$$

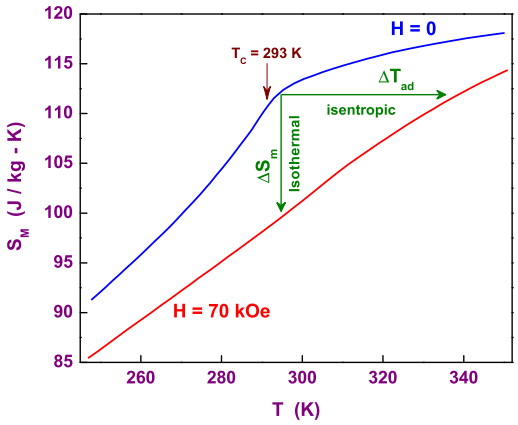

Figure 6.2: Magnetic entropy, S_M, of Gd as a function of temperature for $H = 0$ and $H = 70\ kOe$ [1]. ΔS and ΔT_{ad} are indicated near its Curie temperature

Heat Capacity

Both ΔS and ΔT_{ad} can be determined from $C_H(T)$ measured at various, but fixed, magnetic field (H) values. The total entropy, S, at a fixed field, H, as a function of temperature can be calculated from the temperature-dependent heat capacity C(T,H) as

$$S(T,H) = \int_0^T \frac{C(T,H)}{T}\, dT \tag{6.22}$$

and it can be rewritten as a sum

$$S(T,H) = \frac{1}{2}\sum_{i=1}^{n-1}\left(\frac{C(T_{i+1},H)}{T_{i+1}} + \frac{C(T_i,H)}{T_i}\right)(T_{i+1} - T_i) \tag{6.23}$$

The *isothermal* entropy change, ΔS, for a change in magnetic field is obtained by subtracting the 'zero-field' entropy from the 'in-field' entropy

while the *adiabatic* temperature change, ΔT_{ad}, corresponding to a change in magnetic field is obtained by subtracting the temperature at 'zero-field' from the temperature at a finite field at *constant entropy*, as

$$\Delta T_{ad}(T,H) = T(S,H) - S(S,H=0) \tag{6.24}$$

$$\Delta S(T,H) = S(T,H) - S(T,H=0) \tag{6.25}$$

The method in determining the $\Delta S(T,H)$ and $\Delta T_{ad}(T,H)$ from S(T,H) curves [6] is illustrated in Fig. 6.2 for bulk gadolinium, a ferromagnet with Curie temperature $T_C = 293\ K$ [1]. The difference between the two entropy curves from 'zero-field' to 'in-field' for *isothermal* translation results in ΔS and isentropic subtraction gives ΔT_{ad}.

6.4 Results and Discussion

Magnetization, M, was measured by Superconducting Quantum Interference Device (SQUID) magnetometer (Quantum Design) on nc-Gd samples with average grain sizes of $d = 12\ nm$ and $18\ nm$ as a function of temperature at a number of fixed magnetic fields up to 90 kOe over the temperature range $1.8\ K \leq T \leq 320\ K$. Figure 6.3 displays $M(T,H)$ data for the $d = 12nm$ and $18nm$ nc-Gd samples. Specific heat, $C(T,H)$ was measured by the heat-pulse calorimeter method on the Physical Property Measurement System (PPMS) of Quantum Design make on the nc-Gd samples as a function of temperature at a number of fixed magnetic fields at $H = 0\ Oe$, $20\ kOe$, $40\ kOe$ and $50\ kOe$ over the temperature range $1.8\ K \leq T \leq 320\ K$. Fig.6.4 displays the $C_H(T)$ for $d = 12nm$ and $18nm$ nc-Gd samples. The cusp in $C_{H=0}(T)$ at T_C (285.65(5) K and 287.25(5) K for $d = 12\ nm$ and

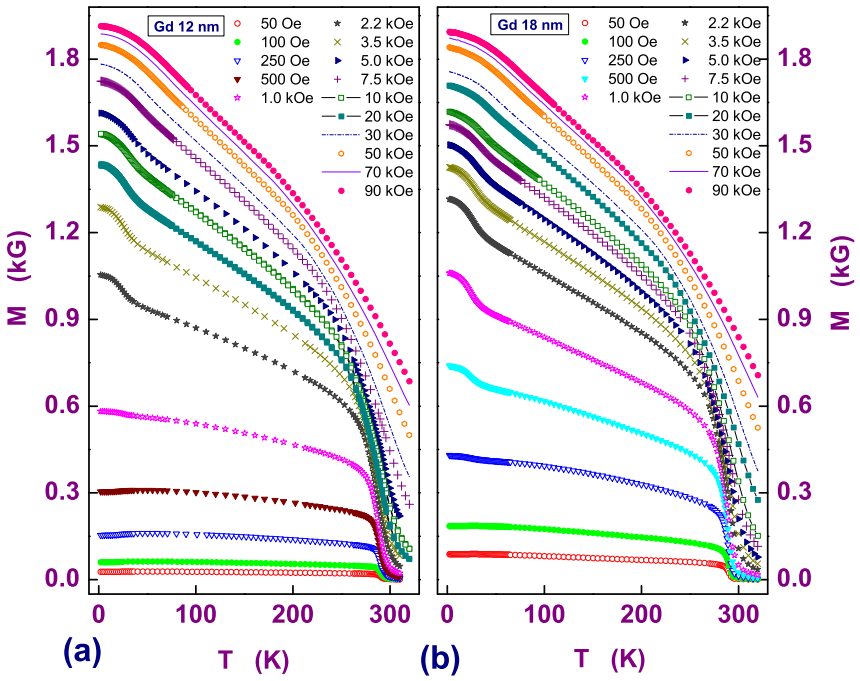

Figure 6.3: Magnetization of nanocrystalline gadolinium with average grain size (a) 12 nm and (b) 18 nm as a function of temperature at fixed fields ranging from 50 Oe to 90 kOe.

18 nm) becomes sharper and the value of $C_{H=0}(T)$ at $T = T_C$, $C_{H=0}(T_C)$, increases as d increases so much so that $C_{H=0}(T)$ in single crystal (sc-) Gd exhibits an extremely sharp cusp at $T_C \simeq 293\ K$ [10] and $C_{H=0}(T_C) = 46.5$, 49.9 and 60.0 J/mol-K for $d = 12nm$, $d = 18nm$ and sc-Gd [10], respectively.

The electronic ($C_{el}(T) = \gamma\ T$) and lattice, $C_{ph}(T)$, (Debye) contributions to the specific heat in the temperature range $1.8\ K \leq T \leq 310\ K$ are generated using the parameters (Θ_D and γ) obtained by fitting the total

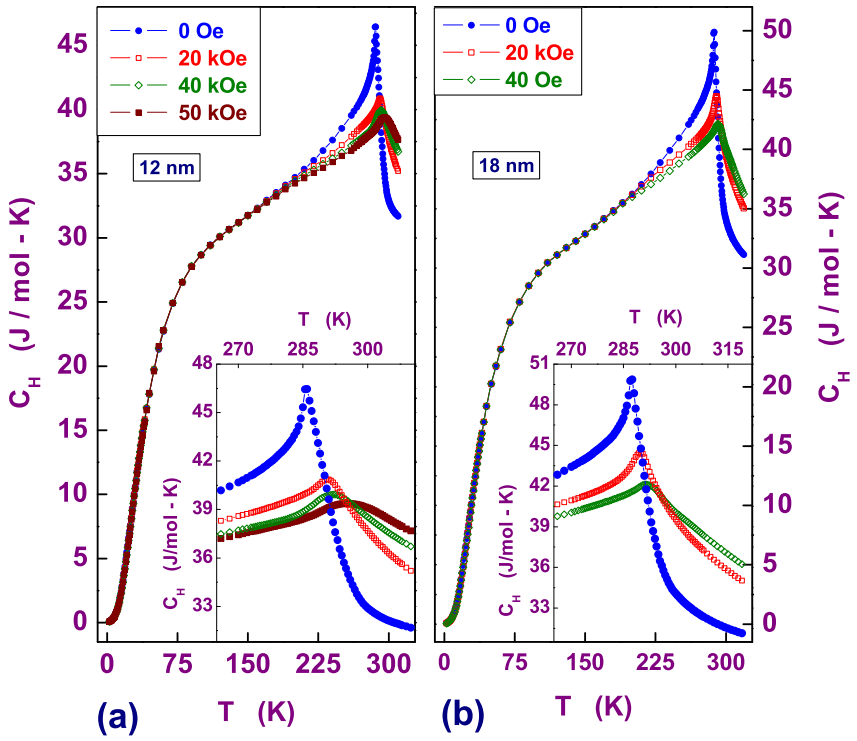

Figure 6.4: Specific heat as a function of temperature at $H = 0\ Oe$, 20 kOe, 40 kOe and 50 kOe, $C_H(T)$ for the nanocrystalline Gd sample with an average grain size of (a) 12 nm and (b) 18 nm. The insets highlight the suppression of the cusp in $C_H(T)$ at T_C by magnetic field.

specific heat ($C_{el}(T) + C_{ph}(T) + C_{mag}(T)$) data in the temperature range 1.8 $K \leq T \leq 25$ K. A detailed discussion of the specific heat results is given in section 4.3.3 (chapter 4).

The magnetic part of specific heat is obtained by subtracting the electronic and lattice contributions from the total specific heat. The electronic, lattice and field-dependent magnetic part of specific heat is displayed in Fig. 6.5. The effect of magnetic field is to progressively suppress the specific heat cusp compared to that in $C_{H=0}(T)$ and shift it to higher temperatures (insets of Fig.6.4). The values of T_C determined from $C_{H=0}(T)$ match those (285.63(2) K for $d = 12nm$ and 287.22(2) K for $d = 18nm$) obtained from an elaborate critical phenomena analysis [11] of the ac susceptibility [12] data taken on the same nc-Gd samples as those used in this work.

6.4.1 *Isothermal* Entropy Change and *Adiabatic* Temperature Change

The *isothermal* magnetic entropy change, $\triangle S_{mag}(T, H)$, and the *adiabatic* temperature change, $\triangle T_{ad}(T, H)$, calculated from the measured magnetization, $M(T, H)$, and specific heat, $C(T, H)$, at different fields, H, using the Maxwell relations, Eqs.(7.8) and (6.18), or from the measured 'zero-field' and 'in-field' specific heat using Eq.(7.12), are plotted against temperature in the range 260 $K \leq T \leq 310$ K in figures 6.6, 6.7, 6.8 and 6.9. At a given field, the $\triangle S_{mag}(T, H)$ values obtained from $M(T, H)$ are in remarkable agreement with those deduced from $C_H(T)$ (Figs. 6.6 and 6.7).

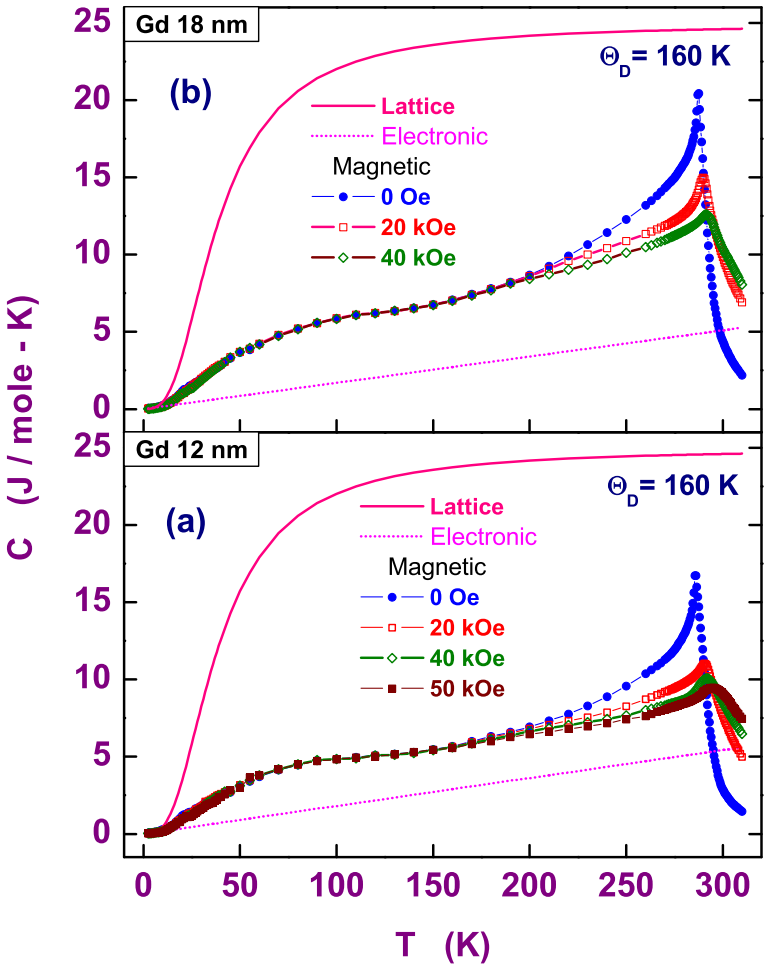

Figure 6.5: The lattice and electronic contribution to specific heat as a function of temperature, generated using the parameters ($\Theta_D = 160\ K$ for both 12 nm and 18 nm and $\gamma = 18.1\ mJ/mole$ for 12 nm and 17.0 $mJ/mole$ for 18 nm) obtained by fitting low-temperature data. The magnetic part of specific heat as a function of temperature at $H = 0\ Oe$, 20 kOe, 40 kOe and 50 kOe for the nanocrystalline Gd sample with average grain size of (a) 12 nm and (b) 18 nm obtained by subtacting the electronic plus lattice contributions from the total (measured) specific heat.

The customary approach of using mean-field (MF) theory to describe $\triangle S_{mag}(T,H)$ and $\triangle T_{ad}(T,H)$ of magnetocaloric materials over a temperature range that embraces the critical region near T_C has met with limited success [6]. Apart from failing to address certain material-specific issues [6], MF theory cannot describe the suppression of critical magnetization fluctuations by H because it neglects spin fluctuations completely. As a step forward, the Arrott-Noakes magnetic equation of state [13] has been used to arrive at the magnetic field dependence of $\triangle S_{mag}$ at $T = T_C$ [14], i.e., $\triangle S_{mag}|_{T=T_C} \sim H^{[(\beta-1)/\Delta]+1}$, where $\Delta = \beta + \gamma$ is the gap exponent while β and γ are the critical exponents for spontaneous magnetization and initial susceptibility, respectively. For the MF values $\beta = 0.5$ and $\gamma = 1$, this relation predicts $\triangle S_{mag}|_{T=T_C} \sim H^{2/3}$, in agreement with the earlier MF result [15]. To obtain a correct theoretical description of $\triangle S_{mag}(T,H)$ within and outside the critical region, we make use of the form of the magnetic equation of state [16]

$$M(\widetilde{\varepsilon},\widetilde{h}) = |\widetilde{h}|^{\beta/\Delta} \;\; \widetilde{f}_{\pm}\left(\frac{|\widetilde{\varepsilon}|}{|\widetilde{h}|^{1/\Delta}}\right) \tag{6.26}$$

in nonlinear scaling variables $\widetilde{\varepsilon} = (T - T_C)/T = \varepsilon/t$; $\varepsilon = (T - T_C)/T_c$ and $\widetilde{h} = H(T_C/T) = H/t$; $t = T/T_C$, that holds [17, 18, 19] over a very wide temperature range around T_C. In Eq.(6.26), $\widetilde{f}_{\pm}$ are the scaling functions for temperatures above (plus) and below (minus) T_C, and these functions approach $\widetilde{f}_0$ (which is analytic at $|\widetilde{\varepsilon}| = 0$) as $\widetilde{\varepsilon} \to 0$. In the limit $|\widetilde{\varepsilon}|/|\widetilde{h}|^{1/\Delta} \ll 1$, the scaling functions $\widetilde{f}_{\pm}(z)$ can be expanded in Taylor series [16] around

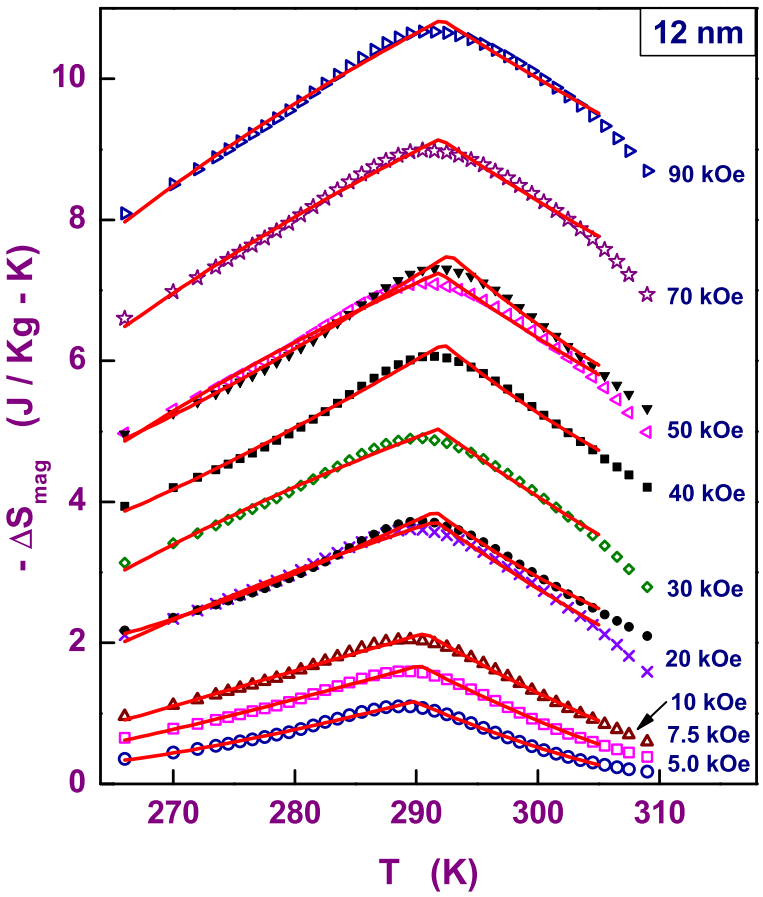

Figure 6.6: The *isothermal* magnetic entropy change computed from the magnetization (open symbols) and specific heat (closed symbols) data taken at several fixed fields in the range 5 $kOe \leq H \leq 90$ kOe on d = 12 nm nanocrystalline Gd. Eq.(6.29) of the text yields the continuous curves through the data.

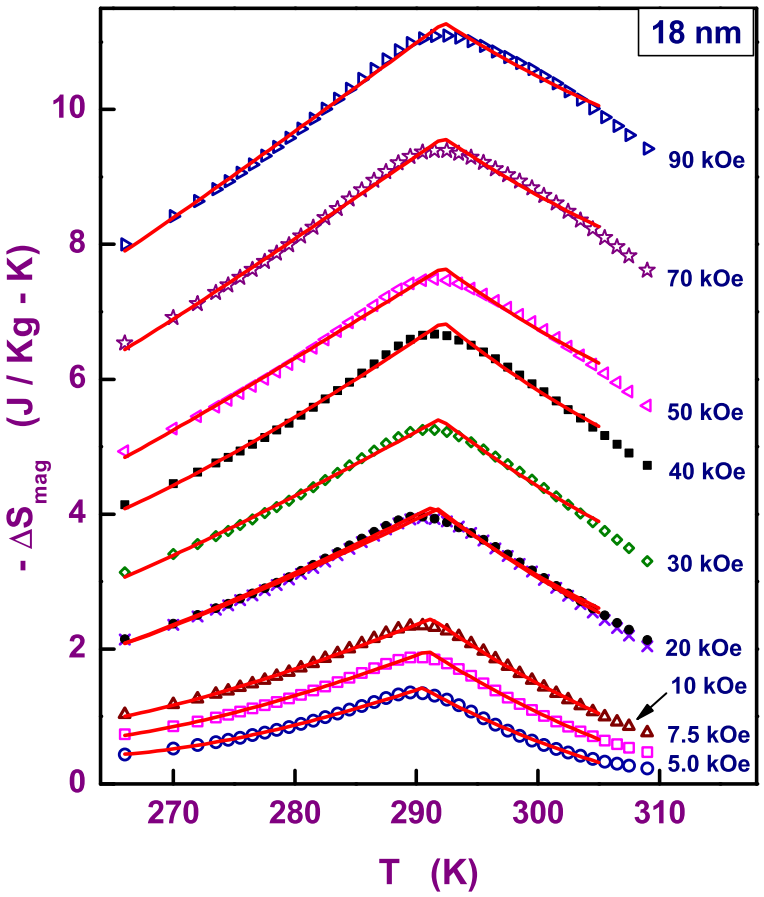

Figure 6.7: The *isothermal* magnetic entropy change computed from the magnetization (open symbols) and specific heat (closed symbols) data taken at several fixed fields in the range 5 $kOe \leq H \leq 90$ kOe on d = 18 nm nanocrystalline Gd. Eq.(6.29) of the text yields the continuous curves through the data.

$z = 0$, i.e., $\widetilde{f}_0(0)$, with the result

$$M(\widetilde{\varepsilon},\widetilde{h}) = |\widetilde{h}|^{\frac{\beta}{\Delta}}\left[\widetilde{f}_0(0) + \frac{|\widetilde{\varepsilon}|}{|\widetilde{h}|^{\frac{1}{\Delta}}}\widetilde{f}_0'(0) + \frac{|\widetilde{\varepsilon}|^2}{2|\widetilde{h}|^{\frac{2}{\Delta}}}\widetilde{f}_0''(0) + \frac{|\widetilde{\varepsilon}|^3}{6|\widetilde{h}|^{\frac{3}{\Delta}}}\widetilde{f}_0'''(0) + \cdots\right]$$
$$= \widetilde{f}_0(0)|\widetilde{h}|^{\frac{\beta}{\Delta}} + \widetilde{f}_0'(0)|\widetilde{\varepsilon}||\widetilde{h}|^{\frac{(\beta-1)}{\Delta}} + \frac{1}{2}\widetilde{f}_0''(0)|\widetilde{\varepsilon}|^2|\widetilde{h}|^{\frac{(\beta-2)}{\Delta}}$$
$$+\frac{1}{6}\widetilde{f}_0'''(0)|\widetilde{\varepsilon}|^3|\widetilde{h}|^{\frac{(\beta-3)}{\Delta}} + \cdots \tag{6.27}$$

Retaining only the first four terms in the expansion to obtain the derivative of $M(T,H)$ with respect to T yields

$$\left(\frac{\partial M(T,H)}{\partial T}\right)_H = -\widetilde{f}_0(0)\left(\frac{\beta}{\Delta}\right)\frac{|\widetilde{h}|^{\frac{\beta}{\Delta}}}{T}$$
$$+\widetilde{f}_0'(0)\left[-\frac{\beta-1}{\Delta}\frac{|\widetilde{h}|^{\frac{(\beta-1)}{\Delta}}}{T}|\widetilde{\varepsilon}| + \frac{1}{t\,T}|\widetilde{h}|^{\frac{(\beta-1)}{\Delta}}\right]$$
$$+\widetilde{f}_0''(0)\left[-\frac{1}{2}\left(\frac{\beta-2}{\Delta}\right)\frac{|\widetilde{h}|^{\frac{(\beta-2)}{\Delta}}}{T}|\widetilde{\varepsilon}|^2 + \frac{|\widetilde{\varepsilon}|}{t\,T}|\widetilde{h}|^{\frac{(\beta-2)}{\Delta}}\right]$$
$$+\widetilde{f}_0'''(0)\left[-\frac{1}{6}\left(\frac{\beta-3}{\Delta}\right)\frac{|\widetilde{h}|^{\frac{(\beta-3)}{\Delta}}}{T}|\widetilde{\varepsilon}|^3 + \frac{1}{2}\frac{|\widetilde{\varepsilon}|^2}{t\,T}|\widetilde{h}|^{\frac{(\beta-3)}{\Delta}}\right] \tag{6.28}$$

When Eq.(6.28) is used in Eq.(7.8), one obtains the final result

$$\triangle S_{mag}(T,H) = a_0\ |\widetilde{h}|^{n_0+1} + a_1\ |\widetilde{h}|^{n_1+1}(t^{-1} - n_1\ |\widetilde{\varepsilon}|)$$
$$+a_2\ |\widetilde{h}|^{n_2+1}\ |\widetilde{\varepsilon}|(t^{-1} - (n_2/2)\ |\widetilde{\varepsilon}|)$$
$$+a_3\ |\widetilde{h}|^{n_3+1}\ |\widetilde{\varepsilon}|^2(t^{-1} - (n_3/3)\ |\widetilde{\varepsilon}|) \tag{6.29}$$

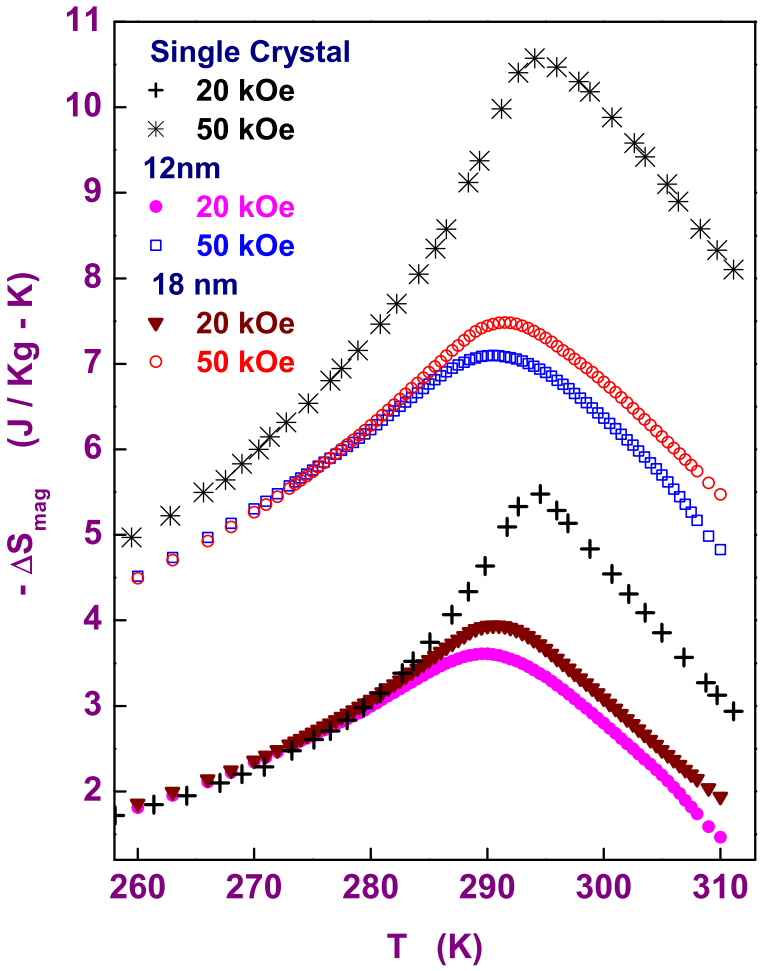

Figure 6.8: Comparison of the *isothermal* magnetic entropy change, $\triangle S_{mag}(T, H)$, observed at $H = 20\ kOe$ and 50 kOe in nanocrystalline Gd having an average grain size of d =12 nm or d = 18 nm with that reported [10] for single crystal Gd.

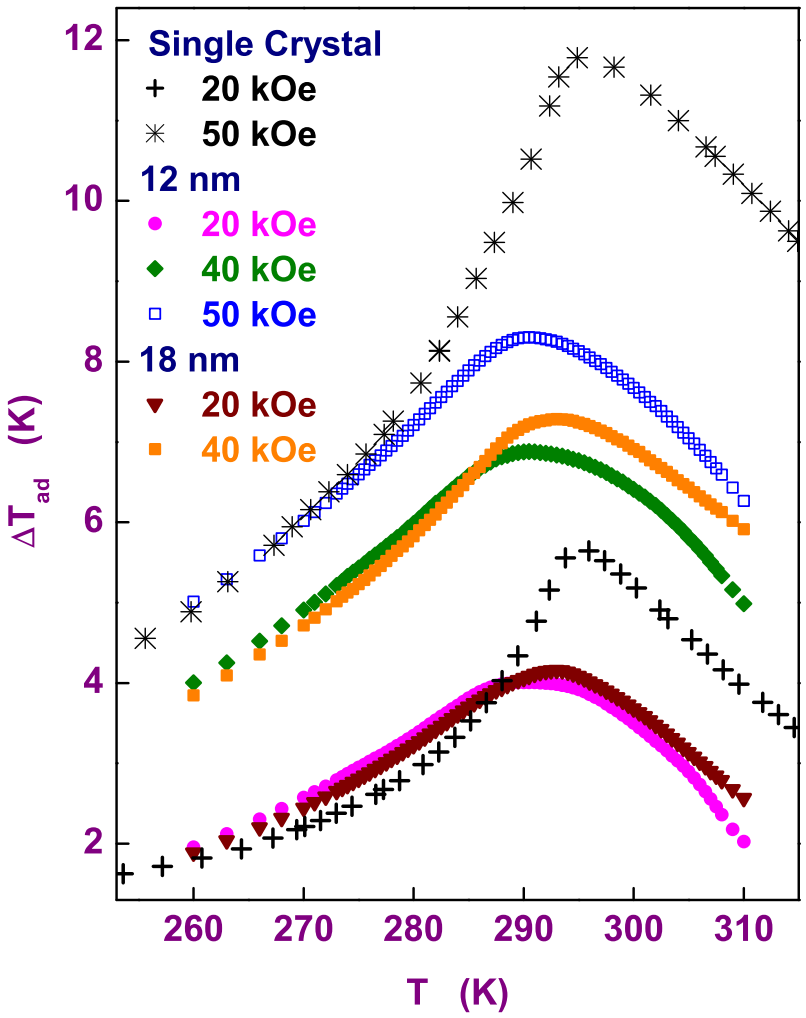

Figure 6.9: Comparison of the *adiabatic* temperature change, $\triangle T_{ad}(T, H)$, observed at $H = 20\ kOe$, 40 kOe and 50 kOe in nanocrystalline Gd having an average grain size of d =12 nm or d = 18 nm with that reported [10] for single crystal Gd.

with

$$
\begin{aligned}
a_0 &= -(\widetilde{f}_0(0)/T_C)\ [n_0/(n_0+1)] \ ; \qquad n_0 = \beta/\Delta \\
a_1 &= (\widetilde{f}_0'(0)/T_C)\ [1/(n_1+1)] \qquad ; \qquad n_1 = (\beta-1)/\Delta \\
a_2 &= (\widetilde{f}_0''(0)/T_C)\ [1/(n_2+1)] \qquad ; \qquad n_2 = (\beta-2)/\Delta \\
a_3 &= (\widetilde{f}_0'''(0)/T_C)\ [1/(n_3+1)] \qquad ; \qquad n_3 = (\beta-3)/\Delta
\end{aligned}
$$

and the derivative functions $\widetilde{f}_0'(0)$, $\widetilde{f}_0''(0)$ and $\widetilde{f}_0'''(0)$, like $\widetilde{f}_0(0)$, treated as constants. The continuous curves through the data in figures 6.6 and 6.7 are obtained by using the MF values $\beta = 0.5$ and $\gamma = 1$, optimizing the parameters a_0, a_1, a_2, a_3, and taking $T_C(H)$ to be the peak temperature at a given field. Eq.(6.29), with the MF choice of critical exponents, adequately describes $\triangle S_{mag}$ over wide ranges of temperature and field but fails to do so in the immediate vicinity of T_{peak}. T_{peak} lies above $T_{_C}$ and increases with H as $H^{1/3}$ such that the difference $T^{peak} - T_{_C}$ increases from $\cong 2.5\ K$ at $H = 5\ kOe$ to $\cong 5\ K$ at $H = 90\ kOe$ (Fig 6.10(b)). Consistent with the above finding that Eq.(6.29) with mean-field exponent values closely reproduces the observed $\Delta S_{mag}(T,H)$ particularly near T_C, at $T = T_C$, $\triangle S_{mag}(T,H)$ does obey the MF prediction $\triangle S_{mag}|_{T=T_{_C}} \sim H^{2/3}$ (Fig.6.10(a)).

Figures 6.8 and 6.9 demonstrate that at $H = 20\ kOe$ and $50\ kOe$, the peak values of $\triangle S_{mag}$ and $\triangle T_{ad}$ at $T = T^{peak}$, $\Delta S_{mag}^{max}|_{T=T^{peak}}$ and $\Delta T_{ad}^{max}|_{T=T^{peak}}$, are reduced by roughly a factor of 1.5 (Fig.6.11) but the corresponding δT_{FWHM} are broader by nearly the same factor of 1.5 (Fig.6.12) in nc-Gd with d = 12 nm and 18 nm compared to those reported [4, 10] previously in sc-Gd. Another important observation is that at a given field, the peaks in $\triangle S_{mag}(T)$ and $\triangle T_{ad}(T)$ shift to lower temperatures, get progressively suppressed and broaden considerably as the average nanocrystallite

size reduces, as expected.

6.4.2 Relative Cooling Power

The relative cooling power (RCP), calculated at different fields from either the *isothermal* entropy change (Fig.6.6 and Fig.6.7), RCP(S), or from the *adiabatic* temperature change (Fig.6.9), RCP(T), using Eqs.(7.1) and (7.2), for the nc-Gd with d = 12nm and 18nm, is compared with that reported [4, 10] for sc-Gd, in figure 6.13 (RCP(S)) and its inset (RCP(T)).

Such a comparison demonstrates that the reduction in the average grain size from a macroscopic size in sc-Gd to d = 12nm in nc-Gd does not alter RCP for fields $H \leq 50\ kOe$ but when $H > 50\ kOe$, RCP, at a given field, increases with the grain size. This is so because the enhancement in δT_{FWHM}, at a given field $H \leq 50\ kOe$, caused by the widening of the grain size distribution as the average grain size decreases, compensates for the reduction in $\triangle S_{mag}(T,H)^{max}$ or in $\triangle T_{ad}(T,H)^{max}$ with the result that the RCP at that field equals, if not exceeds, that of sc-Gd [4, 10]. However, at fixed fields in the range $60\ kOe \leq H \leq 90\ kOe$, RCP *increases* with d because the peak value of $\triangle S_{mag}(T,H)$, or $\triangle T_{ad}(T,H)$ increases but the peak width δT_{FWHM} is either similar in magnitude (e.g. for d = 12 nm and 18 nm) or not large enough compared to that in sc-Gd. The above result vindicates our approach of exploiting the grain size distribution in a nanocrystalline sample to attain reasonably high RCP over a wide temperature range at moderate fields, as required for the magnetic refrigeration applications.

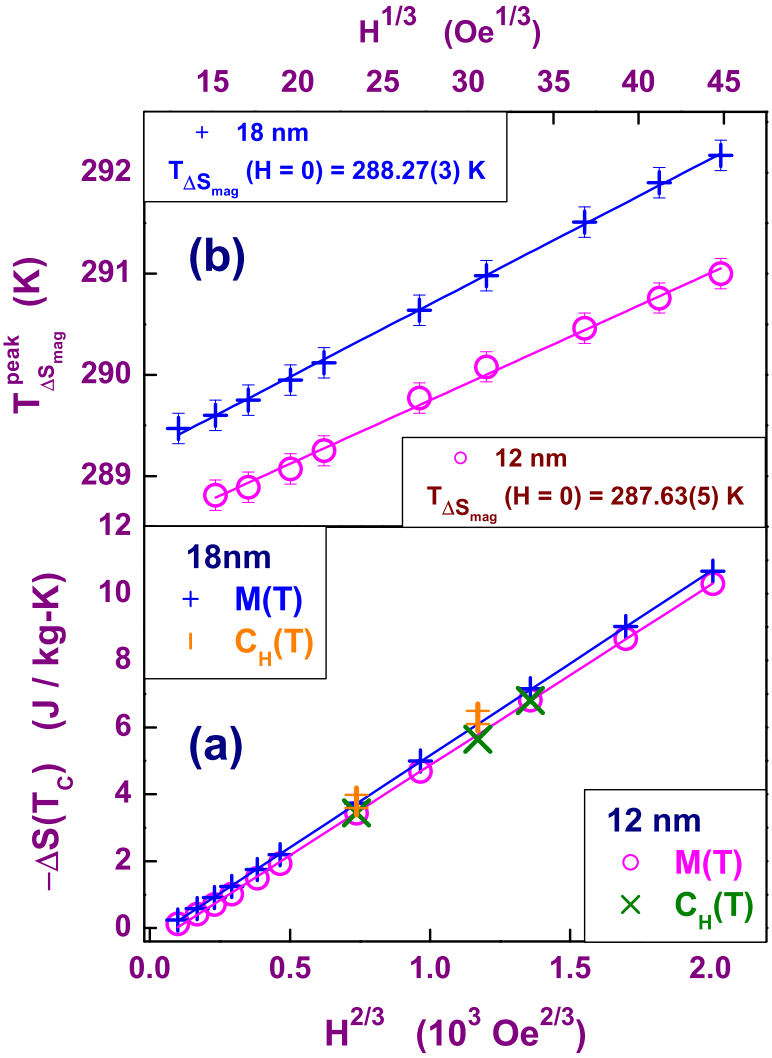

Figure 6.10: (a) The value of $\triangle S_{mag}|_{T=T_C} \sim H^{2/3}$ plotted against $H^{2/3}$ and (b) the temperature at which the peak in $-\triangle S_{mag}$ occurs, T^{peak}, versus $H^{1/3}$.

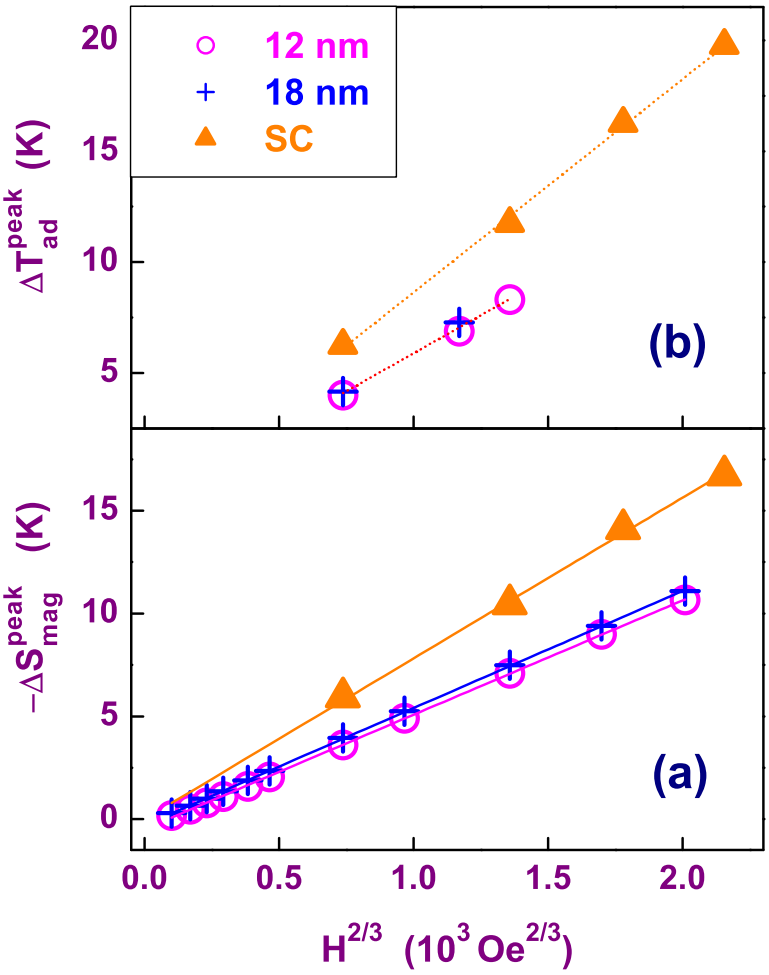

Figure 6.11: The peak value of (a) the isothermal entropy change, $\triangle S_{mag}(T)$, and (b) adiabatic temperature change, $\triangle T_{ad}(T)$, for the nanocrystalline Gd samples with d = 12nm and 18nm as well as for the single crystal (sc) Gd (see Ref. [4] and [10]) plotted against $H^{2/3}$.

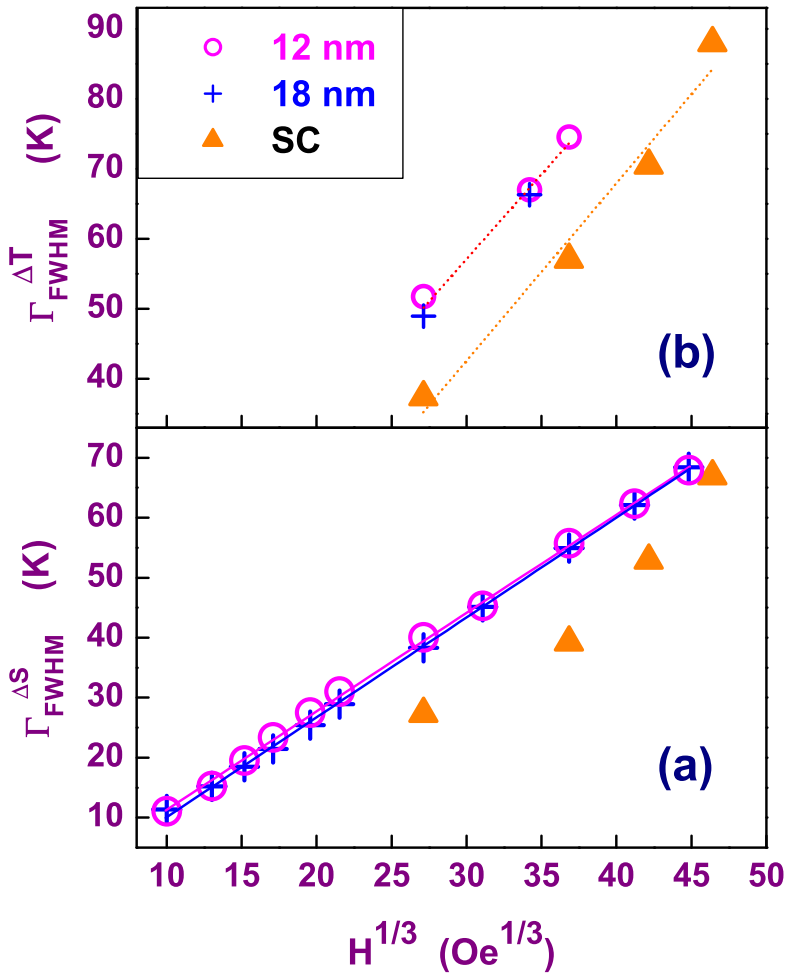

Figure 6.12: The peak width, δT_{FWHM}, of (a) the isothermal entropy change, $\triangle S_{mag}(T)$, and (b) adiabatic temperature change, $\triangle T_{ad}(T)$, for the nanocrystalline Gd samples with d = 12nm and 18nm as well as for the single crystal (sc) Gd (see Ref. [4] and [10]) plotted against $H^{1/3}$.

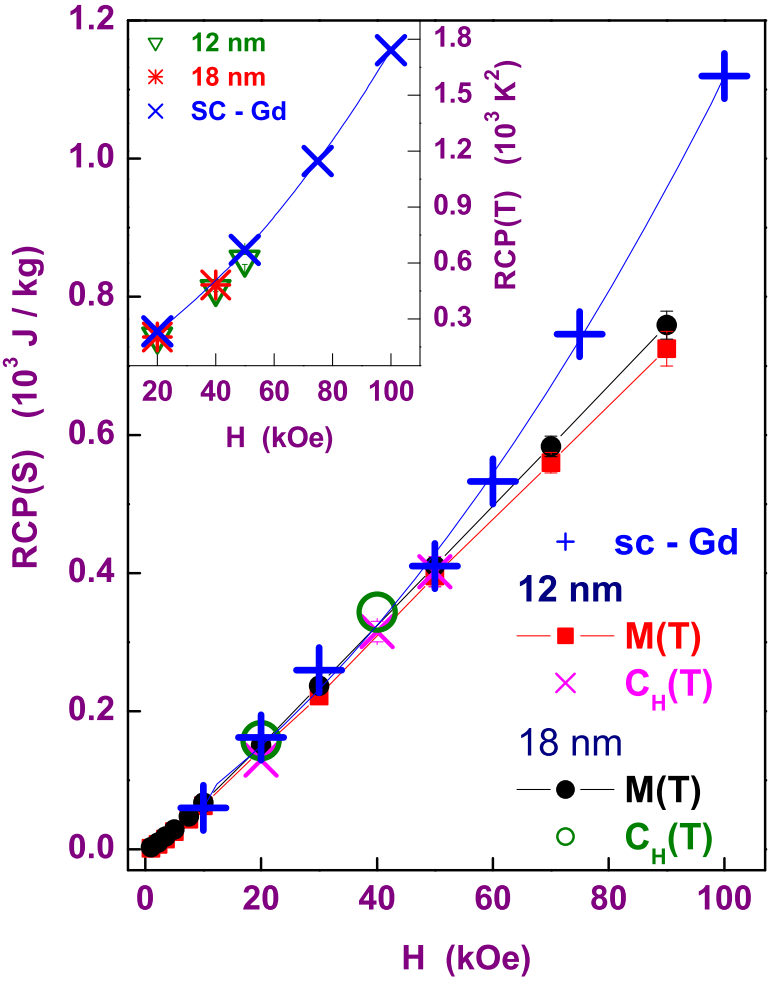

Figure 6.13: The relative cooling power (RCP), calculated from either the *isothermal* entropy change, RCP(S), or the *adiabatic* temperature change, RCP(T) (inset), as a function of magnetic field for the nanocrystalline Gd samples with d = 12nm and 18nm as well as for the single crystal (sc) Gd [4, 10]. $RCP(S)_M$ and $RCP(S)_C$ denote the RCP values obtained from magnetization and specific heat, respectively.

6.5 Summary and Conclusion

High-precision magnetization, $M(T,H)$, and specific heat, $C(T,H)$, measurements have been performed on nanocrystalline gadolinium samples of average grain size d = 12 nm and 18 nm over wide ranges of temperature (T) and magnetic fields (H). From the low-field magnetization (Fig 6.3) and 'zero-field' specific heat (Fig 6.4) data, it is observed that the ferromagnetic-to-paramagnetic transition temperature, T_C, is reduced by $\sim 6\ K$ for $d = 18\ nm$ and $\sim 7.5\ K$ for $d = 12\ nm$ n-Gd sample compared to $T_C = 293\ K$ for single crystal bulk Gd [4, 10]. The decrease in T_C with decreasing grain size, in turn, results in a downward shift in the temperature at which the *isothermal* entropy change or the *adiabatic* temperature change goes through a maximum. It is also observed that the peak value of the 'zero-field' specific heat, $C_{H=0}$ at T_C is also reduced by $\sim 10\ J/mol-K$ for $d = 18\ nm$ and $\sim 13.5\ J/mol-K$ for $d = 12\ nm$ n-Gd sample compared to $60\ J/mol-K$ for single crystal bulk Gd [4, 10]. The *isothermal* entropy change and *adiabatic* temperature change as functions of temperature are obtained from field-dependent magnetization, $M(T,H)$, and specific heat, $C(T,H)$, both peak at grain size dependent T_C. The peak value of *isothermal* entropy change or *adiabatic* temperature change also decreases as the average grain size decreases. The calculations, based on the magnetic equation of state in non-linear scaling variables with mean-field critical exponents, of *isothermal* entropy change are able to reproduce the observed *isothermal* entropy change over a very large temperature range around T_C. The maximum deviation in fit from the observed data is at T_{peak}, which lies above T_C and increases with H as $H^{1/3}$. At $T = T_C$, $\triangle S_{mag}(T,H)$ obeys the MF prediction $\Delta T_{ad}^{max}|_{T=T^{peak}} \sim H^{2/3}$.

The reduction in T_C, peak value of $C_{H=0}$, *isothermal* entropy change and the *adiabatic* temperature, is due to the fact that the grain size limits the divergence of the spin fluctuation - spin fluctuation correlation length. Nevertheless, the full-width at half-maximum, δT_{FWHM}, of $\triangle S_{mag}(T)$ and $\triangle T_{ad}(T)$ increases due to the distribution in grain size such that the RCP is unaltered for fields $H \leq 50\ kOe$. For fields $H \geq 60\ kOe$, RCP increases with grain size, d, because the fields in this range significantly enhance the peak value of $\triangle S_{mag}(T)$ or $\triangle T_{ad}(T)$ but not the δT_{FWHM} of $\triangle S_{mag}(T)$ or $\triangle T_{ad}(T)$. The temperature range around room temperature over which high RCP is maintained can be widened by synthesizing a ferromagnet with T_C higher than room temperature in the nanocrystalline form. The practical utility of using the average nanocrystallite size and size distribution as control parameters to tune the magnetocaloric effect with a view to achieve high cooling power near room temperature has been demonstrated by treating nanocrystalline gadolinium as an example.

References

1. G. V. Brown, *J. Appl. Phys.* **47**, 3673 (1976).

2. V. K. Pecharsky and K. A. Gschneidner Jr., *J. Magn. Magn. Mater.* **200**, 44 (1999).

3. A. M. Tishin and Y. I. Spichkin, *The magnetocaloric effect and its applications* (Institute of Physics Publishing, Bristol, 2003).

4. K. A. Gschneider, Jr. and V. K. Pecharsky, Annu. Rev. Mater. Sci. **30** 387 (2000).

5. K. A. Gschneider, Jr., V. K. Pecharsky and A. O. Tsokoi, *Rep. Prog. Phys.* **68**, 1479 (2005).

6. M. -H. Phan and S. -C. Yu, *J. Magn. Magn. Mater.* **308**, 325 (2007).

7. V. K. Pecharsky and K. A. Gschneidner Jr., *Phys. Rev. Lett.* **78**, 4494 (1997).

8. M. Foldeaki, W. Schnelle, E. Gmelin, P. Benard, B. Koszegi, A. Giguere, R. Chahine and T. K. Bose, *J. Appl. Phys.* **82**, 309 (1997).

9. M. Foldeaki, R. Chahine and T. K. Bose, *J. Appl. Phys.* **77**, 3528 (1995).

10. S. Yu. Dan'kov, A. M. Tishin, V. K. Pecharsky and K. A. Gschneidner, Jr., *Phys. Rev. B* **57**, 6 3478 (1998).

11. S. Srinath, S. N. Kaul and H. Kronmüller, *Phys. Rev. B* **59**, 1145 (1999).

12. A. -C. Probst, private communication.

13. A. Arrott and J. E. Noakes, *Phys. Rev. Lett.* **19**, 786 (1967).

14. V. Franco, J. S. Blázquez and A. Conde, *Appl. Phys. Lett.* **89**, 222512 (2006).

15. H. Oesterreicher and F. T. Parker, *J. Appl. Phys.* **55**, 4334 (1984).

16. S. N. Kaul, *Phase Transitions* **47**, 23 (1994).

17. M. Seeger, S. N. Kaul, H. Kronmüller and R. Reisser, *Phys. Rev. B* **51**, 12585 (1995).

18. M. Sambasiva Rao and S. N. Kaul, *J. Magn. Magn. Mater.* **171**, 341 (1997).

19. P. D. Babu and S. N. Kaul, *J. Phys.: Condens. Matter* **9**, 7189 (1997).

Chapter 7

Electrical- and Magneto-transport

7.1 Introduction

In rare earth metals, the exchange coupling between the spin of the conduction electron and the localized $4f$ moments affects the current carrying capacity. If all the local $4f$ moments are aligned parallel, there would be no net scattering of conduction-electron spins from this ordered system. At finite temperatures, the orientation of the $4f$ moments gets partially randomized and the departure from the ordered state provides a source of conduction electron scattering, called the spin-disorder scattering. De Gennes and Friedel [1] and Kasuya [2] proposed the models in which the conduction electrons are assumed to be scattered by the difference between the actual spin S of the ion at site R and the average value $\langle S \rangle$. J_{sf}, the exchange coupling between the $4f$ moments and the conduction-electron spins, is assumed to be independent of conduction electron wave vector.

The contribution to the total resistivity due to the scattering of conduction electron from a completely disordered spin system ($\langle S \rangle = 0$), taking into account the spin-orbit coupling of the localized moments and evaluated within the Born approximation, is given by

$$\rho_{mag} = (3\pi N m^*/8\hbar e^2 E_F)\ J_{sf}^2\ (g-1)^2 J(J-1) \tag{7.1}$$

where N is the number of scattering centers per unit volume and m^* is the conduction electron effective mass. As expected, Gd exhibits the largest spin disorder resistivity and ρ_{mag} calculated from the c-axis resistivity of the heavy rare earth series Gd - Tm follows the $(g-1)^2 J(J-1)$ dependence (Eq.(7.1)) [3]. Similar results were reported for the basal plane resistivity [4] and the resistivity of polycrystalline rare earth metals [5]. As the surface to volume ratio is considerably large and the grain boundary regions violate translational invariance and hence act as the defect sites, the residual residual resistivity is expected to be large in nanocrystalline rare earth metals compared to their single crystal counterparts. The spins at the grain boundary are disordered in orientation due to the distribution in the RKKY and/or direct exchange bonds caused by the distribution in the inter-atomic distances. Spin disorder within the grain boundary or interfacial regions gives a significant contribution to resistivity besides that arising from the scattering of conduction electrons from the magnons thermally-excited within the grains.

The electrical resistivity measured on single crystal Gd [6] along c-axis and b-axis differ considerably and this indicates the presence of strong temperature-dependent magnetocrystalline anisotropy. Difference between the c-axis and b-axis resistivity also asserts that the electron-phonon scattering contribution to the resistivity depends on the phonon spectrum. The

resistivity of polycrystalline rare earth metals [5] exhibits characteristic features at temperatures where the structural and magnetic transitions take place. For Gd, the dispersion relations for the magnons propagating in the basal plane and along the c-axis are almost linear and quadratic in the wave vector, respectively. Hence, the magnon contribution to the basal plane (c-axis) resistivity varies as T^4 (T^2) [3]. Considerably large difference in the magneto-resistance measured along c-axis and b-axis of single crystal Gd observed by McEwen and Webber [7] was attributed to the strong anisotropy and the difference in the magnon dispersion relation along these crystallographic directions. Hiroaka and Suzuki [8] also reported similar results and they could calculate temperature-dependent magnetocrystalline anisotropy constants using an empirical model.

In addition to the magnetocrystalline anisotropy, the interfacial magnetic anisotropy is also expected to contribute to the magnetoresistance in nanocrystalline Gd. Since the interfacial and intra-grain magnetic anisotropy play a major role in deciding the magnetic properties in nc-Gd, an elaborate study of temperature dependent resistivity and magnetoresistance on nc-Gd was undertaken.

7.2 Theoretical Considerations

The resistivity of a metal is best described in terms of elastic and inelastic scattering mechanisms. In the relaxation time approximation, Matthiessen's rule [9] applies, which states that the total resistivity is the sum of each of the individual resistivity contributions. The different scattering mechanisms are characterized by different powers of temperature. Thus, the total

resistivity is often a polynomial in temperature, T.

7.2.1 Scattering Mechanisms

Defect/imperfection Scattering

Impurities and defects break the periodicity of the lattice and thereby lead to the net scattering of electrons. Since this perturbation of the crystal lattice is unaffected by temperature, this resistivity contribution is temperature-independent. The impurities can be in the form of elemental substitutions on atomic sites or interstitial atoms. Since grain boundary regions have a large concentration of defects, grain boundary scattering contribution to the resistivity is temperature-independent and often quite large.

Electron-electron Scattering

The strong Coulomb interaction between the conduction electrons is the prime reason for electron-electron scattering. The exclusion principle limits the scattering of electrons to partially occupied levels near the Fermi surface. For two electrons to scatter, both must be in this shell of partially occupied levels within the width k_BT on either side of the Fermi level. This leads to a scattering rate and therefore, the resistivity that is proportinal to $(k_BT/\epsilon_F)^2$.

Electron-phonon Scattering

At finite temperatures, the lattice vibrations distort the periodic structure of the lattice. Scattering of electrons off phonons (the quantized amplitudes

of the lattice vibration modes) constitutes an intrinsic source of electrical resistance in crystalline solids. The most widely employed expression for the electron-phonon scattering contribution to resistivity, the Bloch-Grüneisen formula [9] which describes quite well the behaviour of the lattice resistivity of a pure metal as a function of temperature, is given by

$$\rho_L(T) = 4\ \rho_\Theta \left(\frac{T}{\Theta_D}\right)^5 \int_0^{\frac{\Theta_D}{T}} \frac{z^5\ dz}{(e^z-1)(1-e^{-z})} \tag{7.2}$$

where ρ_Θ is a constant characteristic of the metal, Θ_D is the Debye temperature.

At high temperatures ($T \gg \Theta_D$) the integral reduces to

$$\int_0^{\frac{\Theta_D}{T}} z^3 dz = \frac{1}{4}\left(\frac{\Theta_D}{T}\right)^4 \tag{7.3}$$

so that

$$\rho_L(T) \sim \rho_\Theta \left(\frac{T}{\Theta_D}\right) \quad ; \quad (T \gg \Theta_D) \tag{7.4}$$

At low temperatures, the upper limit of the integral is practically infinite, with the result

$$\int_0^{\infty} \frac{z^5\ dz}{(e^z-1)(1-e^{-z})} = 5!\ \zeta(5) = 124.4 \tag{7.5}$$

At such temperatures, the resistivity is proportional to the fifth power of the temperature, and thus falls off much more rapidly than at high temperatures, as

$$\rho_L(T) \sim 497.6\ \rho_\Theta \left(\frac{T}{\Theta_D}\right)^5 \quad ; \quad (T \ll \Theta_D) \tag{7.6}$$

Electron-magnon Scattering

At low temperatures, the main contribution to electrical resistivity in ordered ferromagnets comes from the *coherent* scattering of conduction elec-

trons by the long-wavelength spin waves (magnons) via the s-d or s-f exchange interaction (J_{s-d} or J_{s-f}). This scattering contribution is given by [10]

$$\rho_{SW}(T, H = 0) = \rho_0 \left(\frac{k_B T}{D}\right)^2 \tag{7.7}$$

where, for a given system, ρ_0 is a constant which depends on the material parameter such as the density of states at the Fermi level, J_{s-d} or J_{s-f}, Fermi momentum of conduction electrons, total spin, etc. By contrast, in disordered ferromagnets, the *incoherent* electron-magnon scattering is expected to significantly contribute to the resistivity at low temperatures. Within the framework of spin-disorder model, Richter *et al.* have calculated the $\rho_{mag}(T)$ for an amorphous Heisenberg ferromagnet in the spin-wave approximation as the sum of the contributions due to coherent and incoherent electron-magnon scattering, given by [11, 12]

$$\rho_{mag}(T) = \rho_{mag}(0) + \rho_{incoh}(T) + \rho_{coh}(T) \tag{7.8}$$

with the final result

$$\frac{\rho_{mag}(T)}{\rho_{mag}(0)} = 1 + \frac{\Omega_C}{(2\pi)^2 S}\Gamma(3/2)\xi(3/2)\left[\frac{k_B T}{D}\right]^{3/2} + \frac{1}{J_S(2k_F)}\,\frac{\pi^2}{3S}\left[\frac{k_B T}{D}\right]^2 \tag{7.9}$$

and

$$\rho_{mag}(0) = \frac{2\Omega_C}{3h^3}\left[\left(\frac{\Omega}{N_e e}\right) m S J_{sd}\right]^2 J_S(2k_F), \tag{7.10}$$

where Ω_C and Ω are the atomic and sample volumes, respectively, S is the spin of the local magnetic moment, N_e denotes the number of electrons, D is the spin-wave stiffness given by the magnon dispersion relation $\hbar\omega_k = Dk^2$, Γ and ξ are the gamma and Riemann zeta functions, respectively, J_{sd} is the s-d exchange coupling constant, $J_S(2k_F) = \int_0^{2k_F} k^3 S(k) dk$ and $S(k)$ is the structure factor. In Eq.(7.9), the second term is an outcome of a partial

cancellation of two competing $T^{3/2}$ terms; one arises from the incoherent (momentum non-conserving) electron-magnon scattering and increases with increasing temperature, and the other originates from the elastic scattering of conduction electrons from randomly oriented temperature-dependent local moments and decreases as the temperature is increased, whereas the third term is a coherent electron-magnon scattering term, as in Eq.(7.7).

7.2.2 Magnetoresistance

At temperatures $T \lesssim T_C$, the main contribution to the magnetoresistance in localized spin systems arises from magnons. These spin-wave contribution to the magnetoresistance, $(\Delta\rho/\rho)_{SW}$, is given by [10]

$$(\Delta\rho/\rho)_{SW} = \frac{\rho_{SW}(T,H)}{\rho_{SW}(T,H=0)} - 1$$

$$= [\Gamma(3)\zeta(2)]^{-1}\left[h\ ln(e^h-1) + 2\sum_{n=1}^{\infty}\frac{(-1)^n(e^h-1)^n}{n^2}\right] \quad (7.11)$$

for $(e^h - 1) < 1$, where the reduced field, $h = (g\mu_B H/k_B T)$. In Eq.(7.11), $\rho_{SW}(T, H = 0)$ is given by the expression, Eq.(7.7). In order to make the variations of $(\Delta\rho/\rho)_{SW}$ with h more transparent, the $(e^h - 1)$ term, appearing in Eq.(7.11), is approximated by h for $h \ll 1$ and only the first two (leading) terms in the sum over n are retained, with the result that [10]

$$(\Delta\rho/\rho)_{SW} \cong 0.304\left[-h\ lnh + 2h - \frac{1}{2}h^2\right] \quad (7.12)$$

The first term in Eq.(7.12) becomes important only at very low fields and is completely dominated by the other terms at intermediate and high fields. Therefore, at all temperatures $T \lesssim T_C$ and moderately high fields, the

longitudinal and transverse magnetoresistance both are described by [10]

$$\frac{\Delta\rho_{\shortparallel,\perp}(T,H)}{\rho_{\shortparallel,\perp}(T,H=0)} = \frac{\rho_{\shortparallel,\perp}(T,H) - \rho_{\shortparallel,\perp}(T,H)}{\rho_{\shortparallel,\perp}(T,H=0)}$$

$$= aH - bH^2 \tag{7.13}$$

7.3 Results and Discussion

Electrical resistivity, $\rho(T)$, was measured on the Physical Property Measurement System of Quantum Design make to a relative accuracy of better than 10 ppm on nanocrystalline Gd samples with $d = 12$ nm and 18 nm and of dimensions 5 $mm \times 1$ $mm \times 0.7$ mm using standard four-probe method. Typically, a dc current of 5 mA and current reversal, to eliminate the thermo emf, was used. 32/34 SWG copper wire was used as current/voltage leads. Thin layer of silver paint was applied to improve the electrical contact between the sample and the copper wire, which was tightly fixed over the sample to the rectangular sample holder made of 1 mm thick sapphire sheet. The sample holder was fixed to the resistivity puck using Apiezon-N grease. The Apiezon-N grease, which is in direct contact with the sample through the hole made on the sapphire holder just below the sample, provides a good thermal contact between the sample and the puck platform, beneath which the thermometer is placed.

Electrical resistivity, $\rho(T)$, was measured as a function of temperature at 0.5 K intervals in the range $2\ K \leq T \leq 30\ K$, at 1 K intervals in the range $30\ K < T \leq 50\ K$ and $277\ K \leq T \leq 294\ K$, at 2 K intervals in the range $50\ K < T \leq 100\ K$, $250\ K < T \leq 276\ K$ and $296\ K \leq T \leq 320\ K$ and at

5 K intervals in the range 100 $K < T \leq 250$ K in 'zero-field' and at various fixed magnetic fields ranging from 5 kOe to 90 kOe, applied perpendicular to the sample length/current direction. Magnetoresistance versus magnetic field isotherms were also measured on nc-Gd samples up to fields of 90 kOe at various fixed temperatures starting from 2 K to 300 K.

7.3.1 'Zero-field' Resistivity

The 'zero-field' resistivity, measured on nc-Gd with $d = 12$ nm and 18 nm, is compared with the resistivity data taken along the c-axis and b-axis reported [6] for single crystal Gd and for polycrystalline Gd [5], in figure 7.1. The values of residual resistivity 32 and 20 $\mu\Omega - cm$ for $d = 12$ nm and $d = 18$ nm are an order of magnitude higher than the values 4.4 $\mu\Omega - cm$ for polycrystalline Gd [5] and 3.2/4.9 $\mu\Omega - cm$ along c-axis/b-axis for single crystal Gd [6]. The residual resistivity, arising from the charge scattering of conduction electron from impurities and imperfections as well as the magnetic scattering from the domain walls and the misaligned spins at the grain boundary or within the interfacial regions, exhibits the expected increase with the decreasing grain size in nc-Gd, as the volume fraction of the grain boundary regions increases with decreasing grain size. Note that the spins in the grain boundary regions are oriented at random due to the distribution in the RKKY and/or direct exchange interactions caused by the distribution in the nearest-neighbour distance.

Nigh *et al.* [6] have asserted that a good fit to the experimental data on polycrystalline Gd [5] can be achieved by the use of the relationship

$$\rho_{poly} = \frac{1}{3}(2\rho_b + \rho_c) \tag{7.14}$$

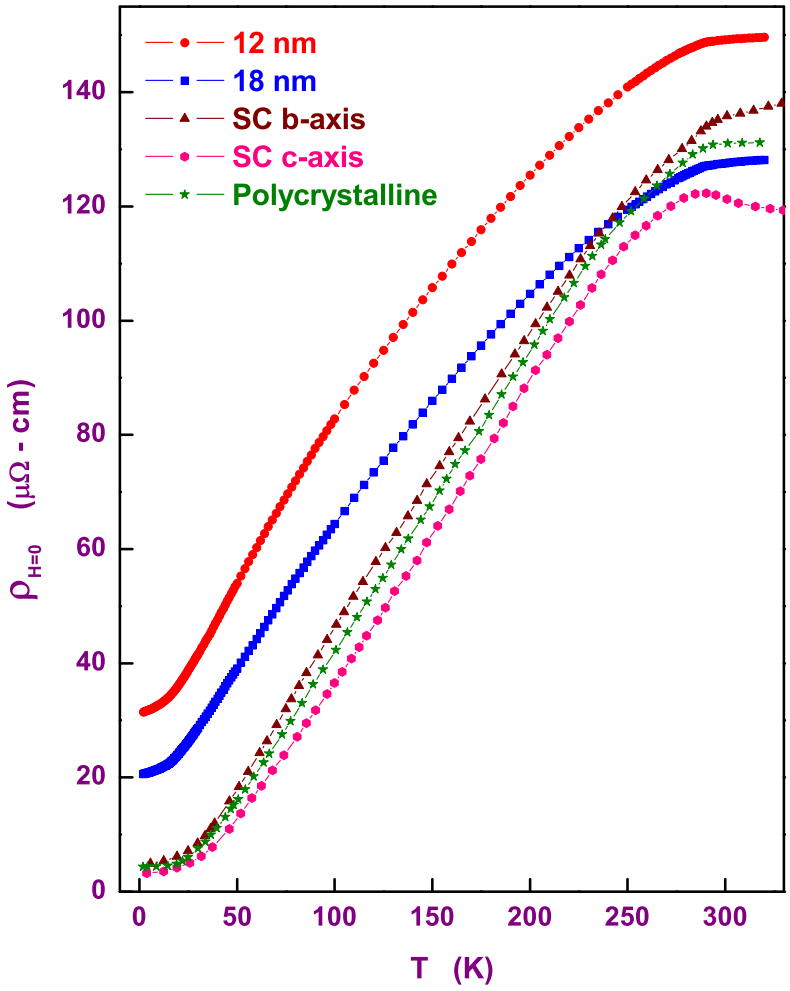

Figure 7.1: The temperature-dependent 'zero-field' resistivity of nc-Gd with the average grain size of $d = 12\ nm$ and $18\ nm$ is compared with that reported for single crystal Gd along b-axis and c-axis [6] and for the polycrystalline Gd [5].

where ρ_{poly} is the calculated polycrystalline resistivity, ρ_b and ρ_c are the b-axis and c-axis resistivity, respectively [6]. Alstad *et al.* [13] have verified this relation for Yttrium. Since the temperature dependence of the resistivity of nc-Gd is similar to that of polycrystalline Gd (Fig.7.1), it follows that the crystallographic directions in different nanocrystalline grains in nc-Gd are randomly oriented.

The lattice contribution to the resistivity along c-axis and b-axis in sc-Gd varies roughly linearly with temperature above the Debye temperature, $\Theta_D = 169\ K$ [14], whereas the slope of resistivity curve measured on nc-Gd with the average grain size of $d = 12\ nm$ and $18\ nm$ is changing continuously through out the temperature range (Fig.7.1), embracing the Debye temperature, $\Theta_D = 172(2)\ K$ $(169(2)\ K)$, determined from specific heat measurements for the $d = 12\ nm$ $(18\ nm)$ sample.

Critical Region

In agreement with the predictions of the theory of Fisher and Langer [15], the electrical resistivity, measured as a function of temperature along b-axis on single crystal Gd [6], $\rho_b(T)$, exhibits an abrupt change in (positive) slope at $T \cong T_C$ (Fiq.7.1). By contrast, the c-axis resistivity, $\rho_c(T)$, goes through a peak at $T \cong T_C$ (Fiq.7.1) due to the anomalous thermal expansion in the c-direction [16, 17] and only after correcting for this thermal expansion does $\rho_c(T)$ conform to the Fisher-Langer prediction. Detailed investigation of the electrical resistivity of a c-axis single crystal of higher-purity Gd metal reveals that [18] the usual power laws in the reduced temperature $\epsilon = (T - T_C)/T_C$ fail to describe $\rho_c(\epsilon)$ in the critical region. Instead, the

expression

$$r(\epsilon) = A_0 + A_1\ \epsilon + B_{\pm}|\epsilon|\ |\ ln|\epsilon||^{1/3} \tag{7.15}$$

with $B_+/B_- \approx -1/4$, predicted by renormalization group (RG) calculations for a three-dimensional uniaxial ferromagnet with dipolar interactions, reproduces the observed $\rho_c(\epsilon)$ in the asymptotic critical region $-8 \times 10^{-4} \leq \epsilon \leq 8 \times 10^{-4}$ with the parameter values [18] $A_0 = 1.00$, $A_1 = -0.32$, $B_+ = -0.06$ and $B_- = 0.22$. In Eq.(7.15), $r(\epsilon) = \rho(\epsilon)/\rho(\epsilon = 0)$ is the reduced resistivity, $\rho(\epsilon = 0)$ is the resistivity at $T = T_C$ and plus/minus sign refers to temperatures above/below T_C. Subsequently, extensive ac susceptibility [19] and magnetization [20] data, taken on high-purity single crystal Gd along the c-axis, conclusively prove that the asymptotic critical of Gd metal is that of a three-dimensional uniaxial dipolar ferromagnet.

At first, an attempt was made to fit the resistivity data, taken in the critical region $-0.02 \leq \epsilon \leq 0.02$ on the nc-Gd samples, to Eq.(7.15) by fixing A_1 at the value -0.32, for both $T < T_C$ and $T > T_C$, and varying A_0, T_C and $B_{\pm}$. The optimum fits to the $r(\epsilon)$ data (dashed curves in Fig.7.2) were obtained for the parameter values $A_0 = 1.000(5)$ for both the samples, $T_C = 285.65(5)\ K$ ($287.25(5)\ K$), $B_- = -0.376(4)$ ($-0.460(18)$) and $B_+ = 0.345(6)$ ($0.299(10)$) for $d = 12\ nm$ ($18\ nm$). However, the coefficients B_+ and B_- have wrong signs and the ratio $B_+/B_- = -0.918(26)$ ($-0.65(5)$) is ≈ 3.5 (2.7) times higher than predicted by the theory. Considering that the easy axis, dictated by the uniaxial anisotropy, varies randomly from grain to grain in the present nanocrystalline samples, the possibility that nc-Gd corresponds to the three-dimensional random uniaxial dipolar universality class was next explored. Accordingly, the following expression

$$r(\epsilon) = A'_0 + A'_1\ \epsilon + B'_{\pm}\ |\epsilon|\ |\ ln|\epsilon||^{1/2}\ exp\ [-2(D|\ ln|\epsilon||)^{1/2}] \tag{7.16}$$

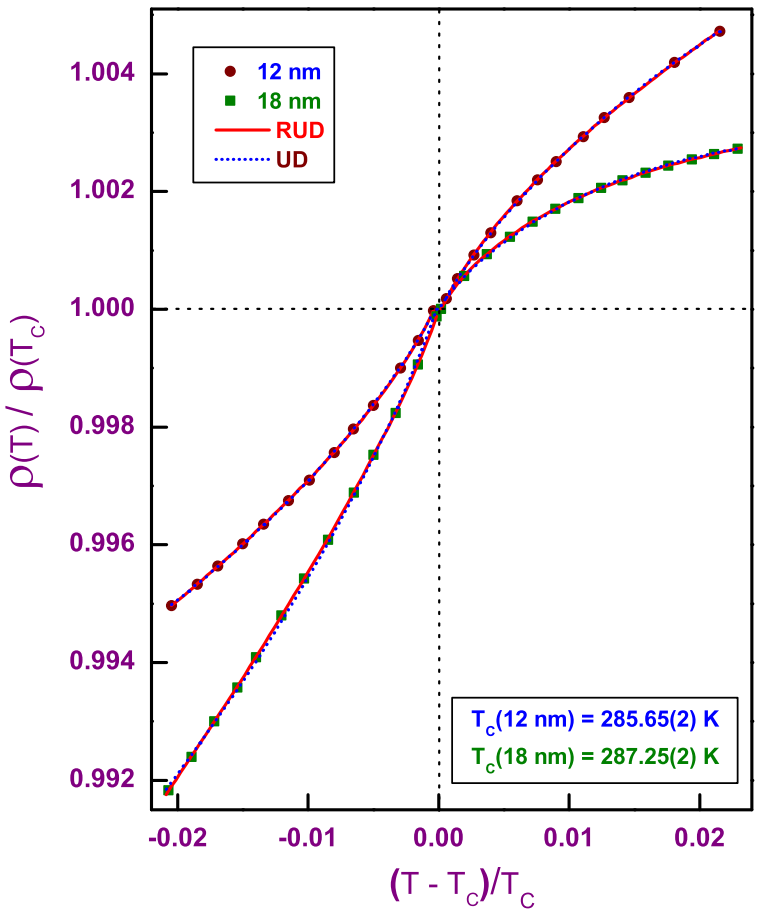

Figure 7.2: The reduced resistivity plotted against reduced temperature in the critical region, for nc-Gd with the average grain size of $d = 12\ nm$ and 18 nm (open symbols), shows a slope change at the critical temperature, T_C. The continuous and dashed lines are the fits to the data based on the expressions Eq.(7.15) and Eq.(7.16), respectively.

with $D = 0.118$, yielded by the RG calculations [21] for a three-dimensional random uniaxial dipolar ferromagnet, was used to analyze the $r(\epsilon)$ data. This exercise revealed that (i) Eq.(7.16) provides better overall fits (solid curves in Fig.7.2) to the $r(\epsilon)$ data over the same temperature range as that used for fits based on Eq.(7.15), (ii) while T_C remains unaltered, the coefficients assume the values $A'_0 = 1.0000(7)$, $A'_1 = 1.85(39)$, $B'_- = 3.20(8)$ $(2.87(3))$ and $B'_+ = -3.09(1)$ $(-3.32(2))$ for $d = 12\ nm$ $(18\ nm)$, and (iii) though the signs of B'_+ and B'_- are now correct, the ratio $B'_+/B'_- = -0.966(28)$ $(-1.157(20))$ is still very large compared to the theoretical value [22] $B'_+/B'_- = -0.25$. Since the correction term in Eq.(7.16) involves the exponential term which becomes important at $T \simeq T_C$, the anomalously large values of the ratio B'_+/B'_- could reflect the fact that the non-asymptotic data (taken in the crossover region or well outside the asymptotic critical region) have been used for the fits based on Eq.(7.16), which is valid only in the asymptotic critical region.

7.3.2 'In-field' Resistivity

Fiqure 7.3 shows the resistivity measured in the presence of fixed magnetic fields in the range $5\ kOe \leq H \leq 90\ kOe$, applied perpendicular to the current direction/sample length, at temperatures $2\ K \leq T \leq 320\ K$ on nc-Gd with $d = 12\ nm$ and $18\ nm$. Since the resistivity is measured in the transverse configuration, Lorenz force tends to increase the electron path length and thereby the resistance. This effect is pronounced only in the low field regime. Application of higher fields progressively suppresses the thermally-excited magnons and hence reduces the resistivity. Beyond a certain field strength, the reduction in resistance due to magnon-suppression

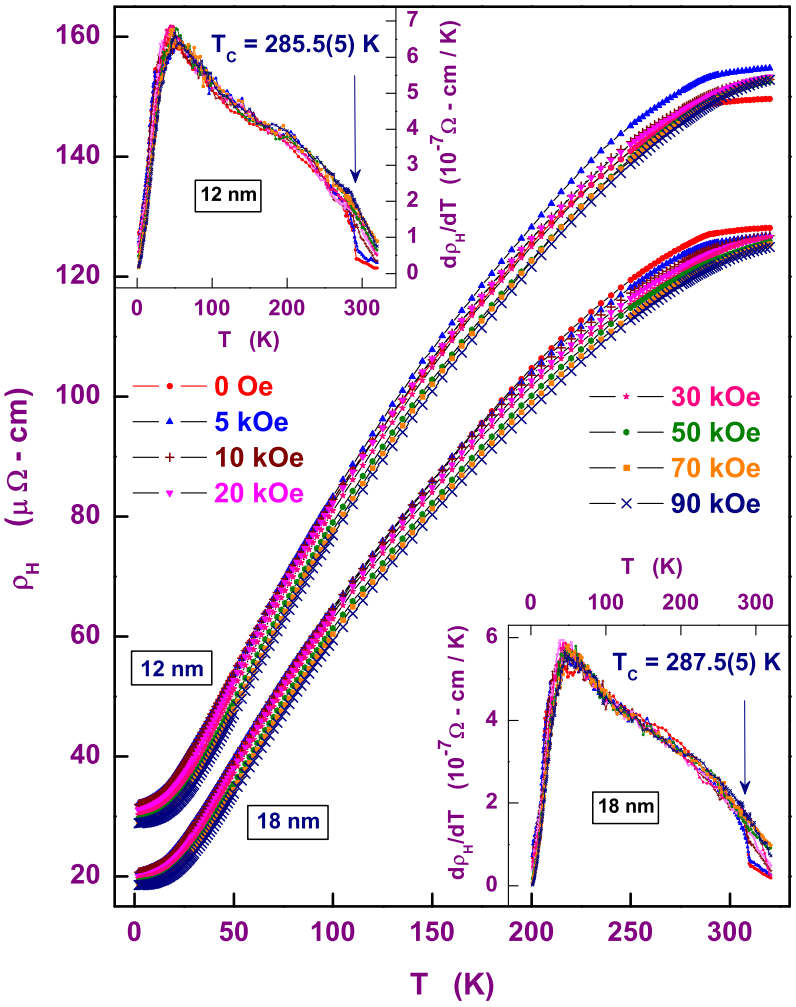

Figure 7.3: The temperature-dependent 'in-field' resistivity, $\rho_H(T)$, measured at various fixed fields starting from 0 Oe to 90 kOe on nc-Gd with the average grain size of $d = 12$ nm and 18 nm. The insets show the temperature derivative of $\rho_H(T)$ at various fields for nc-Gd with average grain size $d = 12$ nm (top) and 18 nm (bottom).

more than offsets the increase in resistance owing to the Lorentz force and a negative magneto-resistance results.

The temperature derivative of the resistivity measured at various fixed fields for nc-Gd with $d = 12\ nm$ and $18\ nm$ are shown in the insets of the figure 7.3. In the low temperature region, where T^5 dependence of lattice contribution to resistivity is expected (Eq.(7.6)), the field-dependent slope is increasing drastically with increasing temperature. At the ferromagnetic (FM)-to-paramagnetic (PM) transition temperature, T_C, where the critical fluctuations of the order parameter (spontaneous magnetization) have the maximum amplitude and above which the long-range ferromagnetic order collapses, an abrupt drop in the temperature derivative of resistivity is observed at low fields and this drop gets progressively smeared out as the critical fluctuations are suppressed by the external field.

Residual Resistivity

The field dependence of residual resistivity (resistivity at the lowest temperature, $T = 1.8\ K$, at various fixed magnetic fields in Fig.7.3) of nc-Gd with $d = 12\ nm$ and $18\ nm$ is shown in figure 7.4. The variation of the residual resistivity with field stands as an evidence for the contribution to resistivity by the spins at grain boundaries and within the domain walls, as hardly any spin waves get excited at temperatures close to $T \cong 0\ K$. The spins in the grain boundary regions are oriented at random due to the distribution in RKKY interactions brought about by the distribution in the nearest-neigbour interatomic distances in such regions. Thus, the scattering of conduction-electron spins from these randomly oriented local spins significantly contributes to the resistivity at very low temperatures. As the

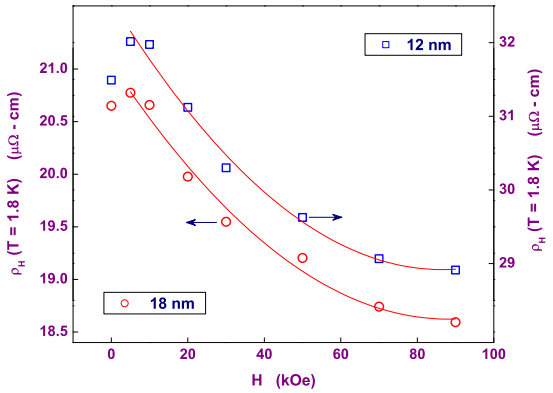

Figure 7.4: The field-dependence of the residual resistivity of nc-Gd (open symbols) with the average grain size of $d = 12\ nm$ and $18\ nm$. The continuous lines are the fits to the data based on the expression, Eq.(7.13).

field increases, magnetic domains and hence the spins within the domain walls as well as those in the grain boundary region get gradually aligned along the field direction, thus reducing the magnetic scattering and leading to negative magnetoresistance (Fig.7.4).

Low-temperature Resistivity

At low temperatures ($T \lesssim 40\ K$), the 'in-field' resistivity, ρ_H, exhibits different temperature variations depending on the magnetic field strength. At $H = 0$ and $H = 5\ kOe$, and low temperatures ($T \lesssim 40\ K$), $\rho_H(T)$ is described well by the relation

$$\rho_H(T) = \rho_H(T = 0) + a\ T^{3/2} \tag{7.17}$$

Table 7.1: Parameter values, based on Eq.(7.17), determined in different temperature ranges for the nc-Gd $d = 12\ nm$ and $d = 18\ nm$ samples.

Sample	H (k Oe)	$1.8\ K \leq T \leq 16.5\ K$ $\rho_H(T=0)$ $(\mu\Omega\text{-}cm)$	a $(n\Omega\text{-}cm\ K^{-3/2})$	$16.5\ K \leq T \lesssim 36\ K$ $\rho_H(T=0)$ $(\mu\Omega\text{-}cm)$	a $(n\Omega\text{-}cm\ K^{-3/2})$
12 nm	0	31.31(2)	45.9(6)	29.67(5)	71.4(3)
	5	31.92(3)	43.8(10)	30.37(7)	71.4(5)
18 nm	0	20.50(2)	32.4(7)	18.78(3)	60.1(2)
	5	20.63(4)	33.2(10)	19.09(5)	60.0(2)

with the parameter values summarized in table 7.1. Figures 7.5 and 7.6 display the $T^{3/2}$ variation of $\rho_H(T)$ and highlight the slope change at $T^+ \simeq 16.5\ K$. The observed $T^{3/2}$-variation is at variance with the T^2 variation of $\rho_H(T)$ at low temperatures expected for a Fermi liquid (electron-electron scattering) and/or for the coherent electron-magnon scattering, Eq.(7.7). Such a departure from the Fermi liquid (commonly referred to as the non-Fermi liquid) behaviour has been reported in numerous spin systems such as heavy Fermion/strongly-correlated electron systems [23] and weak itinerant-electron systems [24, 25, 26, 27].

Considering that the grain boundary/interfacial regions in the nanocrystalline samples could be modelled on the lines of an amorphous solid, the observed $T^{3/2}$ variation of $\rho_H(T)$, as in Eq.(7.9), could arise from a net result of two competing $T^{3/2}$ terms: the incoherent (momentum nonconserving) electron-magnon scattering that *increases* with increasing temperature as $T^{3/2}$, and the elastic scattering of conduction electrons from the randomly

oriented temperature-dependent magnetic moments which *decreases* with increasing temperature as $T^{3/2}$. Thus, if the coefficient 'a' in Eq.(7.17) is identified with the coefficient of the $T^{3/2}$ term in Eq.(7.9), $a \propto D^{-3/2}$ so that the coefficient 'a' is expected to decrease as the spin-wave stiffness, D, increases. Though this relation explains the reduced value of 'a' for $d = 18\ nm$ compared to that for $d = 12\ nm$ since D increases as 'd' increases from 12 to 18 nm but fails to account for the *field-independent* nature of 'a' irrespective of the temperature range as well as the abrupt change in slope at $T^{+} \simeq 16.5\ K$. Thus, the incoherent electron-magnon scattering mechanism, as a possible source of the $T^{3/2}$ term in Eq.(7.17), can be ruled out.

A striking feature of the present results is the change in the slope $d\rho_H(T)/dT^{3/2}$ (Figs.7.5 and 7.6) at a temperature that either equals the Bose-Einstein condensation temperature T_c (for nc-Gd $d = 12\ nm$) or is very close to it (for $d = 18\ nm$). This results will be revisited while discussing the temperature variation of magnetoresistance at various magnetic fields.

As the field increases beyond 5 kOe, the $T^{3/2}$ variation of $\rho_H(T)$ at low temperatures ($T \lesssim 16.5\ K$) changes over to the Fermi liquid T^2 variation with a change in the slope $d\rho_H/dT^2$ at $T^{+}(H)$, which is close to 16.5 K at 10 kOe but shifts up and the slope-change becomes less and less prominant as the field increases. Normally, the non-Fermi liquid behaviour is observed in the vicinity of the quantum critical point (QCP), which is reached either by the application of pressure or by tunning the composition to a critical value whereas the Fermi liquid behaviour is found away from the QCP [23, 24, 25, 26, 27]. In the present case, the application of magnetic field

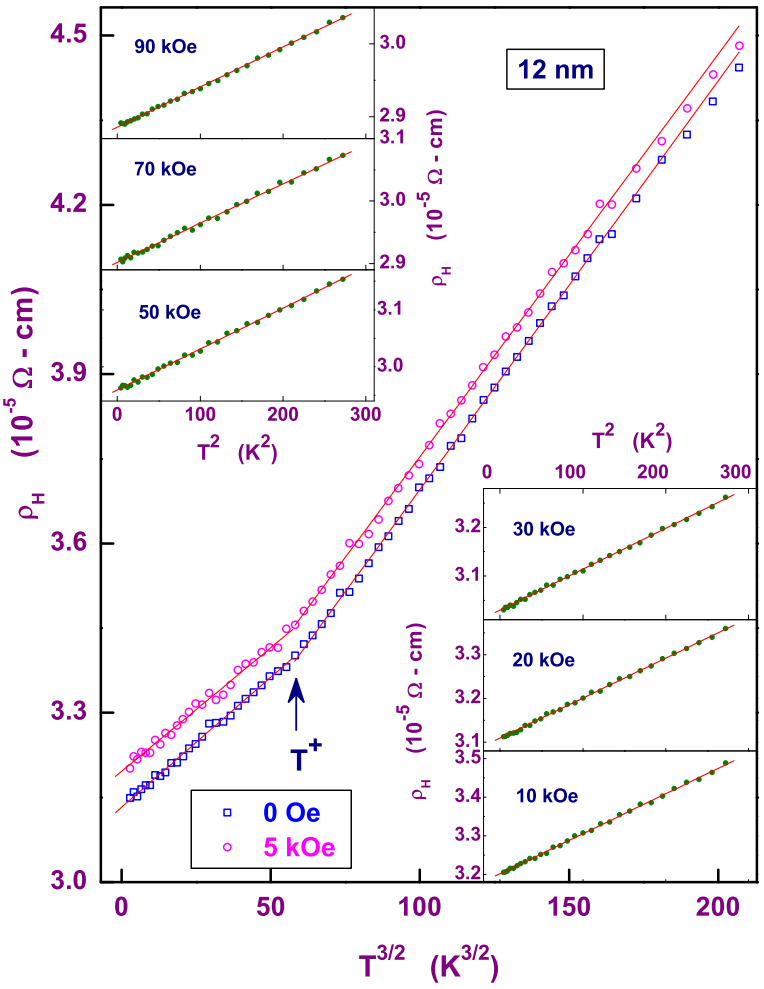

Figure 7.5: The temperature-dependent 'in-field' resistivity, $\rho_H(T)$, measured on nc-Gd with the average grain size of $d = 12\ nm$ at $H = 0\ Oe$ and $5\ kOe$ is plotted against $T^{3/2}$. The straight line fit to the data above and below $T \sim 16.5\ K$ clearly shows a slope change at $T^{+} \simeq 16.5\ K$. The insets show the $\rho_H(T)$ at various field starting from $10\ kOe$ to $90\ kOe$ plotted against T^2.

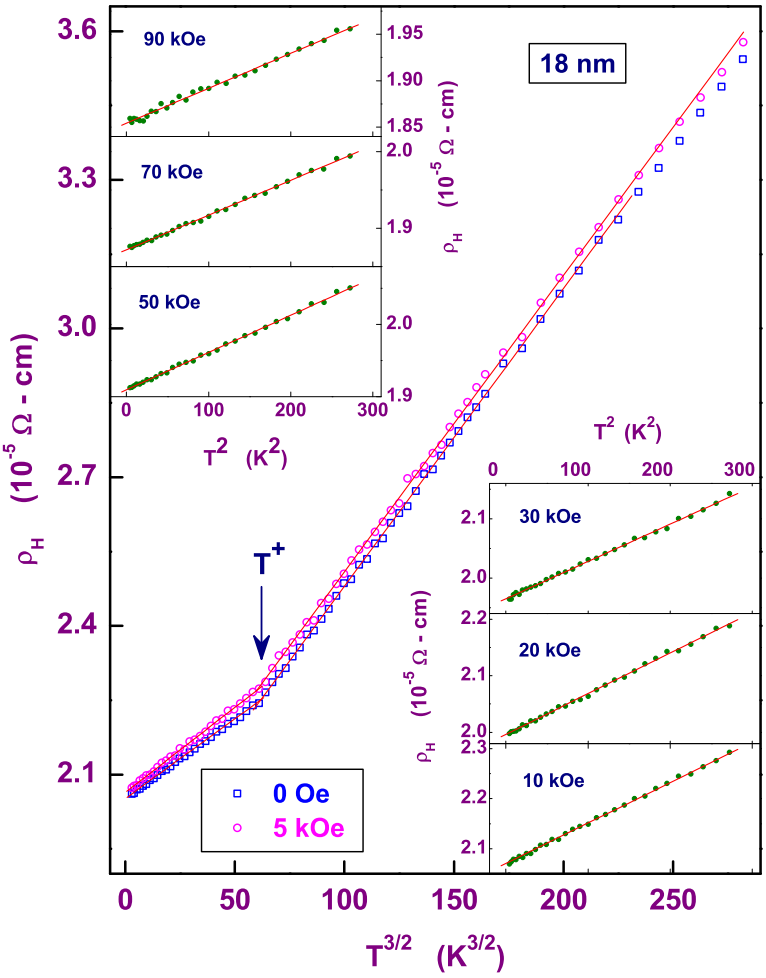

Figure 7.6: The temperature-dependent 'in-field' resistivity, $\rho_H(T)$, measured on nc-Gd with the average grain size of $d = 18\ nm$ at $H = 0\ Oe$ and $5\ kOe$ is plotted against $T^{3/2}$. The straight line fit to the data above and below $T \sim 16.5\ K$ clearly shows a slope change at $T^+ \simeq 16.5\ K$. The insets show the $\rho_H(T)$ at various field starting from 10 kOe to 90 kOe plotted against T^2.

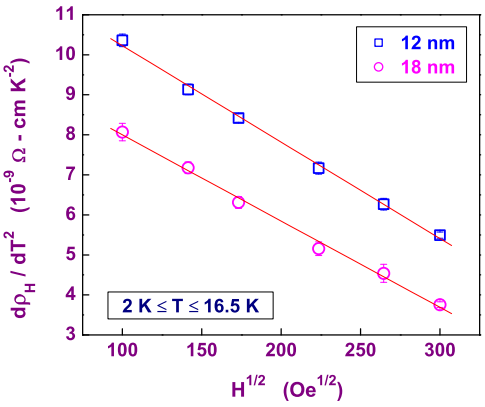

Figure 7.7: The coefficient of the T^2 term in the expression for the 'in-field' resistivity, $\rho_H(T)$, measured on nc-Gd with the average grain sizes of $d = 18\ nm$ and $18\ nm$ at magnetic fields ranging from 10 kOe to 90 kOe, in the temperature range from 2 K to 16.5 K.

seems to drive the system away from a situation that normally prevails near the QCP. The effect of the external magnetic field (H) is to suppress magnons and thereby the electron-magnon contribution. Thus, the coefficient of the T^2 term in Eq.(7.7) decreases with H. The $\sqrt{H}$ suppression of this coefficient $d\rho_H/dT^2$ with field is typical of both itinerant- and localized-electron ferromagnets [27].

7.3.3 Magnetoresistance

The transverse magnetorsistance, $\Delta\rho_\perp(T) = (\rho_H(T) - \rho_0(T))/\rho_0(T)$, calculated from the 'in-field' resistivity ($\rho_H(T)$) and 'zero-field' resistivity ($\rho_0(T)$) as a function of temperature at various fixed fields for nc-Gd with the average grain size of $d = 12\ nm$ and $18\ nm$ are plotted in figure 7.8 and

7.9. The positive magnetoresistance observed at low fields results from the dominance of the Lorenz force, which tends to increase the resistance, over the suppression of the electron-magnon scattering contribution by the external magnetic field, which causes a reduction in the resistance. As observed in the case of 'in-field' resistivity (Figs.7.5 and 7.6), a slope change in temperature-dependent magnetoresistance is observed at $\simeq 16.5\ K$ at fields $< 10\ kOe$ in both the samples. This slope change is clearly seen at low fields and gets smeared out as the field increases beyond $10\ kOe$.

For a ferromagnetic system, transverse magnetoresistance, $\Delta\rho_{\perp}(T)$, is expected to go through a minimum at the ferromagnetic-to-paramagnetic phase transition temperature, T_C, and at the minimum, the negative magnetoresistance, $\Delta\rho_{min}$, is, usually, $8-12$ % at fields as high as $80-90\ kOe$ [27] provided the lattice contribution to the total resistivity near T_C is small compared to the magnetic contribution or, equivalently, $T_C \ll \Theta_D$. The negative magnetoresistance has the highest value at $T \simeq T_C$ because the critical fluctuations of spontaneous magnetization (order parameter) have the largest amplitude at T_C. For nanocrystalline Gd, T_C (285.63(2) K for $d = 12\ nm$ and 287.22(2) K for $d = 18\ nm$ nc-Gd samples) is close to room temperature and is approximately twice the Debye temperature, Θ_D ($= 172(2)\ K$ ($169(2)\ K$) for $d = 12\,nm$ ($18\,nm$) sample, determined from the specific heat data). Hence, the lattice contribution to the 'zero-field' resistivity, $\rho_0(T)$, is overwhelmingly large. Thus, for temperatures close to T_C, the transverse magnetoresistance, defined as $\Delta\rho_{\perp}(T) = (\rho_H(T) - \rho_0(T))/\rho_0(T)$, is expected to be small. Consistent with this expectations, at T_C, $\Delta\rho_{\perp}$ is ~ 2 % (~ 5 %) at $90\ kOe$ for nc-Gd with $d = 12\ nm$ ($18\ nm$), as clearly evidenced in the figures 7.8 and 7.9.

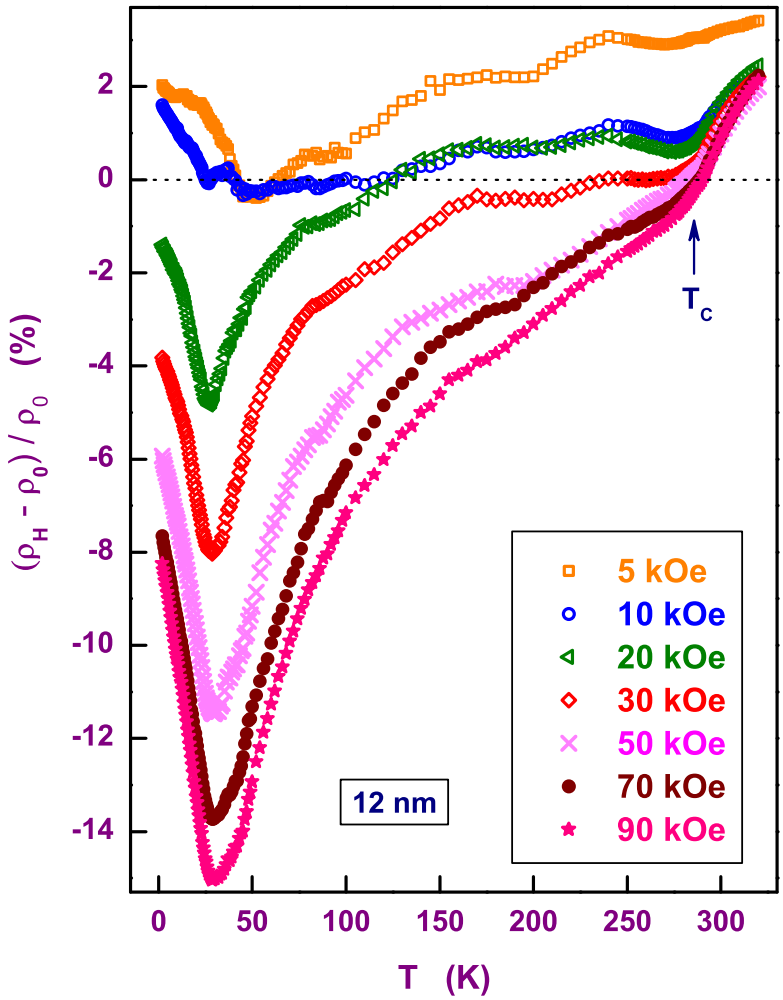

Figure 7.8: The temperature-dependent transverse magnetoresistance, $\Delta\rho_{\perp}(T)$, calculated from the 'in-field' and 'zero-field' resistivity, at various fixed fields for nc-Gd with the average grain size of $d = 12\ nm$.

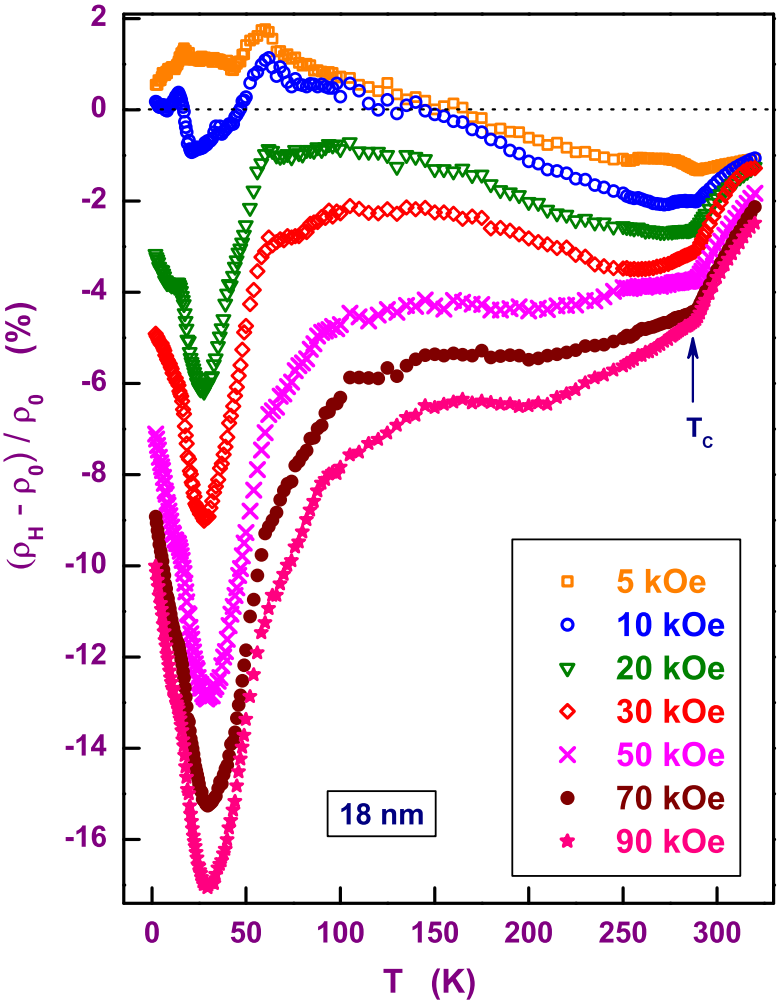

Figure 7.9: The temperature-dependent transverse magnetoresistance, $\Delta\rho_{\perp}(T)$, calculated from the 'in-field' and 'zero-field' resistivity, at various fixed fields for nc-Gd with the average grain size of $d = 18\ nm$.

T_C is marked by a shallow minimum in $\Delta\rho_\perp(T)$ at low fields near $T \approx 285\ K$ and progressively smears out as the field increases. The transverse magnetoresistance, $\Delta\rho_\perp(T)$, goes through a minimum at $T_{min} \simeq 22K$ when $H = 10\ kOe$. T_{min} increases with field as $H^{2/3}$ as displayed in figure 7.10(b). The minimum value of $\Delta\rho_{\perp,min}$ at $T = T_{min}$ decreases exponentially from ~ 0.2 % (1 %) at 10 kOe to 15 % (17 %) at 90 kOe for the nc-Gd sample with $d = 12\ nm$ (18 nm), as shown in figure 7.10(a). The negative magnetoresistance has a much larger value at $T = T_{min}$ than that in a normal ferromagnet at $T = T_C$. In view of our observation that an anomalous softening of spin-wave modes occurs when the temperature falls below $\sim 22\ K$ (which coincides with T_{min}), an extremely large (macroscopic) number of magnons gets thermally excited and forms a Bose-Einstein (BE) condensate at $T \lesssim T_{min}$ and $H \simeq 0$. The magnetic field of increasing strength progressively destroys the BE condensate phase coherence and suppresses the magnons, and with them the electron-magnon scattering contribution. Consequently, the value of negative magnetoresistance at T_{min} grows constantly with field. Note that at such low temperatures, the electron-magnon scattering completely swamps the electron-phonon scattering contribution. The observation that $T_{min}(H)$ increases with increasing magnetic field as $H^{2/3}$ (Fig.7.10(b)) [the field dependence that is characteristic of the Bose-Einstein condensation (BEC)] is consistent with the above interpretation in terms of the BEC picture. $T_{min}(H)$ has the same values, within the error limits, and the field dependence for both the nc-Gd samples, $d = 12\ nm$ and 18 nm (Fig.7.10(b)).

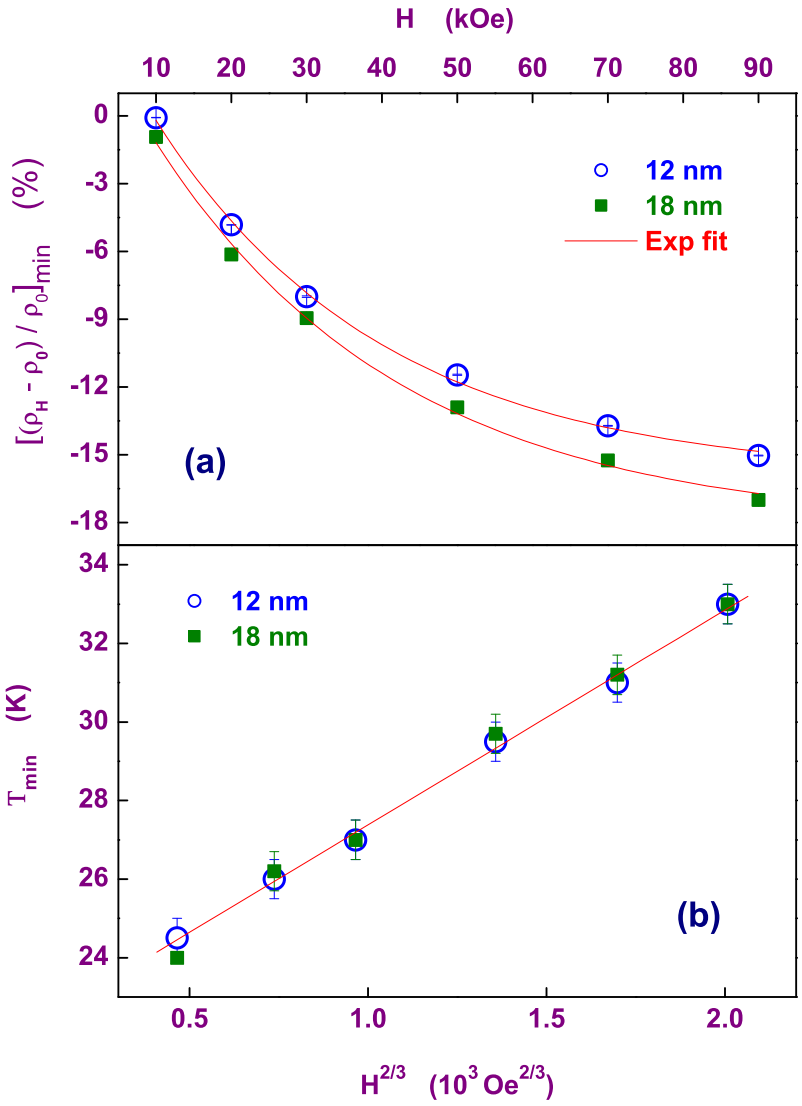

Figure 7.10: (a) The minimum value of the transverse magnetoresistance, $\Delta\rho_{min}$ (symbols), as a function of field along with the exponential fits (continuous lines) and (b) the temperature at which the magnetoresistance goes through a minimum, T_{min}, plotted against $H^{2/3}$ at various fixed fields for nc-Gd with the average grain size of $d = 12\ nm$ and $18\ nm$.

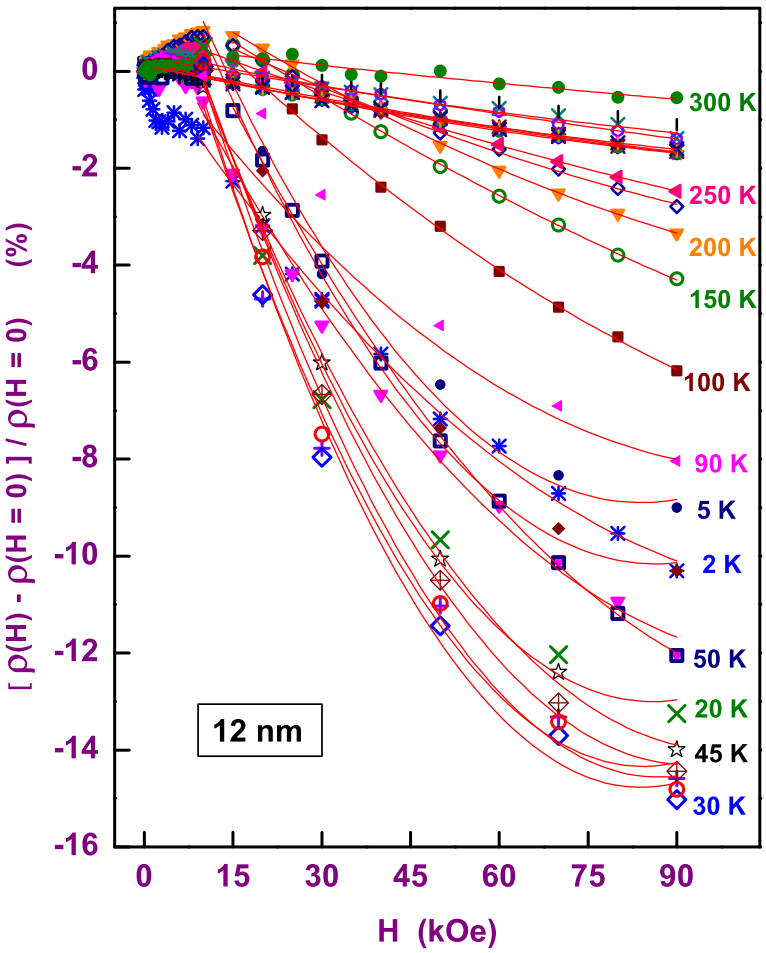

Figure 7.11: The transverse magnetoresistance vs. magnetic field isotherms measured up to 90 kOe at various fixed temperatures from 2 K to 300 K on nc-Gd with the average grain size of $d = 12$ nm. The continuous lines are the fits to the data based on the expression, Eq.(7.13).

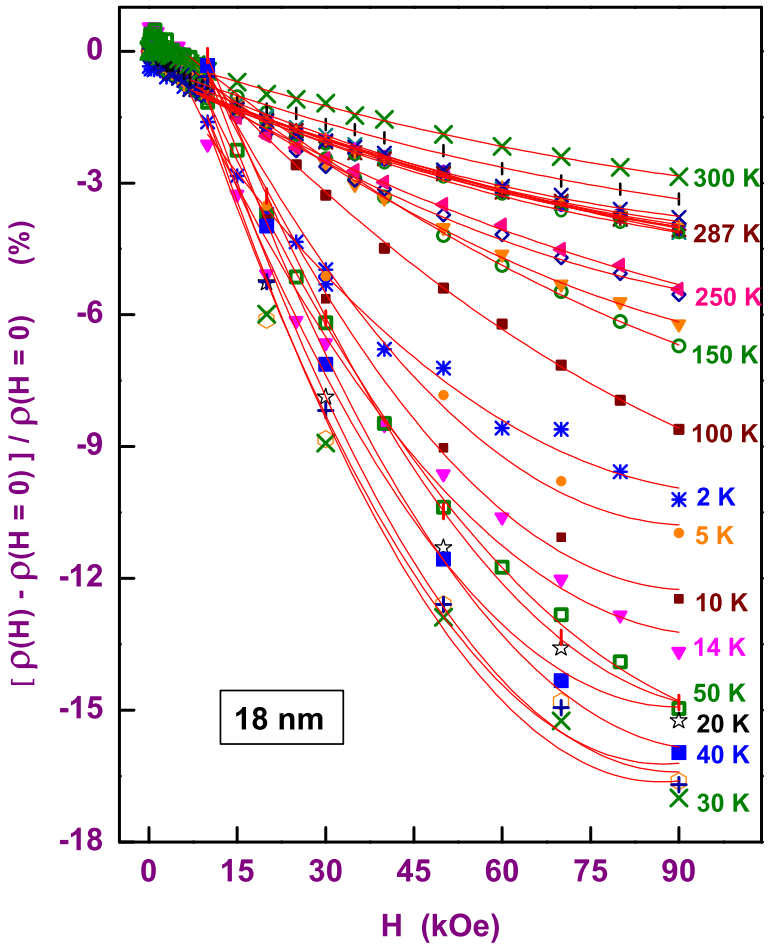

Figure 7.12: The transverse magnetoresistance vs. magnetic field isotherms measured up to 90 kOe at various fixed temperatures from 2 K to 300 K on nc-Gd with the average grain size of $d = 18$ nm. The continuous lines are the fits to the data based on the expression, Eq.(7.13).

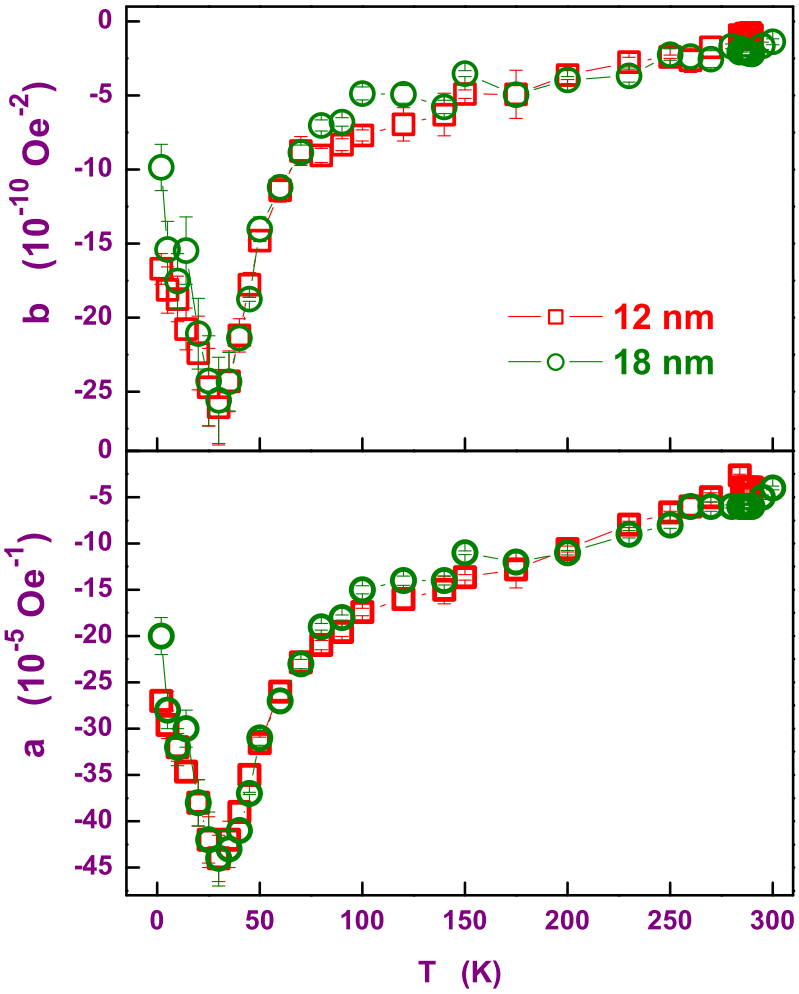

Figure 7.13: The coefficients 'a' and 'b' of the terms linear and quadratic in H in Eq.(7.13), that quantify the suppression of magnetic contribution to resistivity by the magnetic field, H, obtained by fitting Eq.(7.13) to the transverse magnetoresistance - field isotherms measured at various temperatures from 2 K to 300 K on nc-Gd samples with the average grain size of $d = 12$ nm and 18 nm.

Magnetoresistance Isotherms

The transverse magnetoresistance versus magnetic field isotherms, $\Delta\rho_{\perp}(H)$, measured at various fixed temperatures from 2 K to 300 K up to a maximum field of 90 kOe on nc-Gd with $d = 12$ nm and 18 nm are displayed in figures 7.11 and 7.12. The isotherms were measured while reducing the field from a maximum value of 90 kOe to zero field and it resulted in a different magnetic state of the system at low temperatures and low fields compared to that of 'in-field' resistivity measurement, where the system is cooled in 'zero-field' to the lowest temperature and the specific field is applied. Hence, at low fields and low temperatures, the magnetoresistance (MR) is *negative* as opposed to the *positive* MR observed in the magnetoresistance versus temperature data. The field-dependence of MR is significantly different at low fields for the nc-Gd $d = 12$ nm and $d = 18$ nm samples (Figs.7.11 and 7.12). This difference is due to the fact that, at low fields and temperatures, the magnetization state is essentially determined by the effective anisotropy field, which is markedly different (primarily due to the interfacial anisotropy contribution) for nc-Gd with $d = 12$ nm and 18 nm. The decrease in MR at high fields basically reflects the suppression of spin waves by the magnetic field. At relatively high fields, the expression for $\Delta\rho_{\perp}(H)$ isotherm, Eq.(7.13), that takes into account the suppression of magnon contribution to the resistivity, is able to generate good fits (continuous lines) to the $\Delta\rho_{\perp}(H)$ isotherms (symbols) measured at various temperatures ranging from 2 K to 300 K (Figs.7.11 and 7.12). Like the transverse magnetoresistance at $T = T_{min}$ (Figs.7.8 and 7.9), the coefficient 'a' and 'b' as functions of temperature go through a dip at $T \sim 30$ K.

7.4 Summary and Conclusion

The electrical resistivity and magnetoresistance measured on two nc-Gd samples with the average grain size of $d = 12\ nm$ and $18\ nm$ show the overall features similar to that of a polycrystalline Gd. The grain boundary contribution to the residual resistivity increases drastically in nc-Gd with the average grain size of 12 nm compared to that in $d = 18\ nm$. The resistivity in the critical region is better described by the three-dimensional random uniaxial dipolar model than the pure three-dimensional uniaxial dipolar model. While both the models yield the same T_C, the ratio B_+/B_-, obtained in the temperature ranges above and below T_C, is large compared to that theoretically predicted. This anomalous value of the ratio is due to the use of the non-asymptotic data. The variation of the residual resistivity with field provides a strong evidence for the contribution to resistivity by the spins at grain boundaries and within the domain walls. The scattering of conduction-electron spins from these randomly oriented local spins significantly contributes to the resistivity at very low temperatures. At low temperatures ($T \lesssim 40\ K$) and low fields ($H = 0$ and $H = 5\ kOe$), $\rho_H(T)$ varies as $T^{3/2}$ with a slope change at $T^+ \simeq 16.5\ K$. The fact that the slope of $\rho_H(T)$ vs. $T^{3/2}$ is field-independent both below and above T^+, completely rules out the possibility that either the elastic scattering of conduction electrons from the randomly oriented temperature-dependent magnetic moments or the incoherent electron-magnon scattering or both significantly contribute to the resistivity at such fields and temperatures. Instead the $T^{3/2}$ variation of resistivity is taken to reflect the non-Fermi liquid behaviour. As the field increases beyond 5 kOe, the $T^{3/2}$ variation of $\rho_H(T)$ at low temperatures ($T \lesssim 16.5\ K$) changes over to the Fermi liquid T^2 vari-

ation. Normally, the non-Fermi liquid behaviour is observed in the vicinity of the quantum critical point (QCP). In the present case, the application of magnetic field seems to drive the system away from a situation that normally prevails near the QCP. The effect of the external magnetic field (H) is to suppress magnons and thereby the coherent electron-magnon contribution. Thus, the coefficient of the T^2 term decreases with H. The temperature-dependent magnetoresistance goes through a minimum at $T_{min} = 30\ K$ at 90 kOe and has the value $\sim$ 15% (17%) at the minimum for 12 nm (18 nm), a value greater than that at the ferromagnetic-to-paramagnetic phase transition. When the temperature falls below $\sim 22\ K$ (which coincides with T_{min}), an extremely large (macroscopic) number of magnons gets thermally excited and forms a Bose-Einstein (BE) condensate at $T \lesssim T_{min}$ and $H \simeq 0$. The magnetic field of increasing strength progressively destroys the BE condensate phase coherence and suppresses the magnons, and with them the electron-magnon scattering contribution. Consequently, the value of negative magnetoresistance at T_{min} grows constantly with field. T_{min} increases with increasing magnetic field as $H^{2/3}$ [the field dependence that is the characteristic of Bose-Einstein condensation (BEC)] is consistent with the above interpretation of the large negative magnetoresistance at T_{min} in terms of the BEC picture. The magnetoresistance isotherms measured at various fixed temperatures also eslablish that the maximum change in magnetoresistance at 90 $kOe \sim$ 15% (17%) for $d = 12\ nm$ (18 nm) sample is occuring at $T_{min} \sim 30\ K$. Like the transverse magnetoresistance at $T = T_{min}$, the coefficients 'a' and 'b' as functions of temperature go through a dip at $T \sim 30\ K$.

References

1. P. G. De Gennes and J. Friedel, *J. Phys. Chem. Solids* **4**, 71 (1958).

2. T. Kasuya, *Prog. Theor. Phys. (Kyoto)* **22**, 227 (1959).

3. K. A. McEwen, *Handbook on the Physics and Chemistry of Rare Earths*, edited by K. A. Gschneidner, Jr. and L. Eyring (North-Holland Publishing Company, 1978) **Vol 1**, Ch. **6**, p **411**.

4. S. Legvold, *Magnetic Properties of Rare Earth Metals*, edited by R. J. Elliott (London: Plenum, 1972) Ch. **7**.

5. R. V. Colvin, S. Legvold and F. H. Spedding, *Phys. Rev.* **120**, 741 (1960).

6. H. E. Nigh, S. Legvold and F. H. Spedding, *Phys. Rev.* **132**, 1092 (1963).

7. K. A. McEwen, G. D. Webber and L. W. Roeland, *Physica* **88-88B**, 531 (1977).

8. T. Hiroaka and M. Suzuki, *J. Phys. Soc. Japan* **31**, 1361 (1971).

9. J. M. Ziman, *Electrons and Phonons: The Theory of Transport Phenomena in Solids* (Oxford University, London, 1960) p **285**, **364**.

10. S. N. Kaul, *J. Phys.: Condens. Matter* **17**, 5595 (2005).

11. F. Goedsche, A. Möbius and A. Richter, *Phys. Stat. Sol. (b)* **96**, 279 (1979).

12. S. N. Kaul, W. Kettler and M. Rosenberg, *Phys. Rev. B* **33**, 4987 (1986).

13. J. K. Alstad, R. V. Colvin and S. Legvold, *Phys. Rev.* **123**, 418 (1961).

14. S. Yu. Dan'kov, A. M. Tishin, V. K. Pecharsky and K. A. Gschneidner, Jr., *Phys. Rev. B* **57**, 6 3478 (1998).

15. M. E. Fisher and J. S. Langer, *Phys. Rev. Lett.* **20**, 665 (1968).

16. F. J. Darnell, *Phys. Rev.* **130**, 1825 (1963).

17. F. J. Cadieu and D. H. Douglas, Jr., *Phys. Rev. Lett.* **21**, 680 (1968).

18. D. J. W. Geldart, K. De'Bell, J. Cook and M. J. Laubitz, *Phys. Rev. B* **35**, 8876 (1987).

19. S. Srinath and S. N. Kaul, *Phys. Rev. B* **60**, 12166 (1999).

20. S. Srinath, S. N. Kaul and H. Kronmller, *Phys. Rev. B* **59**, 1145 (1999).

21. A. Aharony, *Phys. Rev. B* **13**, 2092 (1976).

22. H. G. Schuster, *Z. Phys. B* **27**, 251 (1977).

23. G. R. Stewart, *Rev. Mod. Phys.* **73**, 797 (2001).

24. P. G. Niklowtiz, F. Beckers, G. G. Lonzarich, G. Knebel, B. Salace, J. Thomasson, N. Bernhoeft, D. Braithwaite and J. Flouquet, *Phys. Rev. B* **72**, 024424(2005).

25. C. Pfeiderer, P. Böni, T. Keller, U. K. Rössler and A. Rosch, *Science* **316**, 1871 (2007).

26. R. P. Smith, M. Sutherland, G. G. Lonzarich, S. S. Saxena, N. Kimura, S. Takashima, M. Nahara and H. Takagi, *Nature* **455**, 1220 (2008).

27. A. C. Abhyankar and S. N. Kaul, *J. Phys.: Condens. Matter* **20**, 445227 (2008).

Chapter 8

Concluding Remarks

8.1 Summary and Conclusion

The irreversibility in magnetization, which sets in at temperatures close to T_C at very low fields and vanishes at a critical field, is due to the existence of metastable magnetization states which become unfavourable in the presence of external magnetic field. These metastable low-magnetization states are separated from the stable high-magnetization states by the temperature- and field-dependent effective anisotropy energy barriers caused by the intragrain and interfacial magnetic anisotropies. The time-dependent magnetization and the temperature- and field-dependent magnetic viscosity result from the thermal activation of domain magnetization over these energy barriers. The magnetic viscosity obtained from the imaginary part of the ac susceptibility, together with the logarithmic time dependence of magnetization suggests that the distribution in the energy barrier heights is very broad. The temperature dependence of the coercivity shows that the shape anisotropy also plays a crucial role in the magnetization reversal process.

The 'approach-to-saturation' is made difficult by the magnetocrystalline and magnetostatic fluctuations in nanocrystalline gadolinium.

The results of the line-shape analysis of temperature-dependent FMR spectra are anomalous in that both resonance field, H_{res}, and peak-to-peak linewidth, ΔH_{pp}, decrease with temperature till the temperature $T^* = 280\ K$, near $T_C = 285.5(1)\ K$, is reached. ΔH_{pp} is abnormally large ($\cong 3.3\ kOe$) at temperatures in the range $113\ K \leq T \leq 185\ K$. $H_{res}(T)$ and $\Delta H_{pp}(T)$, however, show a normal behavior only when T exceeds T^*, where $\Delta H_{pp}(T)$ "peaks" while $H_{res}(T)$ goes through a steep minimum. The 'in-plane' anisotropy field, $H_K(T)$, exhibits a broad peak at the spin-reorientation temperature, $T_{SR} \cong 230\ K$ and falls rapidly in magnitude as the $T_C = 285.5\ K$ is approached. The temperature dependence of M(T) has nearly the same functional dependence on temperature as the 'zero-field-cooled' magnetization observed at a field that is an order of magnitude smaller than $H_{res}(T)$ and a much lower magnitude at all temperatures compared to that expected for a normal ferromagnet. The anomalous features in M(T), $H_{pp}(T)$ and $H_{res}(T)$ are basically due to the strong random intra-grain anisotropy (RIGA) and the interfacial random anisotropy (IRA). The unusual temperature dependence of H_K reflects a strong interplay between these two types of anisotropies with IRA proving more decisive in deciding the functional form of $H_K(T)$. The lineshape analysis of the angle-dependent FMR spectra also reveals that besides the shape anisotropy, the cubic and uniaxial magnetic anisotropies are simultaneously present and they mimic the random intra-grain anisotropy and the interfacial random anisotropy in nanocrystalline Gd.

The observation of the anomalous softening of spin-wave modes at low

temperatures in nanocrystalline gadolinium is interpreted as the Bose-Einstein condensation (BEC) of magnons. The physical quantities that characterize the BEC transition such as the BEC temperature, $T_c(H)$, the average occupation number for the ground state (the BEC order parameter), $\langle n_0 \rangle$, the chemical potential, μ, and the condensate coherence volume, V, have been determined self-consistently for the first time. The volume over which the condensate wavefunction retains its phase coherence shrinks by nearly 14 (6) orders of magnitude from its value 0.0075(5) cm^3 (1.1(6) $\times$ 10^{-11} cm^3) at $H = 0$ for $d = 12$ nm (18 nm) and approaches the volume of a single grain as fields in excess of 30 kOe are applied. The observations that (i) T_c increases with H as $T_c(H) = T_c(H = 0) + aH^{2/3}$, (ii) at $H = 0$, the condensate fraction decreases linearly with $(T/T_c)^{3/2}$ to zero at $T = T_c$ and remains zero for $T > T_c$, (iii) $T_c(H) \propto (field - dependent\ condensate\ fraction)^{2/3}$, (iv) $\mu \to 0$ as $H \to 0$ for $T \leq T_c$ and abruptly falls to large negative values as the temperature exceeds T_c, and (v) the field-induced change in magnetic entropy, ΔS_{mag}, follows the $T^{3/2}$ power law at low temperatures and goes through a peak at $T^*(H)$ establish that magnons in nanocrystalline gadolinium undergo BEC transition at low temperatures ($T \lesssim 20$ K).

The temperature-dependent magnetization, $M(T)$, (specific heat, $C(T)$), measured on nanocrysatlline Gd samples at a number of fixed magnetic fields up to 90 kOe (at H = 0 Oe, 20 kOe, 40 kOe and 50 kOe), shows that the ferromagnetic (FM) - to - paramagnetic (PM) transition temperature, T_C, is shifted down by 7.4 K (5.8 K) compared to the T_C (293 K) of single crystal Gd as well as the peak value of the cusp in $C_H(T)$ smeared out considerably as the grain size is reduced. This is because the finite grain size limits the divergence of the spin-spin correlation length and thereby

causes a size-dependent shift in T_C to lower temperatures. The peak values of the isothermal entropy change, $\Delta S_{mag}(T,H)$, and adiabatic temperature change, $\Delta T_{ad}(T,H)$, calculated from the measured magnetization, $M(T,H)$, and specific heat, $C(T,H)$, at different fields, H, are reduced by roughly a factor of 1.5 but the corresponding full-width-at-half-maximum, δT_{FWHM}, are broader by nearly a factor of 2 in nanocrystalline Gd compared to those reported previously in single crystal Gd. At a given H, the peaks in $\Delta S_{mag}(T,H)$ and $\Delta T_{ad}(T,H)$ shift to lower temperatures, get progressively suppressed and broaden considerably as the average nanocrystallite size reduces. The temperature at which $\Delta S_{mag}(T,H)$ peaks, T_{peak}, lies above T_C and increases with H as $H^{1/3}$. At $T = T_C$, $\Delta S_{mag}(T,H)$ does obey the mean-field prediction $\Delta S_{mag}|_{T=T_C} \sim H^{2/3}$. The reduction in the average grain size from a macroscopic size in single crystal Gd to $d = 12\ nm$ in nanocrystalline Gd does not alter the relative cooling power (RCP, product of the maximum of $\Delta S_{mag}(T,H)$ or $\Delta T_{ad}(T,H)$ and the corresponding δT_{FWHM}, which serves as a figure of merit for the magnetic refrigeration application) for fields $H \leq 50\ kOe$ but when $H \geq 60\ kOe$, RCP, at a given field, increases with the grain size.

The residual resistivity in nanocrystalline Gd is an order of magnitude higher than that in polycrystalline Gd and single crystal Gd. The temperature dependence of resistivity in nanocrystalline Gd, when compared with the resistivity of single crystal Gd measured along the c-axis and b-axis, suggests that the crystallographic directions in different nanocrystalline grains in nanocrystalline Gd are randomly oriented. The change in (positive) slope of the temperature-dependent resistivity in the critical region ($T \cong T_C$), similar to that observed in single crystal Gd, is better described by the

three-dimensional random uniaxial dipolar ferrmagnet model. The observation that the residual resistivity decreases with increasing field provides a strong evidence for the contribution to residual resistivity by the spins at grain boundaries and within the domain walls, as hardly any spin waves get excited at $T \cong 0\ K$. The 'zero-field', $\rho_{H=0}(T)$, and 'in-field' resistivity, $\rho_H(T)$, both vary with temperature as $T^{3/2}$ (non-Fermi liquid behaviour) at low temperatures ($\leq 40\ K$) and fields ($\leq 5\ kOe$) and exhibit a slope change at $T^+ \simeq 16.5\ K$. Normally, the non-Fermi liquid behaviour is observed in the vicinity of the quantum critical point (QCP). As the field increases beyond 5 kOe, the $T^{3/2}$ variation of $\rho_H(T)$ at low temperatures changes over to the Fermi liquid T^2 variation. The transverse magnetoresistance, $\Delta\rho_\perp(T)$, goes through a minimum at $T_{min} \simeq 22\ K$ when $H = 10\ kOe$. T_{min} increases with field as $H^{2/3}$. The minimum value of $\Delta\rho_\perp(T)$ at $T = T_{min}$ decreases exponentially from $\sim 0.2\%$ (1%) at 10 kOe to 15% (17%) at 90 kOe for the nanocrystalline Gd sample with $d = 12\ nm$ (18 nm). The negative magnetoresistance has a much larger value at $T = T_{min}$ than that in a normal ferromagnet at $T = T_C$. The above observations along with finding that an anomalous softening of spin-wave modes occurs when the temperature falls below $T_c \simeq 22\ K$ (which coincides with T_{min}) lead to the conclusion that an extremely large (macroscopic) number of magnons gets thermally excited and forms a Bose-Einstein (BE) condensate at $H \approx 0$ when $T \leq T_{min}$.

The final picture that seems to emerge from the above results is as follows. The interplay between the intra-grain and the interfacial random magnetic anisotropies along with the shape anisotropy results in a non-collinear spin structure at the grain boundary in nanocrystalline gadolin-

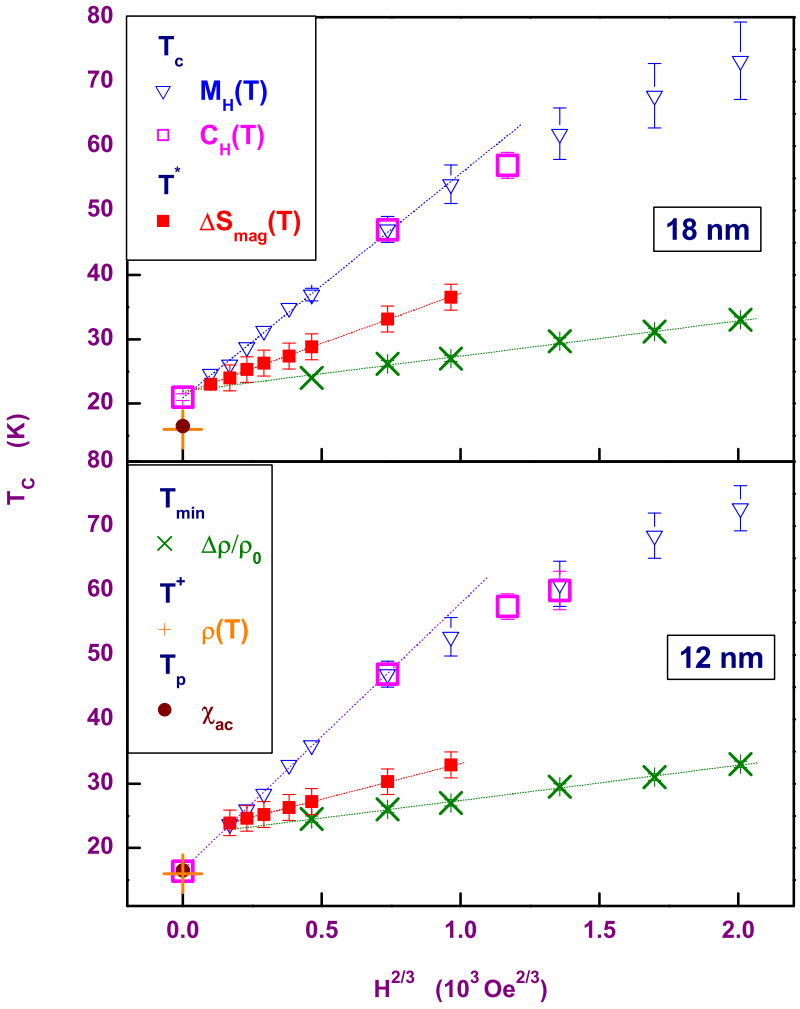

Figure 8.1: The BEC temperatures, T_c, determined from $M(T)$ and $C_H(T)$ or the BEC equivalent characteristic temperature, T^*, determined from $\Delta S_{mag}(T)$, T_{min}, from $\Delta\rho_\perp(T)/\rho_0$, T^+, the temperature at which $\rho(T)$ vs. $T^{3/2}$ has a slope change, and T_p, the temperature at which ac susceptibility peaks, all plotted against $H^{2/3}$.

ium. Since the intra-grain magnetic anisotropy is temperature-dependent, the non-collinear spin structure at the grain boundary varies with temperature. The non-collinear spin state reduces the spin-wave stiffness, and thereby softens the spin wave modes, and establishs spontaneous phase coherence of magnon BE condensate wavefunction as the temperature falls below the BEC transition temperature T_c, which is well-defined only when $H = 0$. With increasing average grain size, the interfacial anisotropy, in particular, is altered and so is the interplay between the intra-grain and interfacial anisotropies. Modified interplay, in turn, causes a reduction in the non-collinearity, increases the spin-wave stiffness D, suppresses the spontaneous phase coherence and hence the condensate fraction. The effective mass of magnons decreases as the spin-wave stiffness increases and consequently, T_c increases with the average grain size. Magnetic field tends to make the spin structure more collinear, destroy phase coherence and thereby reduces the BEC condensate coherence volume, V, and the average occupation number for the ground state $\langle n_0(T = 1.8K)\rangle$ such that $\langle n_0(T = 1.8K)\rangle/V$ increases with H and so does T_c in accordance with the $H^{2/3}$ BEC law (Fig.8.1). Next, we comment upon the observation, based on the data presented in figure 8.1, that the values of the BEC transition temperature or an equivalent BEC characteristic temperature at different fields, as determined from magnetization ($T_c(H)$, $\triangledown$), specificheat ($T_c(H)$, $\square$), entropy change ($T^*(H)$, $\blacksquare$), transverse magnetoresistance ($T_{min}(H)$, $\times$), 'zero-field' resistivity ($T^+(H)$, $+$) and ac susceptibility ($T_p(H)$, $\bullet$), are widely different and yet all of them follow the characteristic BEC $H^{2/3}$ variation. While magnetization and specific heat data yield directly $T_c(H)$, the BEC gets reflected in the remaining measurements *indirectly*. For instance, $T^*(H)$ marks the temperature at which the magnetic field-induced change

in magnon entropy exhibits a change in slope as a function of temperature much the same way as $T_c(H)$ is the temperature at which a slope change in the (absolute) magnon entropy as a function of temperature occurs at different but fixed fields. Similarly, BEC manifests itself indirectly in the field-induced change in the electron-magnon contribution to resistivity, i.e., in the form of a minimum in the negative magnetoresistance at T_{min}. Thus, it is not surprising that the BEC characteristic temperature $T^*(H)$ and $T_{min}(H)$ exhibit the $H^{2/3}$ dependence on H but lie consistently below the BEC transition temperature $T_c(H)$.

8.2 Future Scope

The results of the present investigation underscore the need to map the spin structure within the grains and at grain boundaries in the BEC as well as the normal states in nanocrystalline gadolinium. To this end, the first step could be the magnetic force microscopy and Kerr-microscopy studies. The $T^{3/2}$ variation of resistivity for $H \leq 5\ kOe$ (i.e., the non-Fermi liquid behaviour) at $T \leq 16.5\ K$ is indicative of significant deviations from the conventional magnon dispersion relaxation $\hbar\omega = \Delta + Dk^2$ in that it may not be quadratic in the wave vector k. To ascertain whether or not this is true, inelastic neutron scattering experiments need to be performed on nanocrystalline gadolinium at low temperatures.

List of Publicatins

1. 'Anomalous Resonant Microwave Absorption in Nanocrystalline Gadolinium: Role of Magnetic Anisotropy'.
   S. N. Kaul and S. P. Mathew
   Nanoscience and Nanotechnology Letters (at press).

2. 'Magnons as a Bose-Einstein Condensate in nanocrystalline Gadolinium'.
   S. N. Kaul and S. P. Mathew
   Physical Review Letters **106**, 247204 (2011).

3. 'Bose-Einstein Condensation of Magnons in polycrystalline Gadolinium with nano-size grains'.
   S. P. Mathew and S. N. Kaul
   Journal of Physics: Condensed Matter **23**, 266003 (2011).

4. 'Tuning magnetocaloric effect with nanocrystallite size'.
   S. P. Mathew and S. N. Kaul
   Applied Physics Letters **98**, 172505 (2011).

5. 'Bose-Einstein condensation of magnons in Magnetic systems'.
   S. N. Kaul and S. P. Mathew
   AIP Conference Proceedings (ICMM - 2010) **1347**, 41 (2011).

6. 'Magnetization Processes in nanocrystalline Gadolinium: Role of magnetic anisotropy'.
   S. P. Mathew and S. N. Kaul
   AIP Conference Proceedings (ICMM - 2010) **1347**, 15 (2011).

7. 'Magnetic irreversibility, spin wave excitations and magnetocaloric effect in nanocrystalline Gadolinium'.
   S. P. Mathew, S. N. Kaul, A. K. Nigam, A. -C. Probst and R. Birringer
   Journal of Physics: Conference Series **200**, 072047 (2010).

8. 'Ferromagnetic resonance investigation of nanocrystalline Gadolinium'.
   S. P. Mathew and S. N. Kaul
   Proceedings of DAE Solid State Physics Symposium **54**, 429 (2009).

9. 'Magnetic irreversibility, spin wave excitations and magnetocaloric effect in nanocrystalline Gadolinium'.
   S. P. Mathew, S. N. Kaul, A. K. Nigam, A. -C. Probst and R. Birringer
   Proceedings of DAE Solid State Physics Symposium **53**, 425 (2008).

Manuscripts Under Preparation

1. 'Magnetization reversal, relaxation and approach-to-saturation in nanocrystalline Gadolinium'.

2. 'Electrical- and magneto-transport in nanocrystalline Gadolinium'.

Papers Presented at National and International Conferences

1. 'Magnetization processes in nanocrystalline Gadolinium: Role of magnetic anisotropy'.

S. P. Mathew and S. N. Kaul
International conference on magnetic materials, SINP, Kolkata, October 2010

2. 'Bose-Einstein Condensation of magnons in nanocrystalline Gadolinium'.
   S. P. Mathew, S. N. Kaul and A. K. Nigam
   India Singapore Joint Physics Symposium, University of Hyderabad, Hyderabd, February 2010.

3. 'Ferromagnetic resonance investigation of nanocrystalline Gadolinium'.
   S. P. Mathew and S. N. Kaul
   54th DAE Solid State Physics Symposium, M. S. University, Baroda, December 2009

4. 'Magnetic irreversibility, spin-wave excitations and magnetocaloric effect in nanocrystalline Gadolinium'.
   S. P. Mathew, S. N. Kaul, A. K. Nigam, A. C. Probst, R. Birringer
   International conference on magnetism, Karlsruhe, Germany, July 2009.

5. 'Magnetic irreversibility, spin-wave excitations and magnetocaloric effect in nanocrystalline Gadolinium'.
   S. P. Mathew and S. N. Kaul
   53rd DAE Solid State Physics Symposium, BARC, Mumbai, December 2008.

⋆⋆⋆